

AN ABSTRACT OF THE THESIS OF

Kiernan Michael Kelty for the degree of Master of Science in Civil Engineering presented on June 1, 2021.

Title: Prototype-Scale Physical Model Study of Wave Attenuation by an Idealized Mangrove Forest of Moderate Cross-shore Width

Abstract approved: _____

Daniel T. Cox

The use of natural and nature-based features for coastal hazard mitigation, particularly emergent vegetation such as mangrove forests, have become increasingly popular. However, the protection that these systems can provide has not been fully quantified for engineering design, and the uncertainties in parameterized equations have not been fully defined. In particular, laboratory investigations of wave attenuation by vegetation have typically been conducted at reduced scales using Froude similitude. The drag coefficients derived from these studies have been shown to be a function of the Reynolds number, for which Reynolds similitude cannot be maintained when Froude similitude is achieved in reduced scaled tests. Therefore, the purpose of this thesis is to conduct a prototype-scale physical model study that can quantify the wave attenuation by an idealized mangrove forest and to develop scaling relations to utilize previous and future reduced-scale tests.

For the study, a prototype-scale physical model was constructed in the Large Wave Flume at the O.H. Hinsdale Wave Research Laboratory, Oregon State University. The model trees were constructed based on field observations and parameterizations from Ohira et al. (2013), where the diameter at breast height, D_{BH} , was 0.1143 m, and the diameter of the roots, D_{Root} , was 0.0286 m with 14 roots per tree. Two model forest densities of 0.75 and 0.375 trees/m² were

tested for a forest with 18 m cross-shore width. Half of the experimental tests included a vertical wall on the landward side of the model forest. The wall was intended to represent a coastal structure, and the pressure forces on the wall were measured to determine the model forest's effect on attenuating wave forces. Regular and random waves were tested at 4 water depths that ranged from shallow inundation to storm surge conditions within the model forest. Transient wave cases were also tested for the two lower water depths of the study. In total, 298 tests were completed for the study. A methodology using LiDAR measurements was developed to quantify the projected area of the idealized mangrove forests. The LiDAR results had an error of 5% from the known value for the model tree trunk section. These measurements were used to find an effective diameter, D_e . The method can be practically applied for field applications where destructive or traditional measurements using calipers would be cumbersome or unfeasible.

The results of the regular and random wave cases for the tested layouts without the wall are presented with the focus on estimating the wave attenuation and parameterized drag coefficient, C_D . For random wave cases, wave height decay coefficients for the model trees, $\tilde{\alpha}_m$ were calculated for each case. After removing the attenuation effects of the flume walls and bathymetry, the $\tilde{\alpha}_m$ values were found to be affected by the water depth and forest density. An average ratio of 2.0 was also found between the high-density (HD) to low-density (LD) forests $\tilde{\alpha}_m$ values. This was the same value as the HD/LD tree density ratio, N , ratio indicating a possible linear relationship between $\tilde{\alpha}_m$ and N . Furthermore, wave height attenuation of 14 to 28% and 6 to 16% were found for the HD and LD forests, respectively, where the highest attenuation coincided with the lowest water depth and highest measured projected area. The drag coefficients, C_D , for the study, ranged from 0.40 to 3.75 and were related to the Reynolds number, $Re_{U,De}$, in the range $4.5E3 < Re_{U,De} < 2.9E4$. The largest C_D values was associated with the lowest water depth. Uncertainties for C_D values for the study were also found based on the variability seen in the measured mean projected area per unit height per tree, $A_{t,m}$, of the model forest and the best fit for the wave height decay coefficients, $\tilde{\alpha}_m$. The uncertainty from these two parameters were combined to overall uncertainty for the C_D values. By scaling the Reynolds number according to Froude similitude, it was possible to rescale previous studies to agree well with the C_D estimates for both regular and random wave cases, with the Reynolds number estimated using the diameter at breast height, DBH , and the depth averaged velocity, U . An empirical equation of the form $C_D = a_1 + (a_2/Re_{U,DBH})^{a_3}$ gave a best fit to the combined data with

values $a_1=0.70$, $a_2=26,000$, $a_3=1.0$ with $R^2=0.63$ in the range $4.9E3 < Re_{U,DBH} < 1.9E5$. The coefficients of $a_1=0.6$, $a_2=30,000$, $a_3=1.0$ and $R^2 = 0.63$ are suggested for engineering design so that the asymptote is 0.6, consistent with the work of Sarpkaya and Isaacson (1981) for waves on vertical piles.

©Copyright by Kiernan Michael Kelty

June 1, 2021

All Rights Reserved

Prototype-Scale Physical Model Study of Wave Attenuation by an Idealized Mangrove Forest of
Moderate Cross-shore Width

by

Kiernan Michael Kelty

A THESIS

submitted to

Oregon State University

in partial fulfillment of

the requirements for the

degree of

Master of Science

Presented June 1, 2021

Commencement June 2021

Master of Science thesis of Kiernan Michael Kelty presented on June 1, 2021.

APPROVED:

Major Professor, representing Civil Engineering

Head of the School of Civil and Construction Engineering

Dean of the Graduate School

I understand that my thesis will become part of the permanent collection of Oregon State University libraries. My signature below authorizes release of my thesis to any reader upon request.

Kiernan Michael Kelty, Author

ACKNOWLEDGEMENTS

I would like to sincerely thank the following people for their support on this project:

- Daniel Cox, for the opportunity to pursue my graduate studies, work on this project, and for your guidance for the past two years at Oregon State University.
- Tori Tomiczek, for providing funding for the project and giving valuable feedback, and advice throughout the project.
- Pedro Lomónaco, for your counsel while working at the O.H. Hinsdale Wave Research Laboratory and assisting with the project's data analysis.
- Meagan Wengrove and John Nabeleck for your valuable feedback, and thoughtful questions.
- Tim Maddux, Rebecca Miller, and the rest of the wave lab staff for your assistance with experimental design, instrumentation, and data collection.
- Jamie Shultz, Courtney Beringer, Bruce Kim, and Chuan Lee for your help with the physical model construction.
- Chris O'Day for your help with the field data collection, physical model construction for the project and for being a great friend.
- Will Mitchell for your help with the experimental design, instrumentation, and data collection.
- Esteban Biondi for your mentorship before coming to Oregon State University, participation in the field data collection, thoughtful feedback on the project results, and providing the catalyst for this project.
- Greg Braun, Dave Carson, Carman Vare, Michael Jenkins, and Diego Delgado for your time, knowledge and boat transportation during the field data collection.
- Eric Anderson for the opportunity to present the project results with stakeholders in southeastern Florida.
- Michel Olsen for your advice and help with the framework for the LiDAR methodology presented in the thesis.

- Leica Geosystems for their donation of the Cyclone software used for the LiDAR analysis in this thesis.
- My parents, Shelia O'Brien and Michael Kelty, My brother, Griffin Kelty, and my girlfriend Ana Vega, for all their love, support, and encouragement throughout my time at Oregon State University
- Evan Pesut and Camila Bauer for your friendship and support throughout this thesis.
- All of the friends that I have made since coming to Oregon State University.

The material of this thesis is based upon work supported by the National Science Foundation under the awards 1519679, 1661315, and 1825080. Any opinions, findings, conclusions, or recommendations expressed in this material are those of the author and do not necessarily reflect the views of the National Science Foundation.

TABLE OF CONTENTS

	<u>Page</u>
Chapter 1. Introduction.....	1
1.1. Problem Description and Statement.....	1
1.2. Study Objectives	2
Chapter 2. Background	3
2.1. Literature Review.....	3
2.1.1. Theoretical Background.....	3
2.1.2. Field Studies.....	4
2.1.3. Numerical Studies	5
2.1.4. Laboratory Studies	5
2.1.5. Mangrove Characteristics	7
2.1.6. Mangrove Projected Area Comparison.....	14
2.2. Field Data Collection	15
2.3. Webinar Series	20
Chapter 3. Experimental Setup.....	21
3.1. Safety Protocols.....	21
3.2. Facility and Instrument Descriptions	21
3.2.1. Large Wave Flume and Wavemaker.....	21
3.2.2. Instrumentation	22
3.2.2.1. Free Surface	22
3.2.2.2. Velocity	22
3.2.2.3. Pressure Transducers	22
3.2.2.4. Accelerometers	23
3.2.2.5. Video	23
3.2.2.6. LiDAR	23
3.2.2.7. Data Acquisition	24
3.2.3. Large Wave Flume Configuration.....	24
3.2.4. Mangrove Specimen and Test Section	25
3.2.5. Test Wall	30
3.2.6. Instrument Placement.....	32
3.2.6.1. Incident and Reflected Waves	33

TABLE OF CONTENTS (Continued)

	<u>Page</u>
3.6.2. Wave Attenuation	33
3.6.3. Velocity Profile in Model Forest	33
3.6.4. Test Wall	34
Chapter 4. Experimental Procedures	35
4.1. Selection of Layouts 1 to 6.....	35
4.2. Selection of Water Depth and Generation of Wave Conditions	36
4.2.1. Water Depths	36
4.2.2. Regular Waves	39
4.2.3. Random Waves	42
4.2.4. Transient Waves.....	44
4.3. Test Schedule	44
4.4. LiDAR Scans.....	46
4.1. Data Processing and Quality Control.....	49
4.2. Data Backup and DesignSafe	49
4.3. Data Analysis	49
4.3.1. Incident and Reflected Waves	49
4.3.2. Time Series Analysis	50
Chapter 5. LiDAR Analysis.....	50
5.1. High Density Model Forest	50
5.2. Low Density Model Forest.....	54
5.3. Model Forest Comparison.....	56
5.4. Effective Diameter	60
5.5. Previous Studies Comparison	64
Chapter 6. Experimental Results, Random Waves.....	66
6.1. Frequency versus Time Domain Analysis	66
6.2. Wave Attenuation.....	67
6.3. Drag Coefficients	74
6.3.1. Projected Area Uncertainty	78
6.3.2. Decay Rate Uncertainty	80
6.3.3. Combined Uncertainty	82

TABLE OF CONTENTS (Continued)

	<u>Page</u>
6.3.4. Previous Study Comparisons	84
Chapter 7. Discussion	91
Chapter 8. Conclusions.....	93

LIST OF FIGURES

<u>Figure</u>		<u>Page</u>
2-1	Example of intertwined mangrove root system from multiple trees.....	15
2-2	Map of morning sites (yellow pins) with closest boat ramp (pink pin) and tide gauges (blue pin). Lake Worth, FL	16
2-3	Overview of Site #1 location in the Snook Islands. Lake Worth, FL	17
2-4	Overview of Site #2 location at Beach Point Condo restoration at the water's edge. Lake Worth, FL.....	17
2-5	Overview of Site #3 location at Beach Point Condo restoration further landward into the forest. Lake Worth, FL.....	18
2-6	Map of the afternoon sites (yellow pins) with closest boat ramp (pink pins) and tide gauge (blue pin). Stuart, FL	19
2-7	Overview of Site #4 located at Twin Rivers Park. Stuart, FL	19
2-8	Overview of Site #5, USACE Gabion site located on the northwestern tip of Jupiter Island. Stuart, FL.....	20
2-9	Overview of Site #6 located at in St. Lucie Inlet State Park. Stuart, FL	20
3-1	A). Front-view and top-view of Large Wave Flume (LWF) configuration and layout. B). Zoomed in front-view of the LWF detailing the model forest.....	25
3-2	Example of idealized Ohira et al. (2013) model mangrove tree.	26
3-3	Model tree spacing in each bay, black dashed lines designate rows.	28
3-4	Overview of high-density model forest.	28
3-5	Overview of low-density model forest, dashed lines designate rows.....	29
3-6	Example of forest cross section.	29
3-7	Drawing of test wall installed in Large Wave Flume.	31
3-8	A). Seaward side of the test wall, B). Landward side of the test wall secured by red clips to the walls of the flume.....	31
3-9	Overview of instrument placement in the Large Wave Flume.	32
3-10	Custom mount used for vertical stack of Acoustic Doppler Velocimeters.....	34
3-11	Instrumentation layout on the wall where: PDCR 1830 (orange rectangles), PDCR 830 (grey rectangles), Kistler pressure gauges (green half circles), and Kistler accelerometers (pink diamonds) are shown.....	35
4-1	Layouts 1 to 6 of the Large Wave Flume.	36
4-2	Idealized CAD sketch of model forest cross section in the Large Wave Flume.	37
4-3	Projected area per unit height, A , versus water depth at vegetation, h_v , for model forest cross section in the Large Wave Flume.	38

LIST OF FIGURES (Continued)

<u>Figure</u>		<u>Page</u>
4-4 Non-dimensional plot of H/h versus h/L for the target regular wave cases. Graph source: Pedro Lomónaco.....		40
4-5 Non-dimensional plot of H_{m0}/h_v versus h_v/L_p for the target random wave cases. Graph source: Pedro Lomónaco.....		43
4-6 BLK 360 mounted to tripod scanning the model forest.....		46
4-7 Locations of the high-density (HD) LiDAR scans taken from November 3 rd – 5 th , 2020.....		47
4-8 A). BLK 360 mounted to middle of Unistrut. B). BLK 360 positioned in the middle of the Large Wave Flume.....		47
4-9 Locations of the overhead high-density (HD) LiDAR scans taken on December 1 st , 2020.....		48
4-10 Locations of the overhead low-density (LD) LiDAR scans taken on December 9 th , 2020.....		48
5-1 Location of stencil cross sections (red boxes) extracted from the high-density (HD) model forest.		51
5-2 Pixilated image of the LiDAR scan from high-density (HD) stencil 1 in grayscale color scale.		52
5-3 Projected area per unit height, A , versus water depth at vegetation, h_v , for high-density (HD) stencil 1.....		53
5-4 Projected area per unit height, A , versus water depth at vegetation, h_v , for high-density (HD) mean stencil.		54
5-5 Location of stencil cross sections (red boxes) extracted from the low-density (LD) model forest.		55
5-6 Projected area per unit height, A , versus water depth at vegetation, h_v , for low-density (LD) mean stencil.		56
5-7 Projected area per unit height per tree, A_t , versus the water depth at the vegetation, h_v , for.....		57
5-8 Projected area per unit height per tree, A_t , versus the water depth at the vegetation, h_v , for the high-density (HD) mean half stencil and low-density (LD) mean stencil.		58
5-9 Projected area per unit height per tree, A_t , versus the water depth at the vegetation, h_v , for the high-density (HD) mean half stencil with error bars representing \pm one standard deviation and mean projected area per unit height per tree, $A_{t,m}$, values are shown.		59

LIST OF FIGURES (Continued)

<u>Figure</u>		
		<u>Page</u>
5-10 Example of high-density (HD) mean half stencil image segmented into 10 cm vertical bins.....	61	
5-11 Water depth at the vegetation, h_v , versus the number of roots per tree, n_R , for each 10 cm bin.....	62	
5-12 Comparison of the projected area per unit height per tree, A_t , for the studies high-density (HD) mean half stencil (Blue line and markers), Maza et al. (2019) model tree profile (black line and markers), and Chang et al. (2019) model tree profile (red line and markers).....	64	
6-1 Mean wave period, T_m from the time domain versus the mean wave period, $T_{0,1}$, from the frequency domain for the random wave cases at Array 1 for Layouts 1 to 6.....	66	
6-2 Total spectral estimate of the significant wave height, H_{m0} with respect to x location for wave gauges (WG, circles) and pressure gauges (PD, diamonds) and the incident spectral estimate of the significant wave height, $H_{m0,i}$ (triangles) and reflected spectral estimate of the significant wave height, $H_{m0,r}$ (squares) for the high-density (HD) (dark colors) low-density (LD) (intermediate colors), and baseline (BL) (light colors) layouts for random wave case TI-h3-3.	67	
6-3 Total spectral estimate of the significant wave height, H_{m0} with respect to x location for wave gauges (WG, circles) and pressure gauges (PD, diamonds) with the incident spectral estimate of the significant wave height, $H_{m0,i}$ (triangles), and reflected spectral estimate of the significant wave height, $H_{m0,r}$ (squares), and line of best fit for the high-density (HD) (dark colors) low-density (LD) (intermediate colors), and baseline (BL) (light colors) layouts of the random wave case TI-h3-3.	68	
6-4 Total spectral estimate of the significant wave height, H_{m0} with respect to x location for wave gauges (WG, circles) and pressure gauges (PD, diamonds) with mean (solid line), lower bound (dashed line) and upper bound line of best fit (dash dotted line) for the high-density (HD) layout of the random wave case TI-h3-3.	69	
6-5 Wave height decay coefficient, $\tilde{\alpha}$, versus the water depth at the vegetation, h_v , for the random wave cases at the high-density (HD) (dark blue circles), low-density (LD) (intermediate blue circles), and baseline (BL) (light blue circles) layouts.	70	
6-6 Model forest wave height decay coefficient, $\tilde{\alpha}_m$, versus water depth at the vegetation, h_v , for the random wave cases at the high-density (HD) (dark blue circles), low-density (LD) (intermediate blue circles), and baseline (BL) (light blue circles) layouts.	71	
6-7 Percent of wave attenuation for the random wave cases versus the water depth at the vegetation, h_v for the high-density (HD) (dark blue circles) and low-density (LD) (intermediate blue circles) layouts.	73	

LIST OF FIGURES (Continued)

<u>Figure</u>		<u>Page</u>
6-8	Ratio of the spectral estimate of the significant wave height, H_{m0} over the effective diameter, D_e , versus relative water depth, $k_p h_v$, for the random wave cases at the high-density (HD) (dark blue circles) and low-density (LD) (intermediate blue circles) layout trials compared to Equation 8.60 from Dean and Dalrymple (1991) (solid black line).	75
6-9	Drag coefficient, C_D , versus the Reynolds number, $Re_{U,De}$, for the HD (squares) and LD (triangles) layouts designated by relative water depth, $k_p h_v$, range. Best fit line shown as solid black line.	76
6-10	Drag coefficient, C_D , versus the Keulegan-Carpenter number, $KC_{U,De}$ for the random wave cases at the high-density (HD) (squares) and low-density (LD) (triangles) layouts designated by relative water depth, $k_p h_v$, range.	78
6-11	Drag coefficient, C_D , versus the Reynolds number, $Re_{U,De}$, for the random wave cases at the HD (squares) and LD (triangles) layouts designated by $k_p h_v$ range with limit bars (grey vertical bars) due to the $A_{t,m} \pm \sigma_{t,m}$ uncertainty.	79
6-12	Drag coefficient, C_D , versus the Reynolds number, $Re_{U,De}$, for the random wave cases at the HD (squares) and LD (triangles) layouts designated by $k_p h_v$ range with limit bars (grey vertical bars) due to the $\tilde{a}_m \pm \sigma$ uncertainty.	81
6-13	Drag coefficient, C_D , versus the Reynolds number, $Re_{U,De}$, for the random wave cases at the HD (squares) and LD (triangles) layouts designated by $k_p h_v$ range with limit bars (grey vertical bars) due to the combined uncertainty.	83
6-14	Ratio of the spectral estimate of the significant wave height, H_{m0} , over the effective diameter, D_e , versus relative water depth, $k_p h_v$, for the random wave cases at the high-density (HD) (dark blue circles) and low-density (LD) (intermediate blue circles) layouts and nominally reported values from Maza et al. (2019) compared to Equation 8.60 from Dean and Dalrymple (1991) (solid black line).	85
6-15	Drag coefficient, C_D , versus the Reynolds number, $Re_{U,DBH}$, for the random wave cases at the high-density (HD) (squares), low-density (LD) (triangles) designated by the relative water depth, $k_p h_v$, and compared to Maza et al. (2019) 1:6 scale (light green circles) and rescaled (dark green circles).	87
6-16	Drag coefficient, C_D , versus the Reynolds number, $Re_{U,DBH}$, for the regular wave cases at the high-density (HD) (squares), low density (LD) (triangles) designated by the relative water depth, $k_h v$, and compared to Maza et al. (2019) 1:6 scale (light blue circles), rescaled (dark blue circles), Chang et al. (2019) 1:7 scale (light red circles), and rescaled (dark red circles).	88
6-17	Drag coefficient, C_D , versus the Reynolds number, $Re_{U,DBH}$, for the present study's and previous studies' data. Best fit line – 1 best fit for all studies data combined.	89

LIST OF FIGURES (Continued)

<u>Figure</u>		<u>Page</u>
6-18	Drag coefficient, C_D , versus the Reynolds number, $Re_{U,DBH}$, for the present studies and previous studies data. Alternative best-fit for the combined data the asymptote value 0.6 consistent with wave forces on vertical piles, Sarpkaya and Isaacson (1981).	90
6-19	Drag coefficient C_D , versus $Re_{U,DBH}$, for the present studies data compared to previous mangrove and emergent vegetation studies equations.	91

LIST OF TABLES

<u>Table</u>		<u>Page</u>
2-1	Summary table of mangrove laboratory studies with scale, study type, mangrove data location, species type modeled, model and prototype diameter at breast height D_{BH} , and model and prototype tree density, N	9
2-2	Summary table of mangrove field studies with: study type, data location, species type encountered, diameter at breast height D_{BH} , tree density, and associated field notes..	11
3-1	Summary table of model mangrove tree dimensions: diameter at breast height, D_{BH} , Number of roots, N_R , root diameter, D_{Root} , height the tallest root from the ground H_{Rmax} , and maximum horizontal extent of the highest root from the trunk X_{Rmax}	26
3-2	Summary table of model mangrove tree roots where: Θ is the degrees of rotation clockwise around the trunk relative to the first root, H_{Ri} is the maximum vertical height each respective root pair relative to the ground, X_{Ri} is the maximum horizontal extent of each root from the trunk of the tree.....	27
4-1	Table of target regular wave cases at the test section.....	41
4-2	Table of target random wave cases at the test section.....	43
4-3	Table of the transient wave cases.	44
4-4	Calendar for the study.....	45
5-1	Mean projected area per unit height per tree, $A_{t,m}$, mean standard deviation $\sigma_{t,m}$, and $A_{t,m} \pm \sigma_{t,m}$ for each water depth at vegetation, h_v , tested.	60
5-2	Mean number of roots, n_{Rm} , mean standard deviation of the mean number of roots, σ_{Rm} , and $n_{Rm} \pm \sigma_{Rm}$ for each water depth at vegetation, h_v , tested.....	62
5-3	Mean projected area per unit height per tree, $A_{t,m}$, mean number of roots, n_{Rm} , total number of roots, n_{total} , and effective diameter, D_e , for each water depth at vegetation, h_v , tested.	63
6-1	Summary table of wave height decay, $\tilde{\alpha}_m$, and the HD/LD ratio of the $\tilde{\alpha}_m$ coefficient with corresponding measured H_{m0} and T_p values at PD18-1 for the random wave cases.	72
6-2	Summary table of percent of wave attenuation for the random wave cases with measured values of H_{m0} and T_p at PD18-1.	74
6-3	Summary table of the random wave cases with measured H_{m0} and T_p values at PD18-1, k_{phv} , H_{m0}/D_e , Predominant force based on Figure 6-8, $Re_{U,De}$, $KC_{U,De}$, and C_D values.....	77
6-4	Summary table of random wave cases with measured H_{m0} and T_p values at PD18-1, k_{phv} , $Re_{U,De}$, C_D , C_D , $A_{t,m} + \sigma_m$, and C_D , $A_{t,m} - \sigma_m$ values.	80
6-5	Summary table of the random wave cases with measured H_{m0} and T_p values at PD18-1, k_{phv} , $Re_{U,De}$, $\tilde{\alpha}_m \pm \sigma$, C_D , C_D , $\tilde{\alpha}_m + \sigma$, and C_D , $\tilde{\alpha}_m - \sigma$ values.	82

6-6	Summary table of the random wave cases with measured H_{m0} and T_p values at PD18-1, $k_p h_v$, $Re_{U,De}$, C_D , σ_{CD} , $C_D + \sigma_{CD}$, and $C_D - \sigma_{CD}$ values.....	84
-----	---	----

LIST OF APPENDICES

<u>Appendix</u>		<u>Page</u>
A	Mangrove Specimen.....	104
B	Test Wall	114
C	Instrument Coordinates	117
D	Selection of Water Levels	120
E	Regular Waves	121
F	Random Waves.....	122
G	Transient Waves	122
H	LiDAR Scans.....	124
I	LiDAR Analysis	125
I.1	High-density LiDAR Cross Sections	125
I.2	High-density Cross Section Images	127
I.3	HD Manual Measurement Check	129
I.4	HD Rotation Comparison.....	131
I.5	Low Density LiDAR Cross Sections.....	132
I.6	LD Cross Section Images	135
I.7	Effective Diameter Comparison.....	137
J	Experimental results, Random Waves.....	139
J.1	Time Domain versus Frequency Domain Analysis.....	139
J.2	Wave Attenuation.....	140
J.3	Drag Coefficients	147
J.4	Combined Uncertainty	155
J.5	Previous Studies Comparison.....	157
K	Experimental Results - Regular waves.....	158
K.1	Wave Attenuation.....	158
K.2	Drag Coefficients	175
K.3	Harmonics	185
L	Study Dissemination.....	194

LIST OF APPENDIX FIGURES

<u>Figure</u>		<u>Page</u>
9-1.	Bi-Metal Hole Saw setup with keyed extension on drill press for root pair hole drilling.	105
9-2.	A). Constructed uncoiling device used to temporarily straighten the PEX held down by lead weights. A). Temporarily uncoiled PEX pre-tensioning.	106
9-3.	A). Close up of bolt and chain securing PEX end to ratchet strap. B). Example of ratchet strap secured to fence post. C). Multiple PEX coils attached to fence.....	106
9-4.	A). Prototype tree base being assembled B). Partially finished prototype tree bases with couplings set to be glued.	107
9-5.	A). Prototype tree base being lowered into flume. B). All model bases in flume waiting to be placed. C). Model bases being placed using guide ruler and measuring tape. D). All model bases placed accordingly within flume.	108
9-6.	A). Cinderblocks being placed before fill material was added. B). Fill material being added to the mangrove section via front loader. C). Fill material being evenly spread by hand into the mangrove section.....	109
9-7.	Wave lab personal compacting fill material using a plate compactor and hand dirt tamper.....	109
9-8	A). Overview of different color groupings for model trees in each bay. B). Top view of model tree looking downward oriented normal to piston wavemaker with numbered root pairs.....	110
9-9	A). concrete truck positioned behind concrete pump. B). Close up of concrete truck feeding into the concrete pump.	113
9-10	A). Ariel view of concrete hose extended into the flume using the crane as a boom. B). Overview of concrete being poured into the flume.	114
9-11	Test wall sections being staged beside the landward side of the flume, bay 21 – 22.	115
9-12	Lower section of the wall lifted using the Large Wave Flume crane, cargo straps and eye bolts attached to the ends of the test wall and red clips being placed at each corner of the wall section.	115
9-13	Lower section of the wall lifted using the Large Wave Flume crane, cargo straps and eye bolts attached to the ends of the test wall.	116
9-14	Plot of transient wave cases stroke duration versus Goring and Keck, (1979) estimation of solitary wave period.	123
9-15	Baseline (BL) layout scans taken December 17 th , 2020.....	124
9-16	Baseline (BL) layout scans taken January 14 th , 2021.....	125
9-17	Cleaned high-density (HD) LiDAR cross section stencil 1 – bay 10 – 11.....	125
9-18	Cleaned high-density (HD) LiDAR cross section stencil 2 – bay 10 – 11.....	125

LIST OF APPENDIX FIGURES (Continued)

<u>Figure</u>		<u>Page</u>
9-19	Cleaned high-density (HD) LiDAR cross section stencil 3, Bay 11 to 12.....	126
9-20	Cleaned high-density (HD) LiDAR cross section stencil 4, Bay 11 to 12.....	126
9-21	Cleaned high-density (HD) LiDAR cross section stencil 5, Bay 12 to 13.....	126
9-22	High-density (HD) stencil 1 cross section image, Bay 10 to 11.....	127
9-23	High-density (HD) stencil 2 cross section image, Bay 10 to 11.....	127
9-24	High-density (HD) stencil 3 cross section image, Bay 11 to 12.....	128
9-25	High-density (HD) stencil 4 cross section image, Bay 11 to 12.....	128
9-26	High-density (HD) stencil 5 cross section image, Bay 12 to 13.....	129
9-27	Cleaned high-density (HD) stencil 1 at Bay 10 to 11 with manual measurements (green lines and numbers).	130
9-28	Projected area per unit height, A , versus water depth at the vegetation, h_v , for the high-density (HD) stencil 1 (blue line and markers) and the 180° rotated high-density (HD) stencil 1(red line and markers).....	131
9-29	Cleaned low-density (LD) LiDAR cross section stencil 1 – Bay 8 to 9.....	132
9-30	Cleaned low-density (LD) LiDAR cross section stencil 2 – Bay 8 to 9.....	132
9-31	Cleaned low-density (LD) LiDAR cross section stencil 3 – Bay 9 to 10.....	133
9-32	Cleaned low-density (LD) LiDAR cross section stencil 4 – Bay 9 to 10.....	133
9-33	Cleaned low-density (LD) LiDAR cross section stencil 5 – Bay 10 to 11.....	133
9-34	Cleaned low-density (LD) LiDAR cross section stencil 6 – Bay 10 to 11.....	134
9-35	Cleaned low-density (LD) LiDAR cross section stencil 7 – Bay 11 to 12.....	134
9-36	Low-density (LD) stencil 1 cross section image, Bay 8 to 9.....	135
9-37	Low-density (LD) stencil 2 cross section image, Bay 8 to 9.....	135
9-38	Low-density (LD) stencil 3 cross section image, Bay 9 to 10.....	136
9-39	Low-density (LD) stencil 4 cross section image, Bay 9 to 10.....	136
9-40	Low-density (LD) stencil 5 cross section image, Bay 10 to 11.....	137
9-41	Low-density (LD) stencil 6 cross section image, Bay 10 to 11.....	137
9-42	Low-density (LD) stencil 7 cross section image, Bay 11 to 12.....	137
9-43	Number of roots per tree, n_R , versus the water depth at the vegetation, h_v , for the MATLAB analysis method.....	138
9-44	Mean wave period, T_m , from the time domain versus the mean wave period, $T_{0,1}$, from the frequency domain of array 2 for layouts 1 – 6.....	139

LIST OF APPENDIX FIGURES (Continued)

<u>Figure</u>		<u>Page</u>
9-45	Total spectral estimate of the significant wave height, H_{m0} , with respect to x location for wave gauges (WG, circles) and pressure gauges (PD, diamonds) and the incident wave height, $H_{m0,i}$ (triangles), and reflected wave height, $H_{m0,r}$ (squares), for high-density (HD) (dark colors), low-density (LD) (intermediate colors), and baseline (BL) (light colors) layouts for random wave case TI-h1-1.	140
9-46	Total spectral estimate of the significant wave height, H_{m0} , with respect to x location for wave gauges (WG, circles) and pressure gauges (PD, diamonds) and the incident wave height, $H_{m0,i}$ (triangles), and reflected wave height, $H_{m0,r}$ (squares), for high-density (HD) (dark colors), low-density (LD) (intermediate colors), and baseline (BL) (light colors) layouts for random wave case TI-h1-2.	140
9-47	Total spectral estimate of the significant wave height, H_{m0} , with respect to x location for wave gauges (WG, circles) and pressure gauges (PD, diamonds) and the incident wave height, $H_{m0,i}$ (triangles), and reflected wave height, $H_{m0,r}$ (squares), for high-density (HD) (dark colors) layout for random wave case TI-h1-3.	141
9-48	Total spectral estimate of the significant wave height, H_{m0} , with respect to x location for wave gauges (WG, circles) and pressure gauges (PD, diamonds) and the incident wave height, $H_{m0,i}$ (triangles), and reflected wave height, $H_{m0,r}$ (squares), for low-density (LD) (intermediate colors) and baseline (BL) (light colors) layouts for random wave case TI-h2-1.	141
9-49	Total spectral estimate of the significant wave height, H_{m0} , with respect to x location for wave gauges (WG, circles) and pressure gauges (PD, diamonds) and the incident wave height, $H_{m0,i}$ (triangles), and reflected wave height, $H_{m0,r}$ (squares), for low-density (LD) (intermediate colors) and baseline (BL) (light colors) layouts for random wave case TI-h2-2.	142
9-50	Total spectral estimate of the significant wave height, H_{m0} , with respect to x location for wave gauges (WG, circles) and pressure gauges (PD, diamonds) and the incident wave height, $H_{m0,i}$ (triangles), and reflected wave height, $H_{m0,r}$ (squares), for low-density (LD) (intermediate colors) and baseline (BL) (light colors) layouts for random wave case TI-h2-3.	142
9-51	Total spectral estimate of the significant wave height, H_{m0} , with respect to x location for wave gauges (WG, circles) and pressure gauges (PD, diamonds) and the incident wave height, $H_{m0,i}$ (triangles), and reflected wave height, $H_{m0,r}$ (squares), for high-density (HD) (dark colors), low-density (LD) (intermediate colors), and baseline (BL) (light colors) layouts for random wave case TI-h3-1.	143
9-52	Total spectral estimate of the significant wave height, H_{m0} , with respect to x location for wave gauges (WG, circles) and pressure gauges (PD, diamonds) and the incident wave height, $H_{m0,i}$ (triangles), and reflected wave height, $H_{m0,r}$ (squares), for high density (HD) (dark colors), low-density (LD) (intermediate colors), and baseline (BL) (light colors) layouts for random wave case TI-h3-2.	143

LIST OF APPENDIX FIGURES (Continued)

<u>Figure</u>		<u>Page</u>
9-53	Total spectral estimate of the significant wave height, H_{m0} , with respect to x location for wave gauges (WG, circles) and pressure gauges (PD, diamonds) and the incident wave height, $H_{m0,i}$ (triangles), and reflected wave height, $H_{m0,r}$ (squares), for high-density (HD) (dark colors), low-density (LD) (intermediate colors), and baseline (BL) (light colors) layouts for random wave case TI-h4-1.	144
9-54	Total spectral estimate of the significant wave height, H_{m0} , with respect to x location for wave gauges (WG, circles) and pressure gauges (PD, diamonds) and the incident wave height, $H_{m0,i}$ (triangles), and reflected wave height, $H_{m0,r}$ (squares), for high-density (HD) (dark colors), low-density (LD) (intermediate colors), and baseline (BL) (light colors) layouts for random wave case TI-h4-2.	144
9-55	Total spectral estimate of the significant wave height, H_{m0} , with respect to x location for wave gauges (WG, circles) and pressure gauges (PD, diamonds) and the incident wave height, $H_{m0,i}$ (triangles), and reflected wave height, $H_{m0,r}$ (squares), for high-density (HD) (dark colors), low-density (LD) (intermediate colors), and baseline (BL) (light colors) layouts for random wave case TI-h4-3.	145
9-56	Drag coefficient, C_D , versus the Reynolds number, $Re_{U,Am}$, for the high-density (HD) (squares) and low-density (LD) (triangles) layouts designated by relative water depth, k_{ph_v} , range.	148
9-57	Drag coefficient, C_D , versus the Reynolds number, $Re_{U,DBH}$, for the high-density (HD) (squares) and low-density (LD) (triangles) layouts designated by relative water depth, k_{ph_v} , range.	148
9-58	Drag coefficient, C_D , versus the Reynolds number, $Re_{U,DRoot}$, for the high-density (HD) (squares) and low-density (LD) (triangles) layouts designated by relative water depth, k_{ph_v} , range.	149
9-59	Drag coefficient, C_D , versus the Keulegan-Carpenter number, $KC_{U,Am}$, for the high-density (HD) (squares) and low-density (LD) (triangles) layouts designated by relative water depth, k_{ph_v} , range.	150
9-60	Drag coefficient, C_D , versus the Keulegan-Carpenter number, $KC_{U,DBH}$, for the high-density (HD) (squares) and low-density (LD) (triangles) layouts designated by relative water depth, k_{ph_v} , range.	150
9-61	Drag coefficient, C_D , versus the Keulegan-Carpenter number, $KC_{U,DRoot}$, for the high-density (HD) (squares) and low-density (LD) (triangles) layouts designated by relative water depth, k_{ph_v} , range.	151
9-62	Drag coefficient, C_D , versus the Reynolds number, $Re_{u,De}$, for the high-density (HD) (squares) and low-density (LD) (triangles) layouts designated by relative water depth, k_{ph_v} , range.	151

LIST OF APPENDIX FIGURES (Continued)

<u>Figure</u>		<u>Page</u>
9-63	Drag coefficient, C_D , versus the Reynolds number, $Re_{u,Am}$, for the high-density (HD) (squares) and low-density (LD) (triangles) layouts designated by relative water depth, k_{phv} , range.....	152
9-64	Drag coefficient, C_D , versus the Reynolds number, $Re_{u,DBH}$, for the high-density (HD) (squares) and low-density (LD) (triangles) layouts designated by relative water depth, k_{phv} , range.....	152
9-65	Drag coefficient, C_D , versus the Reynolds number, $Re_{u,DRoot}$, for the high-density (HD) (squares) and low-density (LD) (triangles) layouts designated by relative water depth, k_{phv} , range.....	153
9-66	Drag coefficient, C_D , versus the Keulegan-Carpenter number, $KC_{u,De}$, for the high-density (HD) (squares) and low-density (LD) (triangles) layouts designated by relative water depth, k_{phv} , range.....	153
9-67	Drag coefficient, C_D , versus the Keulegan-Carpenter number, $KC_{u,Am}$, for the high-density (HD) (squares) and low-density (LD) (triangles) layouts designated by relative water depth, k_{phv} , range.....	154
9-68	Drag coefficient, C_D , versus the Keulegan-Carpenter number, $KC_{u,DBH}$, for the high-density (HD) (squares) and low-density (LD) (triangles) layouts designated by relative water depth, k_{phv} , range.....	154
9-69	Drag coefficient, C_D , versus the Keulegan-Carpenter number, $KC_{u,DRoot}$, for the high-density (HD) (squares) and low-density (LD) (triangles) layouts designated by relative water depth, k_{phv} , range.....	155
9-70	Wave height, H , with respect to x location for wave gauges (WG, circles) and pressure gauges (PD, diamonds) for the high-density (HD) (dark colors), low-density (LD) (intermediate colors), and baseline (BL) (light colors) layouts for regular wave case TR-h1-1	158
9-71	Wave height, H , with respect to x location for wave gauges (WG, circles) and pressure gauges (PD, diamonds) for the high-density (HD) (dark colors), low-density (LD) (intermediate colors), and baseline (BL) (light colors) layouts for regular wave case TR-h1-2.....	159
9-72	Wave height, H , with respect to x location for wave gauges (WG, circles) and pressure gauges (PD, diamonds) for the high-density (HD) (dark colors), low-density (LD) (intermediate colors), and baseline, (BL) (light colors) layouts for regular wave case TR-h1-3	159
9-73	Wave height, H , with respect to x location for wave gauges (WG, circles) and pressure gauges (PD, diamonds) for the high-density (HD) (dark colors), low-density (LD) (intermediate colors), and baseline (BL) (light colors) layouts for regular wave case TR-h1-4	160

LIST OF APPENDIX FIGURES (Continued)

<u>Figure</u>		<u>Page</u>
9-74	Wave height, H , with respect to x location for wave gauges (WG, circles) and pressure gauges(PD, diamonds) for the low-density (LD) (intermediate colors), and baseline (BL) (light colors) layouts for regular wave case TR-h2-1.....	160
9-75	Wave height, H , with respect to x location for wave gauges (WG, circles) and pressure gauges(PD, diamonds) for the low-density (LD) (intermediate colors), and baseline (BL) (light colors) layouts for regular wave case TR-h2-2.....	161
9-76	Wave height, H , with respect to x location for wave gauges (WG, circles) and pressure gauges (PD, diamonds) for the low-density (LD) (intermediate colors), and baseline (BL) (light colors) layouts for regular wave case TR-h2-3.....	161
9-77	Wave height, H , with respect to x location for wave gauges (WG, circles) and pressure gauges (PD, diamonds) for the low-density (LD) (intermediate colors), and baseline (BL) (light colors) layouts for regular wave case TR-h2-4.....	162
9-78	Wave height, H , with respect to x location for wave gauges (WG, circles) and pressure gauges (PD, diamonds) for the low-density (LD) (intermediate colors), and baseline (BL) (light colors) layouts for regular wave case TR-h2-5.....	162
9-79	Wave height, H , with respect to x location for wave gauges (WG, circles) and pressure gauges (PD, diamonds) for the low-density (LD) (intermediate colors), and baseline (BL) (light colors) layouts for regular wave case TR-h2-6.....	163
9-80	Wave height, H , with respect to x location for wave gauges (WG, circles) and pressure gauges(PD, diamonds) for the high-density (HD) (dark colors), low-density (LD) (intermediate colors), and baseline (BL) (light colors) layouts for regular wave case TR-h3-1	163
9-81	Wave height, H , with respect to x location for wave gauges (WG, circles) and pressure gauges(PD, diamonds) for the HD (dark colors), LD (intermediate colors), and BL (light colors) layouts for regular wave case TR-h3-2.....	164
9-82	Wave height, H , with respect to x location for wave gauges (WG, circles) and pressure gauges (PD, diamonds) for the high-density (HD) (dark colors), low-density (LD) (intermediate colors), and baseline (BL) (light colors) layouts for regular wave case TR-h3-3	164
9-83	Wave height, H , with respect to x location for wave gauges (WG, circles) and pressure gauges (PD, diamonds) for the high-density (HD) (dark colors), low-density (LD) (intermediate colors), and baseline (BL) (light colors) layouts for regular wave case TR-h3-4	165
9-84	Wave height, H , with respect to x location for wave gauges (WG, circles), and pressure gauges (PD, diamonds) for the high-density (HD) (dark colors), low-density (LD) (intermediate colors), and baseline (BL) (light colors) layouts for regular wave case TR-h3-5	165

LIST OF APPENDIX FIGURES (Continued)

<u>Figure</u>		<u>Page</u>
9-85	Wave height, H , with respect to x location for wave gauges (WG, circles) and pressure gauges (PD, diamonds) for the high-density (HD) (dark colors), low-density (LD) (intermediate colors), and baseline (BL) (light colors) layouts for regular wave case TR-h3-6	166
9-86	Wave height, H , with respect to x location for wave gauges (WG, circles) and pressure gauges (PD, diamonds) for the high-density (HD) (dark colors), low-density (LD) (intermediate colors), and baseline (BL) (light colors) layouts for regular wave case TR-h4-1	166
9-87	Wave height, H , with respect to x location for wave gauges (WG, circles) and pressure gauges (PD, diamonds) for the high-density (HD) (dark colors), low-density (LD) (intermediate colors), and baseline (BL) (light colors) layouts for regular wave case TR-h4-2	167
9-88	Wave height, H , with respect to x location for wave gauges (WG, circles) and pressure gauges (PD, diamonds) for the high-density (HD) (dark colors), low-density (LD) (intermediate colors), and baseline (BL) (light colors) layouts for regular wave case TR-h4-3	167
9-89	Wave height, H , with respect to x location for wave gauges (WG, circles) and pressure gauges (PD, diamonds) for the high-density (HD) (dark colors), low-density (LD) (intermediate colors), and baseline (BL) (light colors) layouts for regular wave case TR-h4-4	168
9-90	Wave height, H , with respect to x location for wave gauges (WG, circles) and pressure gauges (PD, diamonds) for the high-density (HD) (dark colors), low-density (LD) (intermediate colors), and baseline (BL) (light colors) layouts for regular wave case TR-h4-5	168
9-91	Wave height, H , with respect to x location for wave gauges (WG, circles) and pressure gauges (PD, diamonds) for the high-density (HD) (dark colors), low-density (LD) (intermediate colors), and baseline (BL) (light colors) layouts for regular wave case TR-h4-6	169
9-92	Wave height decay coefficient, α , versus the water depth at the vegetation, h_v , for the	169
9-93	Model forest wave height decay coefficient for regular waves, α_m , versus water depth at the vegetation, h_v , for high-density (HD) (dark blue circles), low-density (LD) (intermediate blue circles), and baseline (BL) (light blue circles) layouts.	171
9-94	Percent of wave attenuation for the regular wave cases due to the model forest versus the water depth at the vegetation, h_v , for the high-density (HD) (dark blue circles) and low-density (LD) (intermediate blue circles) layouts.....	173

LIST OF APPENDIX FIGURES (Continued)

<u>Figure</u>	<u>Page</u>
9-95	Ratio of the spectral estimation of the wave height, H , over the effective diameter, D_e , versus the relative water depth, kh_v , for the regular wave cases at the high-density (HD) (dark blue circles) and low-density (LD) (intermediate blue circles) layouts compared to Equation 8.60 from Dean and Dalrymple (1991) (solid black line)..... 175
9-96	Drag coefficient, C_D , versus the Reynolds number, $Re_{U,De}$, for the regular wave cases at high-density (HD) (squares) and low-density (LD) (triangles) layouts designated by relative water depth, kh_v , range. 176
9-97	Drag coefficient, C_D , versus the Keulegan-Carpenter number, $KC_{U,De}$, for the regular wave cases at high-density (HD) (squares) and low-density (LD) (triangles) layouts designated by relative water depth, kh_v , range. 176
9-98	Drag coefficient, C_D , versus the Reynolds number, $Re_{U,De}$, for the regular wave cases (orange scale symbols) and random wave cases (gray scale symbols) at the high-density (HD) (squares) and low-density (LD) (triangles) layouts designated by relative water depths, kh_v , and $k_p h_v$, ranges..... 177
9-99	Drag coefficient, C_D , versus the Reynolds number, $Re_{U,De}$, for the regular wave cases at high-density (HD) (squares) and low-density (LD) (triangles) layouts designated by relative water depth, $k_p h_v$, range with limit bars (grey vertical bars) due to the mean projected area per unit height per tree uncertainty, $A_{t,m} \pm \sigma_{t,m}$ 179
9-100	Drag coefficients, C_D , versus the Reynolds number, $Re_{U,De}$, for the regular wave cases at the high-density (HD) (squares) and low-density (LD) (triangles) layouts designated by relative water depth, kh_v , range with limit bars (grey vertical bars) due to the best fit wave height decay uncertainty, $\alpha_m \pm \sigma$ 181
9-101	Drag coefficient, C_D , versus the Reynolds number, $Re_{U,De}$, for the regular wave cases at the high-density (HD) (squares) and low-density (LD) (triangles) layouts designated by relative water depth, kh_v , range with limit bars (grey vertical bars) from the combined uncertainty of the mean projected area per unit height per tree, $A_{t,m} \pm \sigma_{t,m}$, and the best fit wave height decay, $\alpha_m \pm \sigma$.. 183
9-102	Spectral estimate of the significant wave height, H_{m0} , using harmonics 1 -3 versus the calculated spectral estimate of the significant wave height, H_{m0} , for the regular wave cases for WG 3 – 7 (blue circles) and WG 8 – 12 (orange circles). Black line represents agreement between values..... 185
9-103	Ratio of HD/BL var_{avg} , versus Trial number for harmonic: 1 (blue circles), 2 (orange circles), and 3 (grey circles) for WG 3 – 7. Trial number found in Table 9-32. 188
9-104	Ratio of HD/BL var_{avg} , versus Trial number for harmonic: 1 (blue circles), 2 (orange circles), and 3 (grey circles) for WG 8 – 12. Trial number found in Table 10-33.... 189
9-105	Ratio of LD/BL var_{avg} , versus Trial number for harmonic: 1 (blue circles), 2 (orange circles), and 3 (grey circles) for WG 3 – 7. Trial number found in Table 9-34. 191

LIST OF APPENDIX FIGURES (Continued)

<u>Figure</u>		<u>Page</u>
9-106	Ratio of LD/BL var_{avg} , versus Trial number for harmonic: 1 (blue circles), 2 (orange circles), and 3 (grey circles) for WG 8 – 12. Trial number found in Table 10-35.....	191
9-107	Average variance, var_{avg} , of case TR-h3-4 for harmonic 1 at the baseline (BL) (light blue circles), high-density (HD) (dark blue circles), and low-density (LD) (intermediate blue circles) layouts for WG 3-7 and WG 8 – 12 with limit bars \pm the standard deviation of the average variance, $var_{avg} \sigma$	192
9-108	Average variance, var_{avg} , of case TR-h3-4 for harmonic 2 at the BL (light blue circles), HD (dark blue circles) and LD (intermediate blue circles) for WG 3-7 and WG 8 – 12 with limit bars \pm the standard deviation of the average variance, $var_{avg} \sigma$	192
9-109	Average variance, var_{avg} , of case TR-h3-4 for harmonic 3 at the BL (light blue circles), HD (dark blue circles) and LD (intermediate blue circles) for WG 3-7 and WG 8 – 12 with limit bars \pm the standard deviation of the average variance, $var_{avg} \sigma$	193

LIST OF APPENDIX TABLES

<u>Table</u>		<u>Page</u>
9-1	Model tree root hole locations with hub couple offset included.....	104
9-2	Root lengths and centers for blue model trees.....	111
9-3	Root lengths and centers for red model trees.....	111
9-4	Root lengths and centers for black model trees.....	111
9-5	Root lengths and centers for yellow model trees.....	112
9-6	Coordinates for wave gauges (WG) and ultrasonic wave gauges (USWG) placed in the Large Wave Flume.....	117
9-7	Coordinates for PDCR 1830 pressure gauges (PD18) used in model forest.....	117
9-8	Coordinates for USNA pressure gauges (USNA P) used in model forest.....	118
9-9	Coordinates for the Acoustic Doppler Velocimeters (ADV) used in model forest for Layout 1.....	118
9-10	Coordinates for the Acoustic Doppler Velocimeters (ADV) used in model forest for Layouts 2 to 6.....	118
9-11	Coordinates for PDCR 1830 pressure gauges (PD18) and PDCR 830 pressure gauges (PD8) used for the test wall.....	119
9-12	Coordinates for Kistler pressure gauges (KP) and Kistler accelerometers (ACC) used for the test wall.....	119
9-13	Table of projected area per unit height, A , versus water depth at vegetation,.....	120
9-14	Table of target regular wave cases at the piston wavemaker.....	121
9-15	Table of target random wave cases at the piston wavemaker.....	122
9-16	Stroke durations of transient waves for different delta percent values and scale factors.....	124
9-17	Measured average, standard deviation, and absolute percent error of trunk and root diameters from known values for high-density (HD) stencil 1 LiDAR cross section.....	130
9-18	Mean number of roots, n_{Rm} , mean standard deviation σ_{Rm} , $n_{Rm} \pm \sigma_{Rm}$, and the absolute percent difference from the visual results n_{Rm} values for each water depth at vegetation, h_v , tested.....	139
9-19	Table of wave height decay coefficients, $\tilde{\alpha}$, and $\tilde{\alpha} \pm \sigma$, for the random wave cases with the measured H_{m0} and T_p values at PD18-1.....	146
9-20	Summary table of study cases with measured H_{m0} and T_p values at PD18-1, $k_p h_v$, $Re_{U,Am}$, $Re_{U,DBH}$, $Re_{U,DRoot}$, $KC_{U,DBH}$, $KC_{U,DRoot}$, $KC_{U,Am}$, and C_D values.....	147
9-21	Summary table of study cases with measured H_{m0} and T_p values at PD18-1, $k_p h_v$, $Re_{u,De}$, $Re_{u,Am}$, $Re_{u,DBH}$, $Re_{u,Root}$, $KC_{u,De}$, $KC_{u,Am}$, $KC_{U,DBH}$, $KC_{U,DRoot}$, and C_D values..	147

LIST OF APPENDIX TABLES (Continued)

<u>Table</u>		<u>Page</u>
9-22	Summary table of present and previous studies best fit equations for the drag coefficient, C_D , as a function of the Reynolds number, Re	157
9-23	Table of wave height decay coefficients, α , and $\alpha \pm \sigma$, for the regular wave cases with measured H and T values at PD18-1	170
9-24	Summary table of wave height decay due to model forest, α_m , and the HD/LD ratio of the α_m coefficient with measured H and T values at PD18-1 for regular wave cases.....	172
9-25	Summary table of percent of wave attenuation for the regular wave cases with measured values of H and T at PD18-1.....	174
9-26	Summary table of regular wave cases with measured H and T values at PD18-1, kh_v , H/D_e , Predominant force based on Figure 9-95, $Re_{U,De}$, $KC_{U,De}$, and C_D values.	178
9-27	Summary table of regular wave cases with measured H and T values at PD18-1, kh_v , $Re_{U,De}$, C_D , C_D , $A_{t,m} + \sigma_{t,m}$, and C_D , $A_{t,m} - \sigma_{t,m}$ values.....	180
9-28	Summary table of the regular wave cases with measured H and T values at PD18-1, kh_v , $Re_{U,De}$, C_D , C_D , $\alpha_m + \sigma$, and C_D , $\alpha_m - \sigma$ values.....	182
9-29	Summary table of the regular wave cases with measured H and T values at PD18-1, kh_v , $Re_{U,De}$, C_D , σ_{CD} , $C_D + \sigma_{CD}$, and $C_D - \sigma_{CD}$ values.....	184
9-30	Summary table of the average variance, var_{avg} , for harmonics 1 – 3 at WG 3 – 7 with the corresponding standard deviation of the variance, $var_{avg} \sigma$, for the baseline (BL) layout.	186
9-31	Summary table of the average variance, var_{avg} , for harmonics 1 – 3 at WG 8 – 12 with the corresponding standard deviation of the variance, $var_{avg} \sigma$, for baseline (BL) layout.	187
9-32	Summary table of the average variance, var_{avg} , for harmonics 1 – 3 at WG 3 – 7 with the corresponding standard deviation of the variance, $var_{avg} \sigma$, and ratio of $HD var_{avg} / BL var_{avg}$, for the high-density (HD) layout.	187
9-33	Summary table of the average variance, var_{avg} , for harmonics 1 – 3 at WG 8 – 12 with the corresponding standard deviation of the variance, $var_{avg} \sigma$, and ratio of $HD var_{avg} / BL var_{avg}$, for the high-density (HD) layout.	188
9-34	Summary table of the average variance, var_{avg} , for harmonics 1 – 3 at WG 3 – 7 with the corresponding standard deviation of variance, $var_{avg} \sigma$, and ratio of $LD var_{avg} / BL var_{avg}$, for the low-density (LD) layout.	189
9-35	Summary table of the average variance, var_{avg} , for harmonics 1 – 3 at WG 8 – 12 with the corresponding standard deviation of the variance, $var_{avg} \sigma$, and ratio of $LD var_{avg} / BL var_{avg}$, for the low-density (LD) layout.....	190
9-36	Table of presentations study's results were disseminated.....	194

Prototype-Scale Physical Model Study of Wave Attenuation by an Idealized Mangrove Forest of Moderate Cross-shore Width

Chapter 1. Introduction

1.1. Problem Description and Statement

The use of natural and nature-based features (NNBF) for coastal protection has been growing in both the public and private sectors because of the added social, economic, and ecological benefits that they can also provide to engineering designs. Several government and professional organizations have started initiatives focused on NNBF (United States Army Corps of Engineers (USACE) – Engineering with Nature; Ecoshape – Building with Nature; Permanent International Association of Navigation Congress (PIANC) – Working with Nature) to encourage its use for protecting communities and shorelines from coastal hazards while maintaining ecological habitat, providing carbon sequestration, and improving water quality.

Emergent vegetation such as mangrove forests in tropical latitudes is an NNBF that has been identified by the USACE and others for coastal protection. However, that protection has not been fully quantified for engineering design and the uncertainties in parameterized equations have not been defined. There have been several field, laboratory, and numerical studies that have advanced our understanding of mangroves wave attenuation properties. However, these studies have some limitations.

For example, field studies have generally been conducted under moderate conditions or lacked the means to characterize the protection provided by the mangroves themselves. Numerical studies can help rectify the limitations of field studies by providing a controlled space to investigate the impact of these trees. However, the numerical models usually require a generalized tree geometry, and these models typically rely on the field and laboratory results for parameters such as the drag coefficient, C_D , and the projected area as inputs.

For mangroves, there have been several laboratory experiments conducted at reduced geometric scales using Froude similitude for the kinematic scale. However, these studies present drag coefficients as a function of the Reynolds number, for which Reynolds similitude cannot be maintained when Froude similitude is achieved in reduced scaled tests. Therefore, one of the main purposes of this thesis is to conduct a prototype-scale physical model study that can

quantify the wave attenuation by an idealized mangrove forest and to identify scaling relations that will allow for a better utilization of previous and future reduced-scale tests.

1.2. Study Objectives

For the thesis, the following key objectives were established:

1. Determine the wave attenuation effects of an idealized, prototype-scale model mangrove forest of moderate cross-shore width under a range of mild to extreme conditions for regular, random, and transient waves.
2. Present a methodology using LiDAR to quantify the projected area of the mangrove forest that can be practically applied in future laboratory and field experiments.
3. Quantify the uncertainty of the derived drag coefficients, C_D , due to the projected area per unit height per tree $A_{t,m}$, best fit wave height decay coefficients, $\tilde{\alpha}$, and combined uncertainty from the $A_{t,m}$ and $\tilde{\alpha}$ variables.
4. Determine a relation to compare the present study results with previous laboratory experiments for mangrove forests at reduced scales.
5. Combine the results from the past and present laboratory studies to develop an empirical equation with known uncertainty that can be used for engineering design.

Other objectives determined for the project that are outside the scope of this thesis were:

6. Characterize the wave force reduction provided by the model forest on a coastal structure landward of the forest.
7. Determine the effects of the full-scale model mangrove forest of moderate cross-shore width on a range of transient wave cases.
8. Compare study results with similar 1:2 scale USACE physical model tests conducted at the ERDC facility in Vicksburg, Mississippi.
9. Compare the projected area per unit height of mangrove forests observed in the field to the tested idealized model forest using the LiDAR-based methodology.
10. Calibrate the X-Beach numerical model with laboratory tests for future research quantifying the uncertainty using NNBF for engineering design.

Chapter 2. Background

2.1. Literature Review

2.1.1. Theoretical Background

A force is exerted when a water waves propagates past an array of cylinders such as a pile-supported structure or mangrove prop root system. For the case where the nominal diameter of the structure is small relative to the wavelength, Morison et al. (1950) proposed an equation to estimate the total force by the wave on the structure as the sum of the drag force, F_D ,

and the inertial force, F_I , per differential section given as

$$dF = dF_D + dF_I \quad (1)$$

where

$$dF_D = \frac{1}{2} C_D \rho A u |u| \quad (2)$$

$$dF_I = C_M \rho V \frac{Du}{Dt} \quad (3)$$

where, C_D is the drag coefficient, ρ is the mass density of water, A the projected area of the structure perpendicular to the flow, u is the horizontal wave-induced particle velocity perpendicular to the structure, C_M is the inertial coefficient, V is the volume of the structure, and $\frac{Du}{Dt}$ is the wave-induced particle acceleration perpendicular to the structure. The Morison equation was later used to derive an equation in a National Academy of Sciences Report (NAS, 1997) for estimating the total wave energy loss for waves propagating through emergent vegetation. In the equation, the vegetation was modeled as rigid cylinders, and it was assumed that the energy loss was a function of the drag force only. In other words, the inertial term in Equation (1) was neglected. Further, it was assumed that C_D was constant over the entire depth of the vegetation. The velocity was estimated using linear wave theory and assuming shallow-water wave conditions. The equation from NAS (1977) is given as

$$\frac{H_t}{H_i} = \frac{1}{\left[1 + \frac{C_D H_i d D w}{3 \pi (b^2 h^2)} \right]} \quad (4)$$

where H_t is the transmitted wave height, H_i is the incident wave height before the vegetation, d is the mean wetted height of the vegetation, D is the effective mean diameter of the vegetation, w is

the width of the vegetation patch in direction of wave propagation, b is the mean horizontal spacing of vegetation from their centers, and h is the mean water depth at the vegetation. The equation from (NAS, 1977) was later generalized by Dalrymple et al. (1984) to allow for intermediate and deep-water wave conditions. The extended equation from Dalrymple et al. (1984) is given as

$$\frac{H_t}{H_i} = \frac{1}{1+\alpha x} \quad (5)$$

where

$$\alpha = \frac{4 A_{t,m} N H_i C_D k}{9\pi} \frac{\sinh^3(kd) + 3\sinh(kd)}{\sinh(kh)(\sinh(2kh) + 2kh)} \quad (6)$$

where α is the wave height decay coefficient, $A_{t,m}$ is the mean projected area per unit height per tree, N is the number of vegetation elements per unit area, k is the wave number ($2\pi/L$), and L is the wavelength. Mendez and Losada, (2004) later extended the Dalrymple et al. (1984) equation for random waves assuming a Rayleigh distribution and is given as

$$\frac{H_{rms,t}}{H_{rms,i}} = \frac{1}{1+\tilde{\alpha}x} \quad (7)$$

where

$$\tilde{\alpha} = \frac{A_{t,m} N H_{rms,i} C_D k}{3\sqrt{\pi}} \frac{\sinh^3(kd) + 3\sinh(kd)}{\sinh(kh)(\sinh(2kh) + 2kh)} \quad (8)$$

where H_{rms} denotes the root mean square wave height, and $\tilde{\alpha}$ is the wave height decay coefficient for random waves.

2.1.2. Field Studies

In recent years, several field studies focused on characterizing the wave height decay needed for the Darlymple et al. (1984) and Mendez and Losada (2004) equations. Particularly, studies have focused on wave attenuation for wind waves (Bao, 2011; Horstman et al. 2014; Kibler et al. 2019; Mazda et al. 2006; Mazda et al. 1997; Quartel et al. 2007) boat wakes (Ismail et al. 2017; Thuy et al. 2017; Vinh La et al. 2014), and storm/tidal surge by mangrove forests (Furukawa et al. 1997; Krauss et al. 2009; Mazda et al. 1997a; Montgomery et al. 2018).

However, relatively few field studies presented their results in terms of a drag coefficient (Mazda et al. 1997b; Vinh La et al. 2014). One notable reason for this is the difficulty in, separating the effect of the mangrove forest from other wave attenuation processes such as bottom friction, substrate percolation, and wave breaking (Horstman et al. 2014).

2.1.3. Numerical Studies

Numerical model experiments can help improve our understanding of wave attenuation by vegetation by separately modeling the energy dissipation terms (Chella et al. 2020; Guannel et al. 2015; Narayan et al. 2009; Niazi et al. 2021; K. Zhang et al. 2012). However, these studies require need parameters such as the drag coefficient to inform their models. As Guannel et al. (2015) stressed, better prediction tools are still needed to choose accurate drag coefficients, for emergent vegetation in numerical models.

2.1.4. Laboratory Studies

Several laboratory experiments have focused on developing better estimates of the drag coefficient using artificial vegetation (Anderson and Smith, 2014; Augustin et al. 2009; Ozeren et al. 2014; Wu and Cox, 2015, 2016) and live vegetation (Ozeren et al. 2014). Augustin et al. (2009) concentrated their study on rigid and flexible vegetation for emergent and near emergent conditions for random waves. They also tested different densities for their experiments. The study found the wave attenuation for rigid and flexible vegetation was similar and used the Dalrymple et al. (1984) equation to estimate the drag coefficient, C_D . They related their C_D values to the Reynolds number, Re , and the Keulegan-Carpenter number, KC . They found the C_D value had a dependence on Re under emergent conditions but was more closely correlated to the KC number under near emergent conditions.

Ozeren et al. (2014) also investigated rigid and flexible idealized vegetation as well as, live vegetation. They also considered different vegetation densities for both regular and random wave conditions. The study related, C_D to Re and KC and found that C_D values were higher for live vegetation than the rigid and flexible models. In addition, the study noted that the vertical variation of plant density was a significant factor in the estimation of the drag coefficient, C_D . Wu and Cox (2016) investigated this by testing two model vegetation patches under random wave conditions with uniform and vertically varying stem heights, respectively.

They also constructed the two vegetation patches such that the total vertical projected area was the same despite differences in stem height distributions. The study concluded that the uniform vegetation patch had significantly higher C_D values than the vertically varying patch, with the difference ranging from 140% to 170% depending on relative water depth.

Wu and Cox (2015) also investigated the effect of wave steepness on wave attenuation and drag coefficients for a stand of uniform vegetation. The study tested random wave conditions and identified the C_D values decreased by 23% when the wave steepness doubled. The study also related their drag coefficients to the Re and KC numbers, the relative water depth, kh , and the Ursell number, Ur . Anderson and Smith (2014) extended the investigation of random sea states by considering a singular and bimodal peaked spectrum. Like previous studies, they related the drag coefficient, C_D to the Re and KC numbers and noted a dependence of the C_D value on canopy submergence (height of vegetation, l_{veg} , / water depth, h). They included the ratio by proposing modified versions of the Re and KC numbers. Anderson and Smith (2014) presented these formulations as first drag coefficient estimates of *S. alterniflora* (saltmarsh cordgrass) for engineering applications.

Several laboratory studies have focused on the wave attenuation effects of the *Rhizophora* sp. genus of mangroves (Chang et al. 2019; Maza et al. 2017, 2019; Strusińska-Correia et al. 2014; Tomiczek et al. 2020; Zhang et al. 2015). Tomiczek et al. (2020) specifically focused their study on the influence of a mangrove forest on wave forces and pressures for coastal structures landward of the vegetation. According to previous field measurements (Tomiczek et al. 2019), they modeled their tree geometry from modified parameters of Ohira et al. (2013) at 1:16 scale. The study used PVC rods and galvanized steel wire to represent the tree trunk and roots, respectively. Strusińska-Correia et al. (2014) on the other hand, used a tree model that consisted of an array of clay and steel cylinders with a larger diameter cylinder to represent the trunk and smaller cylinders to represent the roots. They conducted their experiments at 1:20 scale and focused their study on the evolution of wave heights and forces of tsunami-like waves.

Zhang et al. (2015) focused on unidirectional flow, measured velocities within the vegetation patch, and calculated the turbulent kinetic energy (TKE) and drag coefficients. They constructed their models at 1:7.5 scale and used field measurements, photogrammetry, and a material

properties analysis of a mangrove forest in Berlayer Creek, Singapore, to characterize their model tree. Larger diameter aluminum cylinders were used for the trunk and smaller diameter rods for the roots. Zhang et al. (2015) also bent the model roots to resemble the curvature of the measured prop roots and constructed the model such that its porosity value was similar to the field data.

Maza et al. (2017) used geometric parameters from Ohira et al. (2013) to model their tree and constructed it at 1:12 scale out of acrylic tubes for the trunk and brass rods for the roots. The Maza et al. (2017) study also investigated unidirectional flow and focused on TKE and C_D values. Later, Maza et al. (2019) used the same methodology from Ohira et al. (2013) to investigate wave attenuation and drag forces for regular and random waves. The study constructed the model trees at 1:6 scale and used PVC pipe for the trunk and aluminum rods for the roots of the model tree. Conversely, Chang et al. (2019) utilized a 3D-printer to construct their tree model from a polymer plastic based on 3D scan measurement from a 19 year old tree in Vietnam. They completed their study at 1:7 scale and estimated the force coefficients, C_D , and C_M for regular wave conditions.

For all of the *Rhizophora* studies, the drag coefficients were presented as a function of the Reynolds number, and Froude similitude was used to scale the hydrodynamic condition. However, Reynolds similitude cannot be maintained when Froude similitude is achieved in reduced scaled tests. Therefore, the scale effects are unknown for the empirical equations for C_D based on previous reduced-scale tests. This highlights the need for prototype-scale tests. The *Rhizophora sp.* genus was selected for the present study to facilitate comparisons with previous studies.

2.1.5. Mangrove Characteristics

Two of the most important characteristics for modeling wave attenuation by mangroves are the diameter at breast height, D_{BH} , which is the measurement of the trunk diameter measured nominally 1.37 m from the ground, and tree density, N , typically expressed as the number of trees per unit area (e.g., Ohira et al. (2013). Previous laboratory experiments have reported the D_{BH} and N used for experiments (Table 2-1). For the studies, the prototype D_{BH} ranged from 0.06 m for Zhang et al. (2015) to 0.20 m (Maza et al. 2017, 2019; Strusińska-Correia et al. 2014;

Tomiczek et al. 2019). Also, the lowest tree density, 0.063 trees/m² was tested by Maza et al. (2019) with a corresponding D_{BH} of 0.20 m. The largest tree density, 0.6 trees/m² was investigated by Chang et al. (2019) for a D_{BH} of 0.07 m.

Table 2-1 Summary table of mangrove laboratory studies with scale, study type, mangrove data location, species type modeled, model and prototype diameter at breast height D_{BH} , and model and prototype tree density, N .

Study	Scale	Study Type	Mangrove Data Location	Species	D_{BH} [prototype]	N [model]	N [prototype]
(-)	(1:X)	(-)	(-)	(-)	(m)	(stems/m ²)	(stems/m ²)
Chang et al. (2019)	7	Regular Waves	V, 19 yr. old tree	<i>k</i>	0.07	29.40	0.6
Strusińska-Correia et al. 2014	25	Tsunami	JP, AUS, and ID	<i>p</i>	0.20	44	0.07
Hashim and Catherine, 2013	10	Waves/Tsunami	JP, AUS	<i>p</i>	—	11-22	0.11 - 0.22
Maza et al. (2017)	12	Unidirectional Flow	Southwestern FL, USA, Ranong, TH	<i>p</i>	0.20	10.40	0.072
Maza et al. (2019)	6	Regular/Random Waves	Southwestern FL, USA, Ranong, TH	<i>p</i>	0.20	2.25	0.063
Tomiczek et al. (2020)	16	Transient Waves	Key West, FL, USA, Ranong, TH Cuddalore, IN	<i>m</i>	0.203	43.00	0.17
Zhang et al. (2015)	7.5	Unidirectional Flow	Pasir Ris Park and Kranji Natural Trail, SG	<i>p</i>	0.06	12.20	0.217

k *Rhizophora apiculata*, **m** *Rhizophora mangle*, **p** *Rhizophora sp.*

Numerous field studies focused on mangroves have also reported D_{BH} and N values for several locations at tropical latitudes globally (Table 2-2). In Table 2-2, a majority of the studies report the *Rhizophora sp.* genus was either present or dominant at their respective field sites. The D_{BH} values for these studies ranged from centimeters to tens of centimeters. Many had a maximum D_{BH} of ~10 cm, particularly for Florida and the Caribbean. Similar sized trees were also seen in field visits conducted for the present study in Southeastern Florida (Section 2.2).

The reported tree densities, N , varied for the studies where Ward et al. (2006) noted an inverse relationship between D_{BH} and N . The study reported D_{BH} values from 0.011 to 0.10 m and N values from 5.5 to 0.2 trees/m² respectively, based on the study's $D_{BH} - N$ relationship. However, Novitzky, (2010) reported larger tree densities of 0.86, 1.42, and 2.02 trees/m² for comparable D_{BH} ranges to the Ward et al. (2006) study. Jimenez et al. (1985) and Loría-Naranjo et al. (2014) also reported higher tree densities compared to the Ward et al. (2006) estimates. Overall, the comparisons show the variability in D_{BH} and N for mangrove forests depending on the time and location the studies took place.

For the present study, a D_{BH} value of 0.10 m and two tree densities, 0.75 and 0.375 trees/m² were selected to model a mature mangrove forest. The selected values were based on the D_{BH} and N values chosen for previous laboratory experiments and reported in field studies for Florida and the Caribbean (Dawes et al. 1999; Jimenez et al. 1985; Loría-Naranjo et al. 2014; Novitzky, 2010; Ward et al. 2006) Details regarding model tree and forest construction can be found in Section 3.2.

Table 2-2 Summary table of mangrove field studies with: study type, data location, species type encountered, diameter at breast height D_{BH} , tree density, and associated field notes.

Name	Study Type	Study Location	Species	D_{BH}	N	Field Notes
(-)	(-)	(-)	(-)	(m)	(stems/m ²)	(-)
Bao, (2011)	Wave Attenuation	Red River Delta, VN Can Gio, VN	a, b, g, n, s, t	0.075 - 0.12	0.2 - 1.3	32 study plots
Clough et al. (1999)	Aquaculture	Mekong Delta, VN	k	-	0.5 - 2	Shrimp Farming/Mangrove Forest Model
Danielsen et al. (2005)	Tsunami Attenuation	Cuddalore, IN	c, k	0.045 - 0.165	0.14 - 0.26	NA
Dawes et al. (1999)	Tree Structure	Tampa Bay, FL, USA	b, h, m	0.054 - 0.08 (b), 0.073 - 0.087 (h), 0.056 (m)	0.0120 (b), 0.0440 (h), 0.504 (m)	NA
Donnelly et al. (2017)	Restoration Study	East Coast, Central FL, USA	m	-	1.2 - 5.8	5 Year study/restoration project
Furukawa et al. (1997)	Sediment/Organic Carbon Transport	Crains, AUS	d, f, p	0.04	30 - 40	(Includes Roots)
Jimenez et al. (1985)	Tree Mortality Rates	Florida, USA	u	0.041 - 0.119** 0.065 - 0.115***	0.3033 - 0.7611	Basin Forest, ** and ***

a *Aegiceras corniculatum*, **b** *Avicennia germinans*, **c** *Avicennia marina*, **d** *Bruguiera gymnorhiza*, **e** *Bruguiera parviflora*, **f** *Ceriops tagal*, **g** *Kandelia candel*, **h** *Laguncularia racemosa*, **i** *Lumitzera racemosa*, **j** *Pelliciera rhizophorae*, **k** *Rhizophora apiculata*, **l** *Rhizophora lamarckii*, **m** *Rhizophora mangle*, **n** *Rhizophora mucronata*, **o** *Rhizophora racemosa*, **p** *Rhizophora sp.*
q *Rhizophora stylosa*, **r** *Sonneratia alba*, **s** *Sonneratia caseolaris*, **t** *Sonneratia griffithii* **u** *Uspecified*

* Dominant Species, ** Dead trees, *** Live trees

Name	Study Type	Study Location	Species	D_{BH}	N	Field Notes
(-)	(-)	(-)	(-)	(m)	(stems/m ²)	(-)
Jimenez et al. (1985)	Tree Mortality Rates	PR, USA	u	0.082** 0.119***	0.539 - 0.905	Fringe and Basin Forest, ** and ***
Jimenez et al. (1985)	Tree Mortality Rates	PR, USA	u	0.066 - 0.120** 0.075 - 0.173***	0.1760 - 0.9050	Basin Forest, ** and ***
Jimenez et al. (1985)	Tree Mortality Rates	PR, USA	u	0.051 - 0.072** 0.072 - 0.097***	0.2259 - 0.5790	Basin Forest, ** and ***
Jimenez et al. (1985)	Tree Mortality Rates	PAN	u	0.049 - 0.165** 0.074 - 0.254***	0.0473 - 0.3767	Includes Dead and Live Trees
Ong et al. (1995)	Carbon - Nutrient Study	Matang Mangrove Forest Preserve, MY	d, e, k*	0.03 - 0.24 0.12 (mean)	0.243	20 yr. old mangrove tree stand
Loría-Naranjo et al. (2014)	Forest Structure	Portero Grande and Santa Elena, PR USA	b, h, j, m, o*	0.146 - 0.176	0.112 - 0.17	NA

a *Aegiceras corniculatum*, **b** *Avicennia germinans*, **c** *Avicennia marina*, **d** *Bruguiera gymnorhiza*, **e** *Bruguiera parviflora*, **f** *Ceriops tagal*, **g** *Kandelia candel*, **h** *Laguncularia racemosa*, **i** *Lumitzera racemosa*, **j** *Pelliciera rhizophorae*, **k** *Rhizophora apiculata*, **l** *Rhizophora lamarckii*, **m** *Rhizophora mangle*, **n** *Rhizophora mucronata*, **o** *Rhizophora racemosa*, **p** *Rhizophora sp.* **q** *Rhizophora stylosa*, **r** *Sonneratia alba*, **s** *Sonneratia caseolaris*, **t** *Sonneratia griffithii* **u** *Unspecified*

* Dominant Species, ** Dead trees, *** Live trees

Name	Study Type	Study Location	Species	D_{BH}	N	Field Notes
(-)	(-)	(-)	(-)	(m)	(stems/m ²)	(-)
Mazda et al. (1997b)	Drag force, Tidal Flow	Iriomote Island, JP and Hinchinbrook Island, AUS	c, d, g, i, k, l, q, r	0.057 - 0.086	0.8 - 1	-
Montgomery et al. (2018)	Storm Surge Attenuation	Firth of Thames, NZ	c	0.016 - 0.064	0.1 - 1	Fringe
Montgomery et al. (2018)	Storm Surge Attenuation	Firth of Thames, NZ	c	0.015 - 0.102	1 - 12.2	Forest (fringe- highest density)
Montgomery et al. (2018)	Storm Surge Attenuation	Firth of Thames, NZ	c	0.015 - 0.061	5 - 12.4	Forest (landward fringe-highest density)
Novitzky, (2013)	Tree Structure	Gulf Coast, FL, USA	b, h, m*	0.019 - 0.044	0.86	Crystal Bay
Novitzky, (2013)	Tree Structure	Gulf Coast, FL, USA	b, h, m*	0.060 - 0.113	2.02	Cockroach Bay
Novitzky, (2013)	Tree Structure	Gulf Coast, FL, USA	b, h, m*	0.087 - 0.168	1.42	Rookery Bay

a *Aegiceras corniculatum*, **b** *Avicennia germinans*, **c** *Avicennia marina*, **d** *Bruguiera gymnorhiza*, **e** *Bruguiera parviflora*, **f** *Ceriops tagal*, **g** *Kandelia candel*, **h** *Laguncularia racemosa*, **i** *Lumnitzera racemosa*, **j** *Pelliciera rhizophorae*, **k** *Rhizophora apiculata*, **l** *Rhizophora lamarckii*, **m** *Rhizophora mangle*, **n** *Rhizophora mucronata*, **o** *Rhizophora racemosa*, **p** *Rhizophora* sp.
q *Rhizophora stylosa*, **r** *Sonneratia alba*, **s** *Sonneratia caseolaris*, **t** *Sonneratia griffithii* **u** *Unspecified*

* Dominant Species, ** Dead trees, *** Live trees

2.1.6. Mangrove Projected Area Comparison

Estimating the total projected area in the direction of flow is essential to estimating the drag coefficients, C_D , via Dalrymple et al. (1984) and Mendez and Losada, (2004) formulations. For simple geometric emergent and near emergent vegetation such as grasses, the estimation is relatively straightforward.

However, for more complex emergent vegetation such as mangroves, finding the projected area can prove to be difficult due to the complex aerial root structures. Zhang et al. (2015) used photogrammetry in the field to derive the projected area from twenty young trees. The study also noted the presence of older mangrove trees with more complex root systems at their field site. But they could not survey these due to limitations in their method.

Maza et al. (2017) also used photogrammetry in their study to characterize the projected area of one model tree. For the estimation, five images of the model tree were taken and the model was rotated for each image. Later, Maza et al. (2019) expanded on this method using eight images with varying orientations of the model tree to have a more refined representation of the projected area.

Chang et al. (2019) used 3D laser scanning of a 19 year old mangrove tree in Vietnam. Their study used the scans derive the projected are and 3D print their model at reduced scale. The approach of Chang et al. (2019), Zhang et al. (2015), and Maza et al. (2019) considered a single tree to estimate the projected area. However, for fringing mangrove forests, tree roots intertwine, creating a dense network of roots (Figure 2-1). The intertwined root system alters the projected area seen per tree and thus calls for a practical methodology that can extract the projected area of these complex root systems.

This thesis presents a practical methodology to analyze a mangrove forest using LiDAR scans that captures the added complexity of intertwined root structure. Additionally, the method also allows for cross-sections to be selected at intermediate points within the mangrove forest. These sections can then be analyzed to estimate the average projected area and uncertainty for the model forest. There have been previous studies that have used terrestrial-based LiDAR to analyze mangrove forests (Feliciano et al. 2014; Olagoke et al. 2016). These studies were focused on quantifying the biomass without using destructive methods. These studies did not

report projected area. To the author's knowledge, the present study is the first to utilize 3D LiDAR scanning to extract the projected area to account for the complex network of roots in mangrove forests rather than analyze a singular tree.



Figure 2-1 Example of intertwined mangrove root system from multiple trees. Taken: 03/09/2020 St. Lucie Inlet State Park, Stuart, FL.

2.2. Field Data Collection

A field excursion in Southeastern Florida was completed in collaboration with members of Palm Beach County (PBC) Environmental Resources Management and Applied Technology & Management Inc. (ATM) on March 9th, 2020. The purpose of the visit was to meet with local experts, stakeholders, and coastal engineers to better understand mangrove habitat, morphology, and archetypes in the region, and to understand the use of mangroves in engineering design. Additionally, the group aimed to collect LiDAR scans of engineered and natural mangrove systems on the Intracoastal waterway of Lake Worth and Stuart, Florida. The team was guided by Carman Vare (PBC), Dave Carson (PBC) and Greg Braun (ATM) for the first half of the day to three different sites (Figure 2-2).

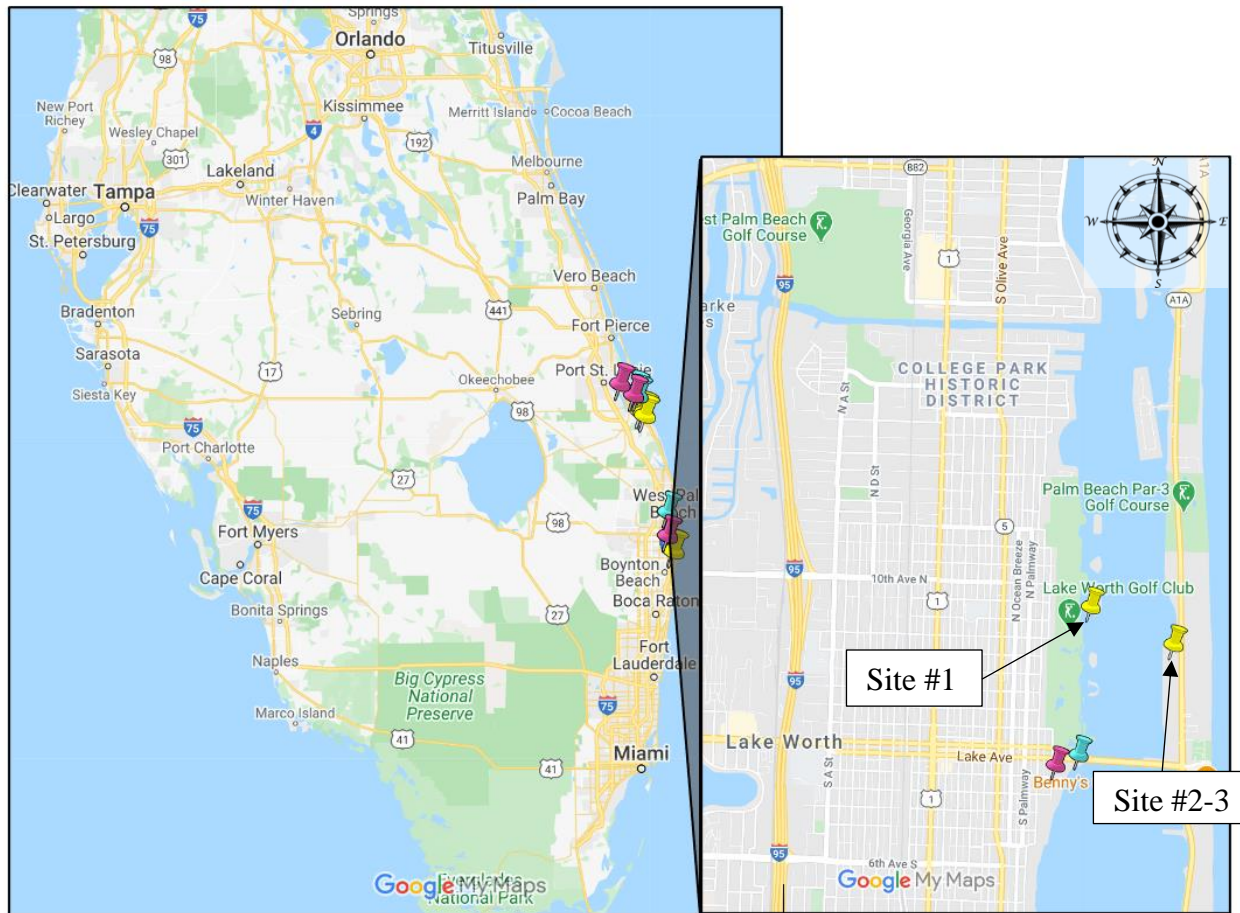


Figure 2-2 Map of morning sites (yellow pins) with closest boat ramp (pink pin) and tide gauges (blue pin). Lake Worth, FL.

The first site was located within the engineered Snook Islands, a collection of roughly 13 spoil islands completed in 2005 by PBC as an extensive restoration effort. The islands were located within the intracoastal lagoon that extends north to south and was populated by red, black, and white mangroves. The first site was located on a larger island with a shallow lagoon at its center and characterized as an over-wash type forest. A singular red mangrove tree was situated in the lagoon center, with the encompassing fringe populated predominantly by red mangroves (Figure 2-3). Five scans were completed around the central mangrove with LiDAR targets strategically attached to various trees around the lagoon. The second and third sites were located east of the Snook Islands site at the Beach Point Condo mangrove restoration completed in 2005 (Figure 2-4 and Figure 2-5). The restored forest was characterized as a fringe forest with Site #2 located on

the water's edge. The second site was dominated by red mangroves (Figure 2-4) with an established canopy that touched the beach. A total of three scans were taken at site 2. Site #3 was located landward of site #2, and contained large red and black mangroves with well-established root structures (Figure 2-5). Four scans were taken at different points at the site.



Figure 2-3 Overview of Site #1 location in the Snook Islands. Lake Worth, FL.



Figure 2-4 Overview of Site #2 location at Beach Point Condo restoration at the water's edge. Lake Worth, FL.



Figure 2-5 Overview of Site #3 location at Beach Point Condo restoration further landward into the forest. Lake Worth, FL.

For the second half of the day, Mike Jenkins, Esteban Biondi, Greg Braun, and Diego Delgado provided transport, guidance, and context for the team at three sites in Stuart, Florida (Figure 2-6). The first site of the afternoon, Site #4 was located in Twin Rivers Park and was a previous restoration project of ATM completed in 2006 (Figure 2-7). The site featured an engineered riprap sill seaward of a mangrove planting that was dominated by red mangroves. The mangroves bordered leeward of the riprap and the land's edge as well, leaving the center of the restored area open. The site was inundated by high tide daily and characterized as a fringe forest. Four scans were taken at the site with three being in the interior of the site and the fourth located on the riprap pointing toward the mangroves.

A boat was used for transport to Site #5, which was located on the northwestern tip of Jupiter Island. The site was characterized by a long stretch of rock gabions that the USACE installed to mitigate shoreline erosion occurring at the site (Figure 2-8). Landward of the gabions a red mangrove fringe was established and extended landward from the shore. A location was chosen along the gabions, and three scans were taken of the mangrove fringe. The last site, Site #6, was located south of Site #5 in St. Lucie Inlet State Park on a main boating corridor for the area. A well-established fringe mangrove forest is located at the site, with a significant number of red mangroves present (Figure 2-9). Site #6 contained the largest mangroves seen for the field day and two scans were taken at the site.

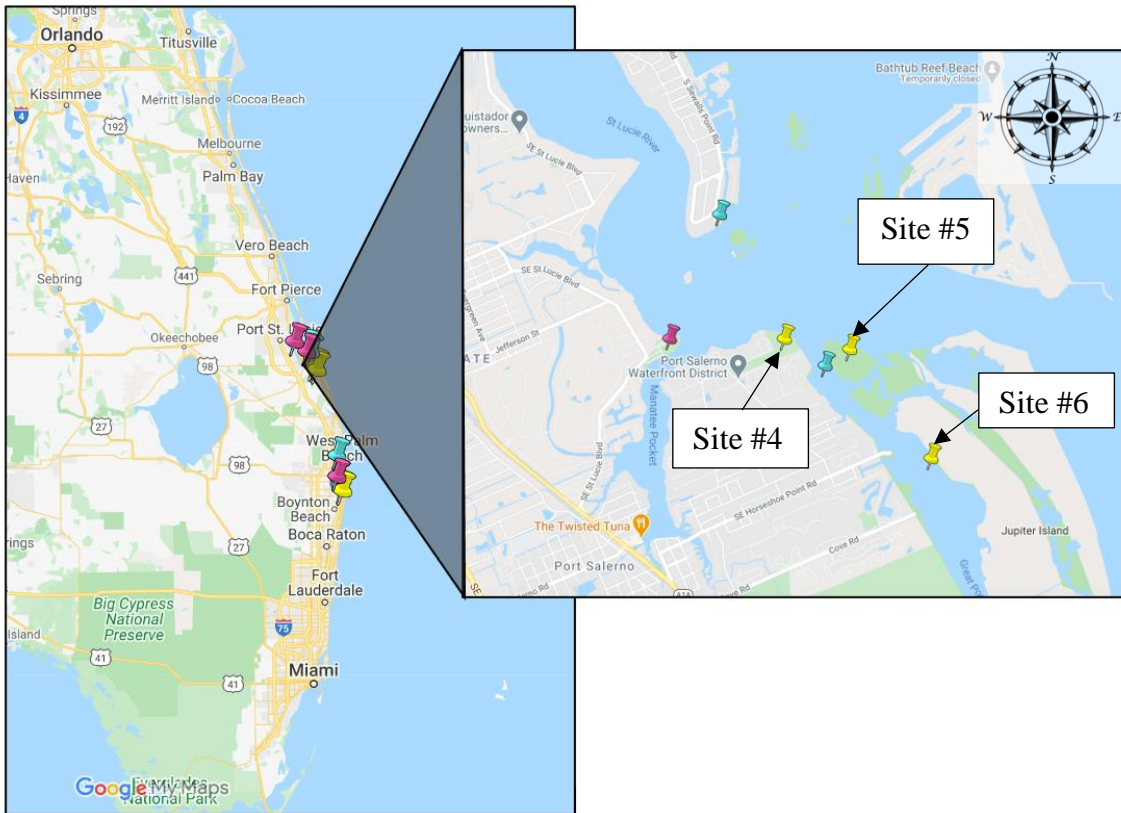


Figure 2-6 Map of the afternoon sites (yellow pins) with closest boat ramp (pink pins) and tide gauge (blue pin). Stuart, FL.



Figure 2-7 Overview of Site #4 located at Twin Rivers Park. Stuart, FL.



Figure 2-8 Overview of Site #5, USACE Gabion site located on the northwestern tip of Jupiter Island. Stuart, FL.



Figure 2-9 Overview of Site #6 located at St. Lucie Inlet State Park. Stuart, FL.

2.3. Webinar Series

A webinar series was coordinated between the research groups at OSU, USNA, USACE-EWN, UVI, IH Cantabria, Kyoto University, and TU Delft. Personnel from Deborah Bronson & Associates and ATM also contributed to the webinar series. The goal of the webinar series was to provide a space where recent research on NNBF could be shared and discussed regarding successes, difficulties, and overall results of the studies. The speakers for the series were Maria Maza (IH Cantabria), Bas Hofland (TU Delft), and Nobuhito Mori (Kyoto University). The presentations and collaboration helped inform the later design and construction of the prototype-scale physical model created for the experiments.

Chapter 3. Experimental Setup

3.1. Safety Protocols

For the study, all personnel were given safety training by the designated O.H Hinsdale Wave Research Laboratory (HWRL) safety officer according to lab and OSU standards. While on the lab floor, all personnel were required to wear a high visibility vest and steel-toed shoes. When working within the Large Wave Flume (LWF), all personnel were required to wear hard hats. Eye, ear, and hand protection were also required while performing particular tasks and operating relevant power tools. Guide cones and spotters were used while heavy machinery was in use.

3.2. Facility and Instrument Descriptions

3.2.1. Large Wave Flume and Wavemaker

The Large Wave Flume (LWF) was a concrete flume that was nominally 104 m long, 3.7 m wide, and 4.6 m tall. The LWF was separated into 22 bays in the cross-shore direction that are nominally 3.66 m long. At the start/end of each bay on the flume walls were two columns of 2.54 cm bolt holes flush to the flume walls. The bolts were spaced 0.203 m and 0.305 m apart, in the horizontal and vertical respectively. The first bolt hole for each column began 0.305 m from the floor of the LWF and each column had a total of 14 bolt holes. The LWF was also equipped with a single channel piston-type system that hydraulically drives a vertical wall referred to as the wavemaker piston. The wavemaker was suspended by a steel support structure that travels back and forth on linear bearings bolted to the flume walls. The maximum stoke of the wavemaker was 4.0 m and maximum speed of 4.0 m/s.

The wavemaker was capable of generating regular, random, tsunami-like, and user-defined type waves with wave periods ranging from 0.8 to 12 seconds with a maximum wave height of 1.7 m at 4-8 seconds. Active reflected wave cancellation was provided by a wave profile measurement at the wave generator, and served as an input to wave board velocity control. That simulated the open boundary condition at sea, minimizing reflection off the wave generator and maintaining the quality of the incident wave environment. For regular, random, and applicable user defined waves, the maximum operational still water depth for the LWF was 2.7 m. For tsunami-like waves the maximum operational still water depth was 2.0 m. The LWF had a cartesian coordinate system with the origin placed at the center of the wavemaker piston, where it

intersected with the floor of the LWF. The positive x -direction was oriented in the landward direction from the wavemaker , the y -direction was to the west following the right-hand rule, and the z -direction was up.

3.2.2. Instrumentation

3.2.2.1. Free Surface

Two types of instruments were used to measure the free surface displacement directly. The first was a wire resistance wave gauge (WG) that was constructed of T304 stainless steel cable wire rope with dimensions 0.061 cm 1 x 7, and two aluminum rod mounts of 0.46 m in nominal length. The aluminum mounts were threaded normal to the flume wall into either a WG array frame or the bolt holes of the LWF such that they were in line with each other. The cable wire was then strung between the two aluminum mounts and tensioned using brass rope sleeves, wire clamps, and threaded cup hooks. An electrical current was then run through the steel cable wire to measure free surface fluctuations via changes in voltage. The second instrument was a Senix ToughSonic® TS-30S1-IV distance sensor (USWG) that utilizes ultrasonic pulses to measure free surface fluctuations. The gauge was waterproof but needed to be mounted far enough above the still water surface such that it would not get repeatedly splashed during testing. USWG's were mounted normal to the still water surface and have a range of 0.102 – 4.25 m from the gauge sensor.

3.2.2.2. Velocity

Nortek Vectrino Acoustic Doppler Velocimeter cable probe (ADV) were used to measure the fluid velocity in three dimensions. The ADVs were mounted to aluminum rods that were 0.254 m in length. The aluminum mounts were normal to the flume walls, and the ADV probe was horizontally leveled. The electrical housing of the ADV was secured to the flume walls using custom-made aluminum plates, hose clamps, 2.54 cm bolts, and zip ties.

3.2.2.3. Pressure Transducers

Druck high-performance level 1830 series pressure sensors (PDCR 1830) were used to measure changes in pressure throughout the model forest. The PDCR 1830 was fully submersible, titanium house pressure gauge that used a strain gauge to measure pressure fluctuations. Non-flush mountable PDCR 1830s were used within the model forest. The sensors were secured to

the aluminum rod mounts secured to the flume walls that were 0.254 m in length. The pressure gauges were attached to the mounts using electrical tape and zip ties. RBRsolo³ D pressure gauges provided by the USNA were also deployed in the test section. These gauges operated on battery power and had a sampling rate of 4 to 32 Hz. The USNA pressure gauges were installed using the same methods as the PDCR 1830s and were removed after each layout to download data. The USNA gauges were then reprogrammed and installed before testing resumed.

PDCR 1830 and PDCR 830 pressure gauges were installed in the test wall. The gauges were mounted using custom aluminum mounts and attached to the wall at specific locations detailed in Section 3.6.4. For some trials, Kistler piezoelectric pressure sensors were installed on the test wall to investigate their capabilities. These sensors measured static pressure and small dynamic pressure fluctuations on top of larger static pressures. The Kistler pressure gauges were mounted to the wall by taping holes and securing them using custom mounts.

3.2.2.4. Accelerometers

Kistler ceramic shear triaxial accelerometers were mounted to the wall for the same trials as the Kistler pressure sensors. These accelerometers were capable of measuring the accelerations in the x , y , and z directions and were to be used for underwater vibration testing. The accelerometers were mounted to the wall by drilling a hole in the upper section of the test wall and securing the accelerometers using a threaded bolt.

3.2.2.5. Video

Two overhead closed-circuit overhead cameras were used to record experimental trials for the study. The cameras are secured to the rafters above the LWF and could be oriented via an interface in the control room. For experiments without the wall present, the cameras were oriented such that they captured the entire test section with minimal frame overlap. For the wall experiments, the cameras were repositioned so the test wall and most of the test section could be recorded. Additionally, LED lights were placed within each camera frame so video timestamps could be matched to instrument readings in the LWF.

3.2.2.6. LiDAR

A Leica BLK 360 3D laser scanner was used to scan the LWF. The scanner was 1 kg in weight and uses a range 1 laser with a wavelength of 830 nm and used time of flight. The scanner had a

360° field of view in the horizontal and 300° view in the vertical. The scanner had a range of 0.6 to 60 m with a 4 mm accuracy at 10 m and 7 mm accuracy at 20 m. The BLK 360 was also equipped with a 15 Mpixel 3-camera system and a 150Mpixel full-dome capture for HDR and LED flash calibrated spherical images. The scanner was set up and controlled using an Apple iPad running the Leica BLK 360 field application. Scans were also initiated by momentarily pressing the power button after the initial setup.

3.2.2.7. Data Acquisition

The data acquisition system (DAQ) was based on a National Instruments PXI architecture and used a real-time version of the LabVIEW programming environment. All in-situ instruments were calibrated using standards linked to the National Institute of Standard and Technology (NIST). All recorded measurements were written continuously on the DAQ. The data was then copied to an independent server that held an archive of each file before it was transferred to the HWRL shared drive. The HWRL shared drive was located in a separate building from the wave lab and was the responsibility of the College of Engineering's information technology support team. The process allowed for three independently backed-up copies of each data file to be made before it was shared for post-processing and quality control.

3.3. Large Wave Flume Configuration

Figure 3-1, (A) shows the overall configuration of the flume. The piston-type wavemaker with the vertical wall is in neutral position. (A) also shows the numbered bays for the LWF with the corresponding bolt holes at each bay number for the bathymetry construction. The bathymetry was constructed of 3.66 m x 3.66 m x 0.154 m concrete slabs. The first slab spanned from Bay 2 to 3 and anchored the proceeding 1:12 foreshore slope 7 m in length from Bays 3 to 5. This created a false floor 0.85 m above the flume floor. After the foreshore slope, a flat section 11 m in length was created from Bays 5 to 8. This was followed by an 18 m long model forest test section from Bays 8 to 13. At either end of the test section, plywood retaining walls, 3.66 m in width and 0.686 m in height, were built to hold fill material to support the model forest (B). Another flat section 7 m in length was constructed after the test section from Bays 13 to 15. At Bay 15, the test wall was installed for half of the layouts considered for the study. Further details

regarding the test wall can be found in Section 3.5. From Bays 15 to 22, a 1:12 dissipative beach that was 26 m in length was constructed to reduce wave reflection back into the test section.

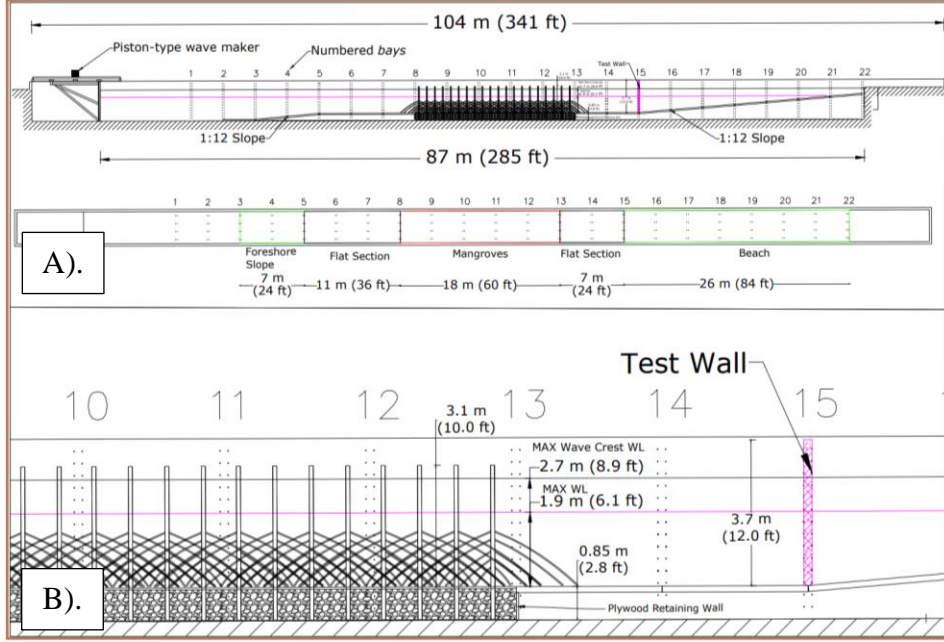


Figure 3-1 A). Front-view and top-view of Large Wave Flume (LWF) configuration and layout. B). Zoomed in front-view of the LWF detailing the model forest.

3.4. Mangrove Specimen and Test Section

The model mangrove trees were constructed based on previous field experiments and the methods presented by Ohira et al. (2013) for a mangrove with a D_{BH} of 0.1143 m. The Ohira et al. (2013) parameterization yielded a representative model tree with 14 roots and a mean root diameter, D_{Root} , of 0.0286 m with the tallest root, H_{Rmax} , located 1.35 m from the ground. The maximum horizontal extent of the tallest root, X_{Rmax} , was 2.10 m from the base of the model tree (Table 3-1 and Figure 3-2).

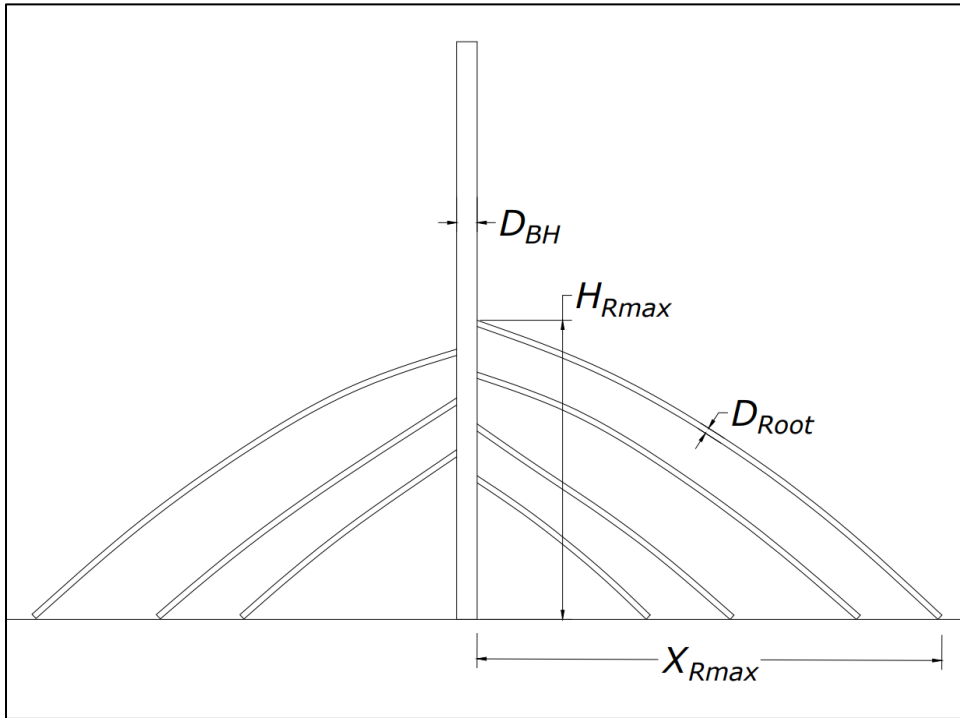


Figure 3-2 Example of idealized Ohira et al. (2013) model mangrove tree.

Table 3-1 Summary table of model mangrove tree dimensions: diameter at breast height, D_{BH} , Number of roots, N_R , root diameter, D_{Root} , height the tallest root from the ground, H_{Rmax} , and maximum horizontal extent of the highest root from the trunk, X_{Rmax} .

D_{BH}	N_R	D_{Root}	H_{Rmax}	X_{Rmax}
(m)	(-)	(m)	(m)	(m)
0.1143	14	0.0286	1.35	2.10

The Ohira et al. (2013) parameterization was then modified where 7 of the 14 individual roots were chosen and made into root pairs (duplicate roots on either side of the tree) to simplify construction and to be consistent with panned experiments at the USACE at 1:2 scale. The chosen roots were selected so that the number of roots per tree, N_R , and total length of roots per tree were similar to the initial model tree from Ohira et al. (2013). Table 3-2 contains information regarding root pairs for the model tree where root pair 1 corresponds to the smallest root and 7 to the largest root. In Table 3-2, Θ represents the rotation in degrees of each root pair clockwise relative to the first root pair, H_{Ri} is the height of each root pair, and X_{Ri} is the horizontal extent of the root pair on either side of the trunk. PVC and PEX pipe were chosen for

the physical model materials and were consistent with planned experiments at the USACE at 1:2 scale.

Table 3-2 Summary table of model mangrove tree roots where: Θ is the degrees of rotation clockwise around the trunk relative to the first root, H_{Ri} is the maximum vertical height each respective root pair relative to the ground, X_{Ri} is the maximum horizontal extent of each root from the trunk of the tree.

Root Pair (-)	Θ (deg, °)	H_{Ri} (m)	X_{Ri} (m)
1	0	0.58	0.67
2	45	0.71	0.91
3	90	0.84	1.14
4	135	0.97	1.38
5	180	1.09	1.62
6	225	1.22	1.86
7	270	1.35	2.10

50 model trees were constructed for the high-density forest (HD) of 0.75 trees/m². With five bays making up the forest test section, this resulted in 10 trees per bay. For each bay, the trees were separated into five rows (Figure 3-3 – black dashed lines) with two trees in each row. The rows were spaced 0.69 m apart in the alongshore direction and offset by 0.91 m in the cross-shore. The rows were also spaced 0.46 m in the cross-shore direction from the start and end of the bay. In addition, Rows 1 and 5 were spaced 0.46 m from the flume walls (Figure 3-4). This resulted in a ‘diamond’ pattern similar to the pattern used in many wave attenuation experiments. All of the model trees were oriented with their largest root pair approximately normal to the wavemaker with some adjustment to simplify construction. To achieve the low density (LD) forest (0.375 trees/m²), 25 trees were selected from the test section to yield five trees in each bay and one tree in each row of the bay. The pattern differed in each bay (Figure 3-5). The LD model forest pattern was applied after all HD testing had been completed. Details of the layout order can be found in Section 4.1.

Roots were precut for the model trees to account for the flume walls (Figure 3-6). The root cuts were determined using Autodesk AutoCAD 2018 with an idealized 2-D sketch of the LWF and drawn model tree. Four different tree groups were identified and detailed in Appendix A.

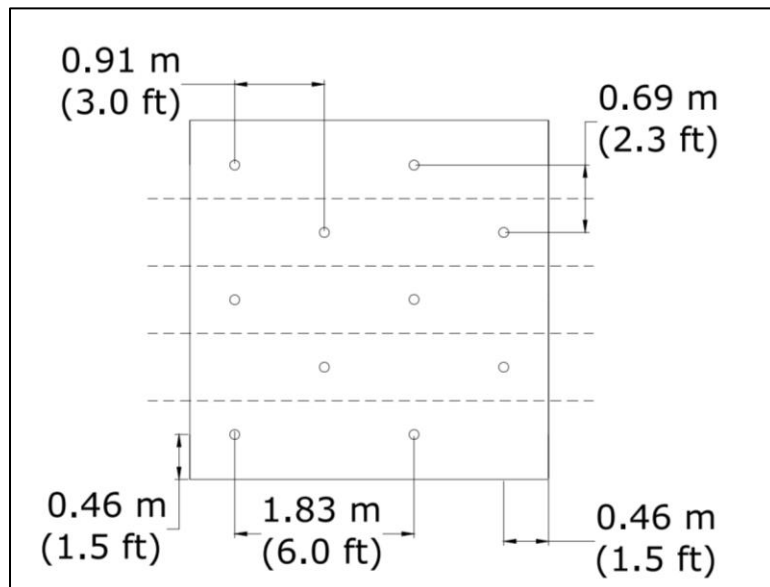


Figure 3-3 Model tree spacing in each bay, black dashed lines designate rows.

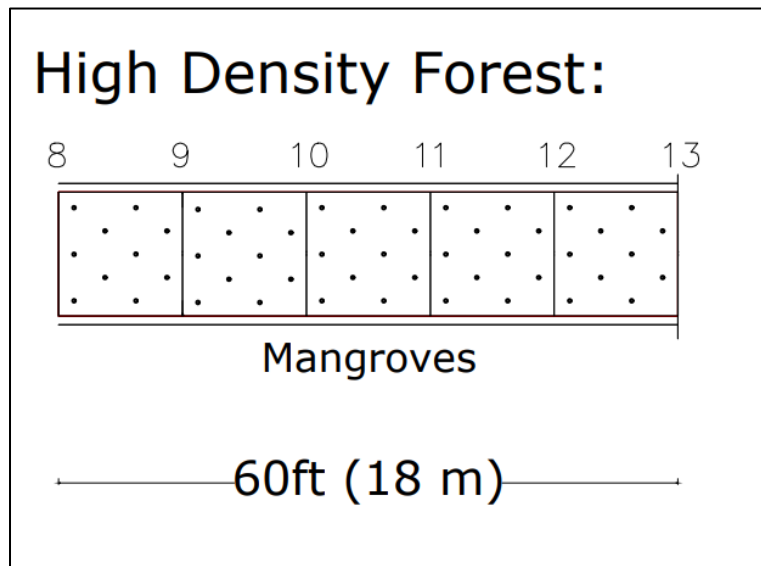


Figure 3-4 Overview of high-density model forest.

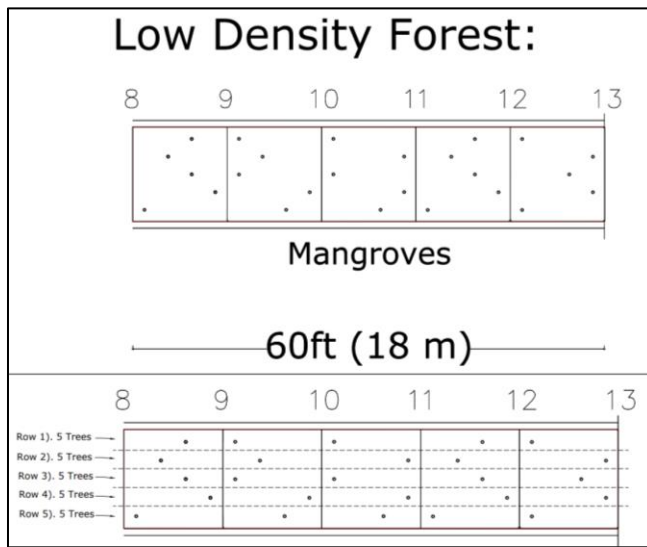


Figure 3-5 Overview of low-density model forest, dashed lines designate rows.

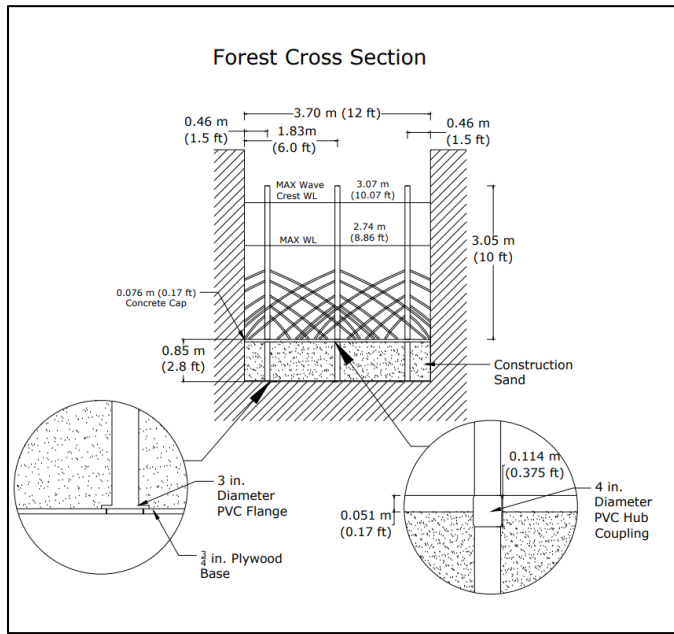


Figure 3-6 Example of forest cross section.

The model trees were secured to bases in the test section that were constructed of 10.16 cm schedule 40 PVC pipe, 1.91 cm plywood, 7.62 cm PVC flange, and 10.16 cm schedule 40 PVC hub couplings. The void space around these bases was filled by construction sand and concrete masonry units. The section was sealed by a 0.076 m thick concrete cap that also secured the root ends of the model tree. In total, fifty 10.16 cm x 3.05 m schedule 40 PVC pipes were used for the

trunks and a total length of 1178.66 m of 2.54 cm PEX pipes were used for the roots of the model trees. An estimated 55.98 m³ of construction sand, and 350 concrete masonry units were used to fill the test section. The masonry unit deemed to have been unnecessary in reduction the overall volume and that the setup would have been simpler using construction sand only. An estimated 9.92 m³ of self-consolidating concrete (SCC) used to seal the section. Further details of the model tree and test section construction can be found in Appendix A.

3.5. Test Wall

The test wall was constructed out of two aluminum sections, each 1.83 m tall and 3.66 m wide (Figure 3-7). Each section had a seaward face made of an aluminum plate braced by support beams on the landward side. The lower section of the wall had its supports covered by another aluminum plate, while the upper section had the supports exposed (Figure 3-8). On the sides of each wall section, rubber strips were also attached to create a seal during testing and minimize flow past the test wall. Two 10.16 x 15.24 cm wooden posts were placed below and on top of the lower section of the wall to help align the two sections and provide an additional seal during testing. The seam between each of the sections were taped over using Nashua 7.62 cm Aqua-Seal tape to further reduce flow past the test wall. Each wall section was then secured to the flume walls using a series of red iron clips that bolted to each wall section and the flume walls using 2.54 cm bolts.

Each wall section had a series of holes to allow for pressure gauges to be mounted. Details of the pressure transducer layout on the test wall are found in Section 3.6.4. Holes without pressure transducers were taped using the Nashua 7.62 cm Aqua-Seal tape to provide an additional seal during testing.

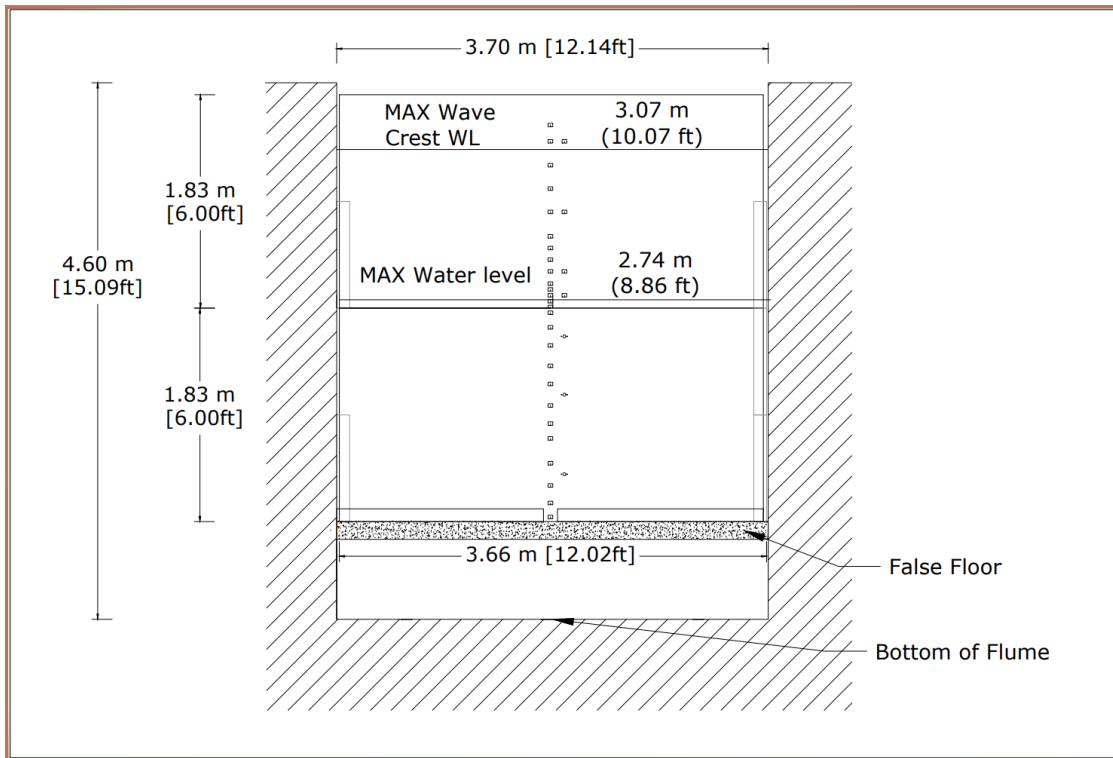


Figure 3-7 Drawing of test wall installed in Large Wave Flume.

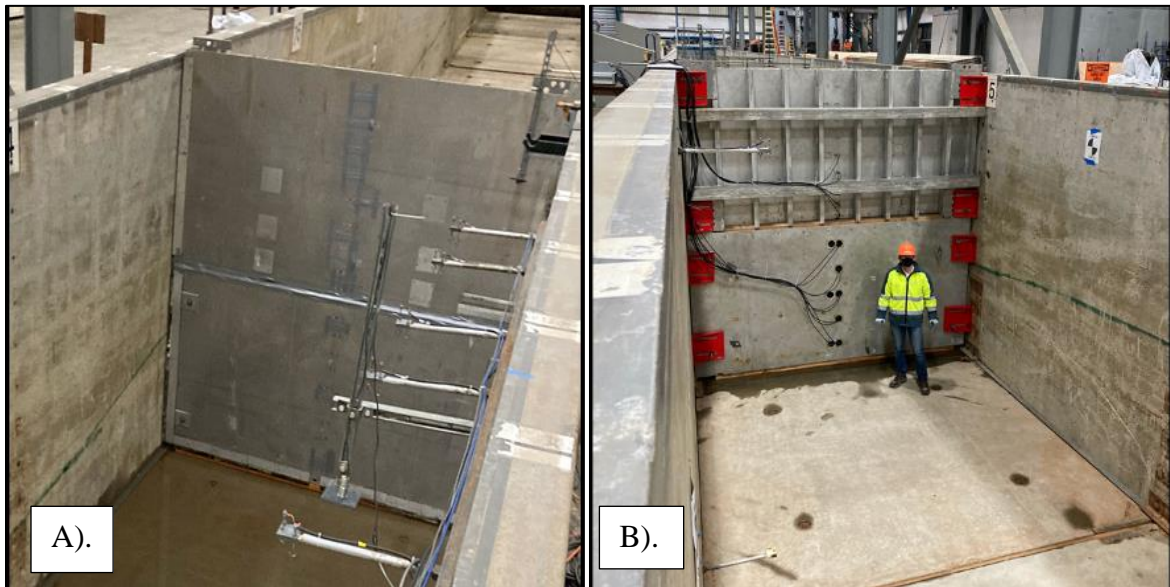


Figure 3-8 A). Seaward side of the test wall, B). Landward side of the test wall secured by red clips to the walls of the flume.

3.6. Instrument Placement

Figure 3-9 shows the overall instrumentation layout for the experiments. Red pillars denote wave gauges (WG), green pillars denote ultrasonic wave gauges (USWG), yellow circles denote USNA pressure gauges (USNA P), orange rectangles denote to PDCR 1830 pressure gauges (PD18), and teal triangles denote Acoustic Doppler Velocimeters (ADV).

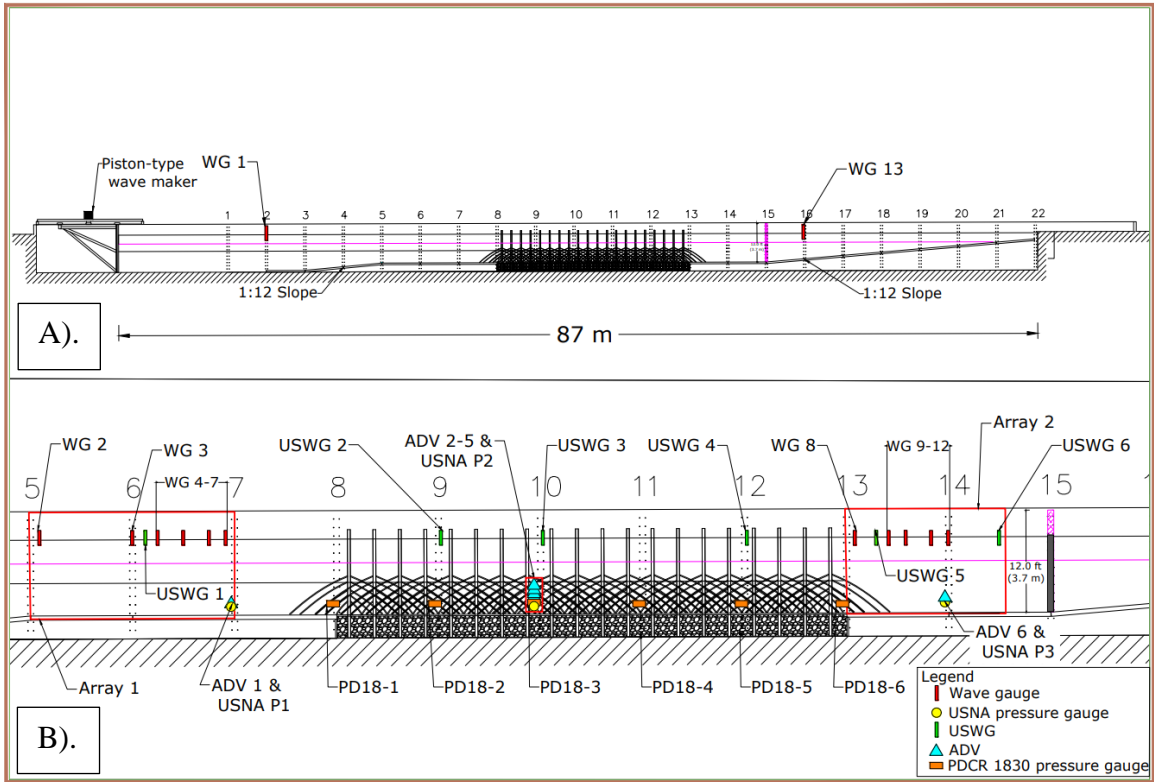


Figure 3-9 Overview of instrument placement in the Large Wave Flume.

In (A), the most seaward (WG 1) and landward (WG 13) wave gauges are shown. These gauges were placed to record the wave cases before and after they propagated through the test section. In (B), the forest test section is shown in detail with the corresponding instrumentation. In total, 13 WGs, 6 USWGs, 6 PD18s, 3 USNA Ps, and 6 ADVs were used for the test section. For the test wall, 3-PD18s, 12-PDCR 830s pressure gauges (PD8), 6 Kistler pressure gauges (KP), and 3 Kistler accelerometers (ACC) were installed. A detailed layout for the test wall is shown in Section 3.6.4. Overall, 55 instruments were used for the study where the sampling rate was 100 Hz for the WGs, USWGs, PD18s, and PD8s. A sampling rate of 4 to 32 Hz was used for the

USNA Ps depending on the layout. Details regarding the purpose of placement and coordinates of the instruments for the test section and wall are detailed in the proceeding sections.

3.6.1. Incident and Reflected Waves

Two-gauge arrays were established seaward and landward of the model forest to measure the incident and reflected waves. The first array spanned from Bays 5 to 7 and consisted of 9 instruments: WG 2 to 7, USWG 1, USNA P1, and ADV 1, respectively (Figure 3-9). The second array was located from Bay 13 to the middle of Bay 14 to 15 and consisted of 9 instruments. These were: WG 8 to 12, USWG 5 and 6, USNA P3, and ADV 6, respectively (Figure 3-9). Furthermore, ADVs 1 and 6 were both lowered after Layout 1 testing since they were exposed at the lowest water depth. Coordinate tables expressing the change in location for ADVs 1 and 6 and the locations of the other instruments for the study are detailed in Table 9-6 to Table 9-10 in Appendix C.

3.6.2. Wave Attenuation

Ten instruments were placed within the model forest to characterize the wave height decay. PD18 – 1 to 6 were placed at the most seaward bolthole of Bays 8 to 13 (Figure 3-9). Additionally, USNA P 2 was also placed in tandem with PD18 – 3 (Figure 3-9). USWGs 2 to 4 were placed at Bay 9, 10, and 12 to provide an alternative measurement of the free surface. These were also co-located with PD18 – 2, PD18 – 3, and PD18 – 5, respectively (Figure 3-9). Coordinate tables showing the x-y-z locations of the instruments in the two arrays can be found in Table 9-6 to Table 9-10 in Appendix C.

3.6.3. Velocity Profile in Model Forest

A vertical stack of ADVs were deployed within the model forest to capture the velocity profile of the water column. ADVs 2 to 5 were used for the stack and mounted to the flume walls at Bay 10 using a custom mount of Unistrut and aluminum rods (Figure 3-10).

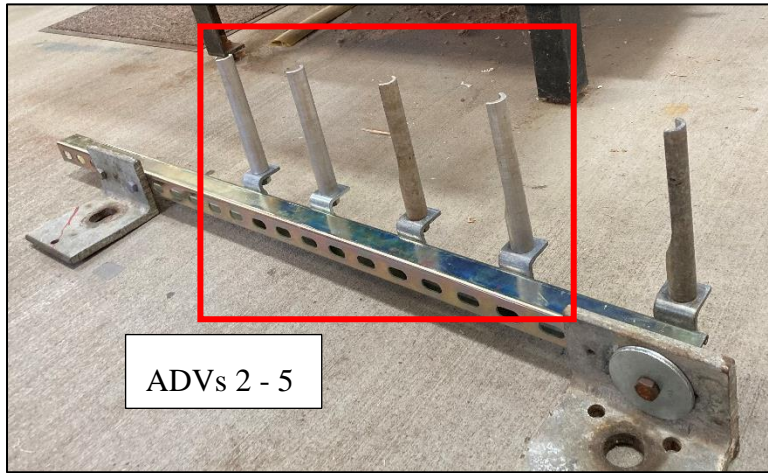


Figure 3-10 Custom mount used for vertical stack of Acoustic Doppler Velocimeters.

The ADVs were mounted to the four upper aluminum rod mounts, and their coordinate locations can be found in Table 9-9 and Table 9-10 in Appendix C.

3.6.4. Test Wall

Twelve instruments were installed on the test wall (Figure 3-11). Figure 3-11 shows the locations of the instruments where PDCR 1830 (orange rectangles), PDCR 830 (grey rectangles), Kistler pressure gauges (green half-circles), and Kistler accelerometers (pink diamonds) were installed. The PDCR 1830 and 830 pressure gauges were installed for all the trials and layouts in the study. The Kistler instruments were only installed for a demonstration day on January 5th, 2021. The unused instrument holes (black squares) were sealed using Nashua 7.62 cm Aqua-Seal tape for the duration of testing. Coordinates of the installed instruments on the test wall can be found in Table 9-11 and Table 9-12 in Appendix C.

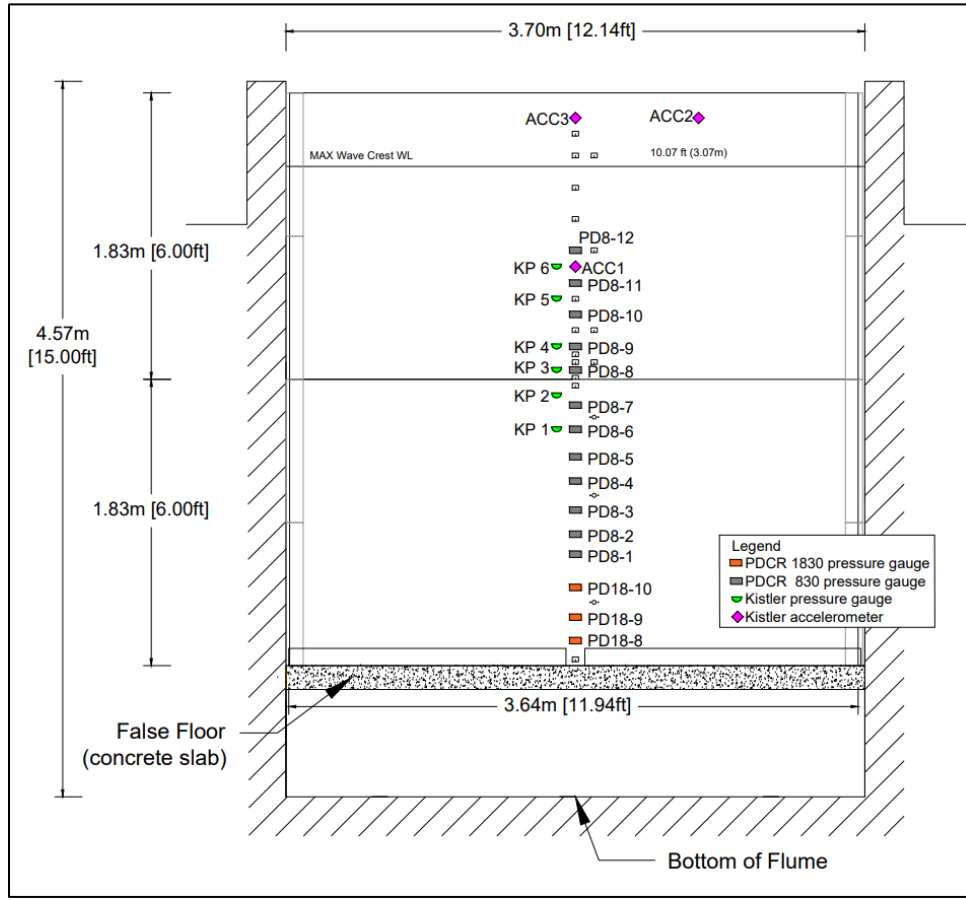


Figure 3-11 Instrumentation layout on the wall where: PDCR 1830 (orange rectangles), PDCR 830 (grey rectangles), Kistler pressure gauges (green half circles), and Kistler accelerometers (pink diamonds) are shown.

Chapter 4. Experimental Procedures

4.1. Selection of Layouts 1 to 6

Six layouts were established for the study that considered the HD and LD forests as well as the baseline (BL) case with and without the test wall. The order of the layouts for the study are as follows: HD with no wall, HD with the wall, LD with the wall, LD with no wall, BL with no wall, and BL with the wall (Figure 4-1). This order was deemed most productive based on the operational standards and protocols of the HWRL.

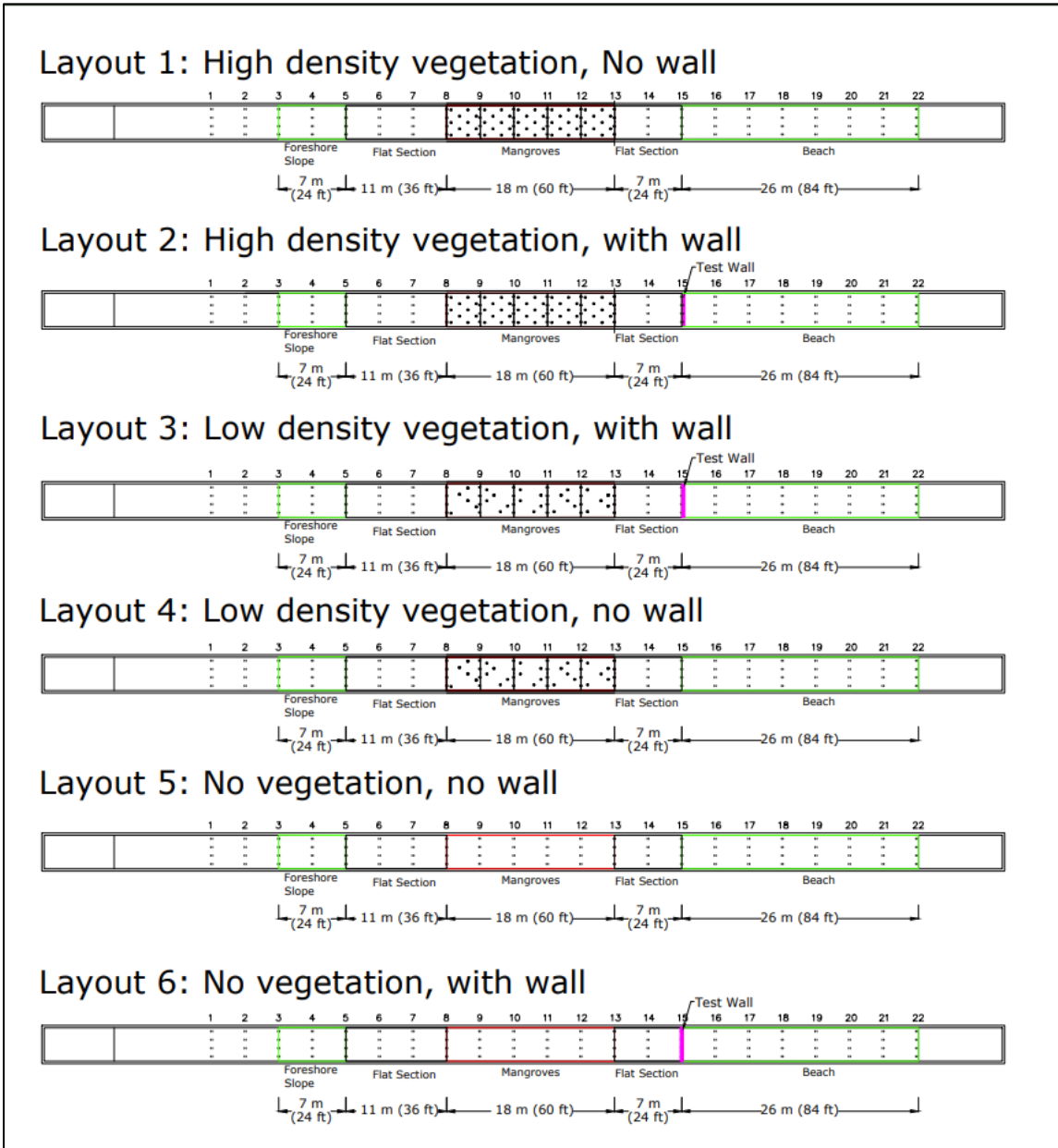


Figure 4-1 Layouts 1 to 6 of the Large Wave Flume.

4.2. Selection of Water Depth and Generation of Wave Conditions

4.2.1. Water Depths

An idealized CAD sketch of the cross-section of the model forest in the LWF was created to determine the water levels for the study. The cross-section was discretized into 10 cm bins and the projected area totaled for each bin. (Figure 4-2). The totaled projected area was then divided by the height of the bin (10 cm) to get the projected area per unit height, A . The projected area

per unit height, A , was plotted against the water depth at the vegetation, h_v (Figure 4-3). For Figure 4-3, the left-hand side y-axis denotes the water depth at the vegetation, h_v , while the right-hand side y-axis denotes the water depth at the wavemaker, h . Both y-axes for the figure do not begin at zero. The x -axis for the figure describes the projected area per unit height, A , for the idealized cross-section that includes three model trees within it. The grey horizontal line in the figure represents the false floor created for the study that was a flat slope within the model forest. Four water depths: $h_v = 0.73, 1.03, 1.48$, and 1.85 m are also shown in Figure 4-2.

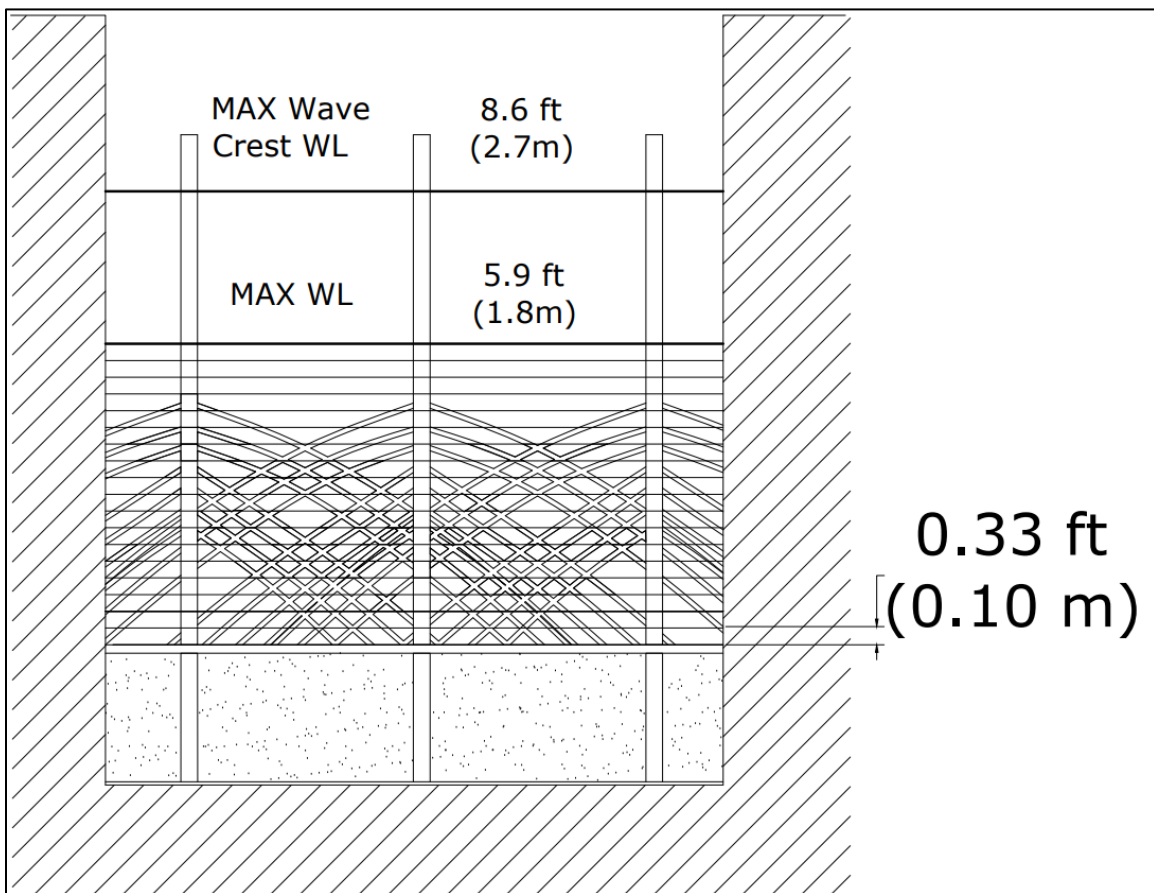


Figure 4-2 Idealized CAD sketch of model forest cross section in the Large Wave Flume.

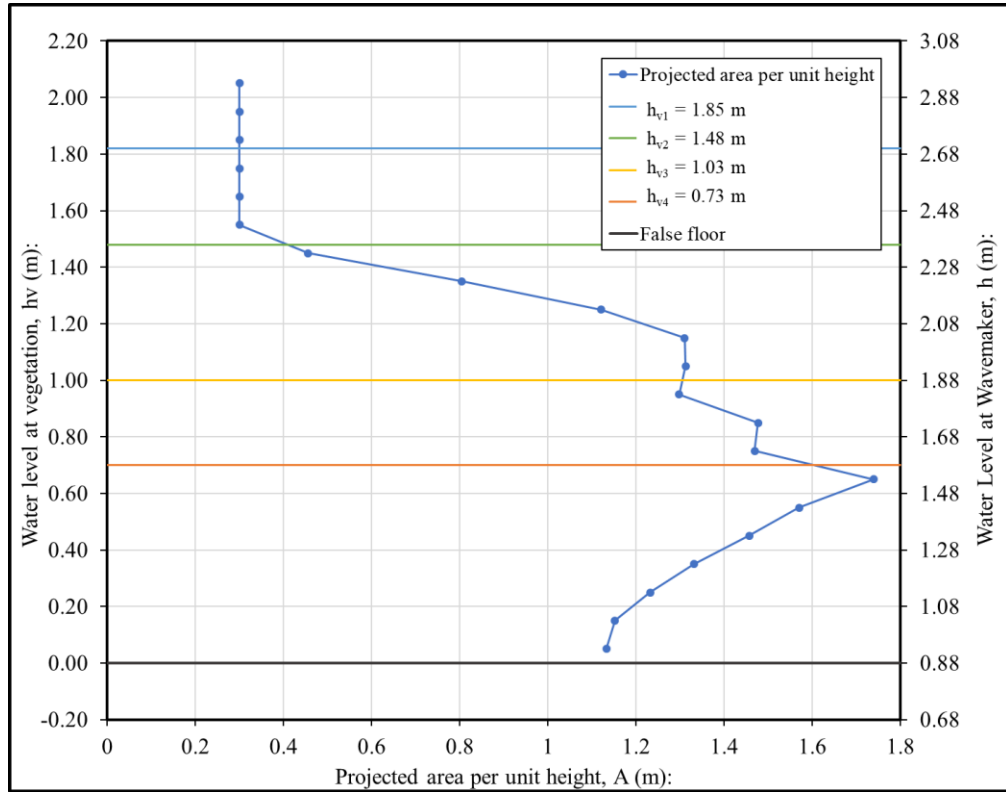


Figure 4-3 Projected area per unit height, A , versus water depth at vegetation, h_v , for model forest cross section in the Large Wave Flume.

The four water depths were chosen based on the projected area profile in Figure 4-3. The lowest water depth ($h_v = 0.73$ m) was selected so it was close to the largest estimated projected area per unit height, A , value. The second water depth ($h_v = 1.03$ m) on the other hand, considered the transition zone where the projected area per unit height, A , value decreased with increasing water depth. The highest water depth ($h_v = 1.85$ m) fell at the point where the projected area per unit height, A , value was the smallest due to the trunk being the only contributor. The $h_v = 1.85$ m water depth was also the maximum operational water depth for the LWF.

During testing, concerns were raised after the sidewalls of the flume were almost exceeded during Layout 1 (HD model forest, no wall). A reduced testing scheme for the $h_v = 1.85$ m water depth used for the remaining layouts to mitigate possible operational hazards for layouts where the test wall was present. The additional water depth, $h_v = 1.48$ m (green line, Figure 4-3) was added to the testing scheme for Layouts 2 to 6. It allowed for the larger test cases to be safely run and at a water depth close to $h_v = 1.85$ m. The new water depth was not tested for Layout 1 due

to time constraints for the study. A table of the projected area per unit height, A , profile plotted in Figure 4-3 can be found in Table 9-13 in the Appendices.

4.2.2. Regular Waves

For the study, regular wave cases were determined based on the non-dimensional parameters, target wave height, H , over water depth at vegetation, h_v , (H/h_v) and the water depth at the vegetation, h_v , over the target wavelength, L (h_v/L). The nondimensional variables allowed for cases to be chosen that varied in nonlinearity (H/h_v) and relative water depth (h_v/L). Six non-dimensional cases were chosen, with 20 waves run for each case. The target wave height, H , and wave period, T , were changed at each of the tested water depths so the same six non-dimensional cases were tested (Figure 4-4). Keeping the same non-dimensional values allowed for the effect of the vertically varying projected area of the model tree to be isolated. Figure 4-4, shows H/h_v on the y-axis and the relative water depth, h_v/L , on the x-axis. The trials at the first water level $h_v = 1.85$ m, are represented as yellow triangles, the second water level $h_v = 1.48$ m as orange triangles, the third water level $h_v = 1.03$ m as green triangles, and the fourth water level $h_v = 0.73$ m as blue triangles. The shaded region in the figure shows the range the 6 non-dimensional cases covered. Table 4-1 contains the non-dimensional target values plotted in Figure 4-4 with the corresponding trial name, number of waves, layouts tested, water depth at the vegetation, target wave height H , target wave period T , and target wavelength L . The table includes the non-dimensional parameters: ratio of forest length, to target wavelength (L_{veg}/L) and ratio of target wavelength to the LWF width, (L_{veg}/W).

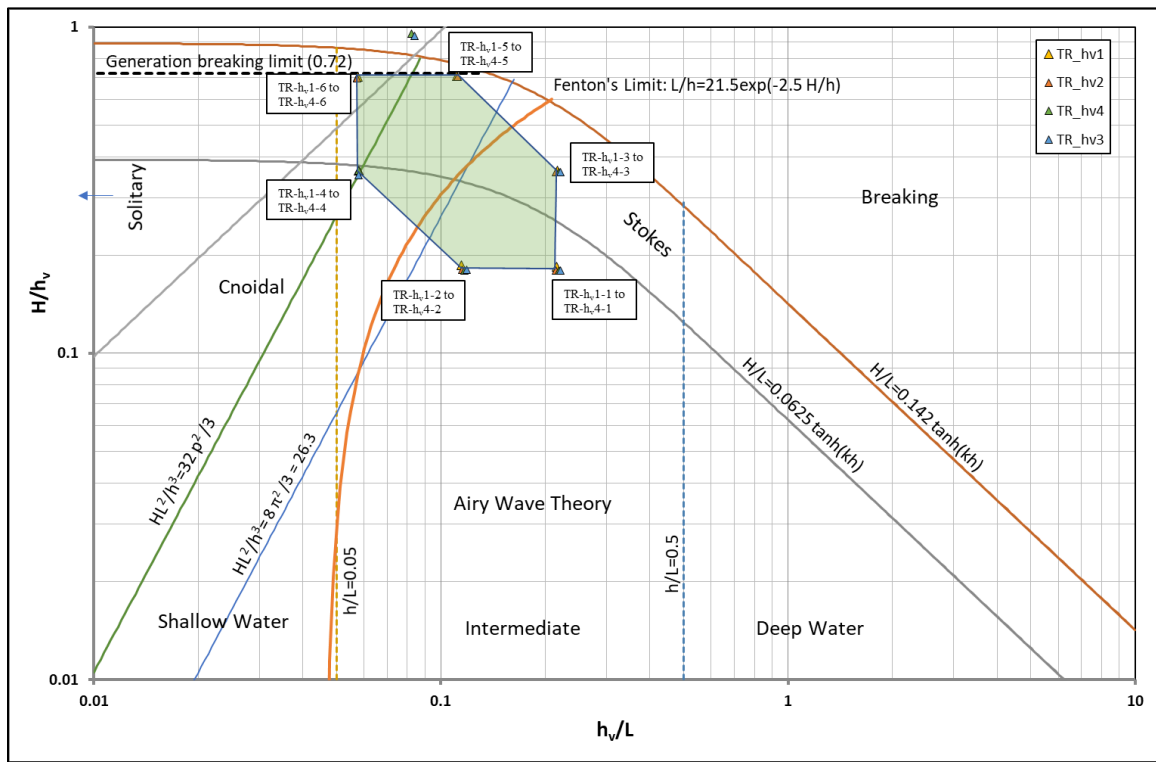


Figure 4-4 Non-dimensional plot of H/h versus h/L for the target regular wave cases. Graph source: Pedro Lomónaco.

Table 4-1 Table of target regular wave cases at the test section.

Trial	Layouts	Number of Waves	h_v	H	T	L	h_v/L	H/h_v	L_{veg}/L	L/W
(-)	(-)	(-)	(m)	(m)	(m)	(m)	(-)	(-)	(-)	(-)
TR-h1-1	1 to 6	20	1.85	0.34	2.51	8.6	0.215	0.184	2.1	2.3
TR-h1-2	1 to 6	20	1.85	0.34	4.10	16.2	0.114	0.186	1.1	4.4
TR-h1-3	1 to 6	20	1.85	0.67	2.50	8.6	0.216	0.363	2.1	2.3
TR-h1-4	1 to 6	20	1.85	0.67	7.65	31.9	0.058	0.363	0.6	8.7
TR-h1-5	1	20	1.85	1.31	4.20	16.6	0.111	0.706	1.1	4.5
TR-h1-6	1	20	1.85	1.30	7.70	32.1	0.058	0.703	0.6	8.8
TR-h2-1	2 to 6	20	1.48	0.27	2.25	6.9	0.214	0.180	2.6	1.9
TR-h2-2	2 to 6	20	1.48	0.27	3.65	12.9	0.115	0.181	1.4	3.5
TR-h2-3	2 to 6	20	1.48	0.53	2.25	6.9	0.214	0.359	2.6	1.9
TR-h2-4	2 to 6	20	1.48	0.54	6.80	25.4	0.058	0.364	0.7	6.9
TR-h2-5	2 to 6	20	1.48	1.04	3.75	13.3	0.111	0.704	1.4	3.6
TR-h2-6	2 to 6	20	1.48	1.03	6.90	25.7	0.057	0.699	0.7	7.0
TR-h3-1	1 to 6	20	1.03	0.19	1.85	4.7	0.219	0.180	3.8	1.3
TR-h3-2	1 to 6	20	1.03	0.18	3.00	8.8	0.117	0.179	2.0	2.4
TR-h3-3	1 to 6	20	1.03	0.37	1.85	4.7	0.219	0.360	3.8	1.3
TR-h3-4	1 to 6	20	1.03	0.37	5.70	17.7	0.058	0.363	1.0	4.8
TR-h3-5	1 to 6	20	1.03	0.98	4.10	12.5	0.082	0.953	1.4	3.4
TR-h3-6	1 to 6	20	1.03	1.09	5.70	17.7	0.058	1.055	1.0	4.8
TR-h4-1	1 to 6	20	0.73	0.13	1.55	3.3	0.221	0.179	5.4	0.9
TR-h4-2	1 to 6	20	0.73	0.13	2.50	6.2	0.118	0.181	2.9	1.7
TR-h4-3	1 to 6	20	0.73	0.26	1.55	3.3	0.221	0.359	5.4	0.9
TR-h4-4	1 to 6	20	0.73	0.26	4.80	12.6	0.058	0.352	1.4	3.4
TR-h4-5	1 to 6	20	0.73	0.69	3.40	8.7	0.084	0.939	2.1	2.4
TR-h4-6	1 to 6	20	0.73	0.76	4.75	12.4	0.059	1.039	1.4	3.4

Table 9-14 contains the generation values used for the piston-type wavemaker. The target wave height, H , for the test section was estimated using Linear wave theory that considered the effect of shoaling.

4.2.3. Random Waves

Three non-dimensional cases were chosen for the random wave cases, and their target spectral estimate of the significant wave height at the test section, H_{m0} , and peak wave period at the test section, T_p , were plotted used in Figure 4-5 to show the center point of each random wave case. The y-axis shows the non-dimensional parameter H_{m0}/h_v , while the x-axis displays the relative water depth h_v/L_p where L_p is the wavelength of the peak wave period, T_p . The random wave cases are also shown for each water depth where; yellow triangles denote the trials for $h_v = 1.85$ m, orange triangles for $h_v = 1.48$ m, green triangles for $h_v = 1.03$ m, and blue triangles for $h_v = 0.73$ m. In the figure, 300 individual waves were theoretically generated using a Joint North Sea Wave Project (JONSWAP) spectrum with $\gamma = 3.3$ for each of the non-dimensional random wave cases. The first nondimensional case TI-hv1-1 to TI-hv4-1, are represented as yellow squares, TI-hv1-2 to TI-hv4-2 is represented as purple squares, and TI-hv1-3 to TI-hv4-3 are represented as blue squares. The 300 waves for each nondimensional case covered a large area in the figure and allowed the study to consider a wide range of wave nonlinearities, steepness, and relative water depths with the three random wave cases. Table 4-2 lists the non-dimensional target values plotted in Figure 4-5 with the corresponding trial name, the layouts tested, number of waves, water depth at the vegetation, h_v , target wave height , H_{m0} , target peak wave period, T_p , and target peak period wavelength, L_p . The non-dimensional parameters: ratio of forest length to target wavelength (L_{veg}/L_p) and ratio of wavelength to the LWF width (L_{veg}/W) are included in the table. Table 9-15 contains the same information as Table 4-2 but for the target values used as inputs for the piston-type wavemaker. The target wave height, H , for the test section was estimated using linear wave theory that considered the effect of shoaling.

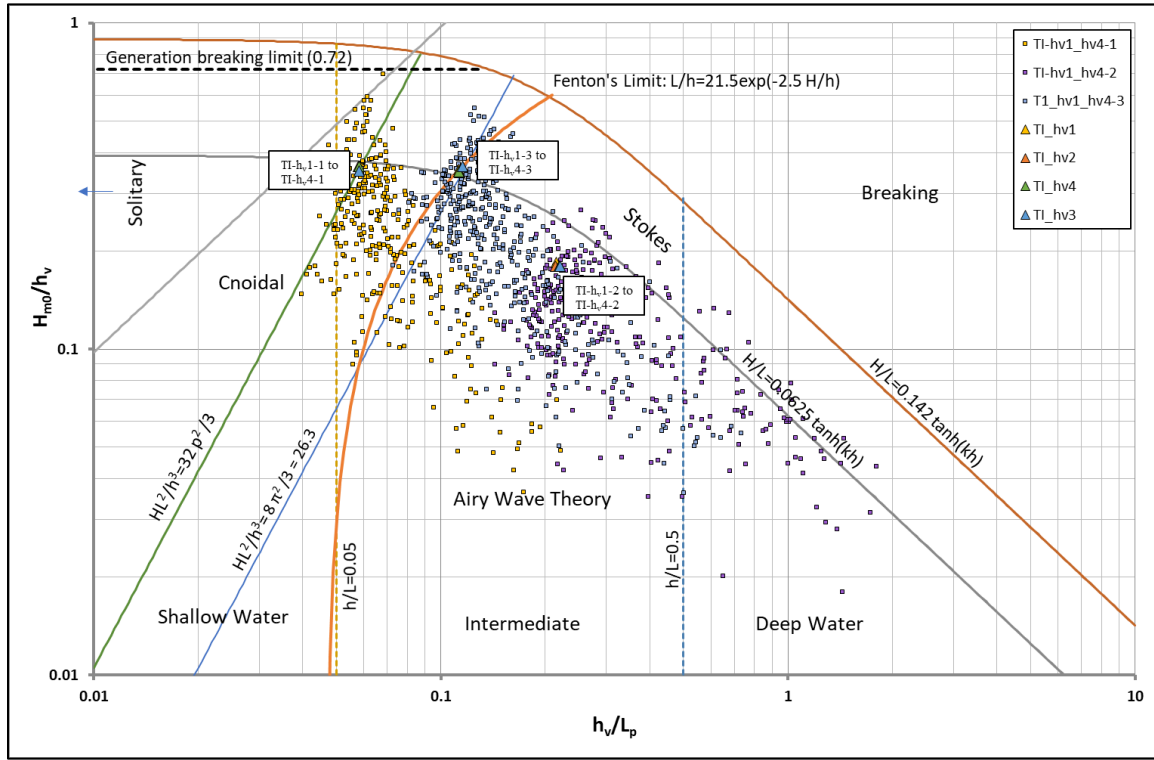


Figure 4-5 Non-dimensional plot of H_{m0}/h_v versus h_v/L_p for the target random wave cases. Graph source: Pedro Lomónaco.

Table 4-2 Table of target random wave cases at the test section.

Trial	Layouts	Number of Waves	h_v	H_{m0}	T_p	L_p	h_v/L_p	H_{m0}/h_v	L_{veg}/L_p	L_p/W
(-)	(-)	(-)	(m)	(m)	(m)	(m)	(-)	(-)	(-)	(-)
TI-h1-1	1 to 6	300	1.85	0.671	7.65	31.9	0.058	0.363	0.6	8.7
TI-h1-2	1 to 6	300	1.85	0.341	2.51	8.6	0.215	0.184	2.1	2.3
TI-h1-3	1	300	1.85	0.658	4.15	16.4	0.113	0.356	1.1	4.5
TI-h2-1	2 to 6	300	1.48	0.539	6.80	25.4	0.058	0.364	0.7	6.9
TI-h2-2	2 to 6	300	1.48	0.266	2.25	6.9	0.214	0.180	2.6	1.9
TI-h2-3	2 to 6	300	1.48	0.515	3.70	13.1	0.113	0.348	1.4	3.6
TI-h3-1	1 to 6	300	1.03	0.373	5.70	17.7	0.058	0.363	1.0	4.8
TI-h3-2	1 to 6	300	1.03	0.185	1.85	4.7	0.219	0.180	3.8	1.3
TI-h3-3	1 to 6	300	1.03	0.361	3.10	9.1	0.113	0.350	2.0	2.5
TI-h4-1	1 to 6	300	0.73	0.257	4.80	12.6	0.058	0.352	1.4	3.4
TI-h4-2	1 to 6	300	0.73	0.131	1.55	3.3	0.221	0.179	5.4	0.9
TI-h4-3	1 to 6	300	0.73	0.265	2.55	6.3	0.116	0.363	2.9	1.7

4.2.4. Transient Waves

The wavemaker was capable of generating transient waves for water depths at the vegetation, $h_v \leq 1.15$ m. Two of the selected water depths met this criterion: $h_v = 1.03$ m and $h_v = 0.73$ m. At $h_v = 1.03$ m a range of transient wave cases with scale factors: 700, 600, 400, 300, 200, and 100, respectively, were tested for Layout 1 to investigate their interaction with the model forest. After the preliminary investigation, the cases with scale factors of 600, 400, and 200 were chosen for further testing at the remaining water depths and layouts. Table 4-3 summarizes the transient waves tested for the study, including the trial name, layouts tested at, number of waves run, water depth at the vegetation h_v , scale factor, and stroke duration. An explanation of how the stroke duration was calculated can be found in Appendix G.

Table 4-3 Table of the transient wave cases.

Trial	Layouts	Number of Waves	h_v	Scale Factor	Stroke Duration
(-)	(-)	(-)	(m)	(-)	(s)
TT-h3-1	1	1	1.03	700	40.2
TT-h3-2	1 to 6	1	1.03	600	34.5
TT-h3-3	1 to 6	1	1.03	400	23.0
TT-h3-4	1	1	1.03	300	17.2
TT-h3-5	1 to 6	1	1.03	200	11.5
TT-h3-6	1	1	1.03	100	5.7
TT-h4-1	1 to 6	1	0.73	600	34.5
TT-h4-2	1 to 6	1	0.73	400	23.0
TT-h4-3	1 to 6	1	0.73	200	11.5

4.1. Test Schedule

The study's construction and instrumentation setup were completed from October 26th, 2020, to November 16th, 2020. Testing for the experiment was then completed from November 17th, 2020, to January 15th, 2021. Demolition of the model forest test section and concrete removal occurred from February 8th – 10th, 2021 (Table 4-4).

Table 4-4 Calendar for the study.

	Monday	Tuesday	Wednesday	Thursday	Friday	Saturday	Sunday
Oct 26- Nov 1st	Construction/Installation						
Nov 2nd - 8th	Construction/Installation / LiDAR scans				Concrete Pour		
Nov 9th - 15th	Instrumentation Setup		Veterans Day	Instrumentation Setup	Instrumentation Setup / Fill Flume		
Nov 16th - 22nd	Instrumentation / Shakedown Testing	Testing Layout 1		Testing Layout 1 / Drain Flume	Install Wall / LiDAR Survey / Fill Flume		
Nov 23rd - 29th	Testing Layout 2			Thanksgiving Holiday			
Nov 30th - Dec 6th	Testing Layout 2/ Drain Flume	Remove Half of Trees / LiDAR Survey / Fill Flume	Chlorine-Concrete Salts Dissipation	Calibrate Flume Water level / Testing Layout 3	NHERI Presentation / Outreach Day / Testing Layout 3		
Dec 7th - 13th	Testing Layout 3	Testing Layout 3 / Drain Flume	Remove Wall / LiDAR Scan / Fill Flume	Chlorine Dissipation	Calibrate Flume Water level / Testing Layout 4		
Dec 14th - 20th	Testing Layout 4		Testing Layout 4 / Drain Flume / LiDAR Scan	Remove all Trees / Fill Flume / Survey Instrumentation	Chlorine- Concrete Salts Dissipation / Paint Wall		
Dec 21st - 27th	Calibrate Flume Water Level / Testing Layout 5	Testing Layout 5		Testing Layout 5 / Drain Flume Christmas Eve	Christmas Day		
Dec 28th - Jan 3rd	Install Wall / Survey P-Gauges	Fill Flume/ Calibrate Flume Water level		New Years Eve	New Years Day		
Jan 4th - 10th	Testing Layout 6	Kister Visit / Test Wall Repair	Test Wall Repair				
Jan 11th - 17th	Testing Layout 6		Testing Layout 6 / Drain Flume	LiDAR Scan with Wall/ Remove Wall / LiDAR Scan w/o Wall			
Jan 18 - 24th	MLK Day						
Jan 25th - 31st							
Feb 1st - 7th							
Feb 8th - 14th	Test Section Demolition / Removal						

4.2. LiDAR Scans

The LWF was LiDAR scanned for the high-density model forest (HD, Layouts 1 and 2), low-density model forest (LD, Layouts 3 and 4), and baseline (BL, Layouts 5 and 6) cases. The HD and LD scans are detailed in the current section. The BL layout scans are described in Appendix H. Furthermore, the HD forest was LiDAR scanned twice. The first scans took place from November 3rd – 5th, 2020, while model forest construction was occurring. Scans were taken with a tripod placed on the ground and paper targets taped to various points in the LWF walls (Figure 4-6). Sixteen scans were taken for the HD forest during construction (Figure 4-7). In Figure 4-7, the locations of the HD LiDAR scans were taken from November 3rd – 5th as red x's with the cross-shore location x-axis shown. The origin of the x-axis was the piston wavemaker in neutral position.



Figure 4-6 BLK 360 mounted to tripod scanning the model forest.

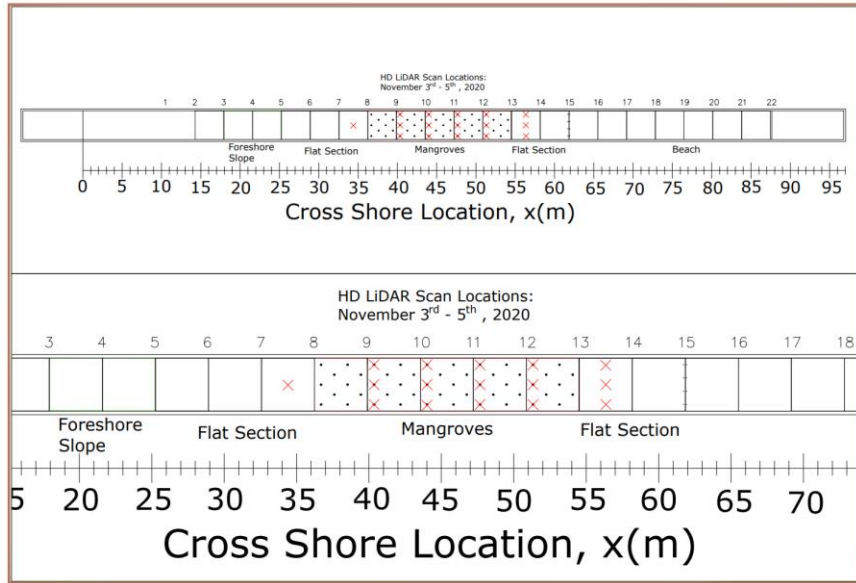


Figure 4-7 Locations of the high-density (HD) LiDAR scans taken from November 3rd – 5th, 2020.

Additional scans of the HD model forest were also taken on December 1st, 2020, and the BLK360 was mounted above the test section using Unistrut, rope, and two operators (Figure 4-8).

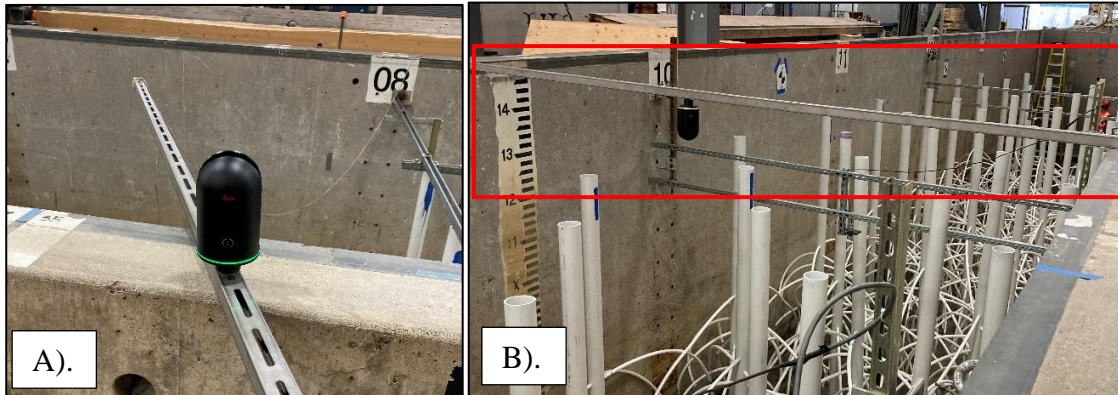


Figure 4-8 A). BLK 360 mounted to middle of Unistrut. B). BLK 360 positioned in the middle of the Large Wave Flume.

Seven scans were taken of the high-density forest using the overhead setup, and a scan of the test wall was also included (Figure 4-9). Figure 4-9 shows the locations of the HD LiDAR scans taken on December 1st, 2020, as red lines with the cross-shore location x -axis shown.

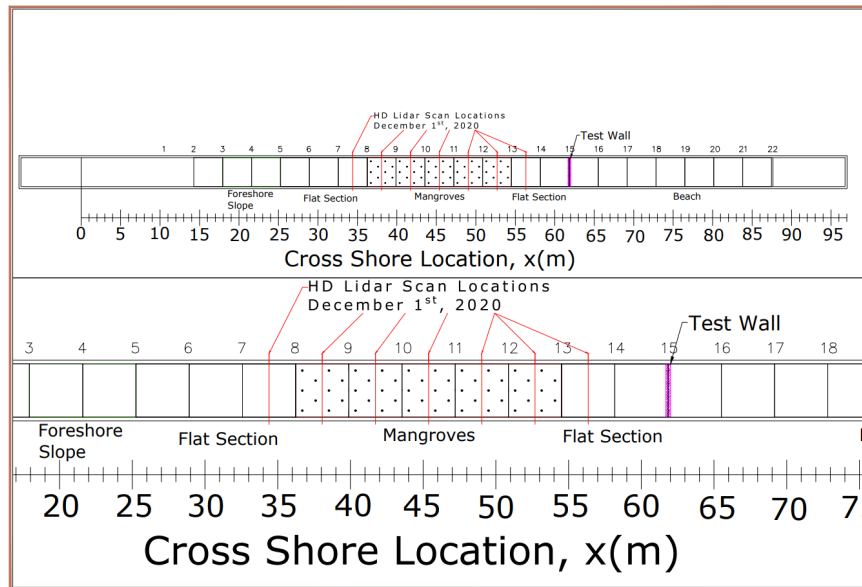


Figure 4-9 Locations of the overhead high-density (HD) LiDAR scans taken on December 1st, 2020.

The LD forest was scanned on December 9th, 2020, using the same overhead configuration as the second set of HD forest scans. A total of 7 scans were taken of the LD forest (Figure 4-10). Figure 4-10 shows the locations of the LD LiDAR scans taken from December 9th, 2020, as red lines.

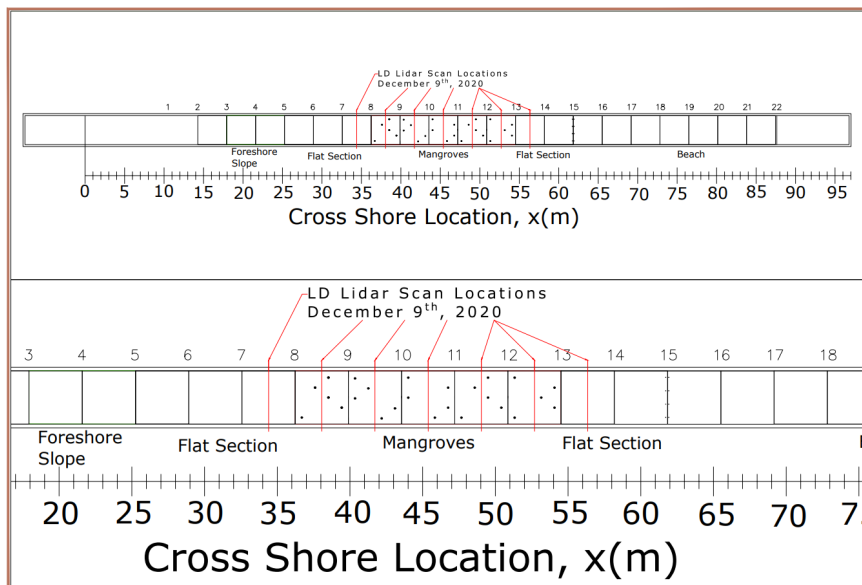


Figure 4-10 Locations of the overhead low-density (LD) LiDAR scans taken on December 9th, 2020.

4.1. Data Processing and Quality Control

After completing each trial, the raw data signals of the instruments were evaluated for quality control. If any significant errors were found, the instruments were adjusted accordingly and the trial was retested. The raw data from each trial was cropped and converted to physical units by HWRL staff using pre-established MATLAB scripts for the wave gauges, pressure gauges, and ultrasonic wave gauges. The scripts also applied a despiking routine to the USWGs and ADVs signals that truncates large spikes in the signals' measurements. The processed data was then saved in a new subdirectory folder titled inter-data.

4.2. Data Backup and DesignSafe

For each day of testing, data was copied to the local data processor located at the lab as well as the HWRL shared drive operated by the College of Engineering in a separate building from the HWRL. The data was also backed from the local processor and shared drive into separate backup drives. The study's data was also uploaded to NHERI DesignSafe at the end of each test day to be stored and made available later.

4.3. Data Analysis

4.3.1. Incident and Reflected Waves

The instrument signals for Arrays 1 and 2 (Figure 3-9) of the random wave cases from Layouts 1 to 6 (Figure 4-1) were processed using the program WaveLab v3.83. The full 7-gauge array from each Array 1 and 2 was initially used for analysis and produced results in both the frequency and time domains. During testing, a cross-tank mode was noted for several cases at each water level and layout. The cross-tank mode separation option within the reflection analysis was chosen for the initial processing of the trials. The cross-mode option used a method proposed by (Gronbech et al. 1997) that separated incident and reflected waves and accounted for cross modal activity using an arbitrary number of wave gauges. The Gornbech et al. (1997) method requires at least three wave gauges and was verified using numerical and physical experiments. The method showed good agreement to both the physical and numerical experimental results.

The Gornbech et al. (1997) method was used if significant energy was detected in a cross mode. However, if Wavelab v3.3 could not reliably detect a cross-mode, it would default to the method proposed by (Zelt and Skjelbreia, 1993) for incident and reflected analysis of irregular waves.

The Zelt and Skjelbreia, (1993) method utilized linear wave theory to separate incident and reflected waves with an arbitrary number of wave gauges. However, the method's accuracy increased if more than three wave gauges were used.

After initial analysis, the results were reviewed for each trial, and unrealistic values of the reflection coefficient were identified for the dissipative beach. Gauge signals were reevaluated for these trials, and it was found that USWG for Arrays 1 and 2 in these trials contributed considerable error to the analysis results. The USWG signals were then excluded from the analysis for each array on a trial-by-trial basis to reduce analysis error. The analysis results can be seen in Figures 10-45 to 10-55 and Appendix J.2.

4.3.2. Time Series Analysis

The random and regular wave cases of Layouts 1, 4, and 5 for the wave gauges, pressure gauges, and ultrasonic wave gauge signals were evaluated in the frequency domain using WaveLab v3.83. For the pressure gauge signals, the program utilized linear wave theory to convert the pressure signals to free surface elevation given as

$$\eta = \frac{p + \rho g z}{g K_p(z)} \quad (9)$$

where η is the free surface elevation, p is the total pressure, ρ is the density of water, g is the acceleration due to gravity, z is the defined water depth, and $K_p(z)$ is the pressure response factor given as

$$K_p(z) = \frac{\cosh(h+z)}{\cosh(kh)} \quad (10)$$

where h is the water depth. A frequency domain analysis was then performed on the pressure signals after the conversion to free surface elevations.

Chapter 5. LiDAR Analysis

5.1. High Density Model Forest

The two sets of HD model forest (Figure 4-7 and Figure 4-9) LiDAR scans were transferred from the BLK 360 scanner and uploaded to the Leica software Cyclone. In the application, the registration process, or the act of relating multiple scans on a common coordinate system, was completed for each set of HD forest scans. All scans were used for the first HD forest scans

completed on November 3rd – 5th, 2020. For the second set of HD LiDAR scans completed on December 1st, 2020, all scans were registered except for the most seaward scan. It was found to be corrupt and could not be used for further analysis (Figure 5-1 – blue circle).

The quality of the two merged scan worlds were compared after registration. The overhead LiDAR scans of the HD forest completed on December 1st, 2020, were better quality and used for further analysis. The selected HD model forest was then unified in a new model space, and an alongshore Y-Z cut plane was established at the seaward boundary of the forest section. A stencil (repeating pattern of trees) was identified within the forest, and five stencils were extracted from the HD LiDAR scans (Figure 5-1, red boxes). The stencils were 2.0 m in cross-shore width and selected from Bays 10 to 13 for the HD forest. Images of the cross-sections can be found in Appendix I.1.

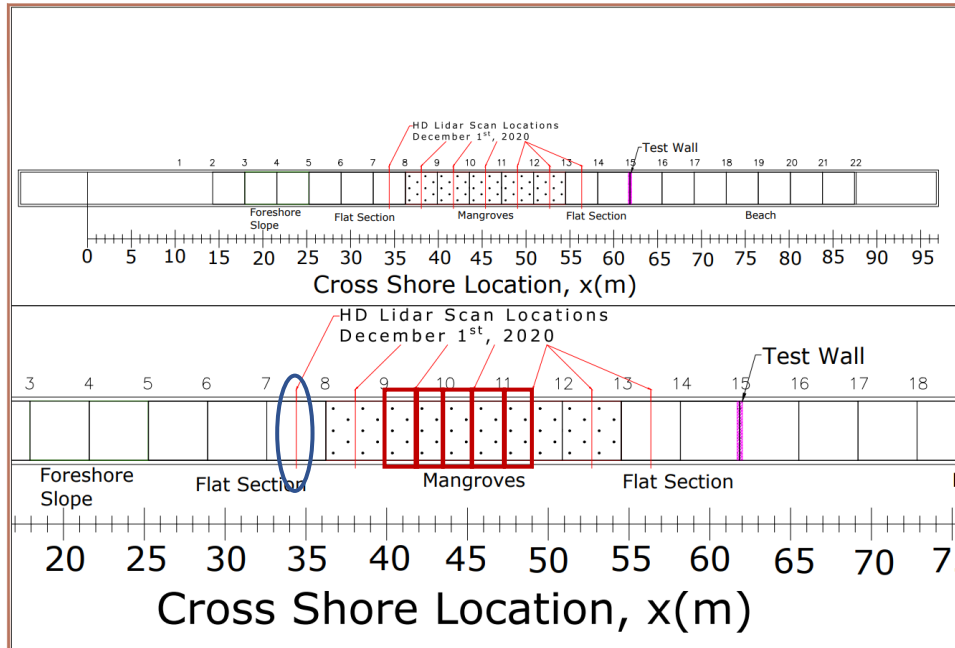


Figure 5-1 Location of stencil cross sections (red boxes) extracted from the high-density (HD) model forest.

The 5 extracted stencils for the HD model forest were manually cleaned for scatter and drift points. Manual measurements of the trunk and root diameters of the first extracted stencil were taken and compared to the known values of $D_{BH} = 0.1143$ m and $D_{Root} = 0.0286$ m. The LiDAR

measurements underestimated the trunk and root diameter by 2% and 10%, respectively. Details regarding the manual measurement comparison can be found in Appendix I.3.

The first extracted cleaned HD stencil was exported from Cyclone and uploaded to the open-source software CloudCompare v2. In CloudCompare v2, the flume side walls were removed from the first stencil cross-section. The rasterize tool in CloudCompare v2 was used to create a 1 cm x 1cm pixelated image of the LiDAR cross-section in grayscale color scale (Figure 5-2).



Figure 5-2 Pixelated image of the LiDAR scan from high-density (HD) stencil 1 in grayscale color scale.

The image of HD stencil 1 was exported and analyzed in MATLAB using image analysis tools. In MATLAB, the number of pixels in every 1 cm horizontal slice were counted and multiplied by the dimensions of one cell (1 cm x 1 cm) to get the projected area. This value was converted into the projected area per unit height, A , by dividing the projected area by the height of the horizontal slice (1 cm). The calculated projected area per unit height, A , for each centimeter bin was plotted as a function of the water depth at the vegetation, h_v (Figure 5-3).

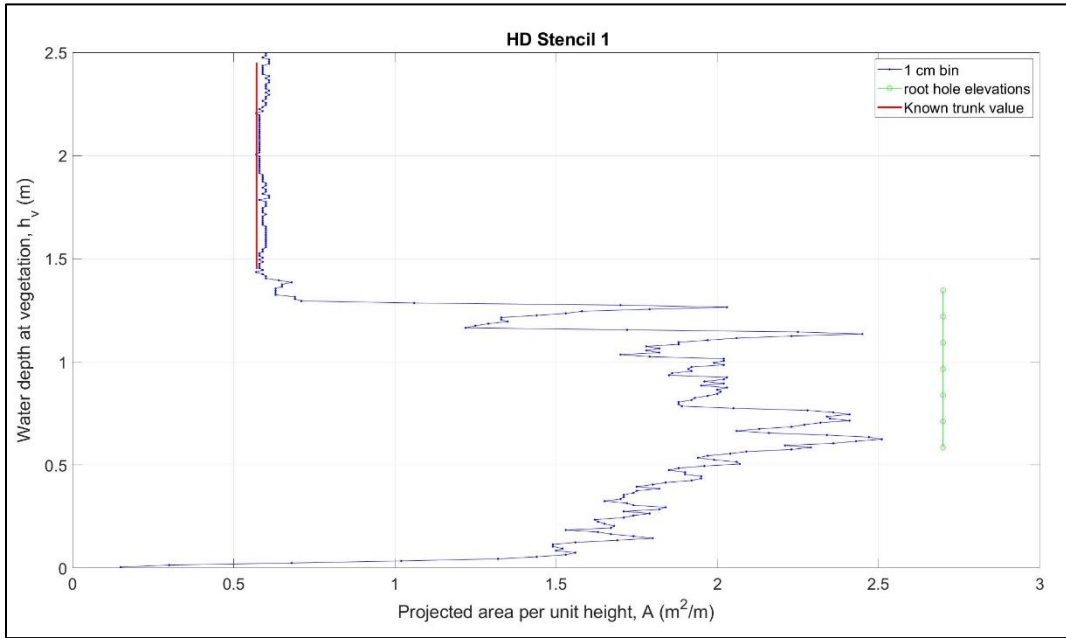


Figure 5-3 Projected area per unit height, A, versus water depth at vegetation, h_v , for high-density (HD) stencil 1.

Figure 5-3 shows the water depth at the vegetation, h_v , versus the projected area per unit height, A . The location of the root holes for the constructed model trees are shown by the green line and makers, and the known projected area per unit height, A , for the trunk section ($h_v \geq 1.35$ m), is shown by the red line. The measured value for the trunk section was on average 3.5% greater than the known value for the first HD stencil. To further test the method's validity, the first HD stencil cross-section was rotated 180° around the z -axis. Its projected area per unit height, A , was compared to the original cross-section (Figure 5-3), where the average variance was $5.62 \times 10^{-6} \text{ m}^2$. The comparison showed that the analysis methods were not impacted by the direction (landward or seaward) that the cross-section was analyzed. Further details of the rotational comparison can be found in Appendix I.4.

After the analysis method was validated, the process was repeated for the remaining HD stencils, and an average was taken of the projected area per unit height, A , for all of the HD stencils. By averaging the HD stencils projected area per unit height profiles, one representative mean profile was created for the entire HD model forest (Figure 5-4). Images of the HD cross sections in grayscale are shown in Appendix I.2.

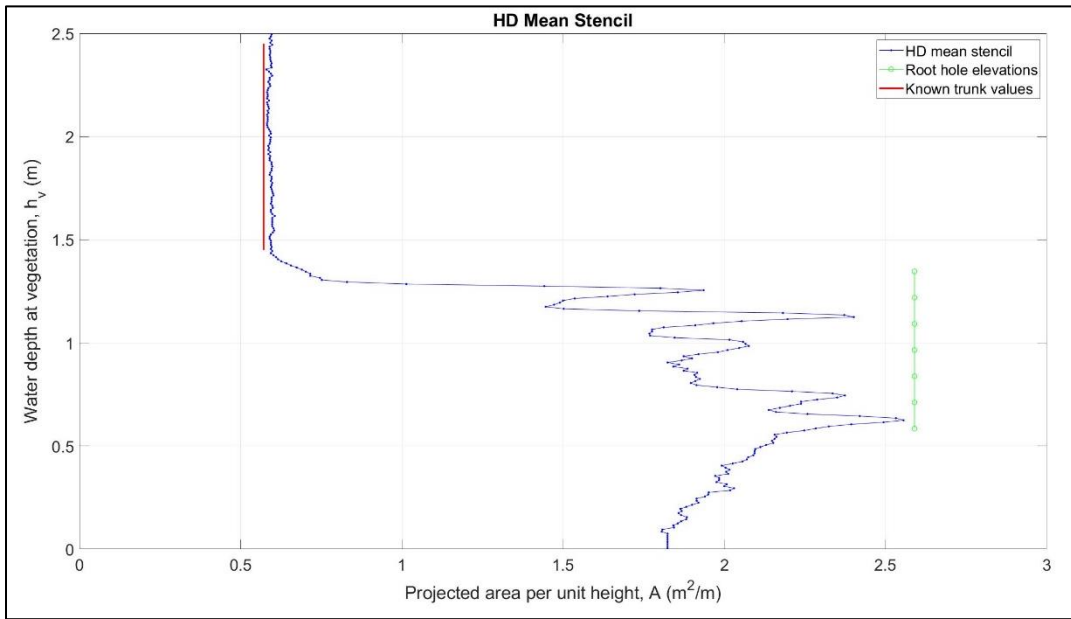


Figure 5-4 Projected area per unit height, A , versus water depth at vegetation, h_v , for high-density (HD) mean stencil.

In Figure 5-4, the y-axis describes the water depth at the vegetation, h_v , and the x-axis depicts the projected area per unit height, A . The HD mean stencil's projected area is represented as a blue line and markers. Additionally, the figure shows the known trunk diameter as a red line and the root hole elevations for the model tree as green line and markers. In general, the HD mean profile shows the projected area per unit height, A , gradually increasing until the first root hole. The projected area per unit height, A , then starts to gradually decrease with some variability until the highest root hole. After the highest root hole, the projected area quickly decreases until it becomes relatively constant at the trunk section ($h_v \geq 1.35$ m). The HD mean stencil overestimates from the known trunk value by 3.9% on average.

5.2. Low Density Model Forest

The LD model forest scans were also loaded into the Leica software Cyclone and registered together. All 7 scans were able to be used for the registration (Figure 4-10). The merged scans were then unified in a new model space, and a Y - Z cut plane was established at the seaward boundary of the forest section. The same stencil definition as in the HD model forest was used and 7 stencil cross-sections were identified and extracted from the LD model forest (Figure 5-5-red boxes).

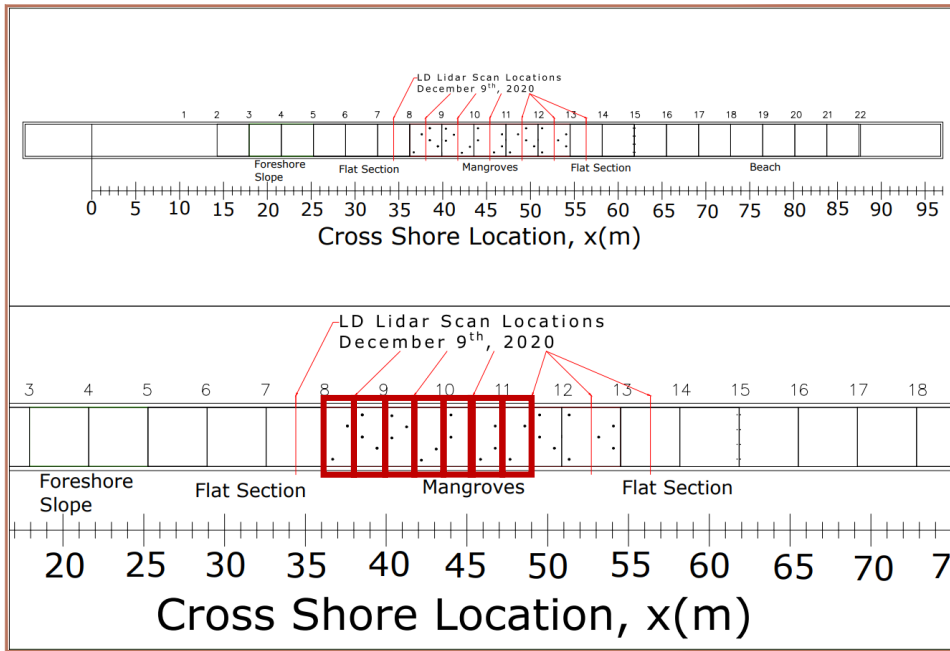


Figure 5-5 Location of stencil cross sections (red boxes) extracted from the low-density (LD) model forest.

More stencils were extracted from the LD forest to account for the greater variability in the LD forest pattern. The established analysis routine from the HD model forest was also used and a mean projected area per unit height, A , profile was generated from the 7 cross-sections (Figure 5-6). Images of the LiDAR cross-sections and their grayscale cross-section images can be found in Appendix I.5 and Appendix I.6, respectively.

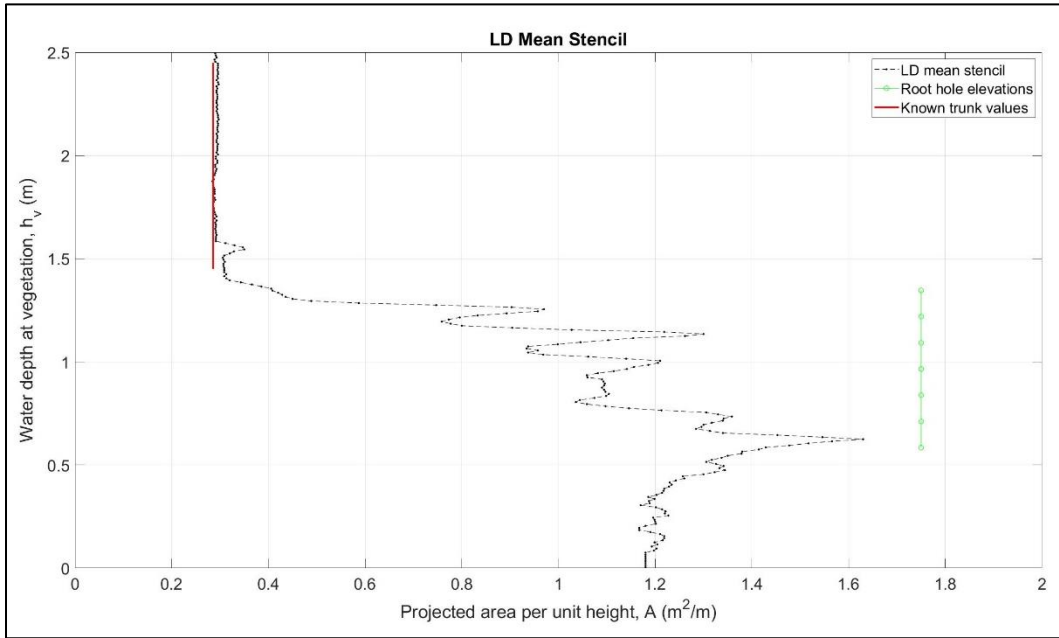


Figure 5-6 Projected area per unit height, A, versus water depth at vegetation, h_v , for low-density (LD) mean stencil.

In Figure 5-4, the y-axis shows the water depth at the vegetation, h_v , and the x-axis displays the projected area per unit height, A . The LD mean projected area is represented as a black dashed line and markers. In general, the LD mean profile shows the projected area per unit height, A , gradually increasing until the first root hole. The projected area per unit height, A , starts to gradually decrease with some variability until the highest root hole. After the highest root hole, the projected area quickly decreases until it becomes relatively constant at the trunk section ($h_v \geq 1.45$ m). The LD mean for the trunk section overestimates the known value by 3.2% on average.

5.3. Model Forest Comparison

Each of the mean profiles were divided by the mean number of trees in the analyzed cross-sections. The division allowed for the mean projected area per unit height, A , of the HD and LD model forests to be compared on a per tree basis. The mean projected area per unit height per tree, A_t , profile for the HD and LD model forest were then compared in Figure 5-7.

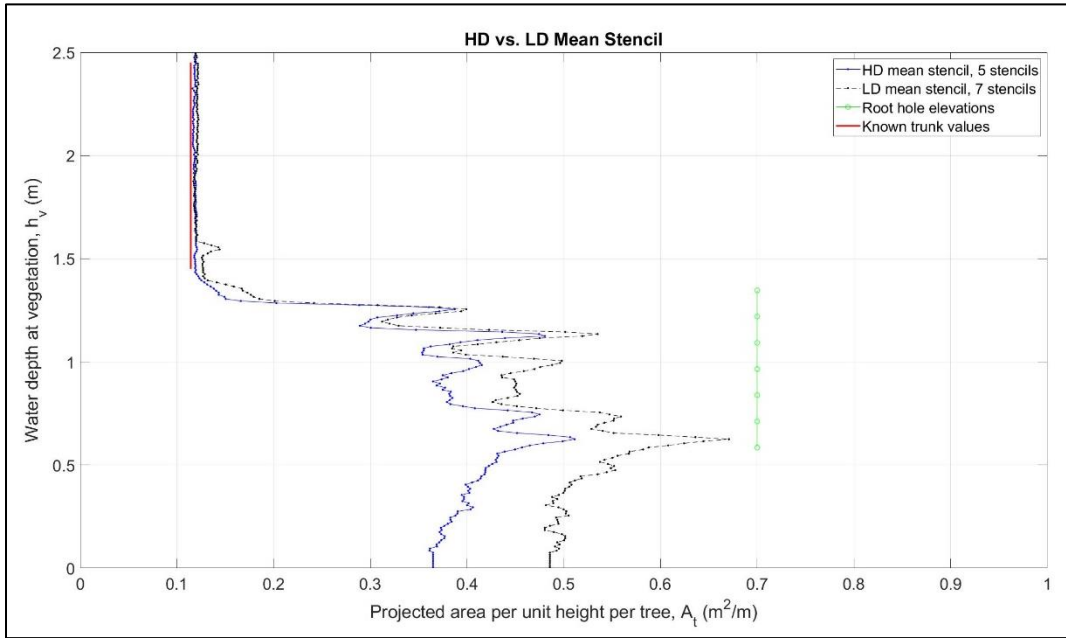


Figure 5-7 Projected area per unit height per tree, A_t , versus the water depth at the vegetation, h_v , for the high-density (HD) mean stencil and low-density (LD) mean stencil.

In Figure 5-7, the projected area per unit height per tree, A_t , versus the water depth at the vegetation, h_v , for the HD mean stencil (solid blue line, blue circles) and LD mean stencil (dashed black line, black circles) are shown. The figure shows that for the HD mean stencil, the projected area per unit height per tree, A_t , is lower than the LD mean stencil for the root section ($h_v = 0$ to 1.35 m). The difference is 14% on average. For the trunk section ($h_v > 1.35$ m), the LD mean stencil is on average 0.94% greater than the HD mean stencil values. The difference in the roots projected area per unit height per tree, A_t , for the two mean stencils indicates that there is root overlap occurring in the HD mean stencil, causing an underestimate of the projected area per unit height per tree, A_t . The root overlap was investigated by splitting the HD stencils in half and analyzing each half stencil. The 10 HD half stencils were then averaged and compared to the LD mean stencil (Figure 5-8).

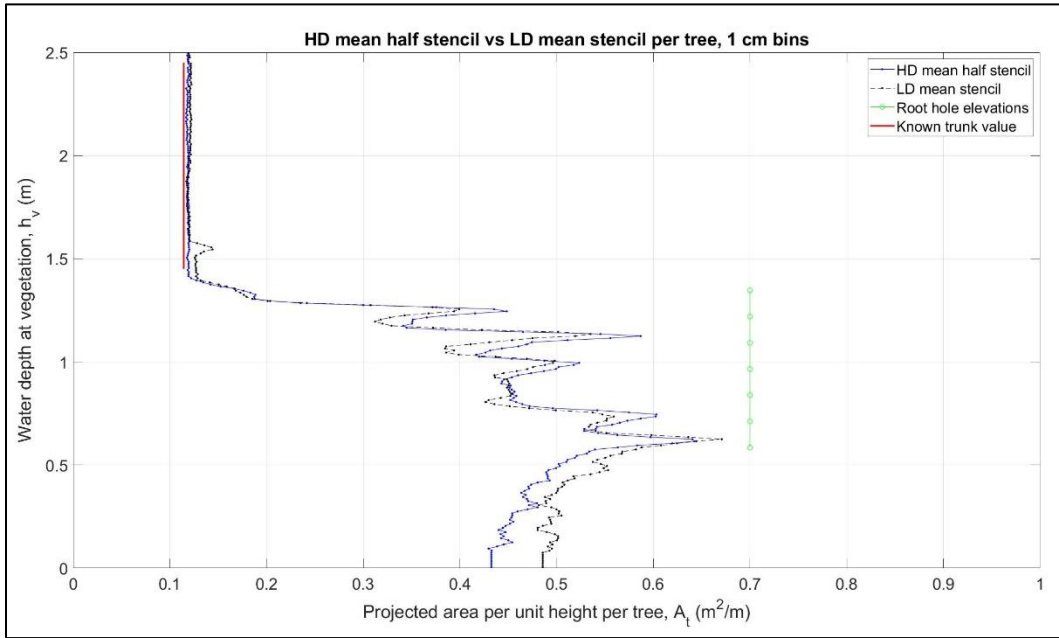


Figure 5-8 Projected area per unit height per tree, A_t , versus the water depth at the vegetation, h_v , for the high-density (HD) mean half stencil and low-density (LD) mean stencil.

Figure 5-8 shows the projected area per unit height per tree, A_t , versus the water depth at the vegetation, h_v , for the HD mean half stencil (blue line, dots) and the LD mean stencil (black line, dots). The profiles of the HD mean half stencil and the LD mean stencil show better agreement with each other than the profiles shown in Figure 5-7. The HD mean half stencil's projected area per unit height per tree, A_t , is 1.4% smaller than the LD mean stencil on average for the root section ($0 \leq h_v \leq 1.35$ m). For the trunk section ($h_v > 1.35$ m), the HD mean half stencil is on average 1.9% smaller than the LD mean stencil. The relation further verifies the underestimation by the HD mean stencil of the projected area per unit height per tree, A_t , due to root overlap. The HD half mean stencil was used for further analysis in the study (Figure 5-9).

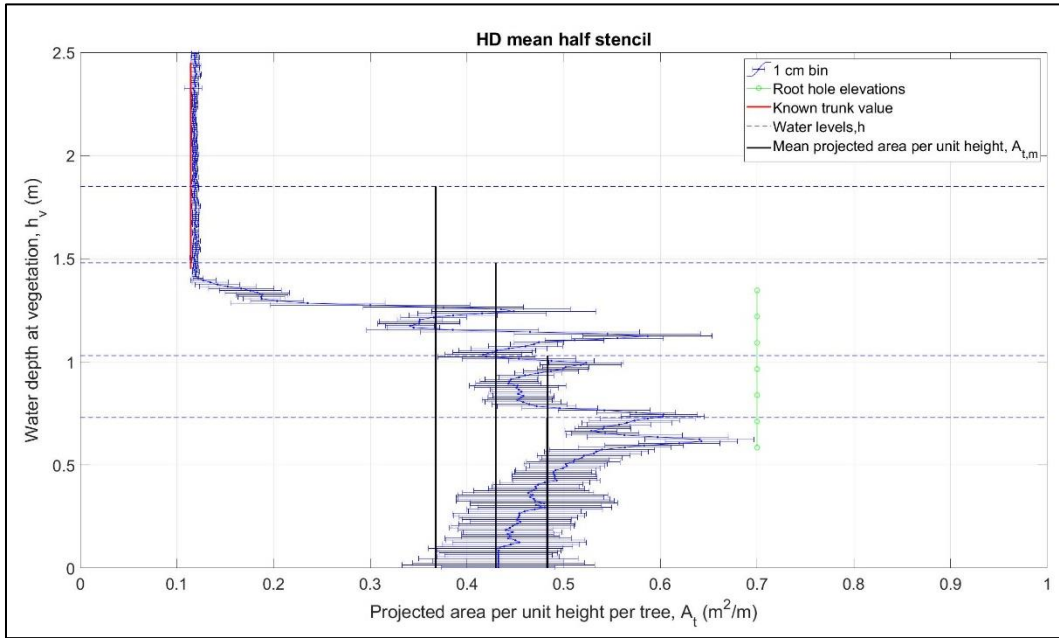


Figure 5-9 Projected area per unit height per tree, A_t , versus the water depth at the vegetation, h_v , for the high-density (HD) mean half stencil with error bars representing \pm one standard deviation and mean projected area per unit height per tree, $A_{t,m}$, values are shown.

For Figure 5-9, the mean projected area per unit height per tree for the HD mean half stencil (blue line, circles) and the corresponding error bars \pm one standard deviation (horizontal blue lines) at each bin are shown. Furthermore, water levels at the vegetation, h_v that were tested (blue dashed line) are displayed along with the mean projected area per unit height per tree, $A_{t,m}$ (solid black line) for each water depth. The $A_{t,m}$ values were calculated by integrating the HD mean half stencil curve to each tested water level. For the first two $A_{t,m}$ values, the figure shows little difference despite the difference in water levels. At the third water level $h_v = 1.48$ m, the $A_{t,m}$ value decreases as the influence of the roots section decreases as well. By the fourth water depth, $h_v = 1.85$ m, the $A_{t,m}$ value is the lowest due to the influence of the trunks. The horizontal lines in Figure 5-9 denote the error bars for each 1 cm bin, \pm one standard deviation. The error bars show there is more variability in the root section ($0 \leq h_v \leq 1.35$ m) for the measured projected area per unit height per tree than in the trunk section ($h_v > 1.35$ m). The standard deviation at each bin was used to calculate a mean standard deviation, σ_m , using the same integration routine for the $A_{t,m}$ values. The variability of the mean projected area per unit height per tree, $A_{t,m} \pm \sigma_m$ was then calculated. Values for the $A_{t,m}$ and $\sigma_{t,m}$ parameters and $A_{t,m} \pm \sigma_{t,m}$ for each water level are reported in Table 5-1.

Table 5-1 Mean projected area per unit height per tree, $A_{t,m}$, mean standard deviation $\sigma_{t,m}$, and $A_{t,m} \pm \sigma_{t,m}$ for each water depth at vegetation, h_v , tested.

h_v (m)	$A_{t,m}$ (m^2/m)	$\sigma_{t,m}$ (m^2/m)	$A_{t,m} - \sigma_{t,m}$ (m^2/m)	$A_{t,m} + \sigma_{t,m}$ (m^2/m)
1.85	0.368	0.095	0.273	0.462
1.48	0.430	0.116	0.313	0.546
1.03	0.483	0.125	0.358	0.609
0.73	0.483	0.140	0.343	0.623

These parameters are used in later sections to calculate the drag coefficient, C_D , and a range uncertainty around the C_D value due to the variability of the $A_{t,m}$ values.

5.4. Effective Diameter

For the model trees, two different diameter pipes were used for the construction. The larger diameter pipe, D_{BH} , represented the trunk, while the smaller diameter pipe, D_{Root} , represented the roots. There was an order of magnitude of difference between the D_{BH} and D_{Root} diameters. That difference significantly affects how the fluids flow around the two diameters is characterized. Particularly, for parameters such as the Reynolds number, Re and Keulegan-Carpenter number, KC . A weighted average of the trunk diameter and root diameter known as the effective diameter, D_e can be used to characterize the flow around the model trees (Equation 11).

$$D_e = \frac{n_{trunk}*D_{BH}+n_{m,root}*D_{root}}{n_{total}} \quad (11)$$

In Equation (11), n_{trunk} is the number of trunks, D_{BH} is the trunk diameter, n_{root} is the number of roots, D_{Root} is the diameter of the roots, and n_{total} is the total number of elements ($n_{trunk} + n_{Root}$). Equation (11) can be simplified by substituting mean projected area per unit height per tree, $A_{t,m}$ for the numerator ($n_{trunk} * D_{BH} + n_{m,Root} * D_{Root}$) and simplifying n_{total} for a per tree basis to $1 + n_{Rm}$ where n_{Rm} is the mean number of roots at each tested water level (Equation 12).

$$D_e = \frac{A_{t,m}}{(1+n_{Rm})} \quad (12)$$

In Equation (12), the effective diameter is dependent on one unknown, n_{Rm} . The 10 HD half stencil images were segmented into 10 cm vertical bins to calculate the n_{Rm} values for each water level (Figure 5-10). At each bin, the number of roots was visually counted and tabulated for each

cross-section. The number of roots at each bin was then divided by the number of trees present within each cross-section, to get the number of roots per tree at each 10 cm bin. The averaged of each 10 cm bin for the 10 HD mean stencils and the standard deviation were calculated (Figure 5-11). In Figure 5-11, the y-axis shows the water depth at the vegetation, h_v , and the x-axis shows the number of roots per tree, n_R .

Additionally, the black line and markers represent the number of roots at each 10 cm bin. The black horizontal lines represent the n_R values $\pm \sigma_R$, and the horizontal dashed blue lines show the water levels tested for the study. The black vertical lines show the mean number of roots per tree, n_{Rm} , for each water level.

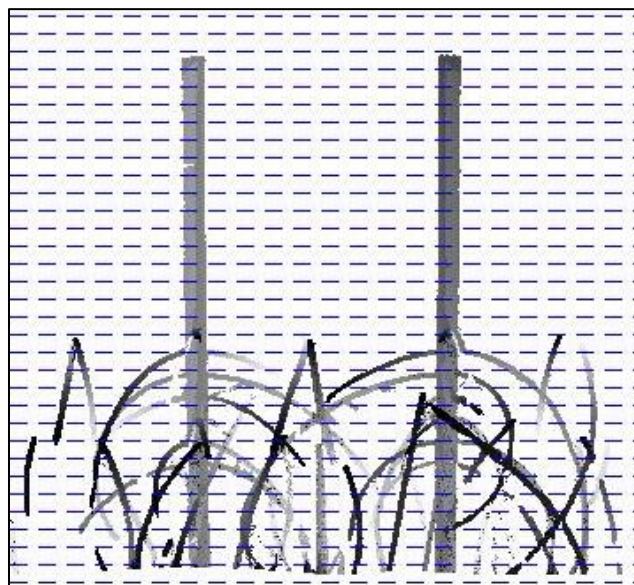


Figure 5-10 Example of high-density (HD) mean half stencil image segmented into 10 cm vertical bins.

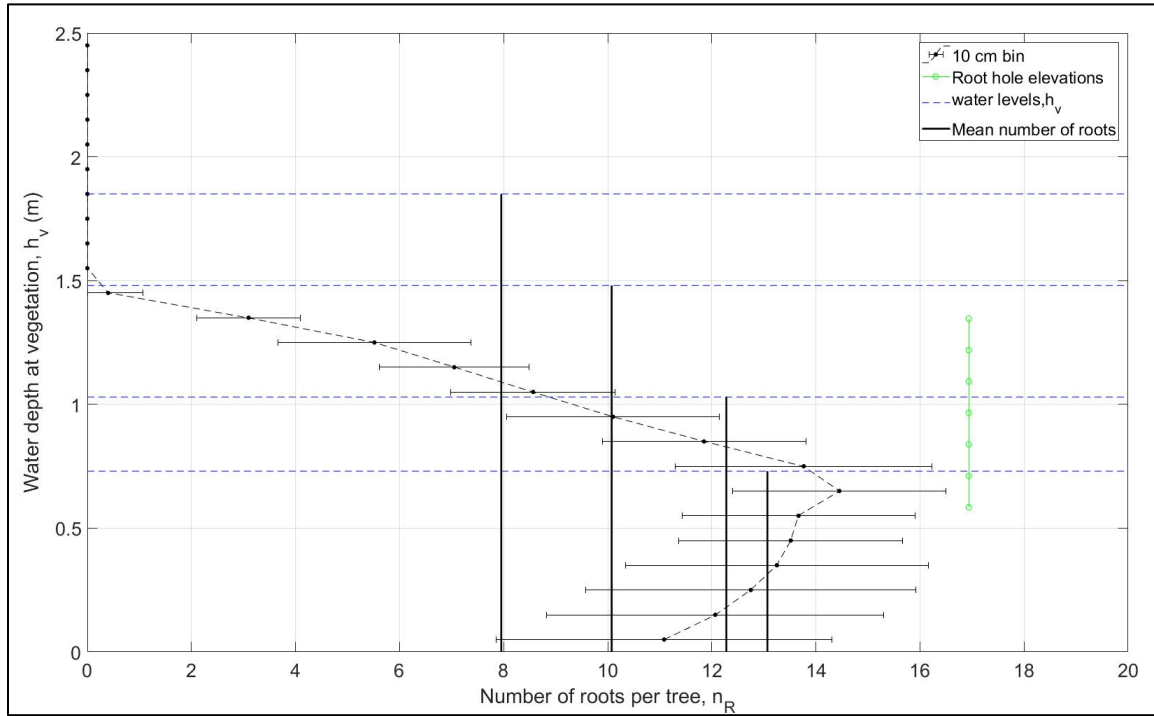


Figure 5-11 Water depth at the vegetation, h_v , versus the number of roots per tree, n_R , for each 10 cm bin.

For the figure, the n_R value increases from the floor of the test section to the midpoint of root holes 1 and 2 before decreasing to 0 by $h_v = 1.55$ m. The largest n_{Rm} values were found at the lowest water depth. The smallest n_{Rm} value corresponded to the highest water depth. The mean standard deviation, σ_{Rm} , for the number of roots was greatest at the lowest water depth but remained constant for the other water depths. Table 5-2 shows the calculated n_{Rm} and σ_{Rm} values and $n_{Rm} \pm \sigma_{Rm}$ for each water level.

Table 5-2 Mean number of roots, n_{Rm} , mean standard deviation of the mean number of roots, σ_{Rm} , and $n_{Rm} \pm \sigma_{Rm}$ for each water depth at vegetation, h_v , tested.

h_v (m)	n_{Rm} (-)	σ_{Rm} (-)	$n_{Rm} - \sigma_{Rm}$ (-)	$n_{Rm} + \sigma_{Rm}$ (-)
1.85	8	2	6	10
1.48	9	2	7	11
1.03	12	2	10	15
0.73	13	3	10	16

To verify the visual method, the known values of the trunk and root diameters, $D_{BH} = 0.1143$ m and $D_{Root} = 0.0286$ m, were used with the MATLAB image analysis results to estimate the n_{Rm} values. The values were compared to the results in Table 5-2. An average absolute percent difference of 7% was found between the methods and indicates reasonable accuracy for the visual method. Details regarding how the n_{Rm} values were calculated using D_{BH} and D_{Root} for comparison with the visual method are detailed in Appendix I.7.

Using Equation (12), effective diameters were calculated for each water level (Table 5-3).

Table 5-3 Mean projected area per unit height per tree, $A_{t,m}$, mean number of roots, n_{Rm} , total number of roots, n_{total} , and effective diameter, D_e , for each water depth at vegetation, h_v , tested.

h_v (m)	$A_{t,m}$ (m^2/m)	n_{Rm} (-)	n_{total} (-)	D_e (m)
1.85	0.368	8	9	0.041
1.48	0.430	9	10	0.041
1.03	0.483	12	13	0.036
0.73	0.483	13	14	0.034

The D_e value is smallest at the lowest water level but increases as the water depth increases. In general, however, the D_e values were relatively the same, with only 5 mm difference seen between the minimum and maximum values. The method to estimate D_e can be extended to field applications with relative ease where the alternative of using estimated D_{BH} and D_{Root} values via conventional methods (e.g., calipers, rulers, measuring tape) could prove to be cumbersome or unfeasible. The visual method could be later automated via computational methods to reduce the analysis time required.

For example, LiDAR scans could capture the variability of a dense mangrove fringe consisting of multiple sizes, ages, and geometry within an hour. Each LiDAR scan takes 5 minutes to complete and can be spaced roughly 1.52 m apart, depending on the complexity of the site, and cover approximately 18 m of the fringe in the allotted time. Conversely, traditional methods would need significantly more time to either cut down or manually measure each aspect of the trees to capture the same detail as the LiDAR scans. Also, the LiDAR scans provide digital documentation of the mangrove forest that can be analyzed at any point in time and compared to future scans of the fringe to see how the fringe has changed over time. The LiDAR method could

quantify how the protection of the mangrove fringe changes after a hurricane has damaged it. Additionally, the recovery of the fringe could also be evaluated using the method by comparing scans of the same forest at different stages of regrowth.

5.5. Previous Studies Comparison

The HD mean half stencil profile of the projected area per unit height per tree, A_t , was compared with the previous studies by Chang et al. (2019) and Maza et al. (2019) model trees at full scale (Figure 5-12). In Figure 5-12, the y -axis shows the elevation, z , while the x -axis shows the projected area per unit height per tree, A_t . The HD mean half stencil is represented by a blue line and markers, the Maza et al. (2019) as a black line and markers, and the Chang et al. (2019) as a red line and markers. Generally, the figure shows that each study considered a model tree with a different root structure, trunk diameter, and overall projected area per unit height per tree, A_t , profile.

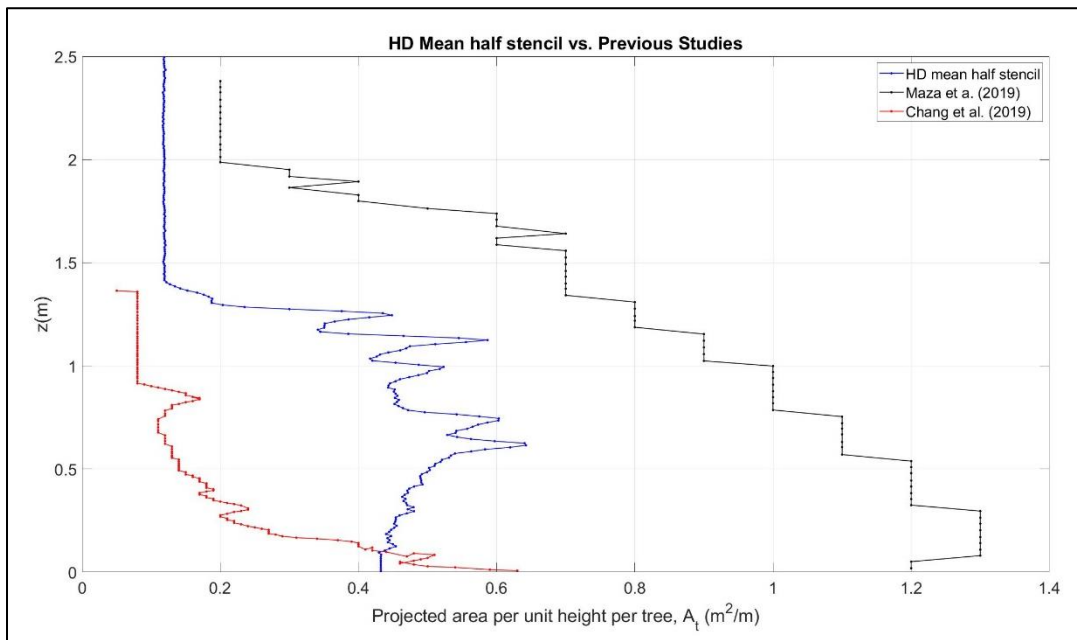


Figure 5-12 Comparison of the projected area per unit height per tree, A_t , for the studies high-density (HD) mean half stencil (Blue line and markers), Maza et al. (2019) model tree profile (black line and markers), and Chang et al. (2019) model tree profile (red line and markers).

The Maza et al. (2019) study profile had the largest projected area at full scale. The Maza et al. (2019) study tested a model tree with a $D_{BH} = 0.2$ m ($z > 2.01$ m), 24 roots per tree, and the highest root located at 2.01 m that contributed to the shape and height of the projected area per

unit height per tree profile in the root section ($z \leq 2.01$ m). On the other hand, the present study had a $DBH = 0.1143$ m ($z > 1.35$ m), 14 roots per tree, and the highest root located at 1.35 m from the ground yielding a smaller projected area per unit height per tree profile for the root section that did not extend as far on the z -axis as the Maza et al. (2019) study. The present study's projected area per unit height per tree profile also differs in shape from the Maza et al. (2019) study, where it initially increases before decreasing with some variation. However, the Maza et al. (2019) study has a projected area per unit height per tree profile that gradually decreases as z increases.

Both the present and Maza et al. (2019) study used Ohira et al. (2013) parameterization for their model trees which are based on samples of *Rhizophora apiculata* and *Rhizophora mucronata* trees for a mangrove forest in the Ranong Province, Thailand. However, the present study chose to modify the parameterization by using root pairs, while Maza et al. (2019) used the exact methodology presented by Ohira et al. (2013). That difference in construction could explain the disparities between the projected area per unit height per tree profile at the lower elevations.

The Chang et al. (2019) study also differed from the present and Maza et al. (2019) studies. In general, the profile was smaller than the Maza et al. (2019) study. The Chang et al. (2019) study was initially greater than the present study ($0 < z < 0.1$ m) before it gradually decreased as it reached the trunk section ($z > 0.91$ m). 3D laser scans taken of a 17 year old tree in Vietnam were used to 3D print the Chang et al. (2019) model tree. For the Chang et al. (2019) model, a $DBH = 0.07$ m, and the highest root was located at 1.10 m. The Chang et al. (2019) model also included primary, secondary, and tertiary roots within the construction of their model. The present study and Maza et al. (2019) only included the primary roots in the construction of their model trees.

Furthermore, both the Chang et al. (2019) and Maza et al. (2019) profiles, show a slight variance in the trunk diameter and perceived location of the highest root for the extracted data compared to the reported values. The slight difference indicates some error associated with the extraction process, although not significant. Moreover, the figure also shows the geometric variability in the tree models tested for the present and past mangrove laboratory experiments. The figure more

importantly, highlights differences between idealized models of the present study and Maza et al. (2019) study with the more realistic representations by Chang et al. (2019).

Chapter 6. Experimental Results, Random Waves

6.1. Frequency versus Time Domain Analysis

The results of incident and reflected wave analysis in the time and frequency domain were compared. The incident mean wave period, T_m , from the time domain and the incident mean wave period, $T_{0,1}$, from the frequency domain for the seaward Array 1 were used for the comparison (Figure 6-1). In Figure 6-1, T_m is shown on the y -axis and $T_{0,1}$ is shown in the x -axis. The values are designated by layout where dark blue circles represent Layout 1, dark orange circles represent Layout 2, intermediate orange circles represent Layout 3, intermediate blue circles represent Layout 4, light blue circles represent Layout 5, and oranges circles represent Layout 6, respectively. The black line shows where the two parameters are equal. Generally, the figure shows good agreement between the measured data and the black line for all layouts, thus, demonstrating agreement between the time and frequency domain results. Similar agreement was also found for Array 2 (Figure 9-44, Appendix J.1).

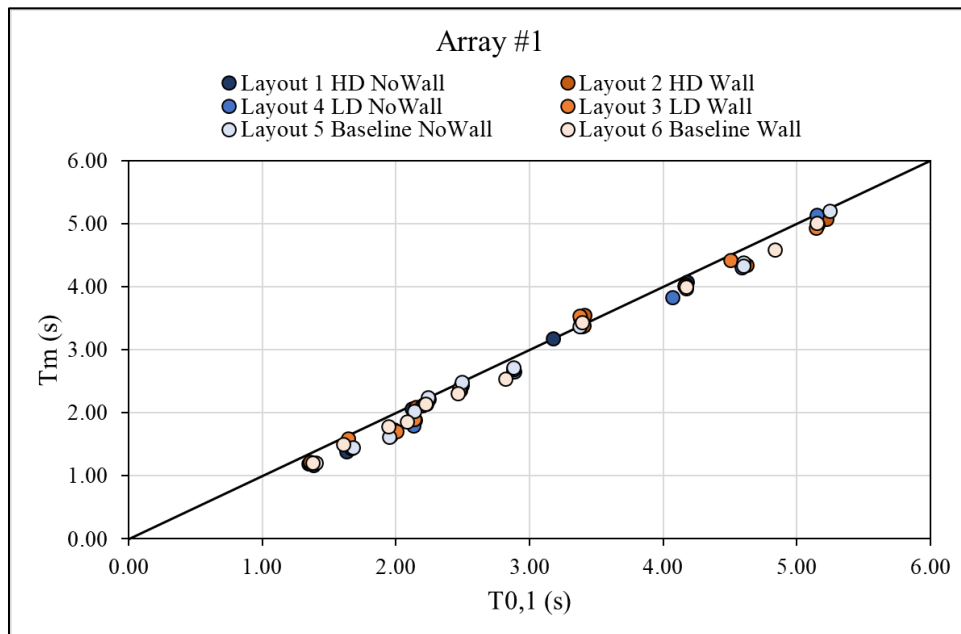


Figure 6-1 Mean wave period, T_m , from the time domain versus the mean wave period, $T_{0,1}$, from the frequency domain for the random wave cases at Array 1 for Layouts 1 to 6.

6.2. Wave Attenuation

The random waves cases for layouts with no test wall, Layout 1, high-density (HD), Layout 4, low-density (LD), and Layout 5, baseline (BL), were analyzed for the incident spectral estimate of the significant wave height, $H_{m0,i}$, and the reflected spectral estimate of the significant wave height, $H_{m0,r}$ for each array. The total spectral estimate of the significant wave height, H_{m0} , for the wave gauges (WG) and pressure gauges (PD18) in the test section (Figure 3-9) were also determined. In Figure 6-2, these results are shown for case TI-h3-3 where $h_v = 1.03$ m, $H_{m0} = 0.310$ m, $T_p = 3.10$ s. The H_{m0} values with respect to the x location are shown (origin of x -axis located at the wavemaker in neutral position) for the wave gauges (WG, circles) and pressure transducers (PD, diamonds) of the HD (dark colors), LD (intermediate colors) and BL (light colors) layouts. The figure also shows the $H_{m0,i}$ (triangles), and $H_{m0,r}$ (squares) values for Arrays 1 and 2, located at the WG they were resolved (WG 2 and WG 8). Starting from the left, the H_{m0} values at WG 1 and for Array 1 are all generally the same for the three layouts but varied slightly among the wave gauges.

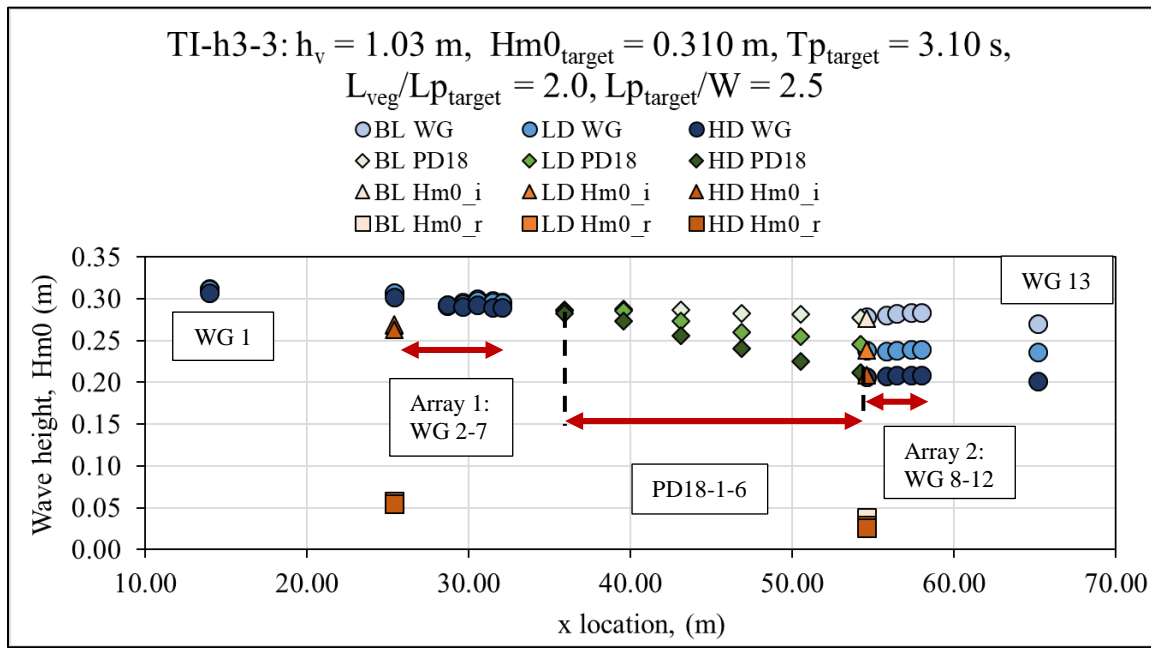


Figure 6-2 Total spectral estimate of the significant wave height, H_{m0} , with respect to x location for wave gauges (WG, circles) and pressure gauges (PD, diamonds) and the incident spectral estimate of the significant wave height, $H_{m0,i}$ (triangles), and reflected spectral estimate of the significant wave height, $H_{m0,r}$ (squares), for the high-density (HD) (dark colors), low-density (LD) (intermediate colors), and baseline (BL) (light colors) layouts for random wave case TI-h3-3.

Similar H_{m0} values were also seen for the HD, LD, and BL layouts at PD18-1, the most seaward pressure gauge. After PD18-1, the H_{m0} values for the HD and LD layouts steadily decreased to PD18-6. There was also a slight decrease seen for the H_{m0} values of the BL layout. However, the HD layout had the greatest decay rate of H_{m0} , followed by the LD layout, indicating higher forest densities yield larger wave height decay rates. Furthermore, the figure shows there was greater variability in the WG H_{m0} values compared to the PD18 measurements. The finding was verified after review of the other random wave cases (Appendix J.2), and it was determined that H_{m0} values from the pressure gauges (PD18-1 to PD18-6) would be used to fit the wave height decay curves for each case. The wave height decay coefficient for random waves, $\tilde{\alpha}$, was fit using Equation (7) and MATLAB fitting functions. The y-intercept for the fit was set at the H_{m0} value of PD18-1 (Figure 6-3).

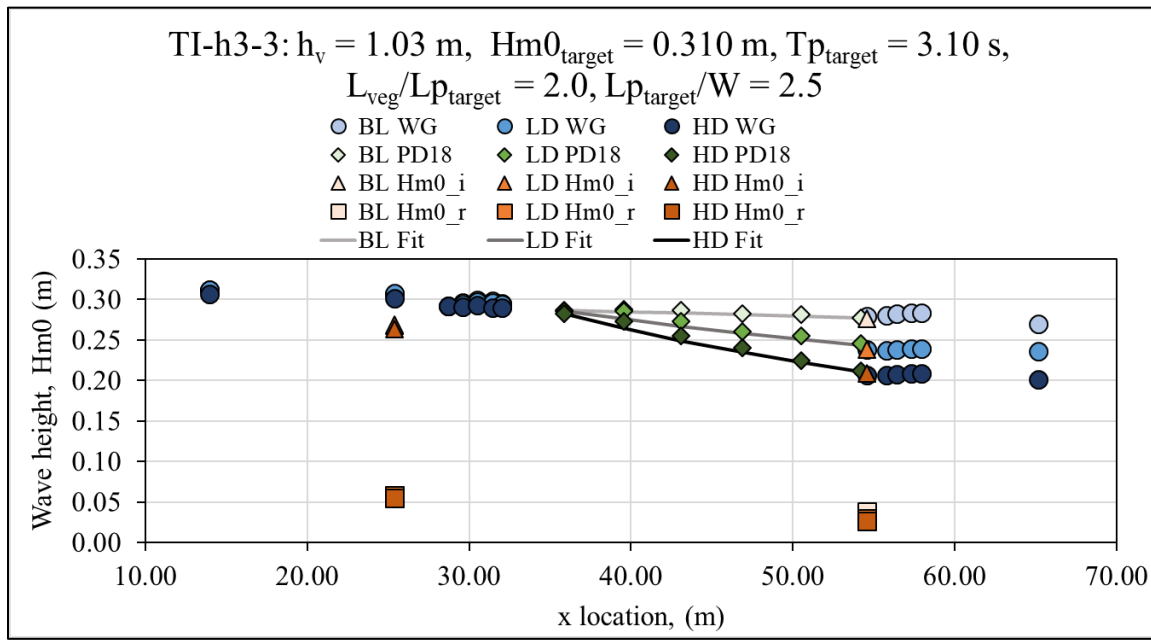


Figure 6-3 Total spectral estimate of the significant wave height, H_{m0} , with respect to x location for wave gauges (WG, circles) and pressure gauges (PD, diamonds) with the incident spectral estimate of the significant wave height, $H_{m0\text{i}}$ (triangles), and reflected spectral estimate of the significant wave height, $H_{m0\text{r}}$ (squares), and line of best fit for the high-density (HD) (dark colors), low-density (LD) (intermediate colors), and baseline (BL) (light colors) layouts of the random wave case TI-h3-3.

In Figure 6-3, the best fit line of the wave height decay rate is represented as a solid line for each of the three layouts. In general, the best fit lines show good agreement with the data. There is, however, uncertainty with the best fit $\tilde{\alpha}$ coefficient and additional values for $\tilde{\alpha}_m \pm \sigma$ for each

wave case and layout (Figure 6-4) were found. In Figure 6-4, the line of best fit for the $\tilde{\alpha}$ coefficient (solid line), $\tilde{\alpha}_m + \sigma$ (dashed line), and $\tilde{\alpha}_m - \sigma$ (dashed-dotted line) are shown for the HD layout of wave case TI-h3-1. All of the best fit lines, begin at the H_{m0} value for PD18-1 but deviate as the lines approach PD18-6. There, the $\tilde{\alpha}$ coefficient line closely estimates the H_{m0} value at PD18-6 while the $\tilde{\alpha}_m + \sigma$ coefficient underestimates and $\tilde{\alpha}_m - \sigma$ overestimates the H_{m0} value. A summary table of the wave height decay coefficients with $\tilde{\alpha}_m \pm \sigma$ for each wave case and layout are reported in Table 9-19 of Appendix J.2.

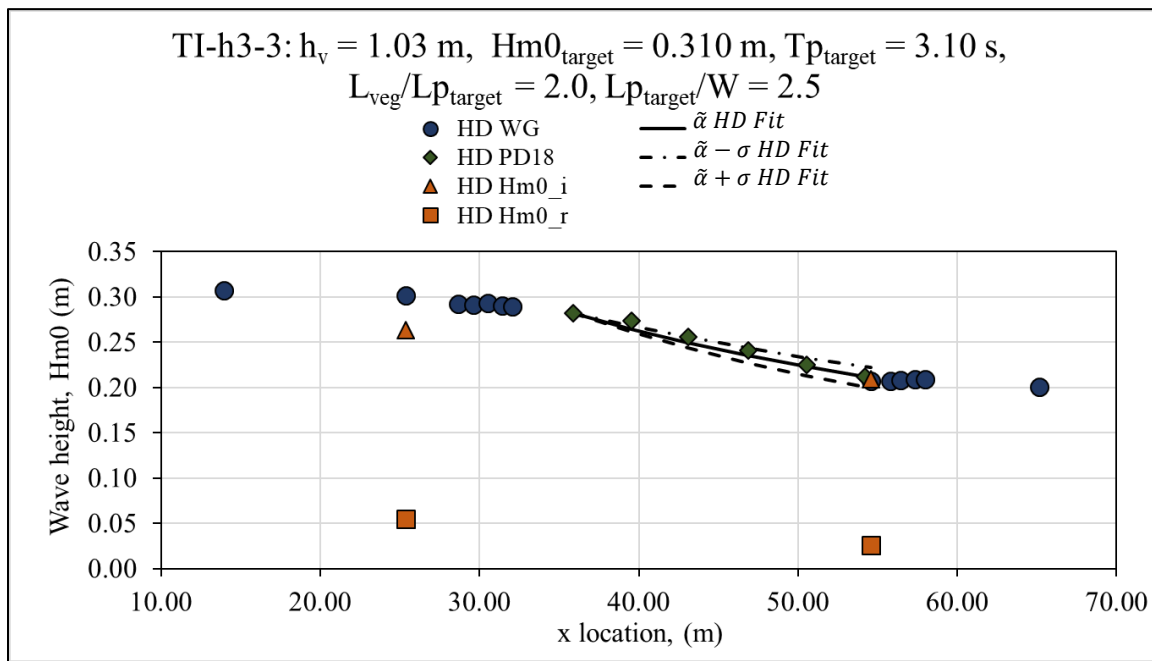


Figure 6-4 Total spectral estimate of the significant wave height, H_{m0} , with respect to x location for wave gauges (WG - circles) and pressure gauges (PD - diamonds) with mean (solid line), lower bound (dashed line) and upper bound line of best fit (dash dotted line) for the high-density (HD) layout of the random wave case TI-h3-3.

The $\tilde{\alpha}$ coefficients were also plotted versus the water depth at the vegetation, h_v (Figure 6-5). In Figure 6-5, the wave height decay coefficient, $\tilde{\alpha}$, is shown on the y-axis, and the water depth in the vegetation is shown in the x-axis. The $\tilde{\alpha}$ coefficients for the HD (dark blue circles), LD (intermediate blue circles), and BL (light blue circles) are displayed in the figure. The figure shows the greatest $\tilde{\alpha}$ coefficients occurring at the shallowest water depth for the HD and LD layout and steadily decreasing as the water depth increased. The BL layout's $\tilde{\alpha}$ values also show

a decrease for the first three water depths ($0.73 \text{ m} \leq h_v \leq 1.48 \text{ m}$). At $h_v = 1.85 \text{ m}$ however, there is an increase in the $\tilde{\alpha}$ coefficients from the values at $h_v = 1.48 \text{ m}$.

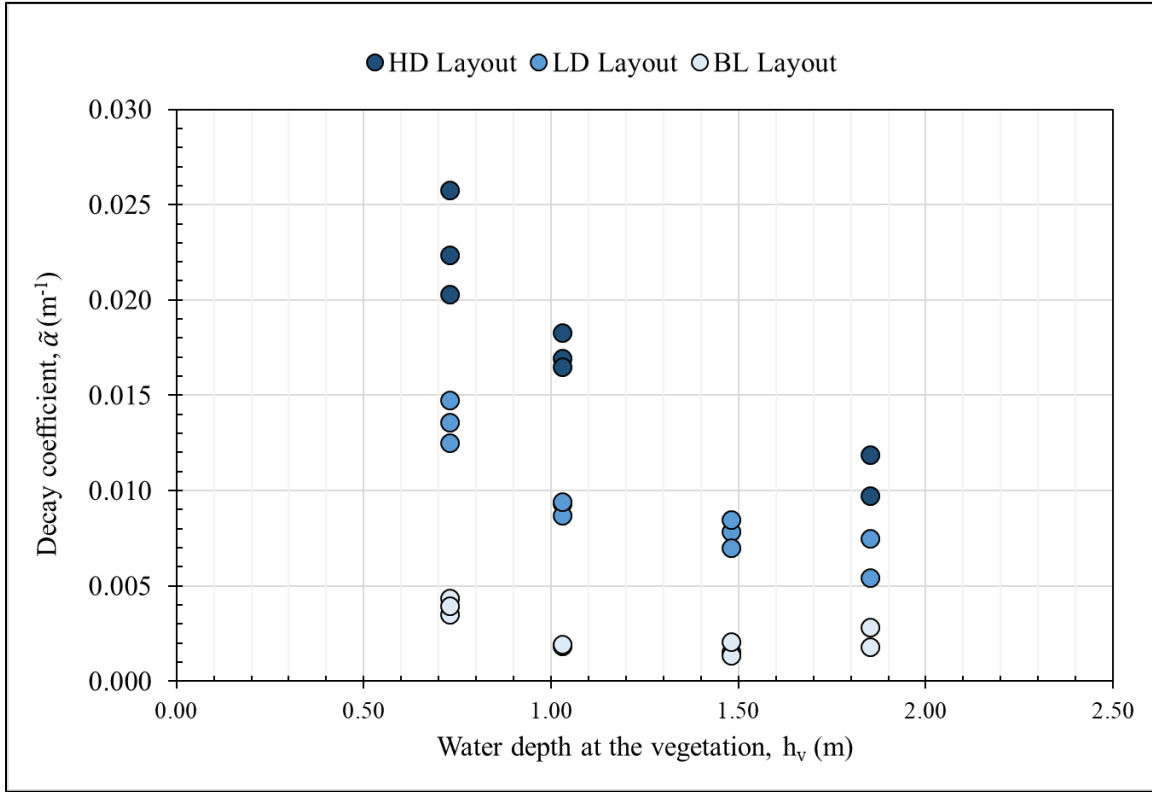


Figure 6-5 Wave height decay coefficient, $\tilde{\alpha}$, versus the water depth at the vegetation, h_v , for the random wave cases at the high-density (HD) (dark blue circles), low-density (LD) (intermediate blue circles), and baseline (BL) (light blue circles) layouts.

The wave height decay due solely from the model forest, $\tilde{\alpha}_m$, can be calculated by subtracting the BL layout's wave height decay rate from the HD and LD layouts $\tilde{\alpha}$ values, respectively. (Figure 6-6). In Figure 6-6, the y-axis shows the wave height decay due to the model forest, $\tilde{\alpha}_m$, and the x-axis displays the water depth at the vegetation, h_v . The figure designates points for the HD (dark blue circles) and LD (light blue circles) layouts.

The figure shows that the highest $\tilde{\alpha}_m$ coefficients occurred at the lowest water depths, where the mean projected area per unit height, $A_{t,m}$, was the largest. Furthermore, results also show that the $\tilde{\alpha}_m$ coefficient does not vary significantly between the different non-dimensional wave cases for each water depth. The finding indicates that the $\tilde{\alpha}_m$ coefficient is predominantly dependent on the water depth at the vegetation, h_v , and subsequently, the mean projected area per unit height,

$A_{t,m}$, influencing the fluid flow. The average ratio of the HD/LD $\tilde{\alpha}_m$ coefficients was 2.0, the same as the HD/LD density ratio of the two model forests. The agreement indicates a possible linear relationship between the $\tilde{\alpha}_m$ coefficient and forest density, N . However, additional testing is needed to verify this relationship. A similar relationship between the wave height decay coefficient and the stem density was found for emergent vegetation by Anderson and Smith, (2014). Table 6-1 contains the $\tilde{\alpha}_m$ coefficient values for each respective case and for the HD, LD, and BL layouts with the corresponding HD/LD $\tilde{\alpha}_m$ ratios. The table also contains the measured H_{m0} and T_p values at PD18-1 for each case.

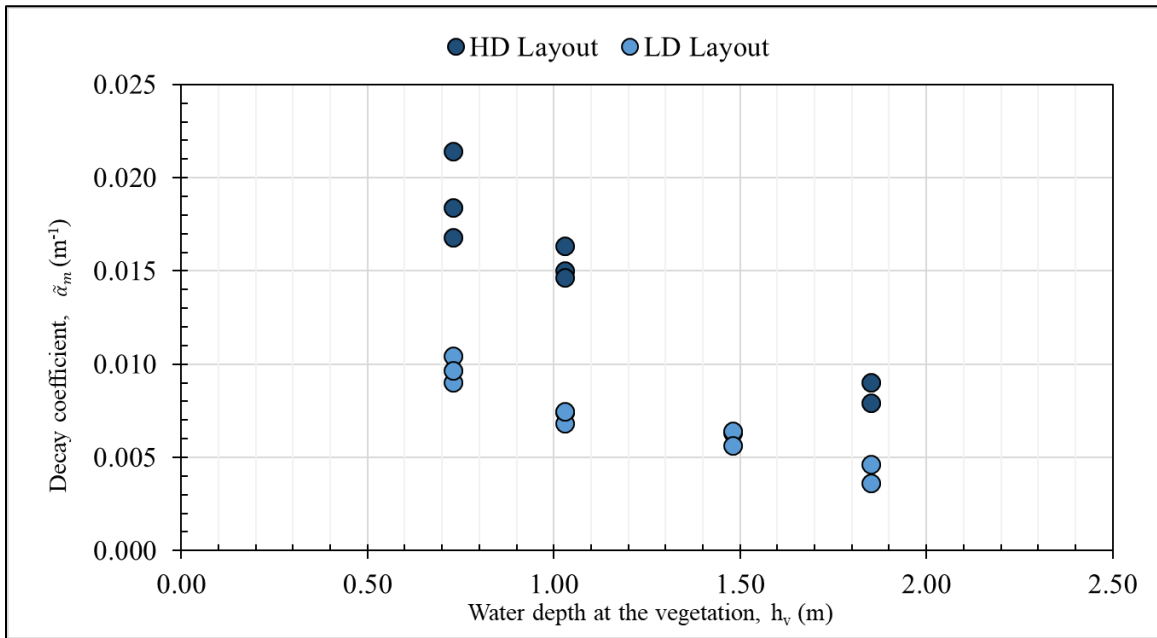


Figure 6-6 Model forest wave height decay coefficient, $\tilde{\alpha}_m$, versus water depth at the vegetation, h_v , for the random wave vases at the high-density (HD) (dark blue circles), low-density (LD) (intermediate blue circles), and baseline (BL) (light blue circles) layouts.

Table 6-1 Summary table of wave height decay, $\tilde{\alpha}_m$, and the HD/LD ratio of the $\tilde{\alpha}_m$ coefficient with corresponding measured H_{m0} and T_p values at PD18-1 for the random wave cases.

Trial	Layout	h_v	H_{m0} PD18 - 1	T_p PD18 - 1	$\tilde{\alpha}_m$	HD/LD ratio	$\tilde{\alpha}_m$
(-)	(-)	(m)	(m)	(s)	(m^{-1})	(-)	(-)
TI-h1-1	HD	1.85	0.71	7.45	0.0090	1.9	
	LD	1.85	0.73	7.45	0.0046		
TI-h1-2	HD	1.85	0.43	2.48	0.0079	2.2	
	LD	1.85	0.43	2.56	0.0036		
TI-h2-1	LD	1.48	0.51	6.30	0.0056	-	
TI-h2-2	LD	1.48	0.28	2.16	0.0063	-	
TI-h2-3	LD	1.48	0.48	3.72	0.0064	-	
TI-h3-1	HD	1.03	0.30	5.85	0.0150	2.0	
	LD	1.03	0.31	5.85	0.0074		
TI-h3-2	HD	1.03	0.15	1.91	0.0146	2.1	
	LD	1.03	0.15	1.91	0.0068		
TI-h3-3	HD	1.03	0.28	3.15	0.0163	2.2	
	LD	1.03	0.29	3.15	0.0075		
TI-h4-1	HD	0.73	0.19	4.82	0.0168	1.9	
	LD	0.73	0.21	4.82	0.0090		
TI-h4-2	HD	0.73	0.10	1.58	0.0214	2.1	
	LD	0.73	0.11	1.58	0.0104		
TI-h4-3	HD	0.73	0.20	2.41	0.0184	1.9	
	LD	0.73	0.19	2.48	0.0096		
Average HD/LD $\tilde{\alpha}_m$ ratio:						2.0	

Using Equation (7), the transmission coefficient and ultimately the wave attenuation percentage for each case were calculated (Figure 6-7). In Figure 6-7, the *y*-axis shows the wave attenuation percentage due to the model forest, and the *x*-axis displays the water depth at the vegetation h_v . The figure designates points for the HD (dark blue circles) and LD (light blue circles) layouts. As with Figure 6-6 and the $\tilde{\alpha}_m$ coefficients, Figure 6-7 shows the highest wave attenuation occurred at the lowest water depths and decreased as h_v value increased. Overall, the study had random wave attenuation values ranging from 6 to 28% for $0.10 \text{ m} \leq H_{m0} \leq 0.73 \text{ m}$, $1.58 \text{ s} \leq T_p \leq 7.45 \text{ s}$, and $0.73 \text{ m} \leq h_v \leq 1.85 \text{ m}$. Table 6-2 summarizes the wave attenuation percentages.

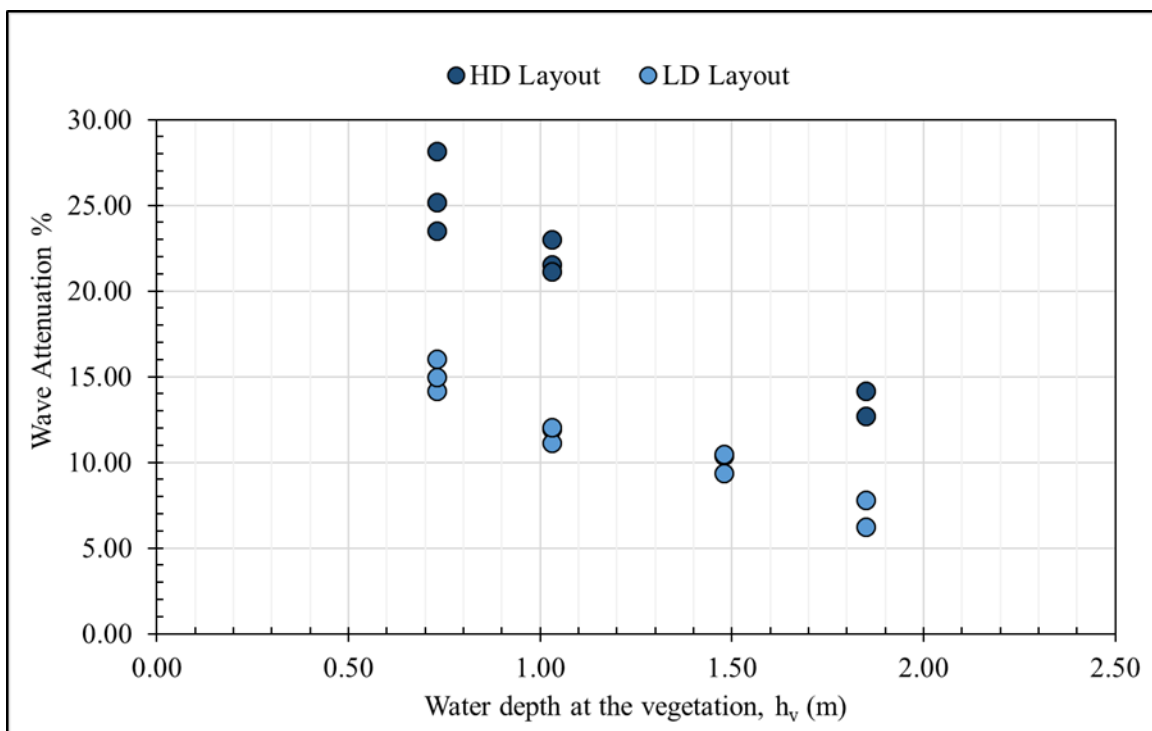


Figure 6-7 Percent of wave attenuation for the random wave cases versus the water depth at the vegetation, h_v for the high-density (HD) (dark blue circles) and low-density (LD) (intermediate blue circles) layouts.

Table 6-2 Summary table of percent of wave attenuation for the random wave cases with measured values of H_{m0} and T_p at PD18-1.

Trial	Layout	h_v	H_{m0} PD18 - 1	T_p PD18 - 1	Wave Attenuation
(-)	(-)	(m)	(m)	(s)	(%)
TI-h1-1	HD	1.85	0.71	7.45	14
	LD	1.85	0.73	7.45	8
TI-h1-2	HD	1.85	0.43	2.48	13
	LD	1.85	0.43	2.56	6
TI-h2-1	LD	1.48	0.51	6.30	9
TI-h2-2	LD	1.48	0.28	2.16	10
TI-h2-3	LD	1.48	0.48	3.72	11
TI-h3-1	HD	1.03	0.30	5.85	22
	LD	1.03	0.31	5.85	12
TI-h3-2	HD	1.03	0.15	1.91	21
	LD	1.03	0.15	1.91	11
TI-h3-3	HD	1.03	0.28	3.15	23
	LD	1.03	0.29	3.15	12
TI-h4-1	HD	0.73	0.19	4.82	23
	LD	0.73	0.21	4.82	14
TI-h4-2	HD	0.73	0.10	1.58	28
	LD	0.73	0.11	1.58	16
TI-h4-3	HD	0.73	0.20	2.41	25
	LD	0.73	0.19	2.48	15

6.3. Drag Coefficients

The drag dominance of each respective case was evaluated (Equation 8.60 from Dean and Dalrymple, 1991) (Equation 13) given as

$$\frac{H}{D} = \frac{C_M \pi}{C_D} \tanh(kh) \quad (13)$$

Where H is the wave height, D is the diameter of the cylinder, C_M is the inertia coefficient, C_D is the drag coefficient, k is the wave number, and h is the water depth. Dean and Dalrymple (1991) simplified Equation 13 by setting C_M/C_D to 0.5 (Equation 14).

$$\frac{H}{D} = \frac{\pi}{2} \tanh(kh) \quad (14)$$

In Figure 6-8, the Equation (14) was plotted for a range of spectral estimate of the significant wave height, H_{m0} , over the effective diameter, D_e , ratios on the y-axis and relative water depths, $k_p h_v$ the x-axis. H_{m0} values at PD18-1 and the measured effective diameter, D_e , were used for the present study's data and differentiated by the HD (dark blue circles) and LD (intermediate blue circles) layouts. Equation (14) is shown as a solid black line where points above the line indicate the wave case is drag predominant and cases below the line correspond to cases that are inertial predominant. From the figure, a majority of the cases tested fell within the predominant drag regime. However, three cases were located within the predominant inertial regime. These cases correspond to the most deep-water relative water depths, $k_p h_v$, values tested for the study. The inertial predominance indicated for these cases could lead to higher estimations of the drag coefficient, C_D , from the Mendez and Losada, (2004) C_D equation (Equation 8) since it only considered the drag force in the derivation. The study did not collect direct force measurements on the model tree specimens so the possible C_D overestimation by the Mendez and Losada (2004) equation for these cases cannot be fully quantified.

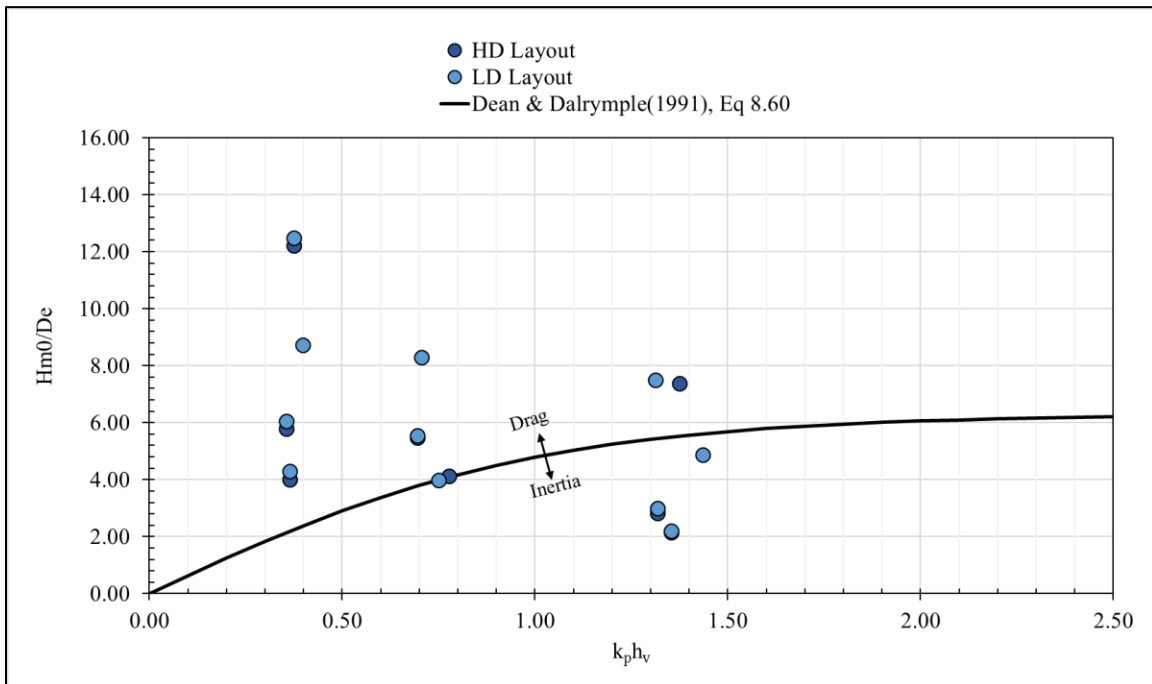


Figure 6-8 Ratio of the spectral estimate of the significant wave height, H_{m0} , over the effective diameter, D_e , versus relative water depth, $k_p h_v$, for the random wave cases at the high-density (HD) (dark blue circles) and low-density (LD) (intermediate blue circles) layout trials compared to Equation 8.60 from Dean and Dalrymple (1991) (solid black line).

The drag coefficients, C_D , for each respective case, were calculated using the $\tilde{\alpha}_m$ coefficients in Table 6-1 and the equation presented by Mendez and Losada, (2004) detailed in Equation (8). The calculated C_D values were then related to the Reynolds number, $Re_{U,De}$, calculated using the depth-averaged velocity, U , and the effective diameter, D_e . The C_D to $Re_{U,De}$ relation is presented in Figure 6-9, differentiated by layout and the relative water depth, $k_p h_v$.

In Figure 6-9, the C_D values are shown on the y-axis, and the $Re_{U,De}$ values are displayed on the x-axis. Additionally, the C_D values are separated by the HD (squares) and LD (triangles) layouts along with the three relative water depth, $k_p h_v$, ranges tested: $0.30 < k_p h_v < 0.40$ (black), $0.70 < k_p h_v < 0.80$ (dark grey), and $1.30 < k_p h_v < 1.45$ (light gray). In the figure, the HD and LD C_D values for each respective case are generally the same. The figure shows lower C_D values for higher Reynolds numbers and lower $k_p h_v$ values. For the study, the minimum C_D value was 0.85 for random waves and corresponded to the second largest $Re_{U,De}$ value and smallest $k_p h_v$ range. The largest C_D value was 3.75 and corresponded with the lowest $Re_{U,De}$ value and largest $k_p h_v$ range.

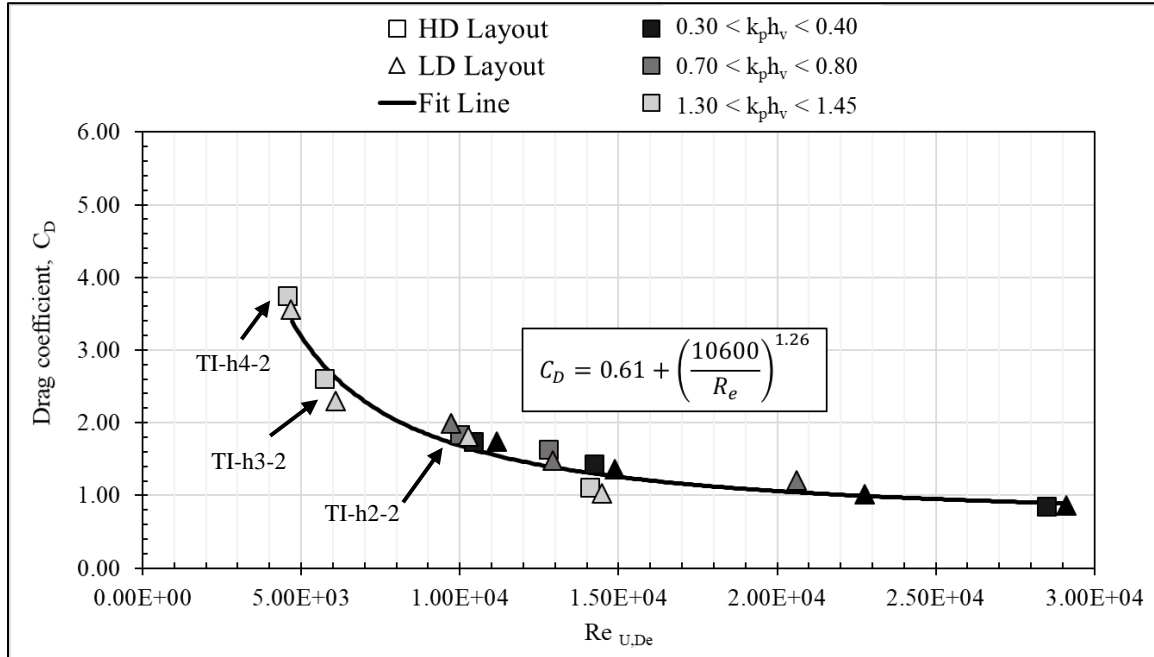


Figure 6-9 Drag coefficient, C_D , versus the Reynolds number, $Re_{U,De}$, for the HD (squares) and LD (triangles) layouts designated by relative water depth, $k_p h_v$, range. Best fit line shown as solid black line.

Cases with larger C_D values also correspond with cases that indicated inertial force predominance (Figure 6-8). These trials are designated by trial name and arrows in Figure 6-9. A best-fit line (solid black line) was fit through the data using the empirical equation form presented in the figure. The line generally shows good agreement with the data and has an asymptote of 0.61 which coincides with findings reported Sarpkaya and Isaacson (1981) for waves on vertical piles. Furthermore, the corresponding trial information of $k_p h_v$, H_{m0}/D_e , predominant force classified by Figure 6-8, $Re_{U,De}$, and C_D values for the random wave are reported in Table 6-3.

The Keulegan-Carpenter number, $KC_{U,De}$ is also shown in Table 6-3 and was determined using the depth-averaged velocity, U , and the effective diameter, D_e . The relationship between the C_D values and $KC_{U,De}$ is shown in Figure 6-10. There, the $KC_{U,De}$ number is shown on the x -axis with the drag coefficient, C_D , on the y -axis. The figure displays a relationship where the lowest C_D value corresponded with the largest $KC_{U,De}$ value, and smallest $k_p h_v$ range. Conversely, the largest C_D was related to the lowest $KC_{U,De}$ value and largest $k_p h_v$ range.

Table 6-3 Summary table of the random wave cases with measured H_{m0} and T_p values at PD18-1, $k_p h_v$, H_{m0}/D_e , Predominant force based on Figure 6-8, $Re_{U,De}$, $KC_{U,De}$, and C_D values.

Trial	Layout	h_v	H_{m0} PD18 -1	T_p PD18 -1	$k_p h_v$	H_{m0}/D_e	Predominant Force	$Re_{U,De}$	$KC_{U,De}$	C_D
(-)	(-)	(m)	(m)	(s)	(-)	(-)	(Drag/Intertia)	(-)	(-)	(-)
TI-h1-1	HD	1.85	0.71	7.45	0.37	12.2	Drag	28485	145	0.85
	LD	1.85	0.73	7.45	0.37	12.5	Drag	29103	148	0.86
TI-h1-2	HD	1.85	0.43	2.48	1.37	7.4	Drag	14084	24	1.12
	LD	1.85	0.43	2.56	1.31	7.5	Drag	14486	25	1.02
TI-h2-1	LD	1.48	0.51	6.30	0.40	8.7	Drag	22769	98	1.02
TI-h2-2	LD	1.48	0.28	2.16	1.44	4.9	Inertia	10274	15	1.81
TI-h2-3	LD	1.48	0.48	3.72	0.71	8.3	Drag	20608	52	1.21
TI-h3-1	HD	1.03	0.30	5.85	0.36	5.8	Drag	14227	72	1.44
	LD	1.03	0.31	5.85	0.36	6.0	Drag	14872	76	1.36
TI-h3-2	HD	1.03	0.15	1.91	1.32	2.8	Inertia	5739	10	2.61
	LD	1.03	0.15	1.91	1.32	3.0	Inertia	6087	10	2.30
TI-h3-3	HD	1.03	0.28	3.15	0.69	5.5	Drag	12794	35	1.63
	LD	1.03	0.29	3.15	0.69	5.5	Drag	12939	35	1.48
TI-h4-1	HD	0.73	0.19	4.82	0.36	4.0	Drag	10419	49	1.74
	LD	0.73	0.21	4.82	0.36	4.3	Drag	11156	53	1.74
TI-h4-2	HD	0.73	0.10	1.58	1.35	2.1	Inertia	4566	7	3.75
	LD	0.73	0.11	1.58	1.35	2.2	Inertia	4676	7	3.56
TI-h4-3	HD	0.73	0.20	2.41	0.78	4.1	Neither	9996	24	1.83
	LD	0.73	0.19	2.48	0.75	4.0	Neither	9723	24	1.99

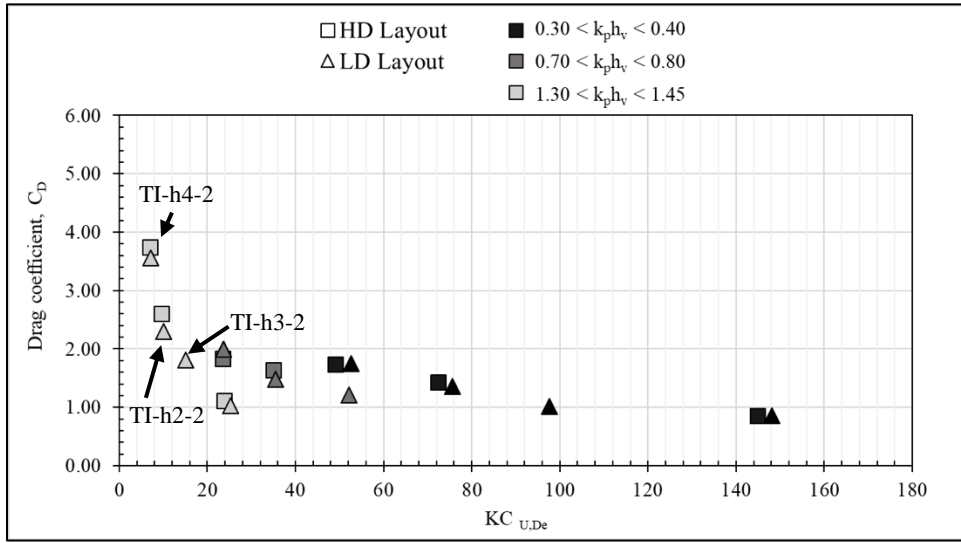


Figure 6-10 Drag coefficient, C_D , versus the Keulegan-Carpenter number, $KC_{U,De}$ for the random wave cases at the high-density (HD) (squares) and low-density (LD) (triangles) layouts designated by relative water depth, $k_p h_v$, range.

There also appears to be a relationship dependent on the $k_p h_v$ range where each range shows a different trend as $KC_{U,De}$ decreases and C_D increases. However, further experimentation would be needed to verify these trends.

Similar to figure 6-9, the indicated inertial predominant cases are marked in the figure with arrows and corresponding trial names. All of these cases have $KC_{U,De}$ values < 25 , a known threshold when the inertial force contributions are significant and verifies the initial indication in Figure 6-8.

The C_D values for the study were also related to the Re and KC numbers that were calculated using the mean projected area per unit height per tree, $A_{t,m}$, trunk diameter, D_{BH} , root diameter D_{Root} , and the near bed velocity, u . A summary table and corresponding figures can be found in Appendix J.3.

6.3.1. Projected Area Uncertainty

The uncertainty of the mean projected area per unit height per tree, $A_{t,m} \pm \sigma_{t,m}$ (Table 5-1) can be applied to calculate the drag coefficients, C_D , get a minimum and maximum C_D value for each respective case (Figure 6-11).

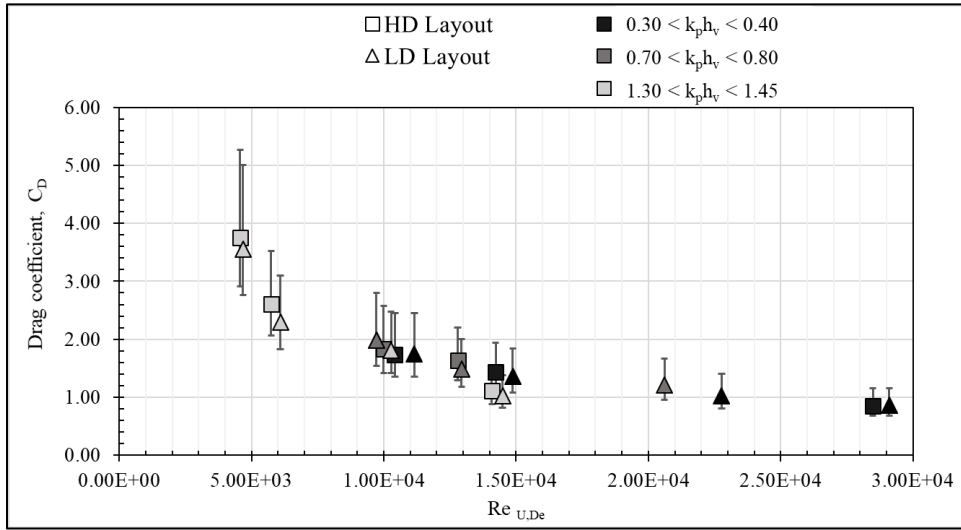


Figure 6-11 Drag coefficient, C_D , versus the Reynolds number, $Re_{U,De}$, for the random wave cases at the high-density (HD) (squares) and low-density (LD) (triangles) layouts designated by $k_p h_v$ range with limit bars (grey vertical bars) due to the $A_{t,m} \pm \sigma_{t,m}$ uncertainty.

In Figure 6-11, the same symbols and axes are used as in Figure 6-10 and the minimum and maximum drag coefficient due to the $A_{t,m}$ values are shown as grey vertical bars. Generally, the error bars increase as the Reynolds number, $Re_{U,De}$, decreases. For each case, the variation of the HD versus the LD layouts is similar. The upper limit of the C_D value is greater than the lower limit for all cases which is due to the inverse mathematical relationship between C_D and $A_{t,m}$ (Equation 6). Table 6-4 summarizes the minimum and maximum C_D values due to the variability in $A_{t,m}$.

Table 6-4 Summary table of random wave cases with measured H_{m0} and T_p values at PD18-1, $k_p h_v$, $Re_{U,De}$, C_D , C_D , $A_{t,m} + \sigma_m$, and C_D , $A_{t,m} - \sigma_m$ values.

Trial	Layout	h_v	H_{m0} PD18 -1	T_p PD18 -1	$k_p h_v$	$Re_{U,De}$	C_D	C_D , $A_{t,m} + \sigma_{t,m}$	C_D , $A_{t,m} - \sigma_{t,m}$
(-)	(-)	(m)	(m)	(s)	(-)	(-)	(-)	(-)	(-)
TI-h1-1	HD	1.85	0.71	7.45	0.37	28485	0.85	0.68	1.15
	LD	1.85	0.73	7.45	0.37	29103	0.86	0.68	1.16
TI-h1-2	HD	1.85	0.43	2.48	1.37	14084	1.12	0.89	1.50
	LD	1.85	0.43	2.56	1.31	14486	1.02	0.81	1.38
TI-h2-1	LD	1.48	0.51	6.30	0.40	22769	1.02	0.80	1.40
TI-h2-2	LD	1.48	0.28	2.16	1.44	10274	1.81	1.42	2.48
TI-h2-3	LD	1.48	0.48	3.72	0.71	20608	1.21	0.95	1.66
TI-h3-1	HD	1.03	0.30	5.85	0.36	14227	1.44	0.00	0.00
	LD	1.03	0.31	5.85	0.36	14872	1.36	1.08	1.84
TI-h3-2	HD	1.03	0.15	1.91	1.32	5739	2.61	2.07	3.52
	LD	1.03	0.15	1.91	1.32	6087	2.30	1.83	3.10
TI-h3-3	HD	1.03	0.28	3.15	0.69	12794	1.63	1.30	2.21
	LD	1.03	0.29	3.15	0.69	12939	1.48	1.17	2.00
TI-h4-1	HD	0.73	0.19	4.82	0.36	10419	1.74	1.35	2.45
	LD	0.73	0.21	4.82	0.36	11156	1.74	1.35	2.45
TI-h4-2	HD	0.73	0.10	1.58	1.35	4566	3.75	2.91	5.27
	LD	0.73	0.11	1.58	1.35	4676	3.56	2.76	5.01
TI-h4-3	HD	0.73	0.20	2.41	0.78	9996	1.83	1.42	2.58
	LD	0.73	0.19	2.48	0.75	9723	1.99	1.54	2.80

6.3.2. Decay Rate Uncertainty

There can also be a minimum and maximum C_D value based on the best fit decay coefficient, $\tilde{\alpha}$ variability (Figure 6-4 and Table 9-19). By subtracting the best fit decay coefficient, $\tilde{\alpha}$, from the BL layouts from the $\tilde{\alpha} + \sigma$ and $\tilde{\alpha} - \sigma$ for each the HD and LD layouts, the variability for the mangroves decay coefficients, $\tilde{\alpha}_m$, was found. The C_D values corresponding to the upper and lower limits of the wave height decay for the HD and LD forest, were then found (Figure 6-12).

For Figure 6-12, the same symbols and axes are used as in Figure 6-10 where the minimum and maximum values of C_D are represented as grey bars due to the decay coefficient variability, $\tilde{\alpha}_m \pm \sigma$. The figure shows greater variability from case to case and not the gradual increase in variability with decrease in $Re_{U,De}$ seen in Figure 6-11. The order of magnitude for the C_D variability from $\tilde{\alpha}_m$ is the same as C_D variability from $A_{t,m}$. The extent of the minimum and maximum limit of C_D from $\tilde{\alpha}_m$ are approximately the same in each respective case and can be

attributed to the direct correlation between C_D and $\tilde{\alpha}_m$ (Equation 6). Table 6-5 summarizes the minimum and maximum C_D values due to the variability in the $\tilde{\alpha}_m$.

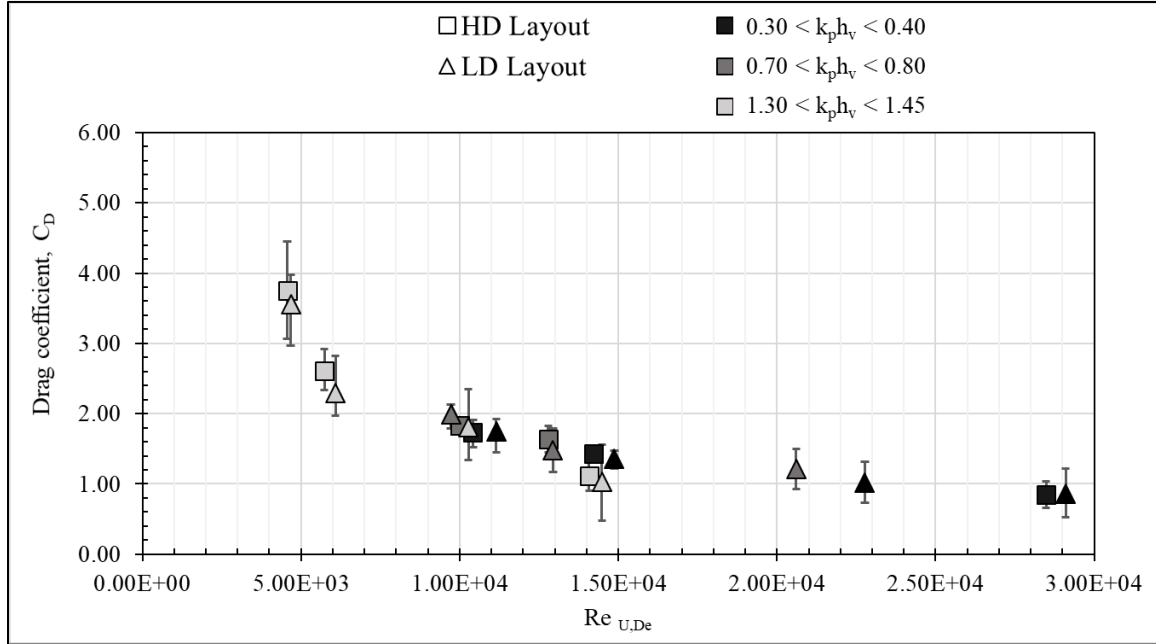


Figure 6-12 Drag coefficient, C_D versus the Reynolds number, $Re_{U,De}$, for the random wave cases at the high-density (HD) (squares) and low-density (LD) (triangles) layouts designated by $k_p h_v$ range with limit bars (grey vertical bars) due to the $\tilde{\alpha}_m \pm \sigma$ uncertainty.

Table 6-5 Summary table of the random wave cases with measured H_{m0} and T_p values at PD18-1, $k_p h_v$, $Re_{U,De}$, $\tilde{\alpha}_m \pm \sigma$, C_D , C_D , $\tilde{\alpha}_m + \sigma$, and C_D , $\tilde{\alpha}_m - \sigma$ values.

Trial	Layout	h_v	H_{m0} PD18 -1	T_p PD18 -1	$k_p h_v$	$Re_{U,De}$	$\tilde{\alpha}_m - \sigma$	$\tilde{\alpha}_m + \sigma$	C_D	C_D , $\tilde{\alpha}_m - \sigma$	C_D , $\tilde{\alpha}_m + \sigma$
(-)	(-)	(m)	(m)	(s)	(-)	(-)	(m^{-1})	(m^{-1})	(-)	(-)	(-)
TI-h1-1	HD	1.85	0.71	7.45	0.37	28485	7.01E-03	1.10E-02	0.85	0.66	1.04
	LD	1.85	0.73	7.45	0.37	29103	2.81E-03	6.58E-03	0.86	0.52	1.22
TI-h1-2	HD	1.85	0.43	2.48	1.37	14084	6.44E-03	9.38E-03	1.12	0.90	1.32
	LD	1.85	0.43	2.56	1.31	14486	6.44E-03	9.38E-03	1.02	0.47	1.56
TI-h2-1	LD	1.48	0.51	6.30	0.40	22769	4.68E-03	8.22E-03	1.02	0.74	1.31
TI-h2-2	LD	1.48	0.28	2.16	1.44	10274	4.90E-03	7.92E-03	1.81	1.34	2.35
TI-h2-3	LD	1.48	0.48	3.72	0.71	20608	4.06E-03	7.25E-03	1.21	0.93	1.49
TI-h3-1	HD	1.03	0.30	5.85	0.36	14227	1.38E-02	1.62E-02	1.44	1.32	1.55
	LD	1.03	0.31	5.85	0.36	14872	6.67E-03	8.37E-03	1.36	1.22	1.53
TI-h3-2	HD	1.03	0.15	1.91	1.32	5739	1.31E-02	1.64E-02	2.61	2.34	2.92
	LD	1.03	0.15	1.91	1.32	6087	5.88E-03	8.42E-03	2.30	1.97	2.83
TI-h3-3	HD	1.03	0.28	3.15	0.69	12794	1.45E-02	1.83E-02	1.63	1.45	1.83
	LD	1.03	0.29	3.15	0.69	12939	5.92E-03	9.04E-03	1.48	1.17	1.79
TI-h4-1	HD	0.73	0.19	4.82	0.36	10419	0.00E+00	0.00E+00	1.74	1.52	1.92
	LD	0.73	0.21	4.82	0.36	11156	7.48E-03	1.03E-02	1.74	1.45	1.99
TI-h4-2	HD	0.73	0.10	1.58	1.35	4566	1.75E-02	2.55E-02	3.75	3.06	4.45
	LD	0.73	0.11	1.58	1.35	4676	8.70E-03	1.16E-02	3.56	2.97	3.97
TI-h4-3	HD	0.73	0.20	2.41	0.78	9996	1.79E-02	1.87E-02	1.83	1.79	1.86
	LD	0.73	0.19	2.48	0.75	9723	8.65E-03	1.03E-02	1.99	1.78	2.13

6.3.3. Combined Uncertainty

The combined uncertainty due to $A_{t,m}$ and $\tilde{\alpha}_m$ can also be found using the simplified relationship in Equation (15) for the drag coefficients. A detailed formulation of Equation (15) can be found in Appendix J.4.

$$\frac{\sigma_{C_D}}{C_D} = \left[\left(\frac{\sigma_{A_{t,m}}}{A_{t,m}} \right)^2 + \left(\frac{\sigma_{\alpha_m}}{\alpha_m} \right)^2 \right]^{\frac{1}{2}} \quad (15)$$

The combined variability, σ_{CD} can be applied to the drag coefficients to show the limits of the C_D based on the combination of the $A_{t,m}$ and $\tilde{\alpha}_m$ uncertainty (Figure 6-13). In Figure 6-13, the combined uncertainty of the drag coefficient values increases for all cases compared to Figure 6-11 and Figure 6-12. Generally, Figure 6-13 shows the error bars gradually increase at the Reynolds number decreases, with some variability between data points. Table 6-5 summarizes the variation of C_D values due to the combined uncertainty.

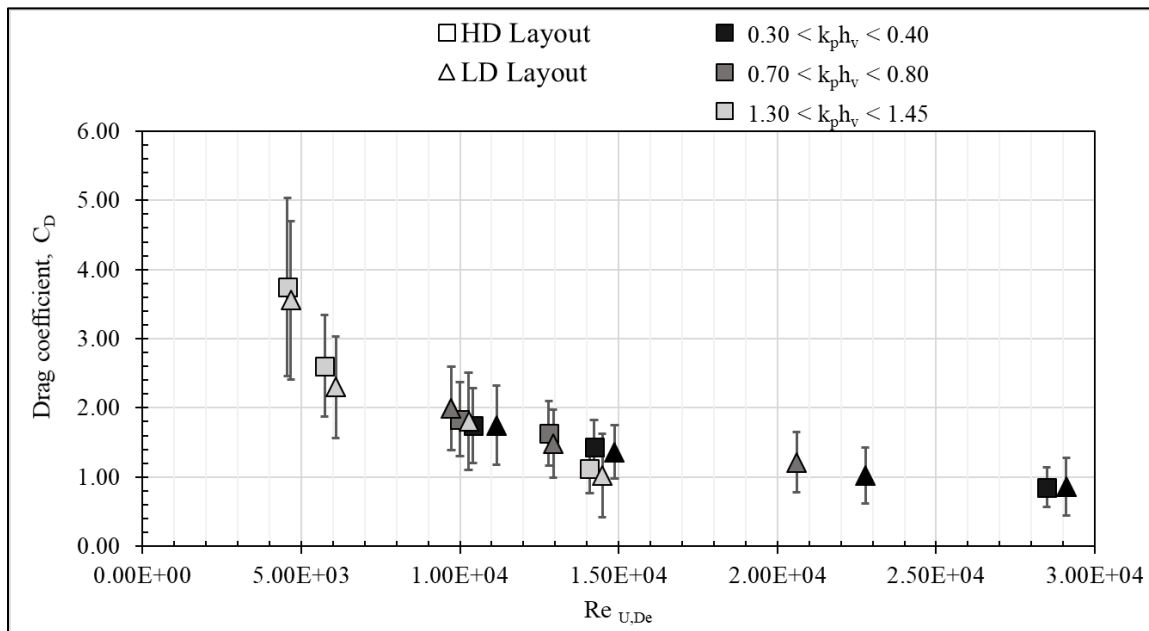


Figure 6-13 Drag coefficient, C_D , versus the Reynolds number, $Re_{U,De}$ for the random wave cases at the HD (squares) and LD (triangles) layouts designated by $k_p h_v$ range with limit bars (grey vertical bars) due to the combined uncertainty.

Table 6-6 Summary table of the random wave cases with measured H_{m0} and T_p values at PD18-1, $k_p h_v$, $Re_{U,De}$, C_D , σ_{CD} , $C_D + \sigma_{CD}$, and $C_D - \sigma_{CD}$ values.

Trial	Layout	h_v	H_{m0} PD18-1	T_p PD18-1	$k_p h_v$	$Re_{U,De}$	C_D	σ_{CD}	$C_D - \sigma_{CD}$	$C_D + \sigma_{CD}$
(-)	(-)	(m)	(m)	(s)	(-)	(-)	(-)	(-)	(-)	(-)
TI-h1-1	HD	1.85	0.71	7.45	0.37	28485	0.85	0.29	0.56	1.14
	LD	1.85	0.73	7.45	0.37	29103	0.86	0.41	0.44	1.27
TI-h1-2	HD	1.85	0.43	2.48	1.37	14084	1.12	0.35	0.76	1.47
	LD	1.85	0.43	2.56	1.31	14486	1.02	0.60	0.42	1.63
TI-h2-1	LD	1.48	0.51	6.30	0.40	22769	1.02	0.40	0.62	1.42
TI-h2-2	LD	1.48	0.28	2.16	1.44	10274	1.81	0.70	1.10	2.51
TI-h2-3	LD	1.48	0.48	3.72	0.71	20608	1.21	0.43	0.78	1.65
TI-h3-1	HD	1.03	0.30	5.85	0.36	14227	1.44	0.39	1.04	1.83
	LD	1.03	0.31	5.85	0.36	14872	1.36	0.39	0.97	1.75
TI-h3-2	HD	1.03	0.15	1.91	1.32	5739	2.61	0.74	1.87	3.34
	LD	1.03	0.15	1.91	1.32	6087	2.30	0.73	1.57	3.03
TI-h3-3	HD	1.03	0.28	3.15	0.69	12794	1.63	0.47	1.17	2.10
	LD	1.03	0.29	3.15	0.69	12939	1.48	0.49	0.99	1.97
TI-h4-1	HD	0.73	0.19	4.82	0.36	10419	1.74	0.54	1.20	2.28
	LD	0.73	0.21	4.82	0.36	11156	1.74	0.57	1.17	2.32
TI-h4-2	HD	0.73	0.10	1.58	1.35	4566	3.75	1.29	2.46	5.03
	LD	0.73	0.11	1.58	1.35	4676	3.56	1.15	2.41	4.70
TI-h4-3	HD	0.73	0.20	2.41	0.78	9996	1.83	0.53	1.30	2.37
	LD	0.73	0.19	2.48	0.75	9723	1.99	0.60	1.39	2.59

6.3.4. Previous Study Comparisons

Maza et al. (2019) completed a comparable study for regular and random waves at 1:6 geometric scale. For the Maza et al. (2019) study, the nominally reported values of all the random wave cases fell within the predominant drag region (Figure 6-14).

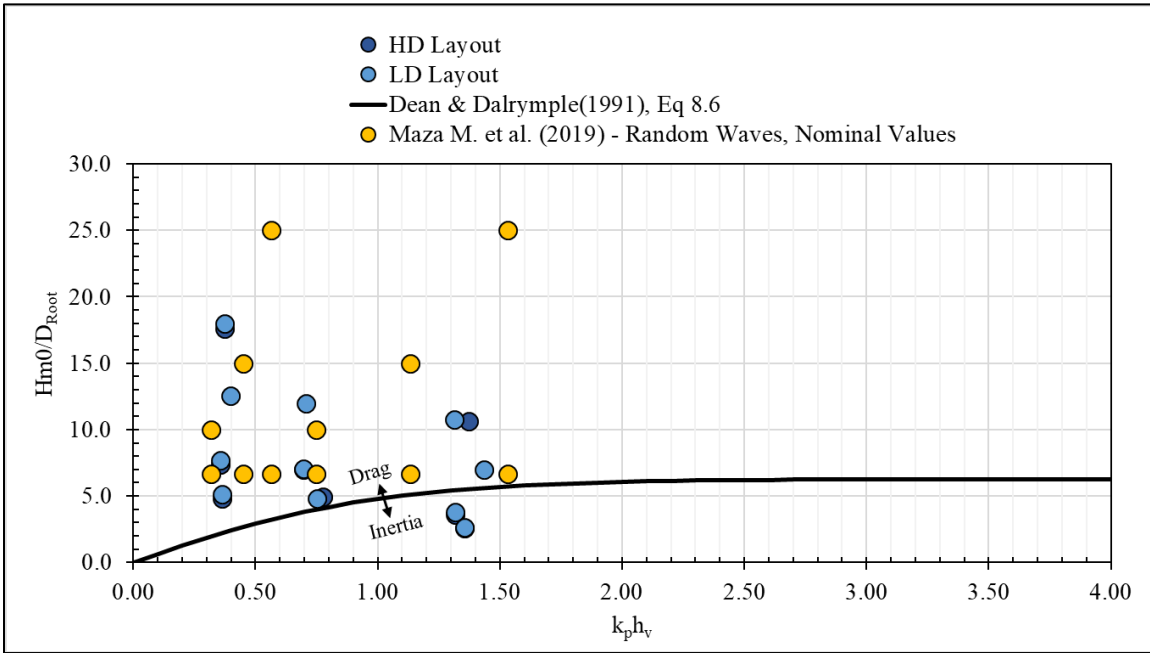


Figure 6-14 Ratio of the spectral estimate of the significant wave height, H_{m0} , over the effective diameter, D_e , versus relative water depth, $k_p h_v$, for the random wave cases at the high-density (HD) (dark blue circles) and low-density (LD) (intermediate blue circles) layouts and nominally reported values from Maza et al. (2019) compared to Equation 8.60 from Dean and Dalrymple (1991) (solid black line).

An effective diameter was not reported for Maza et al. (2019), so the ratio H_{m0}/D_{Root} was used for comparison. In general, the figure shows that the Maza et al. (2019) study testing cases similar to the present with some cases at higher H_{m0}/D_{Root} values than the present study.

Maza et al. (2019) reported drag coefficients for the tested random wave cases as a function of the Reynolds number, Re (Figure 6-15). To relate the scaled studies to the present work, a scaling relation was identified. Generally, the Reynolds number is given as

$$Re = \frac{UD}{\nu} \quad (16)$$

where U is the velocity, D is the diameter, ν is the kinematic viscosity. The scale of the Reynolds number between prototype and model can be expressed in terms of its components given as

$$\lambda_{Re} = \frac{\lambda_U * \lambda_D}{\lambda_\nu} \quad (17)$$

where λ is used to represent the ratio of the model to prototype. The Froude number is generally given as

$$Fr = \frac{U}{\sqrt{g} h} \quad (18)$$

where g is the acceleration due to gravity, and h is the water depth. The Froude number can also have its scaling between prototype and model scales represented by the scale of its components

$$\lambda_{Fr} = \frac{\lambda_U}{\sqrt{\lambda_g \lambda_h}} \quad (19)$$

For Equations (17) and (19), λ_v and λ_g are equal to 1 when water is the working fluid (neglecting changes due to fresh and salt water) and gravity is the same in both the model and prototype. Equations (17) and (19) can be simplified to

$$\lambda_{Re} = \lambda_U \lambda_l \quad (20)$$

$$\lambda_{Fr} = \frac{\lambda_U}{\lambda_l^{\frac{1}{2}}} \quad (21)$$

When Froude similitude is achieved $\lambda_{Fr} = 1$ and Equation (21) simplifies to

$$\lambda_U = \lambda_l^{\frac{1}{2}} \quad (22)$$

Equation (22) can be substituted into Equation (20) to express the scale of the Reynolds number according to Froude similitude.

$$\lambda_{Re} = \lambda_l^{\frac{1}{2}} * \lambda_l \quad (23)$$

Equation (23) can simplify to

$$\lambda_{Re} = \lambda_l^{\frac{3}{2}} \quad (26)$$

Similar scaling of the Reynolds number has also been used in scaled studies focused core material for rubble mound breakwater (Juul Jensen and Klinting, 1983; Losada et al. 2016; Martín et al. 2003).

In Figure 6-15, the Maza et al. (2019) data at 1:6 scale (light green circles) is compared to the present study's data (squares and triangles) using $Re_{U,DBH}$, calculated using the depth averaged velocity, U , and the diameter at breast height, D_{BH} . Generally, the present study's data (gray

scale squares and triangles) and the Maza et al. (2019) data at 1:6 scale (light green circles) do not agree well. However, when the developed scaling relation (Equation 26) is used for the Maza et al. (2019) data where λ_l equals 6, the rescaled Maza et al. (2019) data (dark green circles) and the present studies data agree well, with some of the Maza et al. (2019) values outside the present studies $Re_{U,DBH}$ range. The rescaling method was also applied to the regular wave data from Chang et al. (2019), where λ_l equals 7, and Maza et al. (2019), where λ_l equals 6. The rescaled regular wave data was compared to the present study's results (Figure 6-16). The results for the study's regular wave analysis can be found in Appendix K.

In Figure 6-16, the present study's regular wave data are shown for the HD (squares) and LD (triangles) layouts and differentiated by kh_v value. The regular wave data for the Maza et al. (2019) and Chang et al. (2019) studies are also shown at 1:6 scale (light green squares) and 1:7 scale (light red squares), respectively.

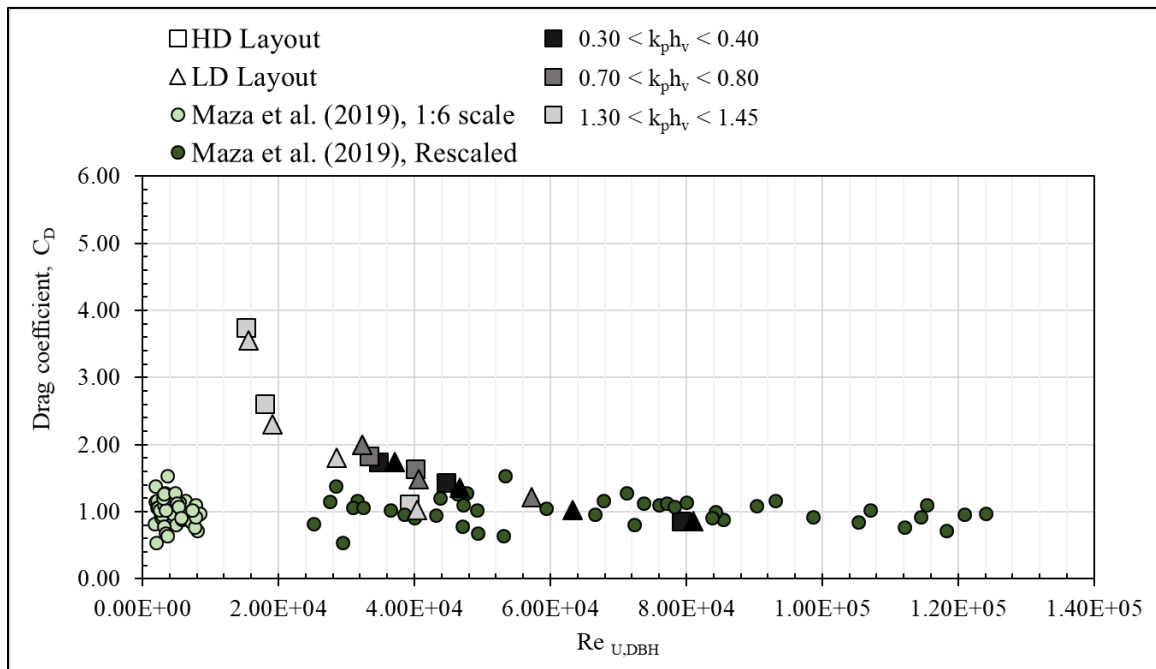


Figure 6-15 Drag coefficient, C_D , versus the Reynolds number, $Re_{U,DBH}$, for the random wave cases at the high-density (HD) (squares) and low-density (LD) (triangles) layouts designated by the relative water depth, k_{ph_v} , and compared to Maza et al. (2019) 1:6 scale (light green circles) and rescaled (dark green circles).

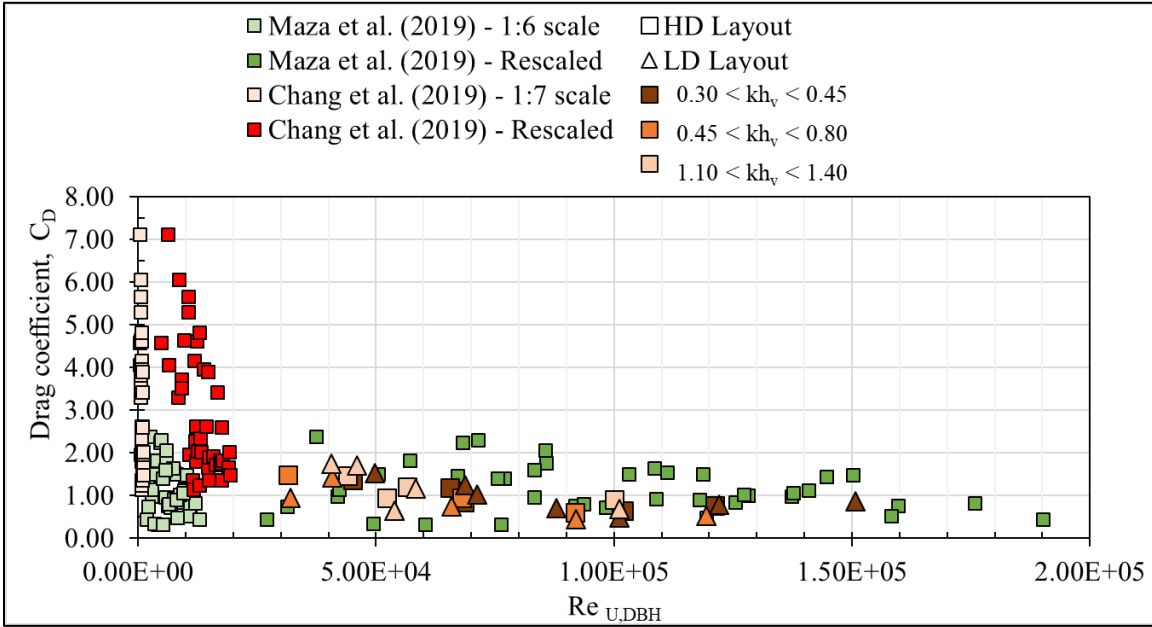


Figure 6-16 Drag coefficient, C_D , versus the Reynolds number, $Re_{U,DBH}$, for the regular wave cases at the high-density (HD) (squares), low density (LD) (triangles) layouts designated by the relative water depth, kh_v , and compared to Maza et al. (2019) 1:6 scale (light blue circles), rescaled (dark blue circles), Chang et al. (2019) 1:7 scale (light red circles), and rescaled (dark red circles).

Both of the unscaled data sets are concentrated on the left-hand side of the figure. However, after rescaling the Reynolds number, both the Chang et al. (2019) (dark red squares) and Maza et al. (2019) (dark green squares) data, both studies generally agree with the present study's findings, showing the method is fairly robust.

Furthermore, the results from Chang et al. (2019) and Maza et al. (2019) were also plotted with the present study's C_D values for the regular (blue squares) and random waves (blue circles) (Figure 6-17).

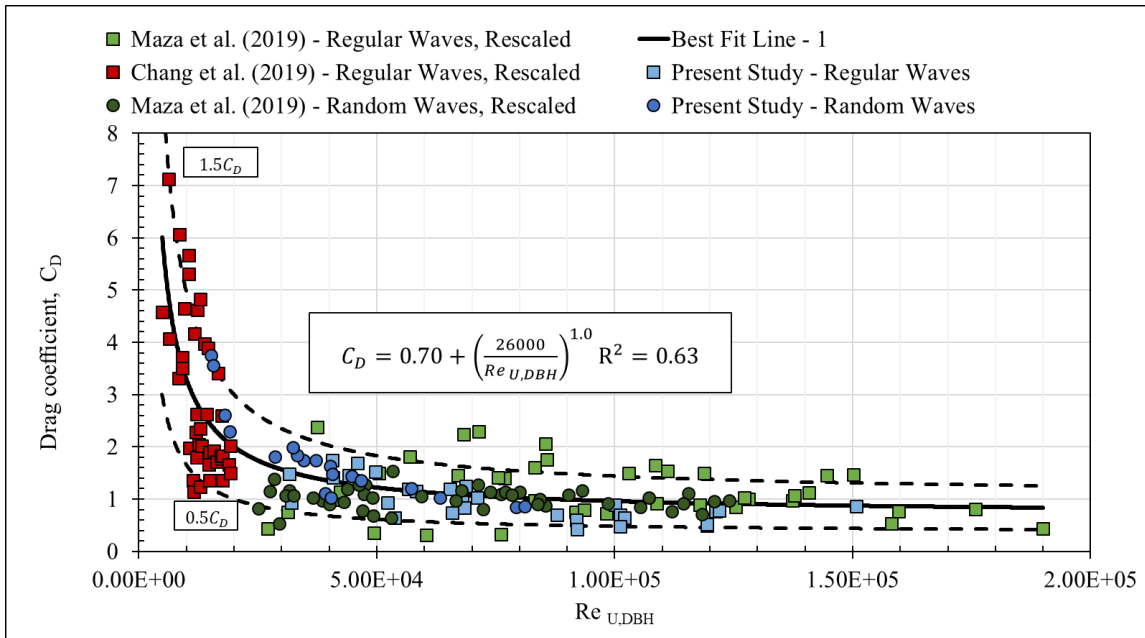


Figure 6-17 Drag coefficient, C_D , versus the Reynolds number, $Re_{U,DBH}$, for the present study's and previous studies' data. Best fit line – 1 best fit for all studies data combined.

In the figure, the rescaled Chang et al. (2019) data are shown as dark red squares and the Maza et al. (2019) data are shown as dark green circles (random waves) and intermediate green squares (regular waves), respectively. Overall, the figure shows good agreement between the present study's data and the results from Chang et al. (2019) and Maza et al. (2019) despite the differences in the three studies' scales, wave conditions, and model tree geometries.

A best-fit line using the empirical equation of the form $C_D = a_1 + (a_2/Re_{U,DBH})^{a_3}$ was found for the combined data with the values $a_1=0.70$, $a_2=26,000$, $a_3=1.0$ and $R^2=0.63$ for the range $4.9E3 < Re_{U,DBH} < 1.9E5$. Following the approach from Chang et al. (2019), the best fit line $\pm 50\% C_D$ is also shown in the figure (black dashed lines). As observed in the figure, these bounds incorporate most of the combined data set within its bounds.

An alternative best-fit line was also determined where $a_1=0.6$, $a_2=30,000$, $a_3=1.0$ with $R^2=0.63$. It also shows good agreement with the combined data set and the best fit line $\pm 50\% C_D$ capturing most of the dataset. The asymptote value, a_1 , was modified to be consistent with results from Sarpkaya and Isaacson (1981) for waves on vertical piles. The alternative best-fit equation is recommended for use in engineering design with mangroves (Figure 6-18) to determine the

correct drag coefficient for mangroves for a range of wave conditions. The Mendez and Losada (2004) equations (Equation 7 and 8) for random waves can then be used to derive the wave weight decay, $\tilde{\alpha}_m$, and subsequently the percent of wave attenuation for the mangrove forest of given cross-shore width.

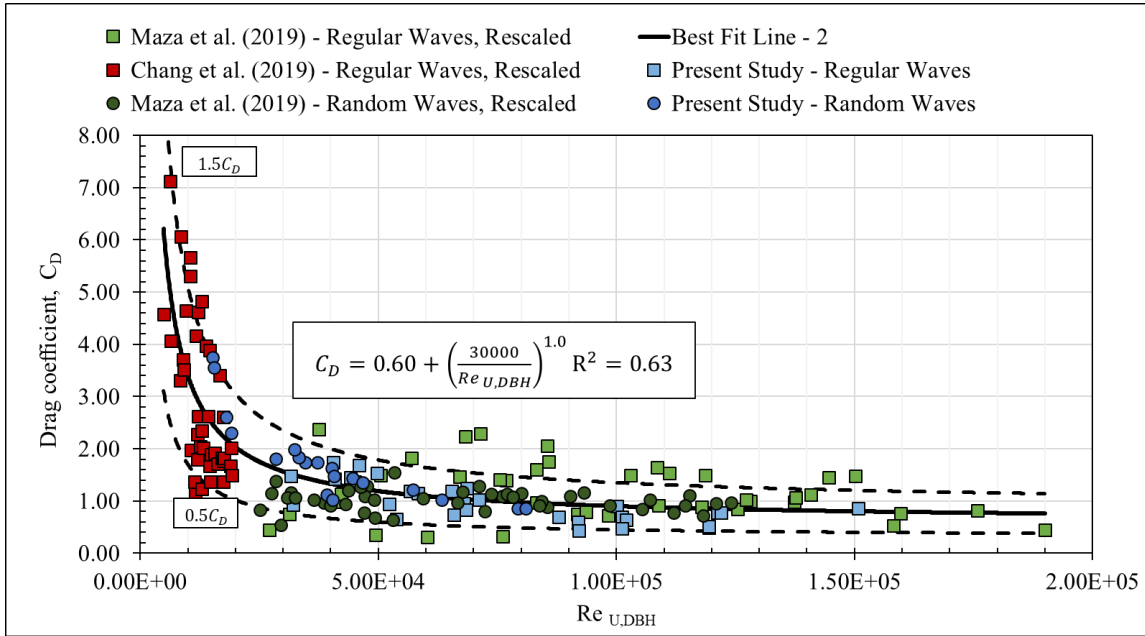


Figure 6-18 Drag coefficient, C_D , versus the Reynolds number, $Re_{U,DBH}$, for the present studies and previous studies data. Alternative best fit for the combined data the asymptote value 0.6 consistent with wave forces on vertical piles, Sarpkaya and Isaacson (1981).

The alternative best-fit line from the combined data set (Figure 6-18) was compared with the present study's best-fit line for random waves as well as previous studies derived C_D - Re equations for emergent and mangrove vegetation (Figure 6-19). In Figure 6-19, the y-axis shows the drag coefficient, C_D , and the x-axis shows the $Re_{U,DBH}$ values. The present study's best fit line for random waves (solid black line) and previous emergent (dashed lines) and mangrove (solid lines) vegetation studies are shown. The best fit line for the combined data of the laboratory mangrove studies is also shown as a black dash-dot line.

The figure shows that the mangrove studies report higher Reynolds numbers than the emergent vegetation studies. One possible reason for the difference is the stem diameters of the emergent vegetation studies were orders of magnitude smaller than the D_{BH} values of the mangrove studies, thus producing smaller Reynolds numbers than the mangrove studies for similar

hydrodynamic conditions. The mangrove studies could have also tested larger wave conditions than the emergent vegetation studies' yielding larger Reynolds numbers. The emergent vegetation studies equations fall around similar $Re_{U,DBH}$ values but vary in the C_D values. For the mangrove studies, Chang et al. (2019) (solid orange line) has the equation fit for lower Reynolds number than the present study and Maza et al. (2019) study (light red and dark red solid lines). The Maza et al. (2019) did not fit equations for their study's data, so two equations were proposed (Table 9-22) using the same empirical equation form as the present study's best-fit lines. The combined studies' best-fit line agrees well with the different mangrove studies' best-fit lines and spans between the different studies equations, reinforcing the equations recommended use for engineering design with mangroves.

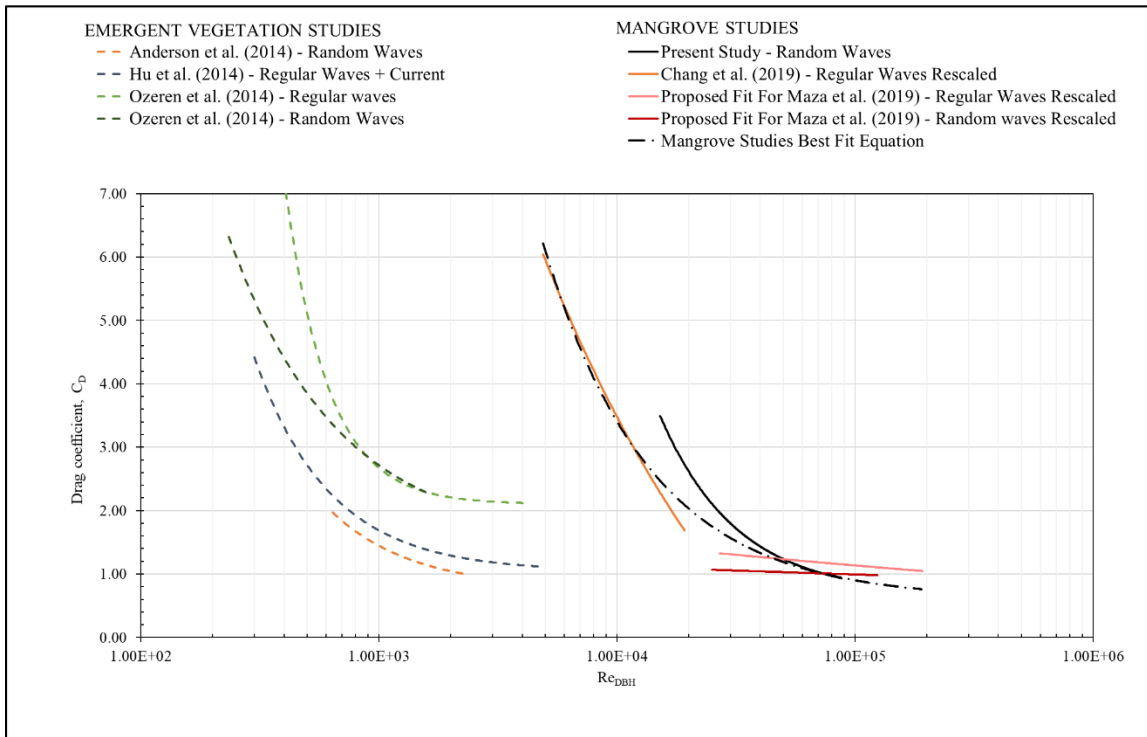


Figure 6-19 Drag coefficient C_D , versus $Re_{U,DBH}$, for the present studies data compared to previous mangrove and emergent vegetation studies equations.

Chapter 7. Discussion

The results included in the combined data set shown in Figures 6-17 and 6-18 were for conditions where the model trees were not submerged for each separate study. As Anderson and Smith (2004) found, submerged conditions alter the drag coefficients for conditions with similar

Reynolds numbers. Thus, the presented equations should only be used for conditions where mangroves are not fully submerged. For mature mangrove forests, submergence would only take place under more extreme conditions where storm surge is large. However, for younger mangrove forests, submergence could be a daily to periodic event depending on the age of the trees, growth rate, tidal range, and relative sea level rise, and frequency of adequate storm surges.

The derived equations came from studies that did not include a canopy for their tested model tree. The canopy's added effects, especially at higher water depths, could alter the drag coefficients found for these studies and, in effect, the two presented equations. However, there have been antidotal reports of hurricane winds completely removing the leaves and some branches from mangrove canopies in the Caribbean (Biondi, 2020). So, the real contribution canopies could provide to wave height reduction could be marginal under extreme conditions. However, the canopies could provide a significant contribution for milder conditions.

Nevertheless, by excluding the canopy from the tested models, the presented equations provide a conservative estimate of the protection provided by the mangroves for the range $4.9E3 < Re_{U,DBH} < 1.9E5$.

Furthermore, both the present study and Maza et al. (2019) study only considered the primary prop root in constructing the model trees. However, the Chang et al. (2019) study included the primary roots with the secondary, and tertiary prop roots branching off of the primary roots, in their tree model. The tertiary and secondary roots provide more projected area and potentially more protection. However, by neglecting these additional roots, the present study and the Maza et al. (2019) study provide conservative models of the mangrove trees. This conservative approach by these two studies is another reason why the two presented equations could be considered a conservative estimate of the drag coefficient, C_D , for mangroves.

The present, Maza et al. (2019), and Chang et al. (2019) studies all constructed models for the *Rhizophora* genus and used identical model trees to create their model forest for each respective study. Mangrove forests, in reality, are made up of trees of different ages, growth stages, and species. For complex forests with multiple ages of *Rhizophora* sp. trees, a weighted average drag coefficient could be calculated if the percentage makeup of the forest for the different diameters at breast height, D_{BH} , are known. The weighted drag coefficient could then be

used to estimate the percent wave height attenuation for the forest via the Mendez and Losada (2004) equation. For mangrove forests of multiple mangrove species, assumptions would need to be made to apply the presented engineering equations for a mean weighted drag coefficient of the forest and could result in an unrealistic representation of the forest.

The present study also considered an idealized bathymetry for the study where there was a flat section before, within, and after the model forest in order to isolate the effects of the model forest to the fullest extent. In reality, mangrove forests are located on sloping bathymetries that can have effects on propagating waves as well. This could alter the waves interaction with the mangroves but additional testing would be needed to verify this.

Furthermore, the protection that mangrove forests can provide is not constant. It can change depending on biological variables such as forest age, growth, and structure. It can also change depending on the damage state post extreme event such as a hurricane or tsunami. Understanding the time needed for these forests to recover, if it does, and how the protection it provides changes as the recovery process takes place is not yet fully understood. This understanding, however, is essential to quantifying the long-term protection these forests can provide. Incorporating gray infrastructure such as rubble mound sills could help give protection to maturing or recovering mangrove forests as well as the shoreline. The same can also be said for other green infrastructures such as salt marshes, oyster reefs, and dunes which can also vary in damage states over time. Therefore, understanding how green and gray can be combined and the protection these hybrid systems provide is crucial to the long-term success of these projects for coastal protection. Future research focused on these hybrid systems is needed to fully answer these questions and identify the critical components for successful design.

Chapter 8. Conclusions

For the study, several accomplishments were made. The study was the first to successfully complete a laboratory experiment for mangroves at a prototype scale. The study also presented a validated methodology for using LiDAR scanning to quantify key geometric parameters such as the projected area per unit height, $A_{t,m}$, and the effective diameter, D_e , of the model forest. This methodology can be practically used in field applications where destructive and traditional measurement techniques would be cumbersome or unfeasible.

For example, precise LiDAR scans could capture the variability of a dense mangrove fringe consisting of multiple sizes, ages, and geometry within an hour. Conversely, traditional methods would need significantly more time to either cut down or manually measure each aspect of the trees to capture the same detail as the LiDAR scans. Also, the LiDAR scans provide digital documentation of the mangrove forest that can be analyzed at any point in time and compared to future scans of the fringe to see how the fringe has changed over time. The LiDAR method could also quantify how the protection of the mangrove fringe changes after a hurricane or strong storm has damaged it. The recovery of the fringe could also be evaluated using the method by comparing scans of the same forest at different stages of regrowth.

The study determined the wave height decay, $\tilde{\alpha}$ for random waves was predominantly dependent on the water depth and forest density. There was also an indication of a linear relationship between forest density and wave height decay, $\tilde{\alpha}$ for random waves although additional testing is needed, to verify the relationship. The study also derived drag coefficients, C_D for regular and random waves, quantified uncertainty for the C_D based on the variability of the mean projected area per unit height $A_{t,m} \pm \sigma_{t,m}$ and best fit of the wave height decay, $\tilde{\alpha}_m \pm \sigma$, and combined the uncertainty of the two variables to get a combined uncertainty for the drag coefficients.

The study successfully applied a rescaling method for the Reynolds number to previously reduced scale laboratory experiments that resulted in good agreement between the present and prior studies results. To the authors knowledge, the rescaling method can be used with confidence up to 1:7 scale for future reduced-scale tests of mangroves. This finding essential for future physical model of wave transformations through mangrove forests given that reduced scaled tests are less time and cost-intensive and more feasible than prototype scale experiments.

The present and past studies' rescaled data sets were also combined, and two empirically derived equations for the drag coefficient, C_D as a function of the Reynolds number, $Re_{U,DBH}$ were found. The equation was of the form $C_D = a_1 + (a_2/Re_{U,DBH})^{a_3}$, and for the combined data set had a best fit with values $a_1=0.70$, $a_2=26,000$, $a_3=1.0$ with $R^2=0.63$ in the range $4.9E3 < Re_{U,DBH} < 1.9E5$. The alternative equation had coefficients of $a_1=0.6$, $a_2=30,000$, $a_3=1.0$ with $R^2 = 0.63$ and is suggested for engineering design so that the asymptote value is 0.6, consistent with the work of Sarpkaya and Isaacson (1981) for waves on vertical piles. For a certain wave condition, the

recommend equation can be used to find the drag coefficient which can be used in the Mendez and Losada (2004) equation for random waves to derive the percent wave attenuation for the mangrove forest of certain cross-shore width.

The recommended equation should only be used for conditions where mangroves are not fully submerged. It should also be considered a conservative design estimate because a canopy, secondary, and tertiary aerial roots branching off of the primary prop roots, were not included in the combined studies physical models.

The protection that mangrove forests provide is not constant. Understanding how the protection changes due to the condition of the forest are essential to quantifying the long-term coastal protection these forests can provide. Incorporating gray infrastructure such rubble mound sills could help given the protection it would provide to the mangrove forest and other NNBF features as they recover. Therefore, understanding how green and gray infrastructure systems can be combined and the resulting protection is crucial to the long-term success of these projects for coastal protection. Future research focused on these hybrid systems is needed to fully answer these questions and identify the critical components for successful design.

References

- Anderson, M. E. and Smith, J. M. (2014). Wave Attenuation by Flexible, Idealized Salt Marsh Vegetation. *Coastal Engineering*, 83, 82–92.
<https://doi.org/10.1016/j.coastaleng.2013.10.004>
- Augustin, L. N. Irish, J. L. and Lynett, P. (2009). Laboratory and Numerical Studies of Wave Damping By Emergent and Near-Emergent Wetland Vegetation. *Coastal Engineering*, 56(3), 332–340. <https://doi.org/10.1016/j.coastaleng.2008.09.004>
- Bao, T. Q. (2011). Effect of Mangrove Forest Structures on Wave Attenuation in Coastal Vietnam. *Oceanologia*, 53(3), 807–818. <https://doi.org/10.5697/oc.53-3.807>
- Biondi, E. (2020). *Design with Nature: Using Mangrove Shorelines, Research Needs and Design Opportunities*. Applied Technology and Management.
- Chang, C.-W. Mori, N. Tsuruta, N. and Suzuki, K. (2019). Estimation of Wave Force Coefficients on Mangrove Models. 土木学会論文集B2 (海岸工学), 75(2), 1105–1110.
- Chella, M. A. Kennedy, A. B. Asce, M. and Westerink, J. J. (2020). *Wave Runup Loading Behind a Semipermeable Obstacle*. [https://doi.org/10.1061/\(ASCE\)0733-950X\(1984\)110:1\(67\)](https://doi.org/10.1061/(ASCE)0733-950X(1984)110:1(67))
- Clough, B. Phillips, M. and Xuan, T. T. (1999). *Mixed Shrimp Farming-Mangrove Forestry Models in the Mekong Delta Termination Report*.
- Dalrymple, R. A. Asce, M. Kirby, J. T. Hwang, P. A. and Members, A. (1984). Wave Diffraction Due to Areas of Energy Dissipation. *J. Waterway, Port, Coastal, Ocean Eng*, 110(1), 67–79. [https://doi.org/https://doi.org/10.1061/\(ASCE\)0733-950X\(1984\)110:1\(67\)](https://doi.org/https://doi.org/10.1061/(ASCE)0733-950X(1984)110:1(67))

- Danielsen, F. Sørensen, M. K. Olwig, M. F. Selvam, V. Parish, F. Burgess, N. D. Hiraishi, T. Karunagaran, V. M. Rasmussen, M. S. Hansen, L. B. Quarto, A. and Suryadiputra, N. (2005). The Asian tsunami: A Protective Role for Coastal Vegetation. *Science*, 310(5748), 643. <https://doi.org/10.1126/science.1118387>
- Dawes, C. Siar, K. and Marlett, D. (1999). Mangrove Structure, Litter and Macroalgal Productivity in a Northern-Most Forest of Florida. In *Mangroves and Salt Marshes* (Vol. 3). <https://doi.org/https://doi.org/10.1023/A:1009976025000>
- Dean, R. G. and Dalrymple, R. A. (1991). *Water Wave Mechanics for Engineers and Scientists* (Vol. 2). World Scientific. <https://doi.org/10.1142/1232>
- Donnelly, M. Shaffer, M. Connor, S. Sacks, P. and Walters, L. (2017). Using Mangroves to Stabilize coastal Historic Sites: Deployment Success Versus Natural Recruitment. *Hydrobiologia*, 803(1), 389–401. <https://doi.org/10.1007/s10750-017-3155-x>
- Feliciano, E. A. Wdowinski, S. and Potts, M. D. (2014). Assessing Mangrove Above-Ground Biomass and Structure using Terrestrial Laser Scanning: A Case Study in the Everglades National Park. *Wetlands*, 34(5), 955–968. <https://doi.org/10.1007/s13157-014-0558-6>
- Furukawa, K. Wolanski, E. and Mueller, H. (1997). Currents and Sediment Transport in Mangrove Forests. In *Estuarine, Coastal and Shelf Science* (Vol. 44).
- Goring, D. G. (1979). *Tsunamis-The propagation of long waves onto a shelf*. <https://doi.org/10.7907/Z9MS3QPH>
- Gronbech, J. Jensen, T. and Andersen, H. (1997). Reflection Analysis With Separation of Cross Modes. *Proceedings of the Coastal Engineering Conference*, 1, 968–980. <https://doi.org/10.1061/9780784402429.076>

- Guannel, G. Ruggiero, P. Faries, J. Arkema, K. Pinsky, M. Gelfenbaum, G. Guerry, A. and Kim, C. K. (2015). Integrated Modeling Framework to Quantify the Coastal Protection Services Supplied by Vegetation. *Journal of Geophysical Research: Oceans*, 120(1), 324–345. <https://doi.org/10.1002/2014JC009821>
- Hashim, A. M. and Catherine, S. M. P. (2013). A Laboratory Study on Wave Reduction by Mangrove Forests. *APCBEE Procedia*, 5, 27–32. <https://doi.org/10.1016/j.apcbee.2013.05.006>
- Horstman, E. M. Dohmen-Janssen, C. M. Narra, P. M. F. van den Berg, N. J. F. Siemerink, M. and Hulscher, S. J. M. H. (2014). Wave Attenuation in Mangroves: A Quantitative Approach to Field Observations. *Coastal Engineering*, 94, 47–62. <https://doi.org/10.1016/j.coastaleng.2014.08.005>
- Ismail, I. Husain, M. L. and Zakaria, R. (2017). Attenuation of Waves from Boat Wakes in Mixed Mangrove Forest of *Rhizophora* and *Bruguiera* species in Matang Park. *Malaysian Journal Geosciences*, 1(2), 29–32. <https://doi.org/10.26480/mjg.02.2017.29.32>
- Jimenez, J. A. Lugo, A. E. and Cintron, G. (1985). Tree Mortality in Mangrove Forests. *Biotropica*, 17(3), 177. <https://doi.org/10.2307/2388214>
- Juul Jensen, O. and Klinting, P. (1983). Evaluation of Scale Effects in Hydraulic Models by Analysis of Laminar and Turbulent Flows. *Coastal Engineering*, 7(4). [https://doi.org/10.1016/0378-3839\(83\)90002-9](https://doi.org/10.1016/0378-3839(83)90002-9)
- Kibler, K. M. Kitsikoudis, V. Donnelly, M. Spiering, D. W. and Walters, L. (2019). Flow-vegetation Interaction in a Living Shoreline Restoration and Potential Effect to Mangrove Recruitment. *Sustainability (Switzerland)*, 11(11). <https://doi.org/10.3390/su11113215>
- Krauss, K. W. Doyle, T. W. Doyle, T. J. Swarzenski, C. M. From, A. S. Day, R. H. and Conner, W. H. (2009). Water Level Observations in Mangrove Swamps During Two Hurricanes in Florida. *The Society of Wetland Scientists*, 29(1), 142–149.

- Loría-Naranjo, M. Samper-Villarreal, J. and Cortés, J. (2014). Structural Complexity and Species Composition of Potrero Grande and Santa Elena Mangrove Forests in Santa Rosa National Park, North Pacific of Costa Rica. *Revista de Biología Tropical*, 62, 33–41. <https://doi.org/10.15517/rbt.v62i4.20030>
- Losada, I. J. Lara, J. L. and del Jesus, M. (2016). Modeling the Interaction of Water Waves with Porous Coastal Structures. *Journal of Waterway, Port, Coastal, and Ocean Engineering*, 142(6), 03116003. [https://doi.org/10.1061/\(asce\)ww.1943-5460.0000361](https://doi.org/10.1061/(asce)ww.1943-5460.0000361)
- Martín, F. Martínez, C. Lomónaco, P. and Vidal, C. (2003). *a New Procedure for the Scaling of Core Material in Rubble Mound Breakwater Model Tests*. July, 1594–1606. https://doi.org/10.1142/9789812791306_0134
- Maza, M. Adler, K. Ramos, D. Garcia, A. M. and Nepf, H. (2017). Velocity and Drag Evolution From the Leading Edge of a Model Mangrove Forest. *Journal of Geophysical Research: Oceans*, 122(11), 9144–9159. <https://doi.org/10.1002/2017JC012945>
- Maza, M. Lara, J. L. and Losada, I. J. (2019). Experimental Analysis of Wave Attenuation and Drag Forces in a Realistic Fringe *Rhizophora* Mangrove Forest. *Advances in Water Resources*, 131. <https://doi.org/10.1016/j.advwatres.2019.07.006>
- Mazda, Yoshihiro, Magi, M. Ikeda, Y. Kurokawa, T. and Asano, T. (2006). Wave Reduction in a Mangrove Forest Dominated by *Sonneratia* sp. *Wetlands Ecology and Management*, 14(4), 365–378. <https://doi.org/10.1007/s11273-005-5388-0>
- Mazda, Y., Wolanski, E. King, B. Sase, A. Ohtsuka, D. and Magi, M. (1997a). Drag Force Due to Vegetation in Mangrove Swamps. *Mangroves and Salt Marshes*, 1, 193–199.
- Mazda, Y., Magi, M. Kogo, M. and Hong, P. N. (1997b). Mangroves as a Coastal Protection From Waves in The Tong King delta, Vietnam. *Mangroves and Salt Marshes*, 1, 127–135.

- Mendez, F. J. and Losada, I. J. (2004). An Empirical model to Estimate the Propagation of Random Breaking and Nonbreaking Waves Over Vegetation Fields. *Coastal Engineering*, 51(2), 103–118.
<https://doi.org/10.1016/j.coastaleng.2003.11.003>
- Montgomery, J. M. Bryan, K. R. Horstman, E. M. and Mullarney, J. C. (2018). Attenuation of Tides and Surges by Mangroves: Contrasting Case Studies From New Zealand. *Water (Switzerland)*, 10(9). <https://doi.org/10.3390/w10091119>
- Morison, J. R. Johnson, J. W. and Schaaf, S. A. (1950). The Force Exerted by Surface Waves on Piles. *Journal of Petroleum Technology*, 2(05), 149–154.
<https://doi.org/10.2118/950149-g>
- Narayan, S. Stive, M. J. F. Ursem, W. N. J. Tuin, B. and Delft, T. U. (2009). *The Effectiveness of Mangroves in Attenuating Cyclone-induced Waves Graduation Committee*.
- National Academy of Sciences. (1977). Methodology for Calculating Wave Action Effects Associated with Storm Surges. *Washington, D.C. 29 Pp.*
- Niazi, M. H. K. Morales Nápoles, O. and van Wesenbeeck, B. K. (2021). Probabilistic Characterization of the Vegetated Hydrodynamic System Using Non-Parametric Bayesian Networks. *Water (Switzerland)*, 13(4).
<https://doi.org/10.3390/w13040398>
- Novitzky, P. (2010). *Analysis of Mangrove Structure and Latitudinal Relationships on the Gulf Coast of Peninsular Florida*. <https://scholarcommons.usf.edu/etd/1726>
- Ohira, W. Honda, K. Nagai, M. and Ratanasawan, A. (2013). Mangrove Stilt Root Morphology Modeling for Estimating Hydraulic Drag in Tsunami Inundation Simulation. *Trees - Structure and Function*, 27(1), 141–148.
<https://doi.org/10.1007/s00468-012-0782-8>

- Olagoke, A. Proisy, C. Féret, J. B. Blanchard, E. Fromard, F. Mehlig, U. de Menezes, M. M. dos Santos, V. F. and Berger, U. (2016). Extended Biomass Allometric Equations For Large Mangrove Trees From Terrestrial LiDAR data. *Trees - Structure and Function*, 30(3), 935–947. <https://doi.org/10.1007/s00468-015-1334-9>
- Ong, J.-E. Khoon, W. and Clough, B. F. (1995). Structure and Productivity of a 20-Year-Old Stand of *Rhizophora apiculata* Bl. Mangrove Forest. *Journal of Biogeography*, 22(3), 417–424.
- Ozeren, Y. Wren, D. G. and Wu, W. (2014). Experimental Investigation of Wave Attenuation through Model and Live Vegetation. *Journal of Waterway, Port, Coastal, and Ocean Engineering*, 140(5), 04014019. [https://doi.org/10.1061/\(asce\)ww.1943-5460.0000251](https://doi.org/10.1061/(asce)ww.1943-5460.0000251)
- Quartel, S. Kroon, A. Augustinus, P. G. E. F. van Santen, P. and Tri, N. H. (2007). Wave Attenuation in Coastal Mangroves in The Red River Delta, Vietnam. *Journal of Asian Earth Sciences*, 29(4), 576–584. <https://doi.org/10.1016/j.jseaes.2006.05.008>
- Sarpkaya, T. and Isaacson, M. (1981). *Mechanics of Wave Forces on Offshore Structures*. <https://doi.org/10.1115/1.3162189>
- Strusińska-Correia, A. Husrin, S. and Oumeraci, H. (2014). Attenuation of Solitary Wave By Parameterized Flexible Mangrove Models. *Coastal Engineering*. <http://1.bp.blogspot.com/-8Sml4yn3onI/TtBlaTrxu->
- Thuy, N. B. Nandasena, N. A. K. Dang, V. H. Kim, S. Hien, N. X. Hole, L. R. and Thai, T. H. (2017). Effect of River vegetation With Timber Piling on Ship Wave Attenuation: Investigation by Field Survey and Numerical Modeling. *Ocean Engineering*, 129, 37–45. <https://doi.org/10.1016/j.oceaneng.2016.11.004>

- Tomiczek, T. , Wargula, A. Jendrysik, M. Goodwin, S. Kennedy, A. B. Lynett, P. Lomonaco, P. and Cox, D. T. (2019). *Physical Model Investigation of Parcel-Scale Effects of Mangroves on Wave Transformation and Force Reduction in the Built Environment. In: Coastal Structures Proceedings.* 1–10.
- Tomiczek, T. Wargula, A. Lomónaco, P. Goodwin, S. Cox, D. Kennedy, A. and Lynett, P. (2020). Physical Model Investigation of Mid-Scale Mangrove Effects on Flow Hydrodynamics and Pressures and Loads in the Built Environment. *Coastal Engineering*, 162. <https://doi.org/10.1016/j.coastaleng.2020.103791>
- Vinh La, T. Yagisawa, J. Tanaka, N. Vinh La Student, T. Yagisawa Asst Professor, J. and Tanaka Professor, N. (2014). *Efficacy of Rhizophora Apiculata and Nypa Fruticans on Attenuation of Boat-Generated Waves under Steep Slope Condition.* <https://www.researchgate.net/publication/275020317>
- Ward, G. A. Smith, T. J. Whelan, K. R. T. and Doyle, T. W. (2006). Regional Processes in Mangrove Ecosystems: Spatial Scaling Relationships, Biomass, and Turnover Rates Following Catastrophic Disturbance. *Hydrobiologia*, 569(1), 517–527. <https://doi.org/10.1007/s10750-006-0153-9>
- Wu, W. C. and Cox, D. T. (2015). Effects of Wave Steepness and Relative Water Depth on Wave attenuation by Emergent Vegetation. *Estuarine, Coastal and Shelf Science*, 164, 443–450. <https://doi.org/10.1016/j.ecss.2015.08.009>
- Wu, W. C. and Cox, D. T. (2016). Effects of Vertical Variation in Vegetation Density on Wave Attenuation. *Journal of Waterway, Port, Coastal, and Ocean Engineering*, 142(2), 04015020. [https://doi.org/10.1061/\(asce\)ww.1943-5460.0000326](https://doi.org/10.1061/(asce)ww.1943-5460.0000326)
- Zelt, J. A. and Skjelbreia, J. E. (1993). Estimating Incident and Reflected Wave Fields Using an Arbitrary Number of Wave Gages. *Proceedings of the Coastal Engineering Conference*, 1, 777–788. <https://doi.org/10.1061/9780872629332.058>

- Zhang, K. Liu, H. Li, Y. Xu, H. Shen, J. Rhome, J. and Smith, T. J. (2012). The Role of Mangroves in Attenuating Storm Surges. *Estuarine, Coastal and Shelf Science*, 102–103, 11–23. <https://doi.org/10.1016/j.ecss.2012.02.021>
- Zhang, X. Chua, V. P. and Cheong, H. F. (2015). Hydrodynamics in Mangrove Prop Roots and their Physical Properties. *Journal of Hydro-Environment Research*, 9(2), 281–294. <https://doi.org/10.1016/j.jher.2014.07.010>

Chapter 9. Appendices

Appendix A Mangrove Specimen

Mangrove specimen construction began with drilling the root holes into each of the model tree trunks. The root holes were marked on the 50 model trunks according to the specifications in Table 9-1 that included the offset for the hub couple and concrete cap.

Table 9-1 Model tree root hole locations with hub couple offset included.

Root Pair (-)	θ (deg, °)	Root Height, H_{Ri} + offset for couple offset & concrete cap (m)
1	0	0.68
2	45	0.81
3	90	0.94
4	135	1.06
5	180	1.19
6	225	1.32
7	270	1.45

The root holes were first drilled using a 2.86 cm, Forstner bit, a drill press, a homemade wooden vice for 10.16 cm pipes, and quick grip bar clamps. It was found however, that the drill press travel depth with the Forstner bit attached was less than 11.43 cm (outside diameter of the 10.16 cm x 3.05 m trunks) so both root pairs holes could not be drilled at one time. A Diablo 2.86 cm x 15.24 cm SPEEDemon Spade Bit was then tested and was able to drill through both sides of the trunk after the press table was raised slightly following the drilling of the first root hole in the pair. The bit was used for fourteen trees until the cutting edge of the bit dulled and began to catch on the PVC. Due to safety concerns, the bit's use was discontinued and a Milwaukee 2.86 cm BI-Metal Hole Saw with a Milwaukee 0.64 cm x 30.48 cm Keyed Extension was used in its stead. This setup was allowed for both root holes sequentially with minimal safety concerns. The setup was used for the remainder of the root holes (Figure 9-1).



Figure 9-1. Bi-Metal Hole Saw setup with keyed extension on drill press for root pair hole drilling.

The roots were constructed from 2.54 cm PEX piping that was ordered in 7 – 91.44 m rolls and 18 -30.48 m rolls for a total of 1178.66 m of PEX tubing. To unravel the tubing, the coils were pulled by hand through a straightening device (Figure 9-2) that temporarily uncoiled the roll. 0.64 cm holes were then drilled in the ends of the pipe and a three-link chain was then fed into each end of the tubing. A 0.64 cm bolt was then placed through the hole in the ends and the chain. The exposed chain end was then attached to a s-hook ratchet strap which in turn was secured to a fence post along the southern fence line of the HWRL. The process was completed for both ends of the PEX lengths and the ratchet straps tightened until the tubing was placed under high tension and was fully straight along the fence (Figure 9-3). The tubing was left tensioned for three days at a minimum to fully straighten the PEX. The PEX ends were then secured to the fence using zip ties before releasing the ratchet straps. The zip ties allowed for tensioning to continue while the ratchet straps were then transferred to other PEX coils.

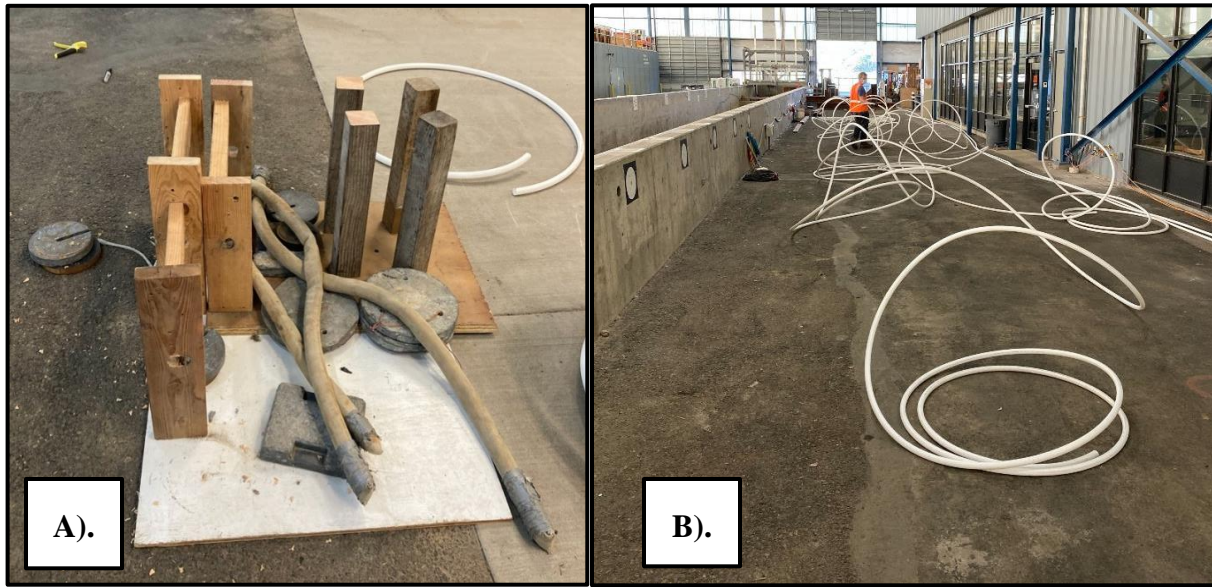


Figure 9-2. A). Constructed uncoiling device used to temporarily straighten the PEX held down by lead weights. A). Temporarily uncoiled PEX pre-tensioning.

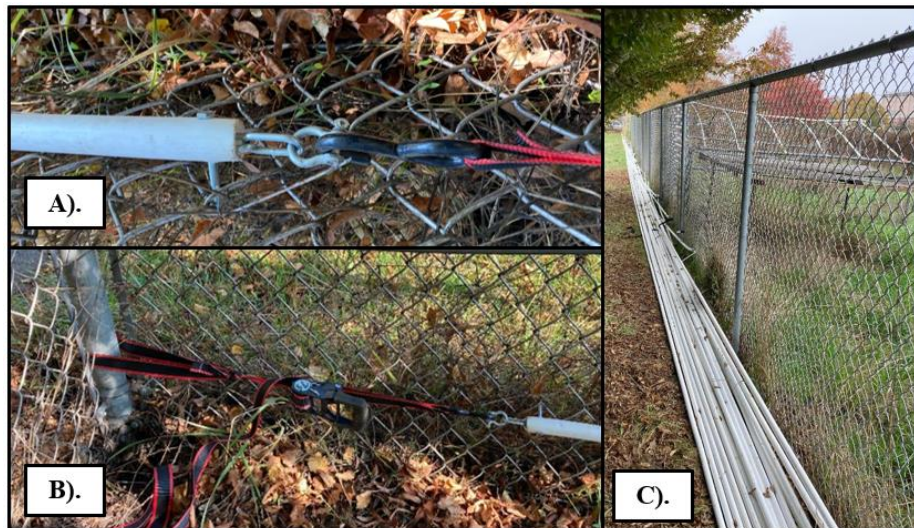


Figure 9-3. A). Close up of bolt and chain securing PEX end to ratchet strap. B). Example of ratchet strap secured to fence post. C). Multiple PEX coils attached to fence.

The model tree bases were constructed out of 1.91 cm plywood cut into 0.61 m x 0.61 m squares. A 7.62 cm PVC Open Toilet Flange was then centered on the bases and secured using 2.86 cm wood screws. Thirteen 10.16 cm x 3.05 m Schedule 40 PVC pipes were then selected and cut into 0.76 m sections until 50 had been cut. Fifty 10.16 cm PVC Hub Couplings were then collected along with 1 QT PVC glue and primer. One end of the cut 0.76 m Schedule 40 PVC

pipes was then glued to the flange/base and tamped down with a piece of scrap wood and mallet. The 10.16 cm PVC hub Couplings were then glued to the other end the cut PVC pipe section for a completed tree base (Figure 9-4). The bases were then lowered into the flume one at a time using a rope secured around the base and staged within the flume. The bases were then placed according to the layout in Figure 3-3 for each bay. A guide ruler with the alongshore locations marked for each row of mangroves and a measuring tape to were used to place the bases. The bases were placed by placing the guide ruler the correct distance from the start of each bay in the nearshore direction and then centering the bases with the markers on the ruler for each of the rows (Figure 9-5). Once the bases were set, cinder blocks on pallets were then lowered into the flume on the seaward side of the test section.

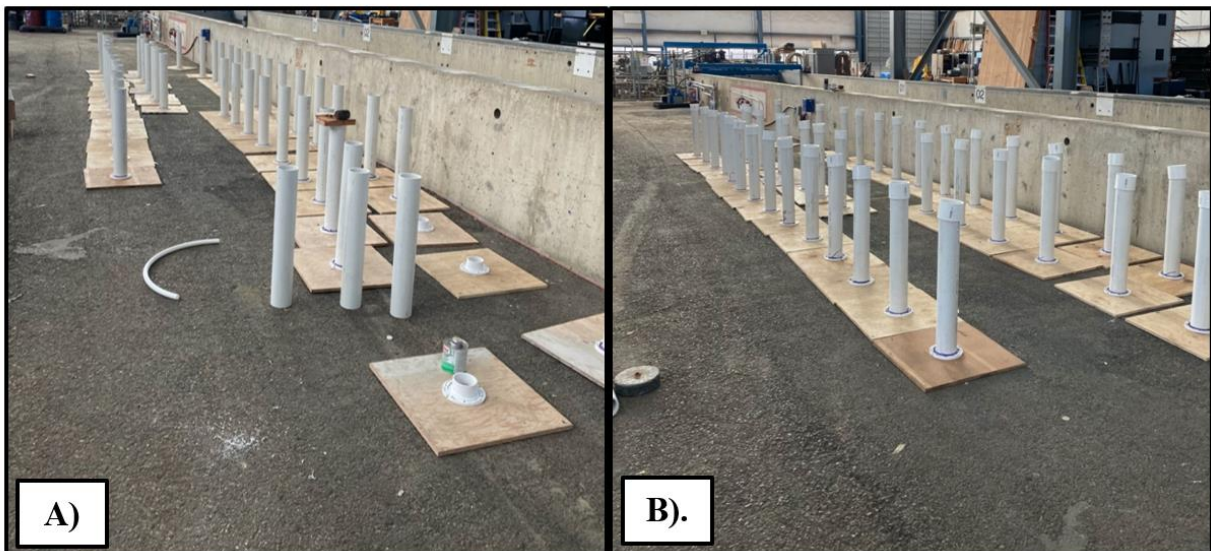


Figure 9-4. A). Prototype tree base being assembled B). Partially finished prototype tree bases with couplings set to be glued.

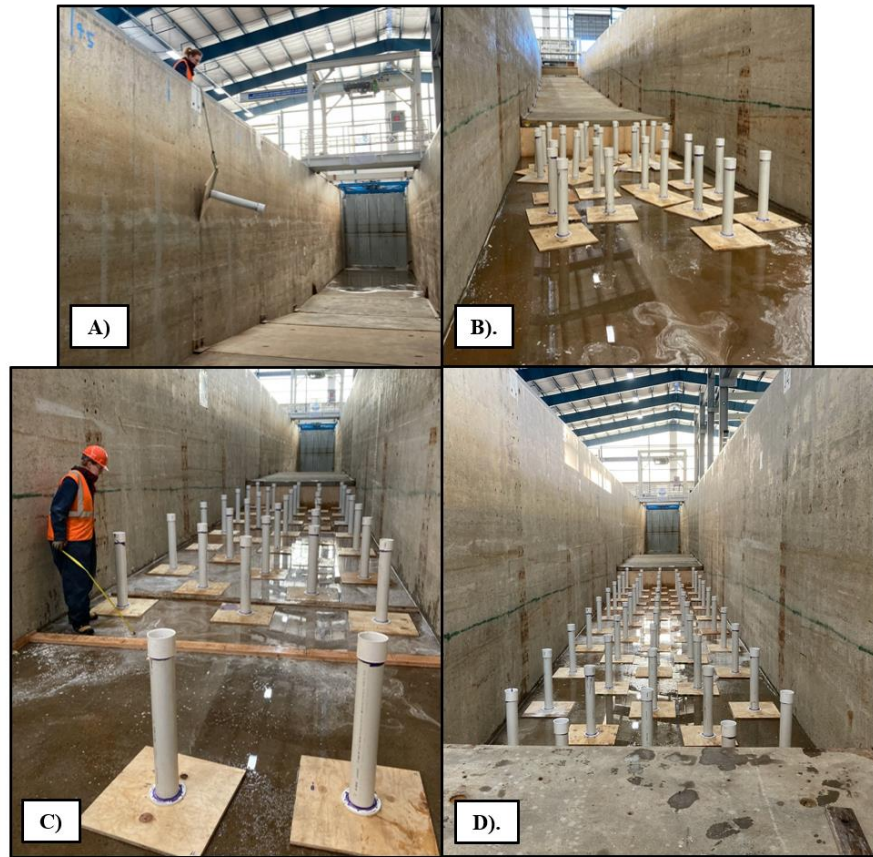


Figure 9-5. A). Prototype tree base being lowered into flume. B). All model bases in flume waiting to be placed. C). Model bases being placed using guide ruler and measuring tape. D). All model bases placed accordingly within flume.

Cinderblocks were placed around the two end sections of the test section (Figure 9-6 – A). The cinderblocks allowed for the bases in these areas to be held down while also taking up void space and reducing the amount of fill material later needed. Construction sand was used as the fill material and placed by unloading the fill onto the set tree bases from the top of the flume via a tractor with front loader attachment. The placement locations were designated using an orange cone and spotter that directed the tractor operator and ensured the placement location was free of personal/hazards before the fill was unloaded. At each placement location, the tractor operator would initially unload buckets of fill gradually into the test section. This allowed for minimal damage to be done to the tree bases directly in the placement location (Figure 9-6 – B). Once the trees base within each placement zone were covered with fill, the operator would then dump the fill directly onto the placement location for the remainder of the buckets needed there. The fill

was then evenly distributed by hand across the flume at each location until it was flush with the trees bases and the concrete slabs on either end of the mangrove section.



Figure 9-6. A). Cinderblocks being placed before fill material was added. B). Fill material being added to the mangrove section via front loader. C). Fill material being evenly spread by hand into the mangrove section.

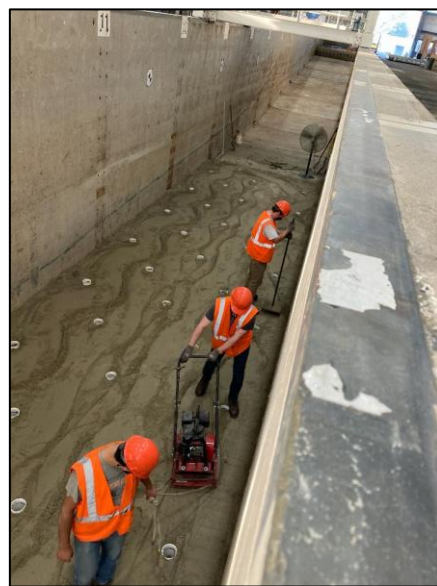


Figure 9-7. Wave lab personal compacting fill material using a plate compactor and hand dirt tamper.

A vibrating road plate compactor and a hand tamper were then used to compact the fill material until it was nominally 5.08 cm from the top of the tree bases and concrete slabs (Figure 9-7).

Before model trees were constructed, roots were cut according to their relative distance to the walls of the flume and location in the layout of Figure 3-3. Four different groups of root cuts were determined using Autodesk AutoCAD 2018 with an idealized 2-D sketch of the LWF and drawn idealized tree model (Figure 9-8 – B). The groups were denoted using the colors: blue, red, black, and yellow and each tree was categorized into one of the color groups (Figure 9-8 - A).

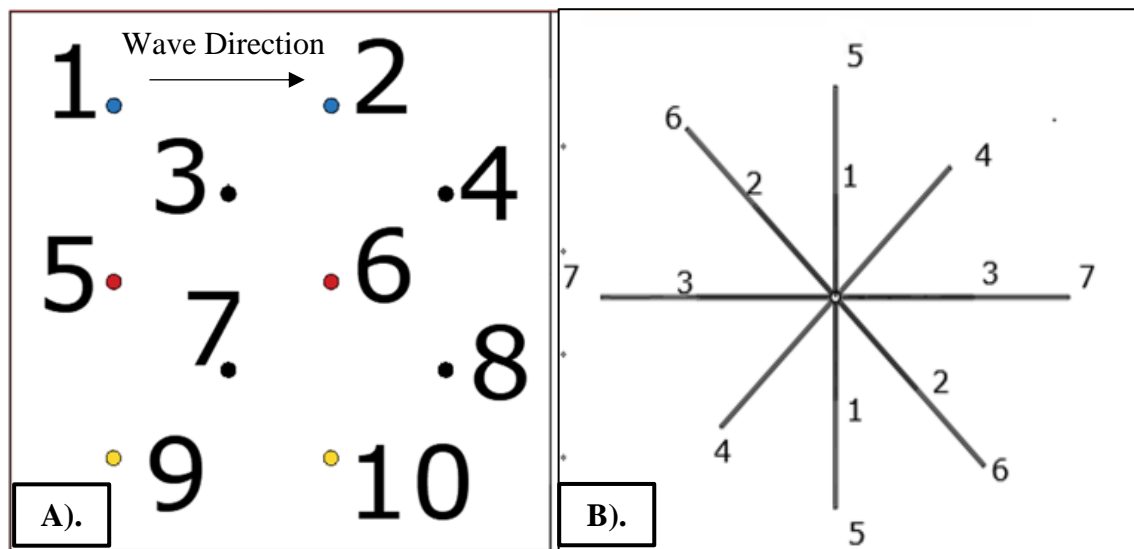


Figure 9-8 A). Overview of different color groupings for model trees in each bay. B). Top view of model tree looking downward oriented normal to piston wavemaker with numbered root pairs.

Tables 10 – 2 to 10 – 5 contain the root lengths and centers for each of the tree group colors. In total 10 blue, yellow, and red and 20 black model tree roots were cut for the model forest, respectively.

Table 9-2 Root lengths and centers for blue model trees.

	Root Length (m)	Root Center (m)
Root Pair 1	1.7	1.03
Root Pair 2	2.6	1.29
Root Pair 3	3.1	1.56
Root Pair 4	2.8	1.83
Root Pair 5	2.8	2.10
Root Pair 6	3.4	2.38
Root Pair 7	5.3	2.67

Table 9-3 Root lengths and centers for red model trees.

	Root Length (m)	Root Center (m)
Root Pair 1	2.1	1.03
Root Pair 2	2.6	1.29
Root Pair 3	3.1	1.56
Root Pair 4	3.7	1.83
Root Pair 5	4.1	2.10
Root Pair 6	4.8	2.38
Root Pair 7	5.3	2.67

Table 9-4 Root lengths and centers for black model trees.

	Root Length (m)	Root Center (m)
Root Pair 1	2.1	1.03
Root Pair 2	2.6	1.29
Root Pair 3	3.1	1.56
Root Pair 4	3.7	1.83
Root Pair 5	3.5	2.10
Root Pair 6	4.3	2.38
Root Pair 7	5.3	2.67

Table 9-5 Root lengths and centers for yellow model trees.

	Root Length (m)	Root Center (m)
Root Pair 1	1.7	1.03
Root Pair 2	2.3	1.29
Root Pair 3	3.1	1.56
Root Pair 4	2.8	1.83
Root Pair 5	2.8	2.10
Root Pair 6	3.4	2.38
Root Pair 7	5.3	2.67

The prototype trees were then fully constructed by starting with bay 8-9 where the first 10 prototype trunks were glued into their respective bases by a three-man team. The first two members of the team applied the PVC primer and glue to the bases PVC coupling and the bottom of the PVC trunk while the third member held the trunk midair. After glue was applied, the trunk was then fit into the base's coupling and rotated if needed to ensure the proper orientation of the trunk and its roots.

After the first 10 trunks had been placed, trunks were marked with either red, blue, yellow, or black spray paint and their corresponding roots were carried into the flume to be installed. The roots were marked with a center line and two guidelines 5.72 cm off the center line. The guidelines were used to line up with the outside of either root hole on the prototype trunk and streamline the instillation of the roots to their correct positions. A 0.635 cm pilot hole was also drilled near the center line of each root before instillation so air could escape once the flume was filled with water. This process was repeated four more times for bays 9-13 until the entire mangrove section had been built.

After prototype tree instillation, a 1.07 cm wide by 4 mm thick plastic barrier was installed vertically on the perimeter of the mangrove section where a portion was buried to keep the plastic in place. 9.9 m³ of SCC concrete with 1.27 cm aggregate size and slump of 8 was then delivered to the HWRL on Friday November 6th, 2020, by Knife River Corporation in two large concrete mixer trucks. A concrete pump was rented from Salem Mobile Mix that was positioned between bays 7- 9 on the east side of the flume. The concrete trucks also positioned themselves

of the east side of the flume from bays 9 to 12 and fed their discharge chute into the concrete pump's intake (Figure 9-9).



Figure 9-9 A). concrete truck positioned behind concrete pump. B). Close up of concrete truck feeding into the concrete pump.

The pump's discharge hose was then fed over the side of the flume and supported by the LWF's crane that acted as a boom for the hose. The hose end was then positioned roughly 0.305 m from the mangrove bases and a rope attached to the end to provide additional mobility with the placement of the concrete while it poured (Figure 9-10). The concrete was poured so it was nominally 0.051 m thick. Once the 0.051 m nominal depth was locally reached, the hose and crane were laterally moved to reposition the hose end. Pouring was then restarted until a 0.051 m nominal pour was achieved throughout the model forest.

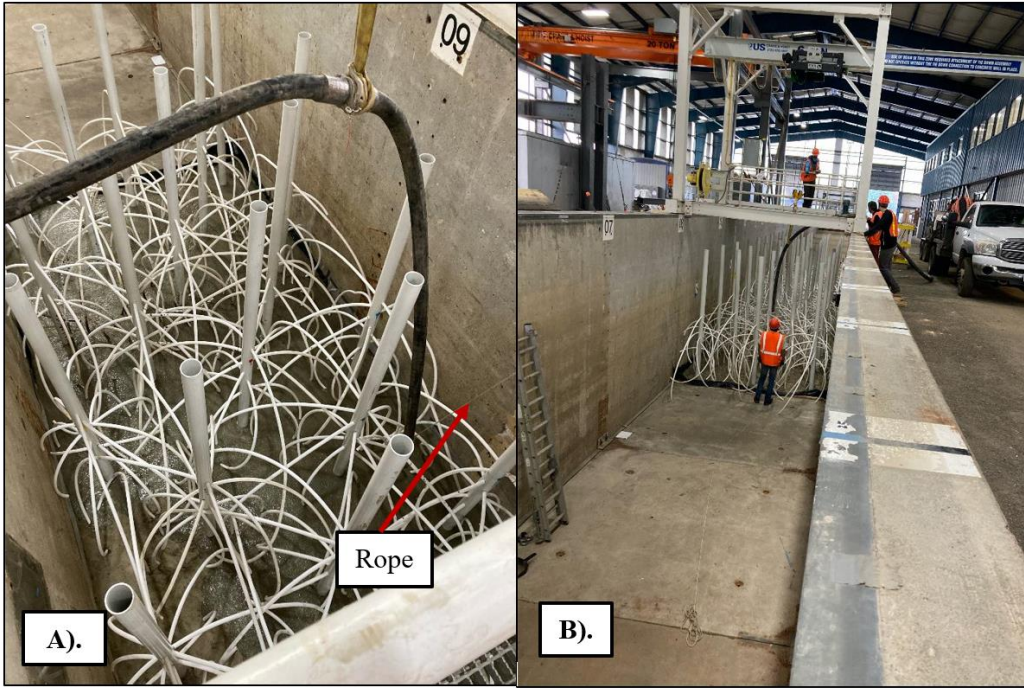


Figure 9-10 A). Arial view of concrete hose extended into the flume using the crane as a boom. B). Overview of concrete being poured into the flume.

The concrete then was then set to cure while instrumentation was placed at either end of the model forest. Instrumentation for the model forest was later installed once the concrete had cured enough.

Appendix B Test Wall

Each section of the test wall was staged beside the flume on 10.16 x 10.16 cm wood posts before they were placed in the flume (Figure 9-11). The red iron clips were preset (Figure 9-12) on the lower wall section before it was placed using the LWF crane (Figure 9-13). The lower wall section was then lowered onto the 10.16 x 15.2 cm wooden post and secured to the walls of the LWF via the red iron clips using 2.54 cm bolts. An additional 10.16 x 15.2 cm wooden post was then placed on top of the lower wall section to help with alignment with the upper section and to further seal the wall seams. The upper half of the test wall was placed in the LWF using a forklift with extended clips attached and cargo straps. The upper portion of the test wall was then secured to the side walls of the LWF via red iron clips and 2.54 cm bolts. Throughout the instillation, the cargo straps were tensioned to provide additional safety. The forklift was used

instead of the LWF crane for the upper section of the test wall because once installed, the section extended above the flume walls. This subsequently would not allow for the LWF crane to move out of the testing area and place the crane electronics at risk due to potential water damage from slashing during testing. The same routine was used for the deinstallation process for the test wall. In total the wall was installed/removed three times for the study.

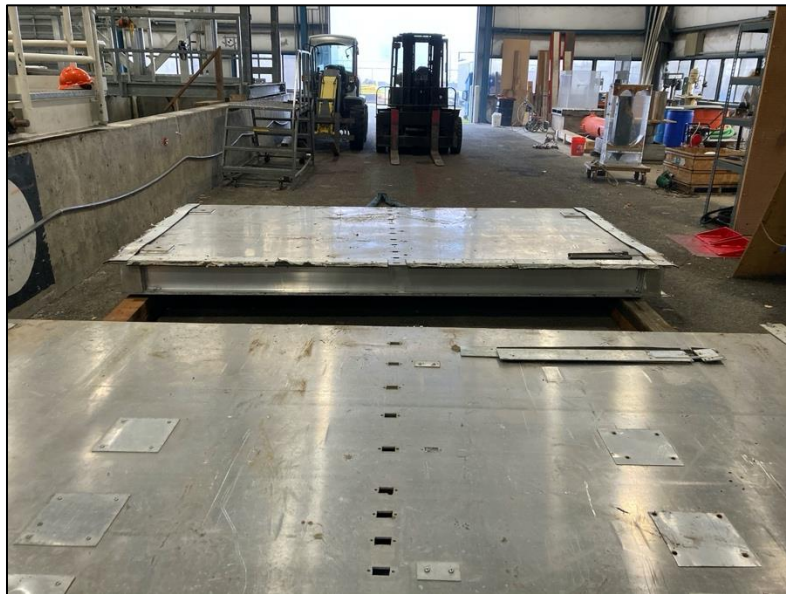


Figure 9-11 Test wall sections being staged beside the landward side of the flume, bay 21 – 22.

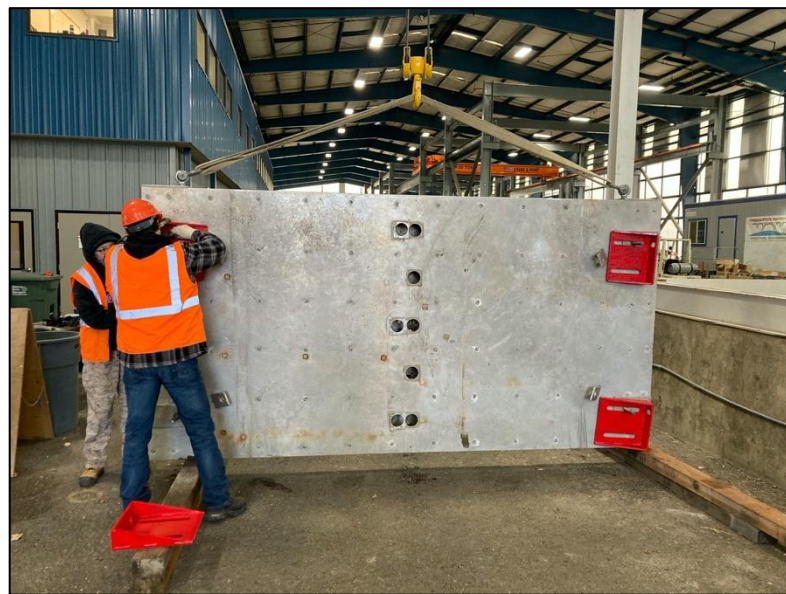


Figure 9-12 Lower section of the wall lifted using the Large Wave Flume crane, cargo straps and eye bolts attached to the ends of the test wall and red clips being placed at each corner of the wall section.



Figure 9-13 Lower section of the wall lifted using the Large Wave Flume crane, cargo straps and eye bolts attached to the ends of the test wall.

Appendix C Instrument Coordinates

Table 9-6 Coordinates for wave gauges (WG) and ultrasonic wave gauges (USWG) placed in the Large Wave Flume.

Sensor	x (m)	y (m)	z (m)
WG 1	13.98	-1.38	-
WG 2	25.36	-1.33	-
WG 3	28.68	-1.31	-
WG 4	29.60	-1.33	-
WG 5	30.52	-1.32	-
WG 6	31.44	-1.32	-
WG 7	32.04	-1.31	-
WG 8	54.60	-1.33	-
WG 9	55.81	-1.32	-
WG 10	56.42	-1.32	-
WG 11	57.33	-1.33	-
WG 12	57.95	-1.33	-
WG 13	65.17	-1.36	-
USWG 1	29.17	-1.27	-
USWG 2	39.76	0.00	-
USWG 3	43.42	0.00	-
USWG 4	50.73	0.00	-
USWG 5	55.37	-1.37	-
USWG 6	59.77	-1.52	-

Table 9-7 Coordinates for PDCR 1830 pressure gauges (PD18) used in model forest.

Sensor	x (m)	y (m)	z (m)
PD18 - 1	35.89	-1.53	1.24
PD18 - 2	39.55	-1.53	1.24
PD18 - 3	43.10	-1.54	1.22
PD18 - 4	46.87	-1.53	1.23
PD18 - 5	50.52	-1.52	1.23
PD18 - 6	54.19	-1.51	1.23

Table 9-8 Coordinates for USNA pressure gauges (USNA P) used in model forest.

Sensor	x (m)	y (m)	z (m)
USNA P1	32.24	-1.40	1.25
USNA P2	43.10	-1.54	1.22
USNA P3	57.83	-1.41	1.38

Table 9-9 Coordinates for the Acoustic Doppler Velocimeters (ADV) used in model forest for Layout 1.

Sensor	x (m)	y (m)	z (m)
ADV 1	32.24	-1.40	1.52
ADV 2	43.09	-1.43	1.40
ADV 3	43.09	-1.43	1.55
ADV 4	43.09	-1.43	1.72
ADV 5	43.09	-1.43	1.86
ADV 6	57.83	-1.41	1.52

Table 9-10 Coordinates for the Acoustic Doppler Velocimeters (ADV) used in model forest for Layouts 2 - 6.

Sensor	x (m)	y (m)	z (m)
ADV 1	32.24	-1.40	1.25
ADV 2	43.09	-1.43	1.40
ADV 3	43.09	-1.43	1.55
ADV 4	43.09	-1.43	1.72
ADV 5	43.09	-1.43	1.86
ADV 6	57.83	-1.41	1.38

Table 9-11 Coordinates for PDCR 1830 pressure gauges (PD18) and PDCR 830 pressure gauges' (PD8) used for the test wall.

Sensor	x (m)	y (m)	z (m)
PD18 - 7	61.20	0.02	1.09
PD18 - 8	61.21	0.02	1.24
PD18 - 9	61.21	0.02	1.43
PD8 - 1	61.22	0.02	1.58
PD8 - 2	61.22	0.01	1.77
PD8 - 3	61.21	0.01	1.92
PD8 - 4	61.21	0.01	2.11
PD8 - 5	61.21	0.01	2.26
PD8 - 6	61.21	0.01	2.44
PD8 - 7	61.21	0.01	2.59
PD8 - 8	61.21	0.02	2.85
PD8 - 9	61.22	0.01	3.00
PD8 - 10	61.22	0.01	3.20
PD8 - 11	61.22	0.01	3.41
PD8 - 12	61.22	0.01	3.61

Table 9-12 Coordinates for Kistler pressure gauges (KP) and Kistler accelerometers (ACC) used for the test wall.

Sensor	x (m)	y (m)	z (m)
KP - 1	61.21	0.11	2.44
KP - 2	61.22	0.11	2.66
KP - 3	61.22	0.12	2.85
KP - 4	61.22	0.12	3.00
KP - 5	61.22	0.11	3.31
KP - 6	61.22	0.11	3.51
ACC 1	61.23	0.01	4.53
ACC 2	61.23	0.01	4.53
ACC 3	61.23	0.01	4.53

Appendix D Selection of Water Levels

Table 9-13 Table of projected area per unit height, A, versus water depth at vegetation, h_v , for the idealized model forest cross section in the Large Wave Flume.

h_v (m)	A (m)
0.05	1.13
0.15	1.15
0.25	1.23
0.35	1.33
0.45	1.46
0.55	1.57
0.65	1.74
0.75	1.47
0.85	1.48
0.95	1.30
1.05	1.31
1.15	1.31
1.25	1.12
1.35	0.80
1.45	0.46
1.55	0.30
1.65	0.30
1.75	0.30
1.85	0.30
1.95	0.30
2.05	0.30

Appendix E Regular Waves

Table 9-14 Table of target regular wave cases at the piston wavemaker.

Trial	Layouts	Number of Waves	<i>h</i>	<i>H</i>	<i>T</i>	<i>L</i>	<i>h/L</i>	<i>H/h</i>	<i>L_{veg}/L</i>	<i>L/W</i>
(-)	(-)	(-)	(m)	(m)	(m)	(m)	(-)	(-)	(-)	(-)
TR-h1-1	1 - 6	20	2.70	0.35	2.51	9.3	0.289	0.130	1.9	2.5
TR-h1-2	1 - 6	20	2.70	0.33	4.10	18.8	0.143	0.122	1.0	5.1
TR-h1-3	1 - 6	20	2.70	0.69	2.50	9.3	0.291	0.256	1.9	2.5
TR-h1-4	1 - 6	20	2.70	0.62	7.65	38.1	0.071	0.230	0.5	10.4
TR-h1-5	1	20	2.70	1.25	4.20	19.4	0.139	0.463	0.9	5.3
TR-h1-6	1	20	2.70	1.20	7.70	38.4	0.070	0.444	0.5	10.5
TR-h2-1	2 - 6	20	2.33	0.28	2.25	7.6	0.307	0.118	2.4	2.1
TR-h2-2	2 - 6	20	2.33	0.26	3.65	15.4	0.151	0.109	1.2	4.2
TR-h2-3	2 - 6	20	2.33	0.55	2.25	7.6	0.307	0.236	2.4	2.1
TR-h2-4	2 - 6	20	2.33	0.49	6.80	31.4	0.074	0.210	0.6	8.6
TR-h2-5	2 - 6	20	2.33	0.99	3.75	15.9	0.146	0.425	1.1	4.3
TR-h2-6	2 - 6	20	2.33	0.94	6.90	31.9	0.073	0.403	0.6	8.7
TR-h3-1	1 - 6	20	1.88	0.20	1.85	5.2	0.360	0.104	3.4	1.4
TR-h3-2	1 - 6	20	1.88	0.18	3.00	11.1	0.170	0.093	1.6	3.0
TR-h3-3	1 - 6	20	1.88	0.39	1.85	5.2	0.360	0.207	3.4	1.4
TR-h3-4	1 - 6	20	1.88	0.33	5.70	23.5	0.080	0.176	0.8	6.4
TR-h3-5	1 - 6	20	1.88	0.89	4.10	16.3	0.115	0.473	1.1	4.4
TR-h3-6	1 - 6	20	1.88	0.96	5.70	23.5	0.080	0.511	0.8	6.4
TR-h4-1	1 - 6	20	1.58	0.14	1.55	3.7	0.425	0.089	4.8	1.0
TR-h4-2	1 - 6	20	1.58	0.13	2.50	8.2	0.193	0.079	2.2	2.2
TR-h4-3	1 - 6	20	1.58	0.28	1.55	3.7	0.425	0.177	4.8	1.0
TR-h4-4	1 - 6	20	1.58	0.22	4.80	18.0	0.088	0.139	1.0	4.9
TR-h4-5	1 - 6	20	1.58	0.61	3.40	12.2	0.130	0.386	1.5	3.3
TR-h4-6	1 - 6	20	1.58	0.65	4.75	17.8	0.089	0.411	1.0	4.9

Appendix F Random Waves

Table 9-15 Table of target random wave cases at the piston wavemaker.

Trial	Layouts	Number of Waves	<i>h</i>	H_{m0}	T_p	L_p	h/L_p	H_{m0}/h	L_{veg}/L_p	L_p/W
(-)	(-)	(-)	(m)	(m)	(m)	(m)	(-)	(-)	(-)	(-)
TI-h1-1	1 - 6	300	2.70	0.62	7.65	38.1	0.071	0.230	0.5	10.4
TI-h1-2	1 - 6	300	2.70	0.35	2.51	9.3	0.289	0.130	1.9	2.5
TI-h1-3	1	300	2.70	0.63	4.15	19.1	0.141	0.233	0.9	5.2
TI-h2-1	2 - 6	300	2.33	0.49	6.80	31.4	0.074	0.210	0.6	8.6
TI-h2-2	2 - 6	300	2.33	0.28	2.25	7.6	0.307	0.118	2.4	2.1
TI-h2-3	2 - 6	300	2.33	0.49	3.70	15.7	0.149	0.210	1.1	4.3
TI-h3-1	1 - 6	300	1.88	0.33	5.70	23.5	0.080	0.176	0.8	6.4
TI-h3-2	1 - 6	300	1.88	0.20	1.85	5.2	0.360	0.104	3.4	1.4
TI-h3-3	1 - 6	300	1.88	0.34	3.10	11.6	0.163	0.181	1.6	3.2
TI-h4-1	1 - 6	300	1.58	0.22	4.80	18.0	0.088	0.139	1.0	4.9
TI-h4-2	1 - 6	300	1.58	0.14	1.55	3.7	0.425	0.089	4.8	1.0
TI-h4-3	1 - 6	300	1.58	0.25	2.55	8.4	0.188	0.158	2.1	2.3

Appendix G Transient Waves

To calculate the stoke duration for the transient waves, a start and stop time needed to be determined. That point was determined using the parameter delta, Δ which is defined as a percentage of the maximum stoke for the LWF (4.0 m),

$$\Delta = \text{Percentage, \%} * \text{maximum stroke.}$$

The first- and last-time stamp where the piston wavemaker was equal to delta value was then recorded. The stroke duration was taken as the difference between the two time stamps.

Percentages of 0.001%, 0.01%, 0.1%, 0.5%, 1%, 5%, and 10% of the maximum stroke were evaluated and the stroke duration was calculated for each. These durations were then compared to Goring and Keck, (1979) equations for solitary wave period.

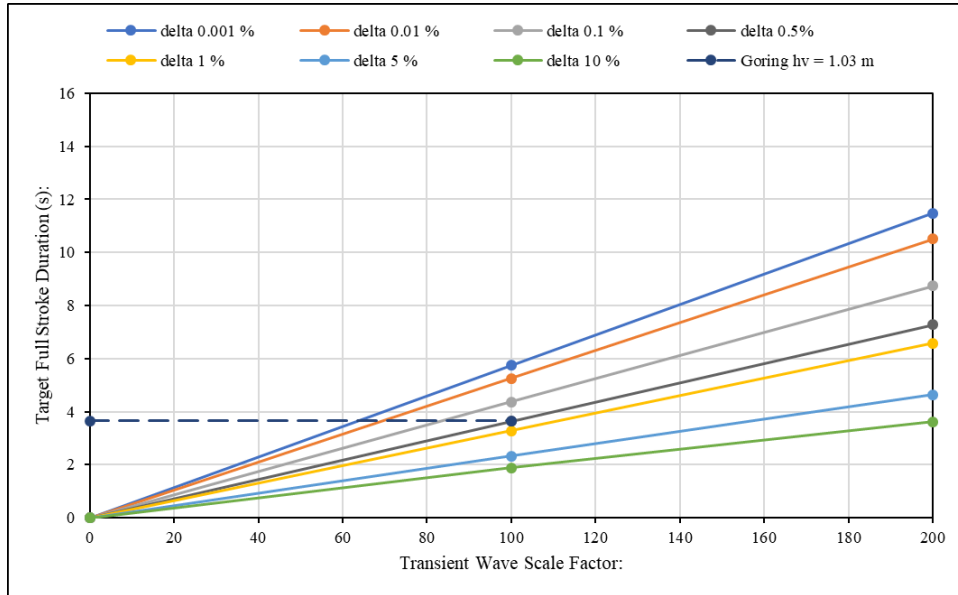


Figure 9-14 Plot of transient wave cases stroke duration versus Goring and Keck, (1979) estimation of solitary wave period.

For Figure 9-14, it shows the target full stroke duration on the y-axis and the Transient wave scale factor on the x-axis. Additionally, the figure also shows the calculated stroke duration for the deltas: 0.001% (intermediate blue line and markers), 0.01% (orange line and markers), 0.1% (light gray line and markers), 0.5% (dark gray line and markers), 1% (yellow line and markers), 5% (light blue line and markers), and 10% (green line and markers) respectively. Goring and Keck, (1979) estimation of wave period for a solitary wave is also shown for $h_v = 1.03$ m (dark blue dashed line and markers). In Figure 9-14, it can be seen that for a scale factor of 100, the Goring and Keck, (1979) estimation of wave period corresponds the closest with the estimation of 0.5% delta. Based on this similarity, the 0.5% delta was used to further calculate the full stroke duration for the rest of the scale factors reported in Table 4-3.

Goring and Keck, (1979) Equations:

$$S = \sqrt{\frac{16Hh}{3}} \quad (27)$$

$$k = \sqrt{\frac{3H}{4h^3}} \quad (28)$$

$$C = \sqrt{g(h + H)} \quad (29)$$

$$T = \frac{2}{kC} * \left(3.8 + \frac{H}{h} \right) \quad (30)$$

T = solitary wave period (s)

C = wave celerity (m/s)

*k = wave number (rad * m⁻¹)*

S = maximum stroke (m)

H = solitary wave height (m)

h = water depth (m)

Table 9-16 Stroke durations of transient waves for different delta percent values and scale factors.

Transient Wave Scale :	Target Full Stroke Duration (s):						
	delta 0.001 %	delta 0.01 %	delta 0.1 %	delta 0.5%	delta 1 %	delta 5 %	delta 10 %
0	0	0	0	0	0	0	0
100	5.74	5.25	4.36	3.64	3.28	2.32	1.88
200	11.48	10.51	8.73	7.28	6.57	4.64	3.62
300	17.22	15.76	13.1	10.92	9.86	6.97	5.43
400	22.96	21.03	17.47	14.56	13.15	9.29	7.24
500	28.7	26.29	21.84	18.21	16.44	11.63	9.05
600	34.45	31.54	26.21	21.85	19.73	13.95	10.87
700	40.19	36.81	30.58	25.49	23.02	16.27	12.68

Appendix H LiDAR Scans

The BL layout was partially LiDAR scanned on December 18th, 2020, using the overhead Unistrut mount (Figure 4-8). A total of 6 scans were taken from bays 8 – 13 (Figure 9-15). Scanning of the BL layout was later completed on January 14th, 2021, where the LWF was fully scanned with test wall in place for a total of 22 scans taken (Figure 9-16).

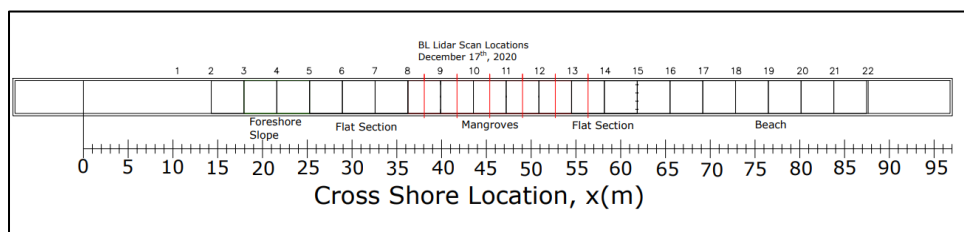


Figure 9-15 Baseline (BL) layout scans taken December 17th, 2020.

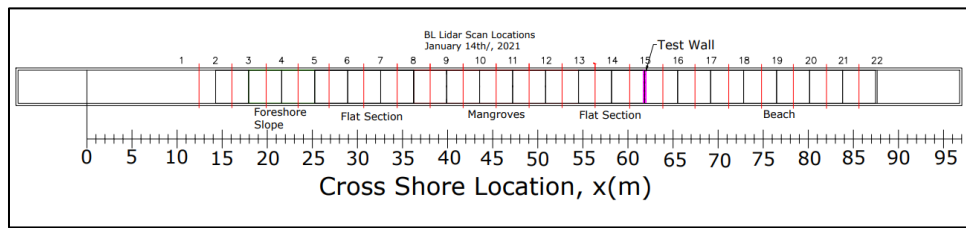


Figure 9-16 Baseline (BL) layout scans taken January 14th, 2021.

Appendix I LiDAR Analysis

Appendix I.1 High-density LiDAR Cross Sections

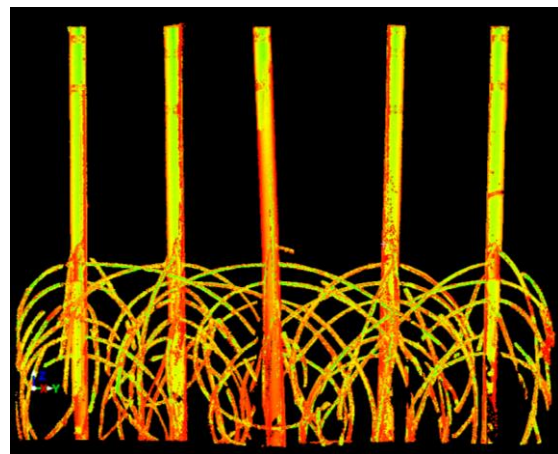


Figure 9-17 Cleaned high-density (HD) LiDAR cross section stencil 1, Bay 10 to 11.

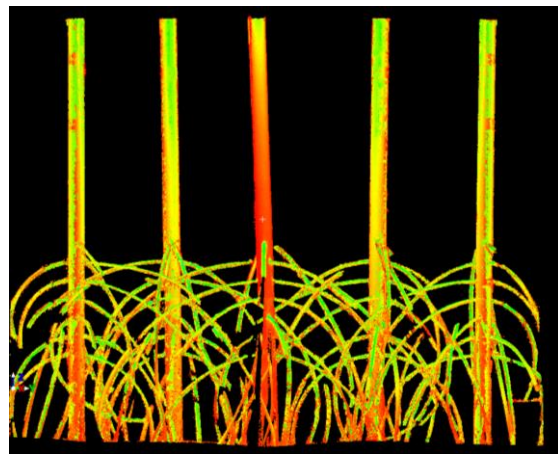


Figure 9-18 Cleaned high-density (HD) LiDAR cross section stencil 2, Bay 10 to 11.

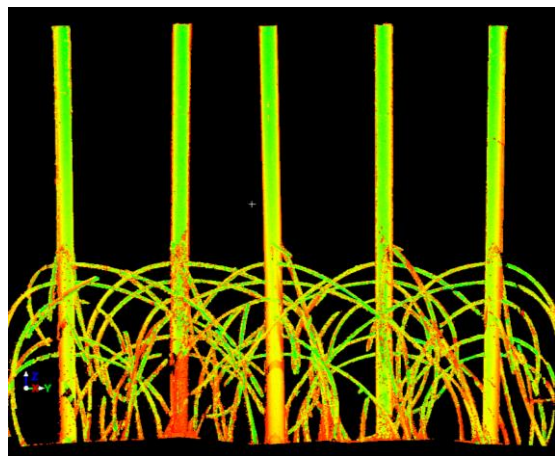


Figure 9-19 Cleaned high-density (HD) LiDAR cross section stencil 3, Bay 11 to 12.

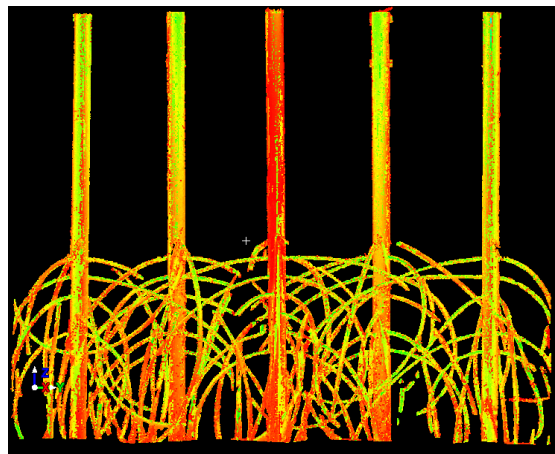


Figure 9-20 Cleaned high-density (HD) LiDAR cross section stencil 4, Bay 11 to 12.

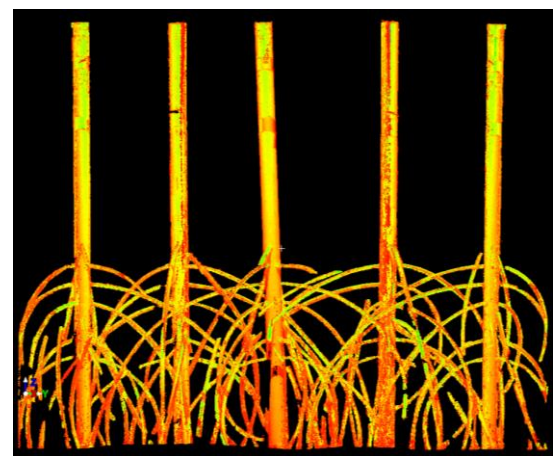


Figure 9-21 Cleaned high-density (HD) LiDAR cross section stencil 5, Bay 12 to 13.

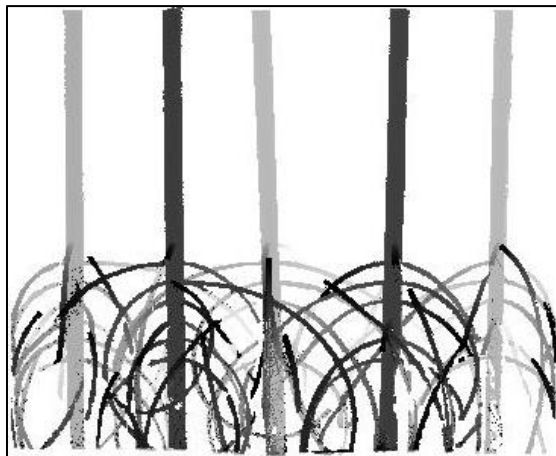
Appendix I.2 High-density Cross Section Images

Figure 9-22 High-density (HD) stencil 1 cross section image, Bay 10 to 11.



Figure 9-23 High-density (HD) stencil 2 cross section image, Bay 10 to 11.



Figure 9-24 High-density (HD) stencil 3 cross section image, Bay 11 to 12.

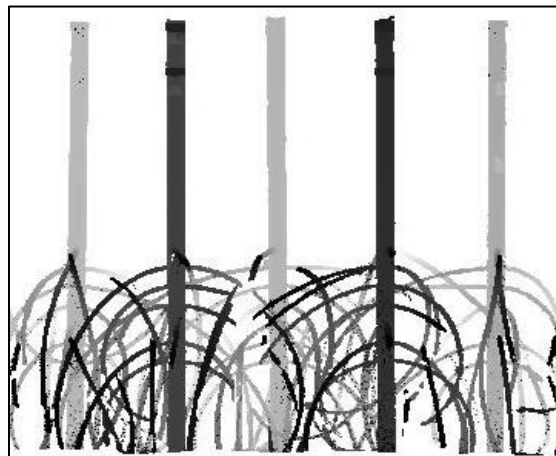


Figure 9-25 High-density (HD) stencil 4 cross section image, Bay 11 to 12.

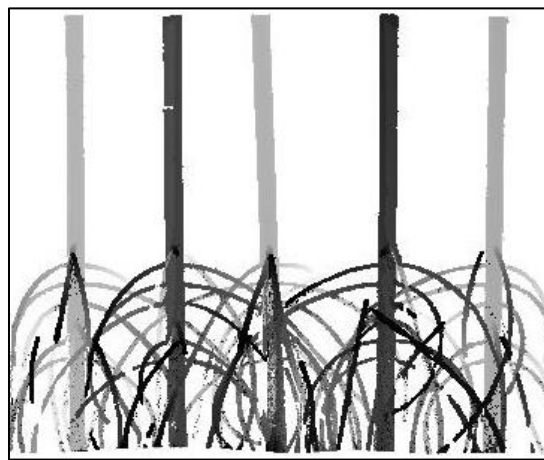


Figure 9-26 High-density (HD) stencil 5 cross section image, Bay 12 to 13

Appendix I.3 HD Manual Measurement Check

For HD stencil one, 20 measurements of the trunk diameter and 40 measurements of the root diameter (green lines and numbers) were taken for each tree in the cross section (Figure 9-27). The measurements were averaged for each tree and a standard deviation was calculated. The average tree measurements were then compared to the known values for the trunk diameter (0.1143 m) and root diameter (0.0286 m) in a percent difference calculation. The percent differences were then averaged for the entire cross section (Table 9-17).

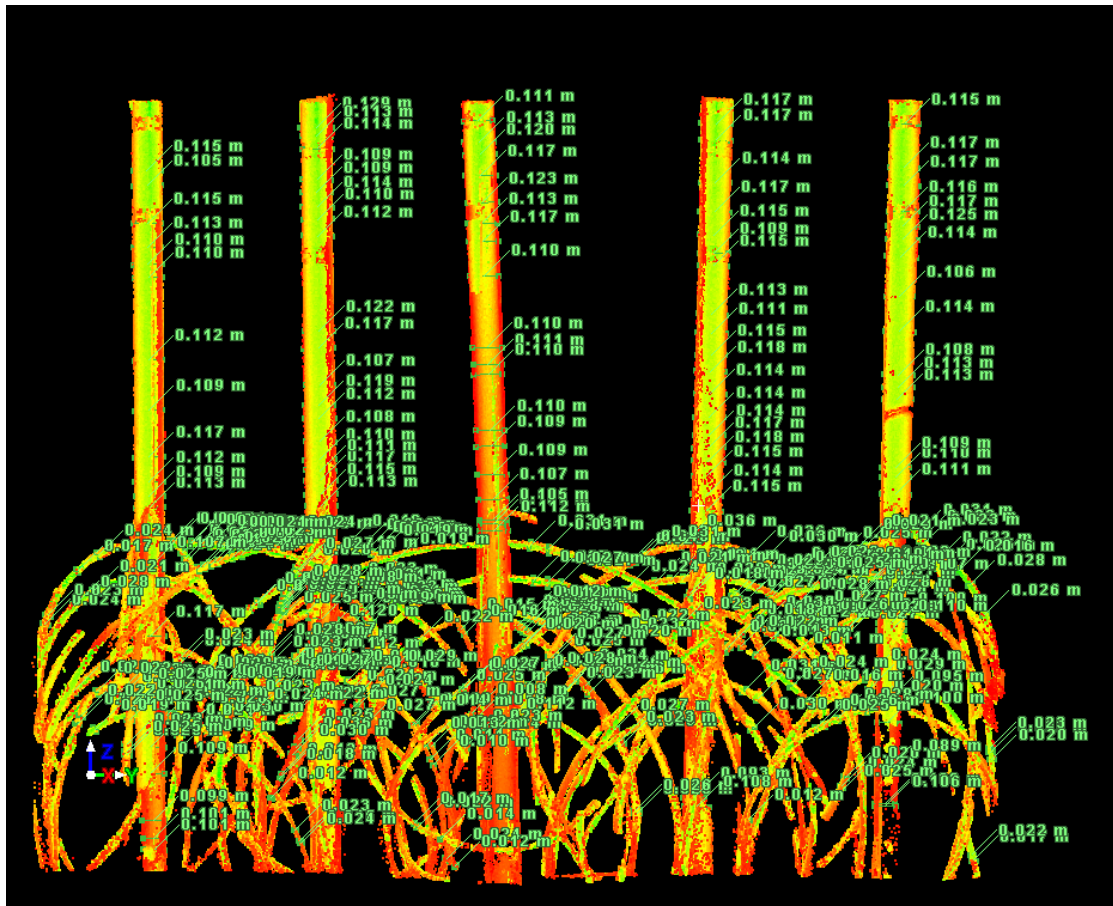


Figure 9-27 Cleaned high-density (HD) stencil 1 at bay 10 to 11 with manual measurements (green lines and numbers).

Table 9-17 Measured average, standard deviation, and absolute percent error of trunk and root diameters from known values for high-density (HD) stencil 1 LiDAR cross section.

Measurement	Trunk diameter	Root diameter
(-)	(m)	(m)
Measured Average:	0.1117	0.0257
Measured Stdv:	0.004	0.005
% Difference:	-2%	-10%

The analysis revealed that LiDAR scans underpredicted the diameters of both the trunk and roots but were consistent across the entire cross section (low standard deviation - 0.004 and 0.005). LiDAR measurements were found to underpredict the known values of $D_{BH} = 0.1143$ m and $D_{Root} = 0.0286$ m by 2% and 10%, respectively.

Appendix I.4 HD Rotation Comparison

The rotation comparison for HD stencil one was completed by rotating the cross section 180° around the z axis in CloudComaparev2. The rasterize tool was applied to the cross section and the corresponding pixilated image was exported. The projected area per unit height, A , was calculated for the 180° rotation and compared to the original HD stencil one (Figure 9-28).

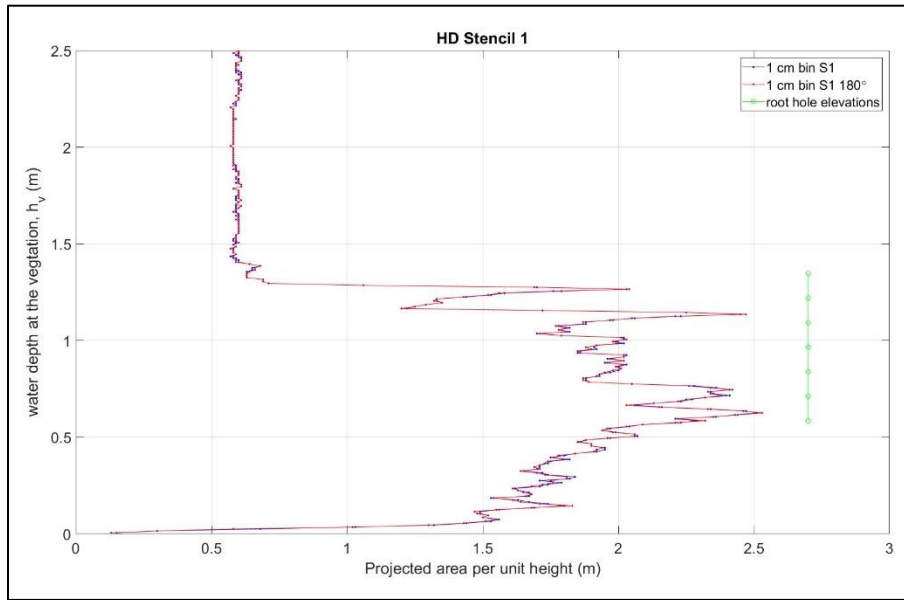


Figure 9-28 Projected area per unit height, A , versus water depth at the vegetation, h_v , for the high-density (HD) stencil 1 (blue line and markers) and the 180° rotated high-density (HD) stencil 1 (red line and markers).

Figure 9-28 shows the projected area per unit height, A , on the x -axis and the water depth at the vegetation, h_v on the y -axis. In the figure, the projected area per unit height, A , for HD stencil one is represented with a blue line and markers and the 180° rotated HD stencil one is represented by a red line and makers. Overall, the figure shows little difference between the profiles of the two cross sections projected areas where the variance between the two found to be $5.62 \times 10^{-6} \text{ m}^2$. The small variance value indicates the analysis method is not affected by the direction (landward or seaward) the cross section is analyzed.

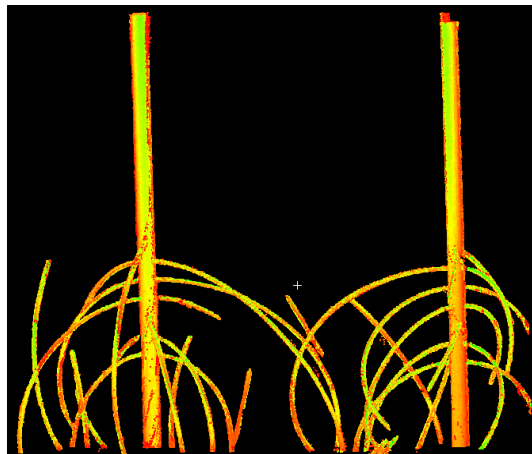
Appendix I.5 Low Density LiDAR Cross Sections

Figure 9-29 Cleaned low-density (LD) LiDAR cross section stencil 1, Bay 8 to 9.

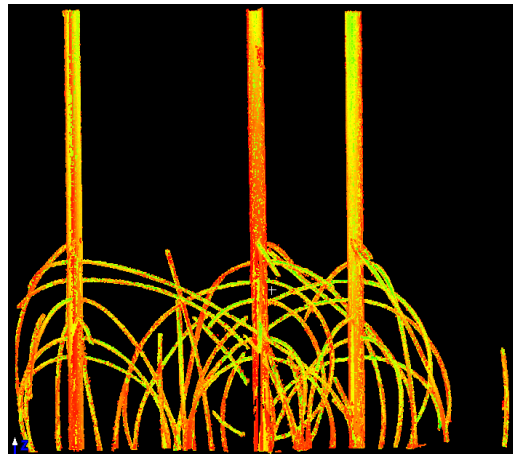


Figure 9-30 Cleaned low-density (LD) LiDAR cross section stencil 2, Bay 8 to 9.

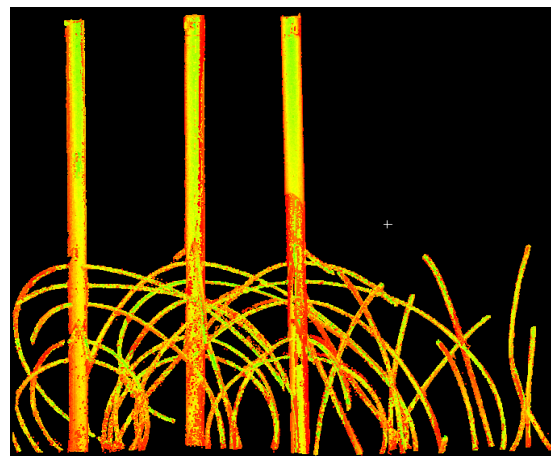


Figure 9-31 Cleaned low-density (LD) LiDAR cross section stencil 3, Bay 9 to 10.

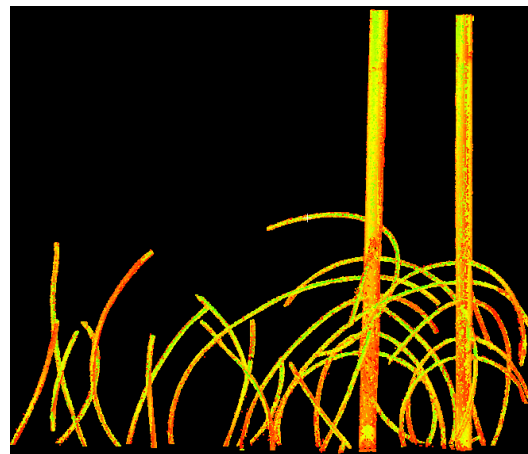


Figure 9-32 Cleaned low-density (LD) LiDAR cross section stencil 4, Bay 9 to 10.

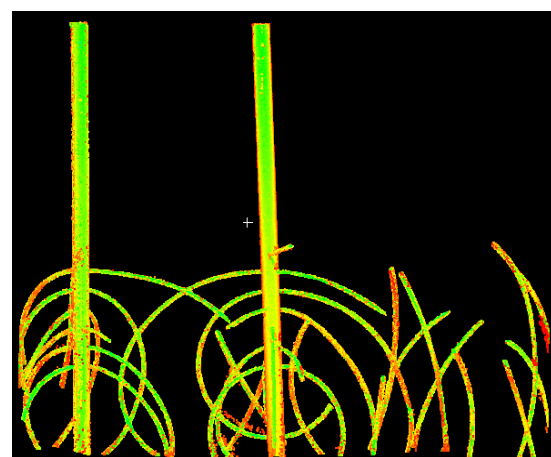


Figure 9-33 Cleaned low-density (LD) LiDAR cross section stencil 5, Bay 10 to 11.

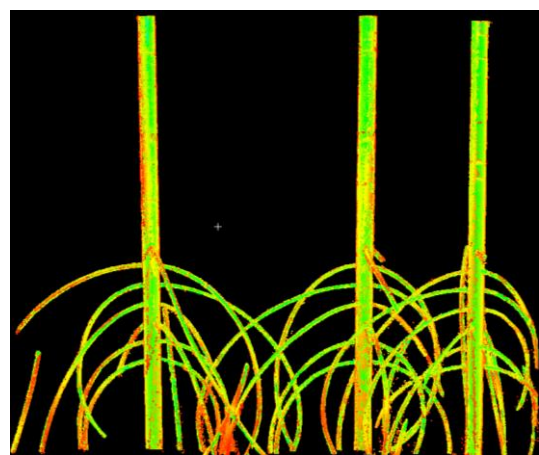


Figure 9-34 Cleaned low-density (LD) LiDAR cross section stencil 6, Bay 10 to 11.

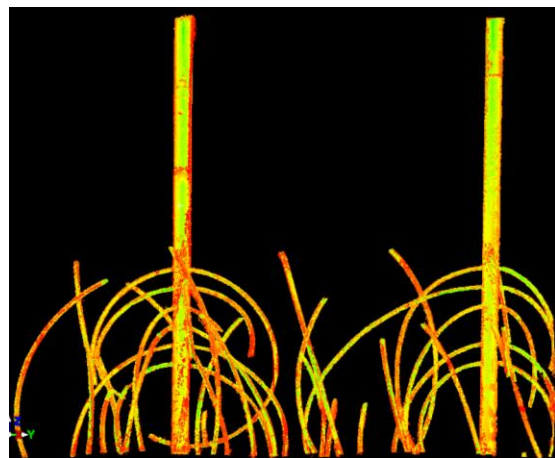


Figure 9-35 Cleaned low-density (LD) LiDAR cross section stencil 7, Bay 11 to 12.

Appendix I.6 LD Cross Section Images

Figure 9-36 Low-density (LD) stencil 1 cross section image, Bay 8 to 9.

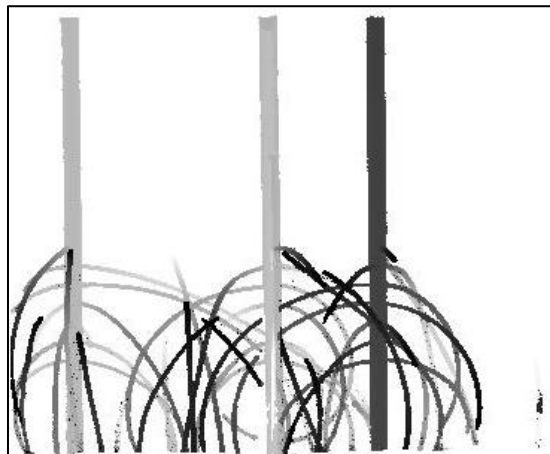


Figure 9-37 Low-density (LD) stencil 2 cross section image, Bay 8 to 9.

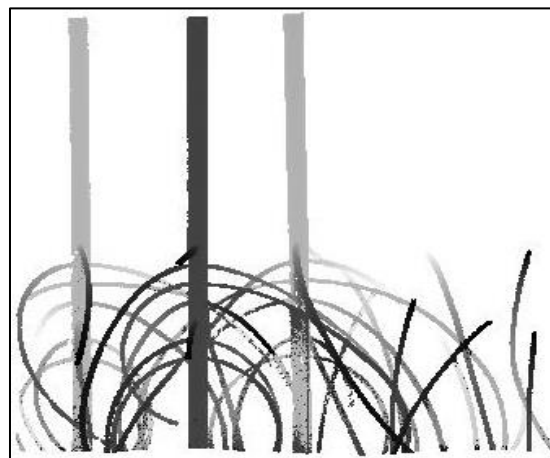


Figure 9-38 Low-density (LD) stencil 3 cross section image, Bay 9 to 10.



Figure 9-39 Low-density (LD) stencil 4 cross section image, Bay 9 to 10.

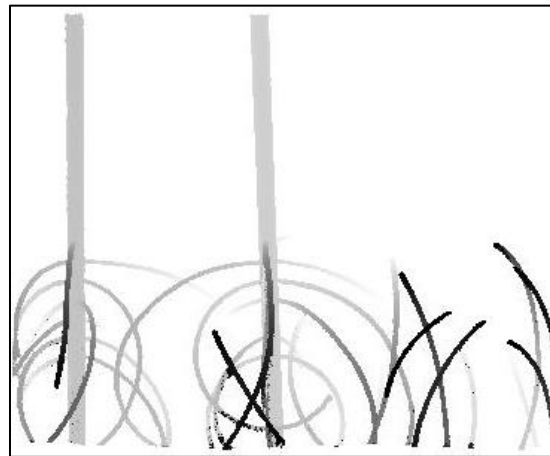


Figure 9-40 Low-density (LD) stencil 5 cross section image, Bay 10 to 11.

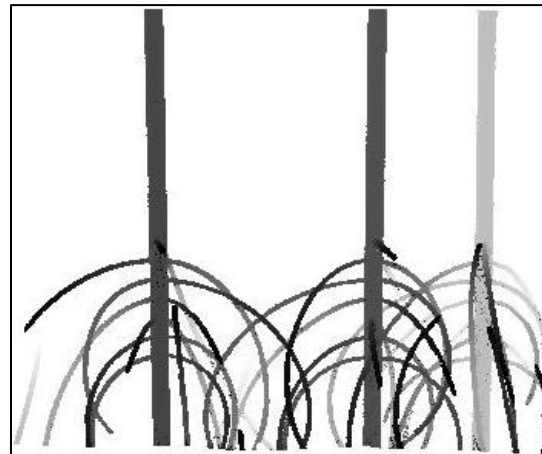


Figure 9-41 Low-density (LD) stencil 6 cross section image, Bay 10 to 11.

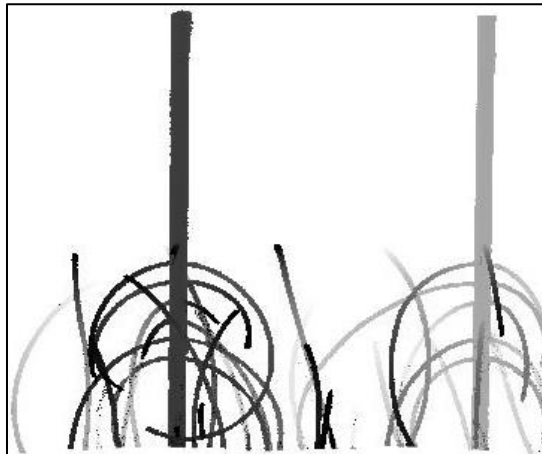


Figure 9-42 Low-density (LD) stencil 7 cross section image, Bay 11 to 12.

Appendix I.7 Effective Diameter Comparison

To calculate number of roots for every 10 cm bin, the known diameter of the trunk, $D_{BH} = 0.1143$ m was subtracted from the projected area per unit height per tree, A_t , value at each bin. The resultant was then divided by the known diameter of the roots, $D_{Root} = 0.00286$ m (Equation 27).

$$n_R = \frac{A - D_{BH}}{D_{root}} \quad (27)$$

The n_R values were then plotted as a function of the water depth at the vegetation, h_v (Figure 9-43). In Figure 9-43, the y-axis displays the water depth at the vegetation, h_v whereas the x-axis

displays the number of roots per tree, n_R . Additionally, the blue line and markers represent the number of roots at each 10 cm bin and the green line and markers show the vertical location of the root hole elevations for the constructed models. The horizontal blue lines represent the n_R values $\pm \sigma_R$ and the horizontal dashed blue lines show the water levels tested for the study and the black vertical lines show the mean number of roots per tree, n_{Rm} for each water level. The n_{Rm} , σ_{Rm} , and $n_{Rm} \pm \sigma_{Rm}$ values for each water level are shown in Table 9-18. The absolute percent difference of the n_{Rm} values from the visual method are shown for each water level along with the overall average absolute percent difference between the two methods.

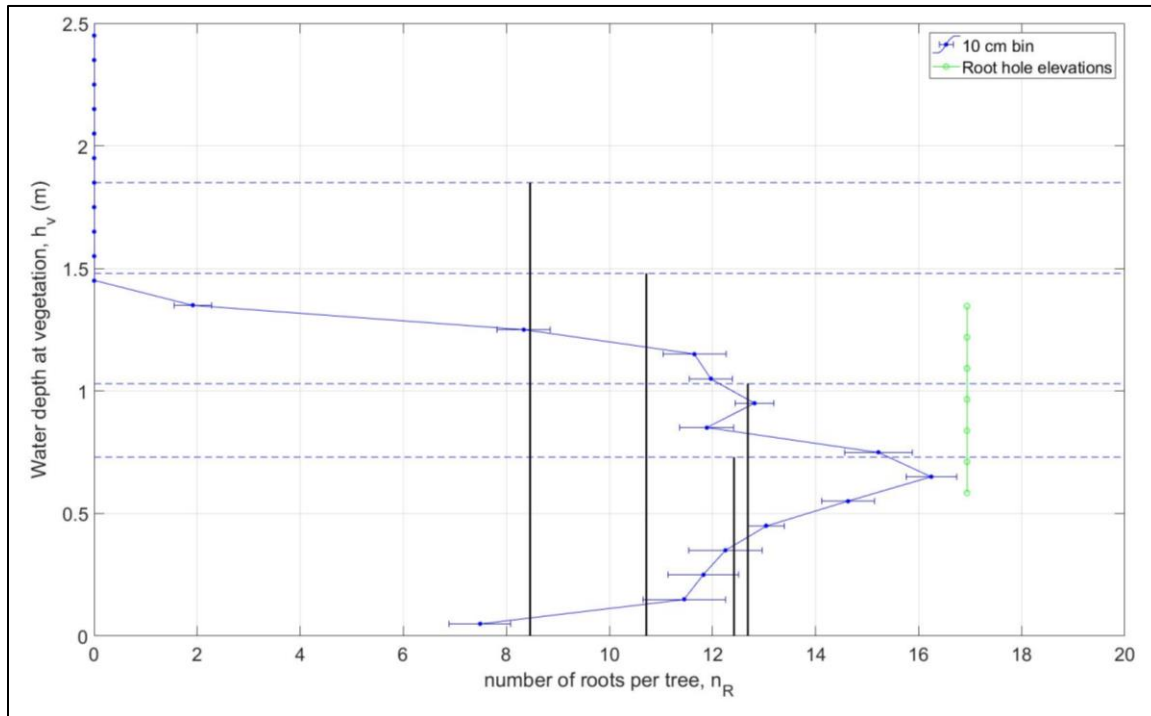


Figure 9-43 Number of roots per tree, n_R , versus the water depth at the vegetation, h_v , for the MATLAB analysis method.

Table 9-18 Mean number of roots, n_{Rm} , mean standard deviation σ_{Rm} , $n_{Rm} \pm \sigma_{Rm}$, and the absolute percent difference from the visual results n_{Rm} values for each water depth at vegetation, h_v tested.

h_v (m)	n_{Rm} (-)	σ_{Rm} (-)	$n_{Rm} - \sigma_{Rm}$ (-)	$n_{Rm} + \sigma_{Rm}$ (-)	Abs Percent Difference (%)
	(m)	(-)	(-)	(-)	
1.85	8	0.4	8	9	6
1.48	11	0.5	10	11	12
1.03	13	0.6	12	13	3
0.73	12	0.6	12	13	5
Average abs % Difference					7

Appendix J Experimental results – Random Waves

Appendix J.1 Time Domain versus Frequency Domain Analysis

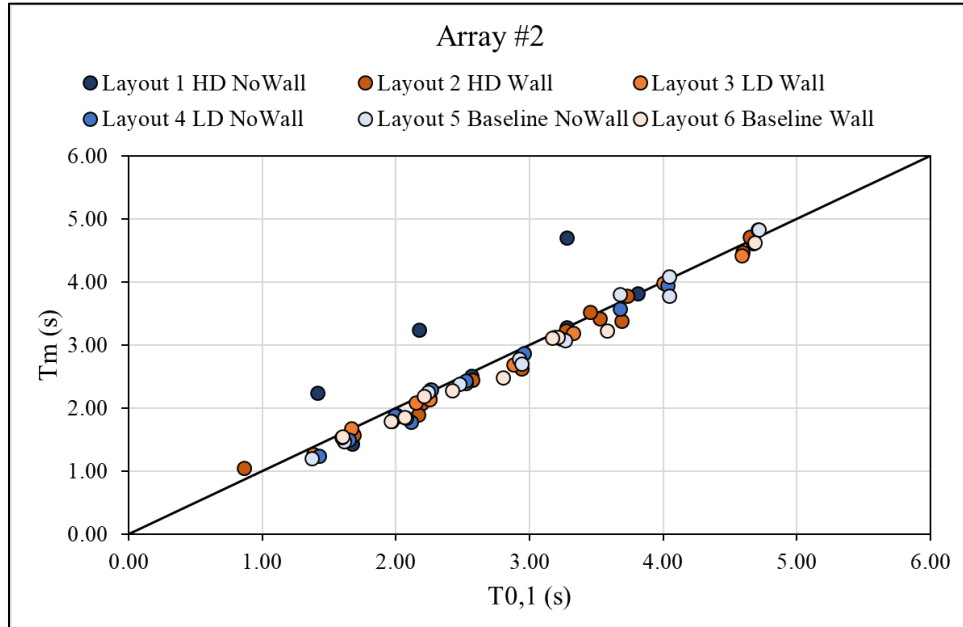


Figure 9-44 Mean wave period, T_m , from the time domain versus the mean wave period, $T_{0,1}$, from the frequency domain of array 2 for layouts 1 – 6.

Appendix J.2 Wave Attenuation

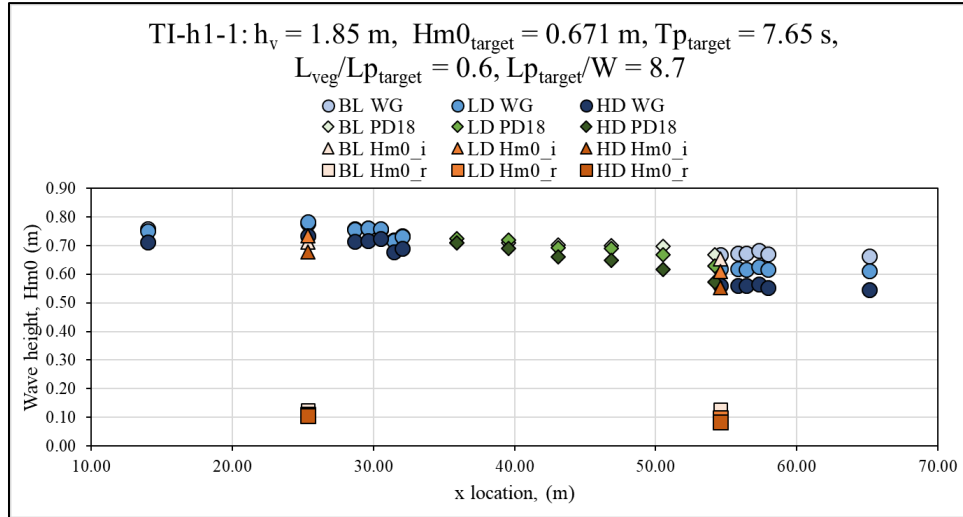


Figure 9-45 Total spectral estimate of the significant wave height, H_{m0} , with respect to x location for wave gauges (WG, circles) and pressure gauges (PD, diamonds) and the incident wave height, $H_{m0,i}$ (triangles), and reflected wave height, $H_{m0,r}$ (squares), for high-density (HD) (dark colors), low-density (LD) (intermediate colors), and baseline (BL) (light colors) layouts for random wave case TI-h1-1.

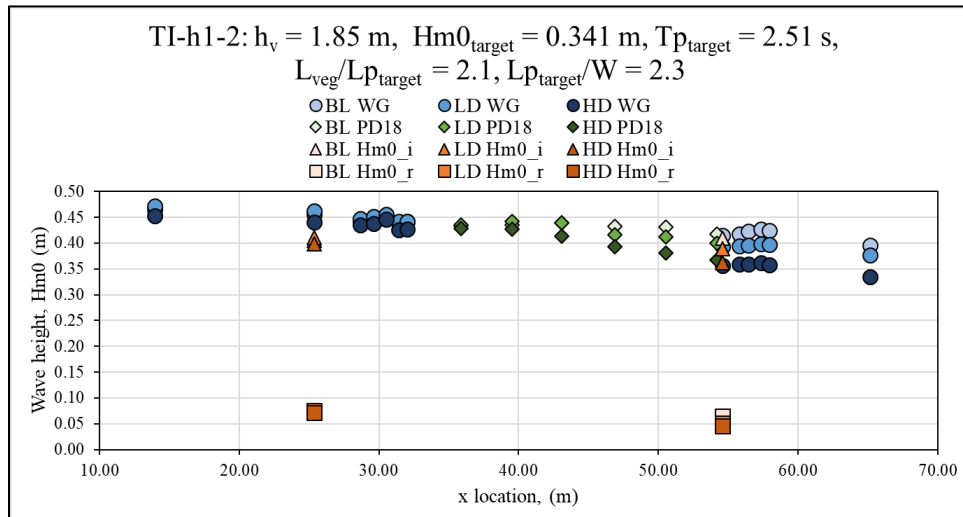


Figure 9-46 Total spectral estimate of the significant wave height, H_{m0} , with respect to x location for wave gauges (WG, circles) and pressure gauges (PD, diamonds) and the incident wave height, $H_{m0,i}$ (triangles), and reflected wave height, $H_{m0,r}$ (squares), for high-density (HD) (dark colors), low-density (LD) (intermediate colors), and baseline (BL) (light colors) layouts for random wave case TI-h1-2.

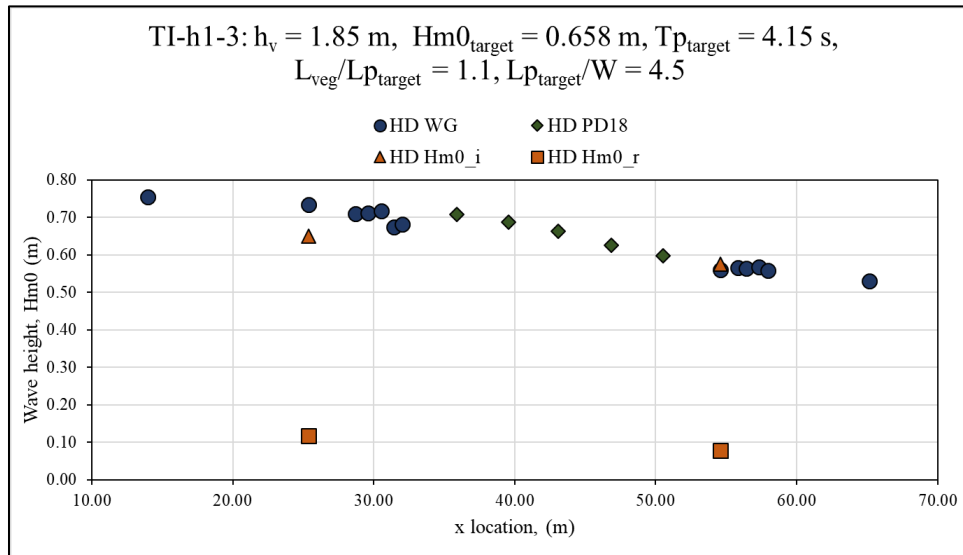


Figure 9-47 Total spectral estimate of the significant wave height, H_{m0} , with respect to x location for wave gauges (WG, circles) and pressure gauges (PD, diamonds) and the incident wave height, $H_{m0,i}$ (triangles), and reflected wave height, $H_{m0,r}$ (squares), for high-density (HD) (dark colors) layout for random wave case TI-h1-3.

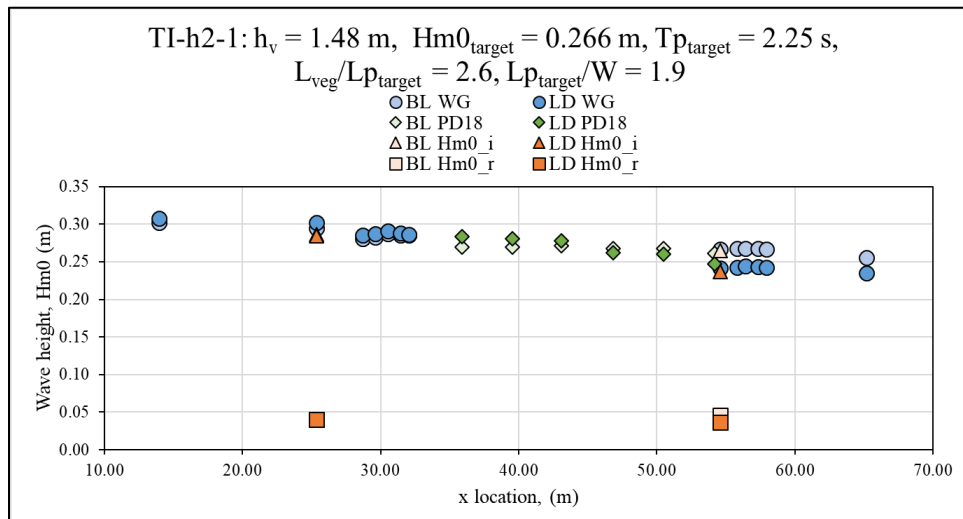


Figure 9-48 Total spectral estimate of the significant wave height, H_{m0} , with respect to x location for wave gauges (WG, circles) and pressure gauges (PD, diamonds) and the incident wave height, $H_{m0,i}$ (triangles), and reflected wave height, $H_{m0,r}$ (squares), for low-density (LD) (intermediate colors) and baseline (BL) (light colors) layouts for random wave case TI-h2-1.

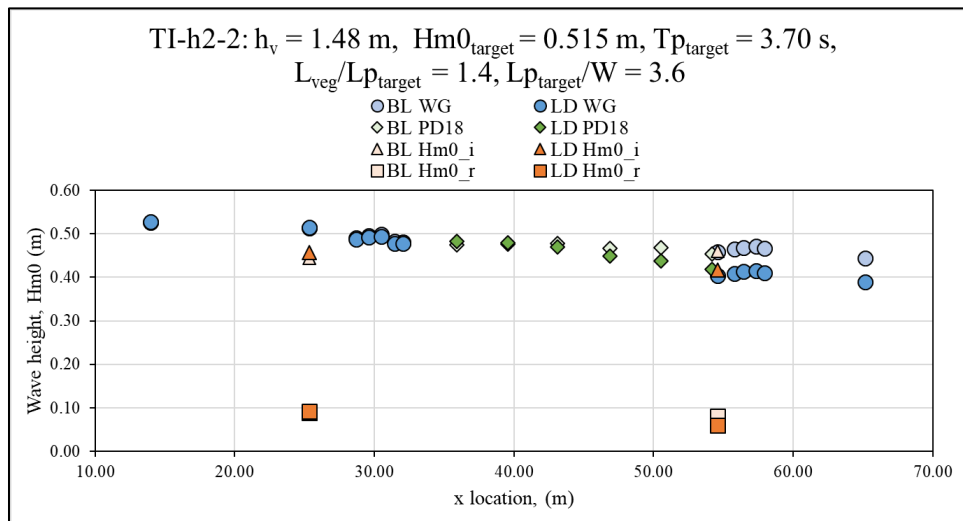


Figure 9-49 Total spectral estimate of the significant wave height, H_{m0} , with respect to x location for wave gauges (WG, circles) and pressure gauges (PD, diamonds) and the incident wave height, $H_{m0,i}$ (triangles), and reflected wave height, $H_{m0,r}$ (squares), for low-density (LD) (intermediate colors) and baseline (BL) (light colors) layouts for random wave case TI-h2-2.

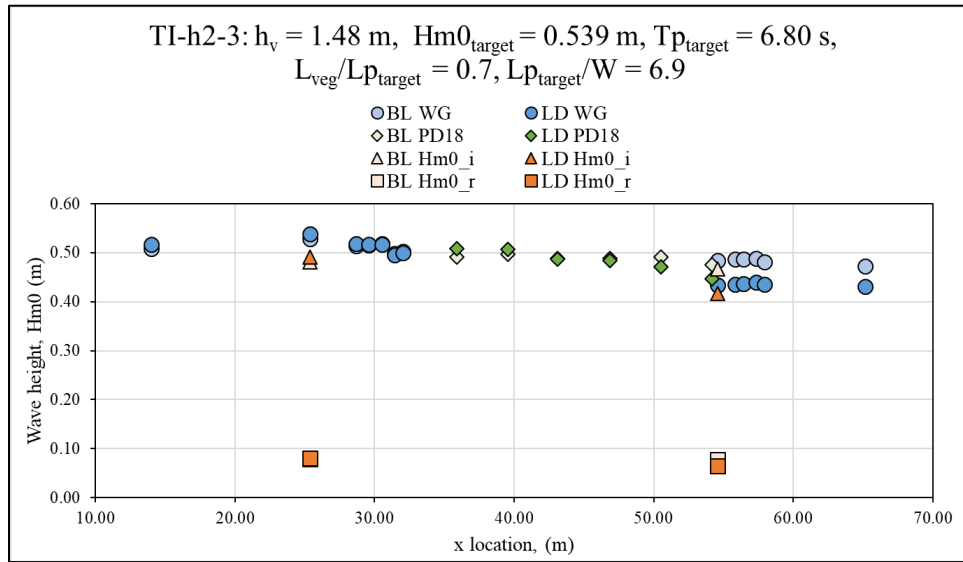


Figure 9-50 Total spectral estimate of the significant wave height, H_{m0} , with respect to x location for wave gauges (WG, circles) and pressure gauges (PD – diamonds) and the incident wave height, $H_{m0,i}$ (triangles), and reflected wave height, $H_{m0,r}$ (squares), for low-density (LD) (intermediate colors) and baseline (BL) (light colors) layouts for random wave case TI-h2-3.

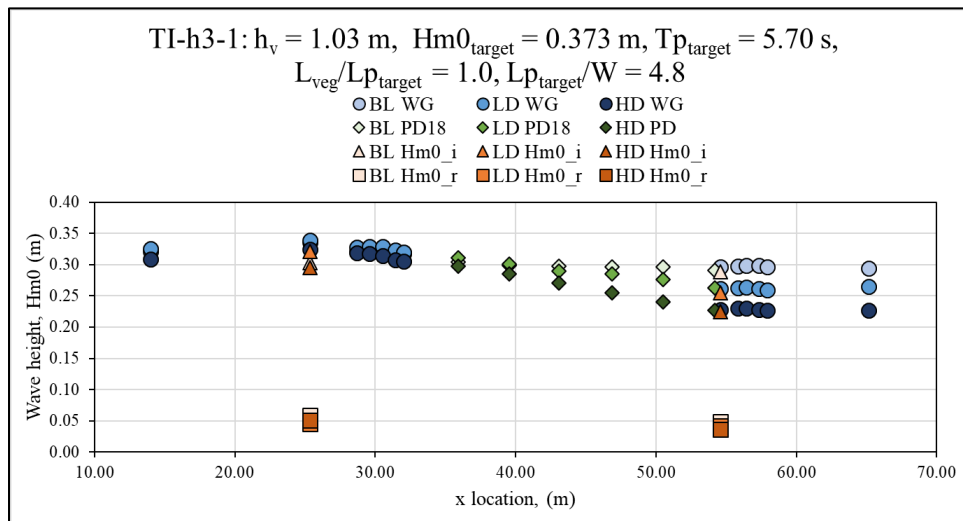


Figure 9-51 Total spectral estimate of the significant wave height, H_{m0} , with respect to x location for wave gauges (WG, circles) and pressure gauges (PD, diamonds) and the incident wave height, $H_{m0,i}$ (triangles), and reflected wave height, $H_{m0,r}$ (squares), for high-density (HD) (dark colors), low-density (LD) (intermediate colors), and baseline (BL) (light colors) layouts for random wave case TI-h3-1.

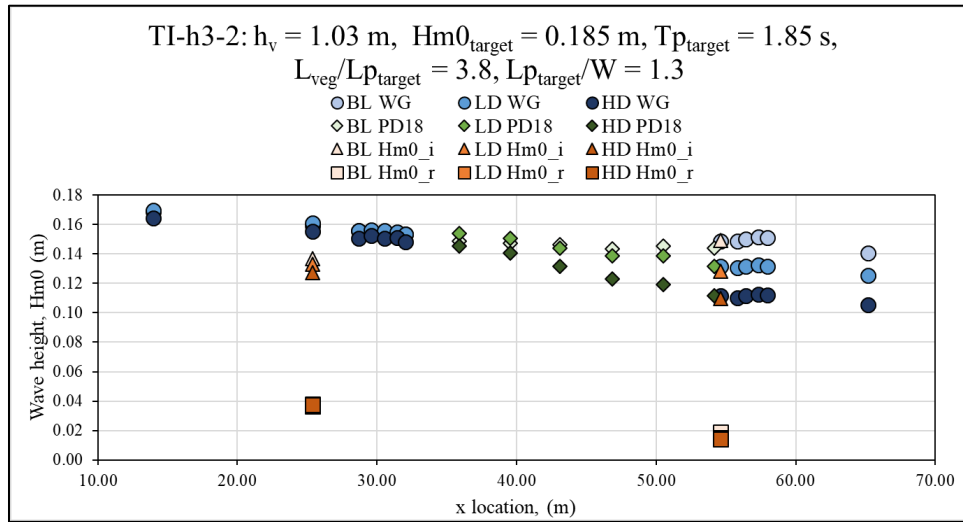


Figure 9-52 Total spectral estimate of the significant wave height, H_{m0} , with respect to x location for wave gauges (WG, circles) and pressure gauges (PD, diamonds) and the incident wave height, $H_{m0,i}$ (triangles), and reflected wave height, $H_{m0,r}$ (squares), for high density (HD) (dark colors), low-density (LD) (intermediate colors), and baseline (BL) (light colors) layouts for random wave case TI-h3-2.

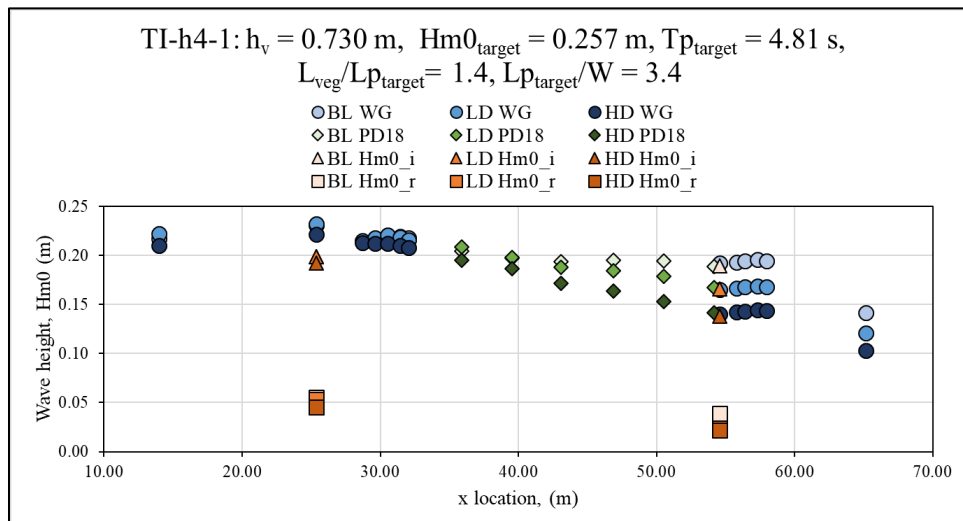


Figure 9-53 Total spectral estimate of the significant wave height, $Hm0$, with respect to x location for wave gauges (WG, circles) and pressure gauges (PD, diamonds) and the incident wave height, $Hm0_i$ (triangles), and reflected wave height, $Hm0_r$ (squares), for high-density (HD) (dark colors), low-density (LD) (intermediate colors), and baseline (BL) (light colors) layouts for random wave case TI-h4-1.

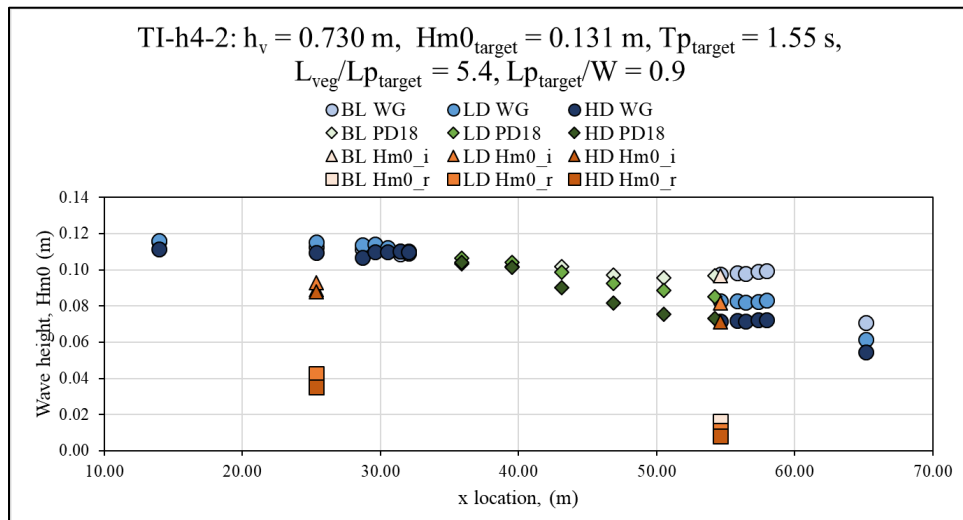


Figure 9-54 Total spectral estimate of the significant wave height, $Hm0$, with respect to x location for wave gauges (WG, circles) and pressure gauges (PD, diamonds) and the incident wave height, $Hm0_i$ (triangles), and reflected wave height, $Hm0_r$ (squares), for high-density (HD) (dark colors), low-density (LD) (intermediate colors), and baseline (BL) (light colors) layouts for random wave case TI-h4-2.

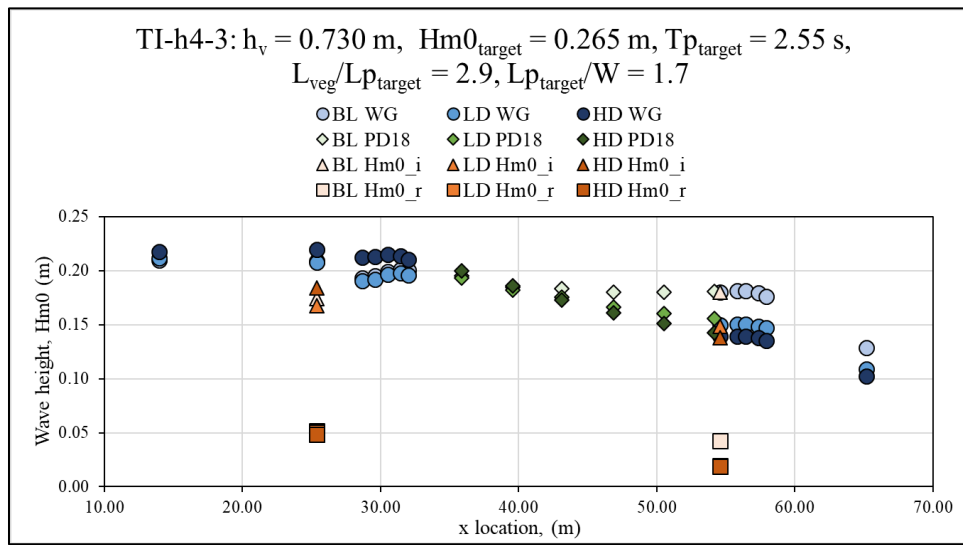


Figure 9-55 Total spectral estimate of the significant wave height, $Hm0$, with respect to x location for wave gauges (WG, circles) and pressure gauges (PD, diamonds) and the incident wave height, $Hm0,i$ (triangles), and reflected wave height, $Hm0,r$ (squares), for high-density (HD) (dark colors), low-density (LD) (intermediate colors), and baseline (BL) (light colors) layouts for random wave case TI-h4-3.

Table 9-19 Table of wave height decay coefficients, $\tilde{\alpha}$, and $\tilde{\alpha} \pm \sigma$, for the random wave cases with the measured H_{m0} and T_p values at PD18-1.

Trial	Layout	h_v	H_{m0} PD18 -1	T_p PD18 -1	$\tilde{\alpha}$	σ	$\tilde{\alpha} - \sigma$	$\tilde{\alpha} + \sigma$
(-)	(-)	(m)	(m)	(s)	(m^{-1})	(m)	(m^{-1})	(m^{-1})
TI-h1-1	HD	1.85	0.71	7.45	1.19E-02	1.99E-03	9.88E-03	1.39E-02
	LD	1.85	0.73	7.45	7.48E-03	1.88E-03	5.60E-03	9.37E-03
	BL	1.85	0.71	7.45	2.85E-03	1.17E-03	1.68E-03	4.03E-03
TI-h1-2	HD	1.85	0.43	2.48	9.74E-03	1.47E-03	8.28E-03	1.12E-02
	LD	1.85	0.43	2.56	5.44E-03	1.94E-03	3.51E-03	7.38E-03
	BL	1.85	0.43	2.56	1.80E-03	1.27E-03	5.30E-04	3.06E-03
TI-h2-1	LD	1.48	0.51	6.30	7.01E-03	1.77E-03	5.24E-03	8.77E-03
	BL	1.48	0.49	6.30	1.37E-03	8.81E-04	4.87E-04	2.25E-03
TI-h2-2	LD	1.48	0.28	2.16	7.85E-03	1.51E-03	6.34E-03	9.35E-03
	BL	1.48	0.27	2.16	1.52E-03	1.26E-03	2.67E-04	2.78E-03
TI-h2-3	LD	1.48	0.48	3.72	8.49E-03	1.59E-03	6.89E-03	1.01E-02
	BL	1.48	0.47	3.72	2.07E-03	9.97E-04	1.07E-03	3.06E-03
TI-h3-1	HD	1.03	0.30	5.85	1.69E-02	1.23E-03	1.57E-02	1.82E-02
	LD	1.03	0.31	5.85	9.35E-03	8.48E-04	8.50E-03	1.02E-02
	BL	1.03	0.30	5.85	1.92E-03	5.80E-04	1.34E-03	2.50E-03
TI-h3-2	HD	1.03	0.15	1.91	1.65E-02	1.63E-03	1.49E-02	1.81E-02
	LD	1.03	0.15	1.91	8.72E-03	1.27E-03	7.45E-03	9.99E-03
	BL	1.03	0.15	1.91	1.87E-03	6.92E-04	1.18E-03	2.56E-03
TI-h3-3	HD	1.03	0.28	3.15	1.83E-02	1.92E-03	1.64E-02	2.02E-02
	LD	1.03	0.29	3.15	9.43E-03	1.56E-03	7.87E-03	1.10E-02
	BL	1.03	0.29	3.03	1.95E-03	5.10E-04	1.44E-03	2.46E-03
TI-h4-1	HD	0.73	0.19	4.82	2.03E-02	1.92E-03	1.84E-02	2.22E-02
	LD	0.73	0.21	4.82	1.25E-02	1.40E-03	1.11E-02	1.39E-02
	BL	0.73	0.20	4.82	3.52E-03	1.31E-03	2.20E-03	4.83E-03
TI-h4-2	HD	0.73	0.10	1.58	2.58E-02	3.97E-03	2.18E-02	2.97E-02
	LD	0.73	0.11	1.58	1.48E-02	1.47E-03	1.33E-02	1.62E-02
	BL	0.73	0.10	1.58	4.34E-03	1.37E-03	2.97E-03	5.71E-03
TI-h4-3	HD	0.73	0.20	2.41	2.24E-02	3.64E-04	2.20E-02	2.27E-02
	LD	0.73	0.19	2.48	1.36E-02	8.40E-04	1.28E-02	1.44E-02
	BL	0.73	0.20	2.48	3.96E-03	1.94E-03	2.02E-03	5.90E-03

Appendix J.3 Drag Coefficients

Table 9-20 Summary table of study cases with measured H_{m0} and T_p values at PD18-1, $k_p h_v$, $Re_{U,Am}$, $Re_{U,DBH}$, $Re_{U,DRoot}$, $KC_{U,DBH}$, $KC_{U,DRoot}$, $KC_{U,Am}$, and C_D values.

Trial	Layout	h_v	H_{m0} PD18 -1	T_p PD18 -1	$k_p h_v$	$Re_{U,Am}$	$Re_{U,DBH}$	$Re_{U,DRoot}$	$KC_{U,DBH}$	$KC_{U,DRoot}$	$KC_{U,Am}$	C_D
(-)	(-)	(m)	(m)	(s)	(-)	(-)	(-)	(-)	(-)	(-)	(-)	(-)
TI-h1-1	HD	1.85	0.71	7.45	0.37	255065	79298	19824	16.2	52.1	208.3	0.85
	LD	1.85	0.73	7.45	0.37	260597	81018	20254	16.5	53.2	212.8	0.86
TI-h1-2	HD	1.85	0.43	2.48	1.37	126110	39207	9802	2.7	8.6	34.3	1.12
	LD	1.85	0.43	2.56	1.31	129716	40328	10082	2.8	9.1	36.4	1.02
TI-h2-1	LD	1.48	0.51	6.30	0.40	237838	63251	15813	9.3	35.1	140.6	1.02
TI-h2-2	LD	1.48	0.28	2.16	1.44	107316	28540	7135	1.4	5.4	21.7	1.81
TI-h2-3	LD	1.48	0.48	3.72	0.71	215267	57248	14312	5.0	18.8	75.2	1.21
TI-h3-1	HD	1.03	0.30	5.85	0.36	188921	44676	11169	5.5	23.0	92.2	1.44
	LD	1.03	0.31	5.85	0.36	197485	46701	11675	5.7	24.1	96.4	1.36
TI-h3-2	HD	1.03	0.15	1.91	1.32	76213	18023	4506	0.7	3.0	12.1	2.61
	LD	1.03	0.15	1.91	1.32	80832	19115	4779	0.8	3.2	12.8	2.30
TI-h3-3	HD	1.03	0.28	3.15	0.69	169890	40175	10044	2.6	11.2	44.6	1.63
	LD	1.03	0.29	3.15	0.69	171817	40631	10158	2.7	11.3	45.2	1.48
TI-h4-1	HD	0.73	0.19	4.82	0.36	146577	34699	8675	3.5	14.7	59.0	1.74
	LD	0.73	0.21	4.82	0.36	156955	37156	9289	3.7	15.8	63.1	1.74
TI-h4-2	HD	0.73	0.10	1.58	1.35	64238	15207	3802	0.5	2.1	8.4	3.75
	LD	0.73	0.11	1.58	1.35	65782	15572	3893	0.5	2.2	8.7	3.56
TI-h4-3	HD	0.73	0.20	2.41	0.78	140636	33292	8323	1.7	7.1	28.3	1.83
	LD	0.73	0.19	2.48	0.75	136796	32383	8096	1.7	7.1	28.3	1.99

Table 9-21 Summary table of study cases with measured H_{m0} and T_p values at PD18-1, $k_p h_v$, $Re_{u,De}$, $Re_{u,Am}$, $Re_{u,DBH}$, $Re_{u,Root}$, $KC_{u,De}$, $KC_{u,Am}$, $KC_{U,DBH}$, $KC_{U,DRoot}$, and C_D values.

Trial	Layout	h_v	H_{m0} PD18 -1	T_p PD18 -1	$k_p h_v$	$Re_{u,De}$	$Re_{u,Am}$	$Re_{u,DBH}$	$Re_{u,DRoot}$	$KC_{u,De}$	$KC_{u,Am}$	$KC_{U,DBH}$	$KC_{U,DRoot}$	C_D
(-)	(-)	(m)	(m)	(s)	(-)	(-)	(-)	(-)	(-)	(-)	(-)	(-)	(-)	(-)
TI-h1-1	HD	1.85	0.71	7.45	0.37	27829	249190	77471	19368	142	15.8	50.9	203.5	0.85
	LD	1.85	0.73	7.45	0.37	28432	254595	79152	19788	145	16.2	52.0	207.9	0.86
TI-h1-2	HD	1.85	0.43	2.48	1.37	10466	93713	29135	7284	18	2.0	6.4	25.5	1.12
	LD	1.85	0.43	2.56	1.31	11031	98776	30709	7677	19	2.2	6.9	27.7	1.02
TI-h2-1	LD	1.48	0.51	6.30	0.40	22181	231698	61618	15404	95	9.1	34.2	137.0	1.02
TI-h2-2	LD	1.48	0.28	2.16	1.44	7442	77739	20674	5168	11	1.0	3.9	15.7	1.81
TI-h2-3	LD	1.48	0.48	3.72	0.71	18990	198367	52754	13188	48	4.6	17.3	69.3	1.21
TI-h3-1	HD	1.03	0.30	5.85	0.36	13933	185007	43750	10938	71	5.3	22.6	90.3	1.44
	LD	1.03	0.31	5.85	0.36	14564	193394	45734	11433	74	5.6	23.6	94.4	1.36
TI-h3-2	HD	1.03	0.15	1.91	1.32	4362	57916	13696	3424	7	0.5	2.3	9.2	2.61
	LD	1.03	0.15	1.91	1.32	4626	61426	14526	3631	8	0.6	2.4	9.8	2.30
TI-h3-3	HD	1.03	0.28	3.15	0.69	11820	156958	37117	9279	32	2.4	10.3	41.2	1.63
	LD	1.03	0.29	3.15	0.69	11954	158738	37538	9385	33	2.5	10.4	41.7	1.48
TI-h4-1	HD	0.73	0.19	4.82	0.36	10193	143400	33947	8487	48	3.4	14.4	57.7	1.74
	LD	0.73	0.21	4.82	0.36	10915	153554	36351	9088	51	3.7	15.4	61.8	1.74
TI-h4-2	HD	0.73	0.10	1.58	1.35	3421	48133	11394	2849	5	0.4	1.6	6.3	3.75
	LD	0.73	0.11	1.58	1.35	3503	49290	11668	2917	5	0.4	1.6	6.5	3.56
TI-h4-3	HD	0.73	0.20	2.41	0.78	9056	127410	30162	7540	21	1.5	6.4	25.6	1.83
	LD	0.73	0.19	2.48	0.75	8867	124751	29532	7383	22	1.5	6.5	25.9	1.99

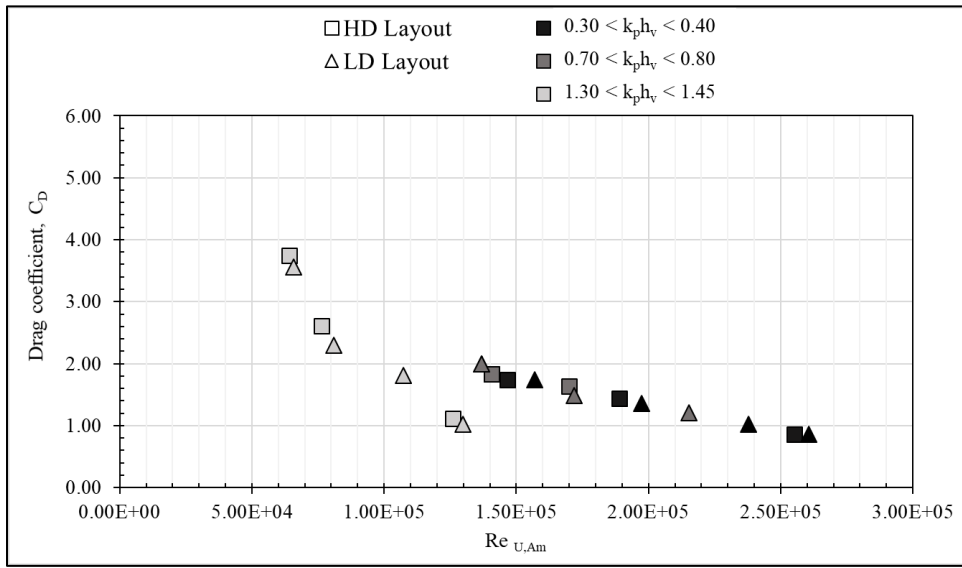


Figure 9-56 Drag coefficient, C_D , versus the Reynolds number, $Re_{U,Am}$, for the high-density (HD) (squares) and low-density (LD) (triangles) layouts designated by relative water depth, $k_p h_v$, range.

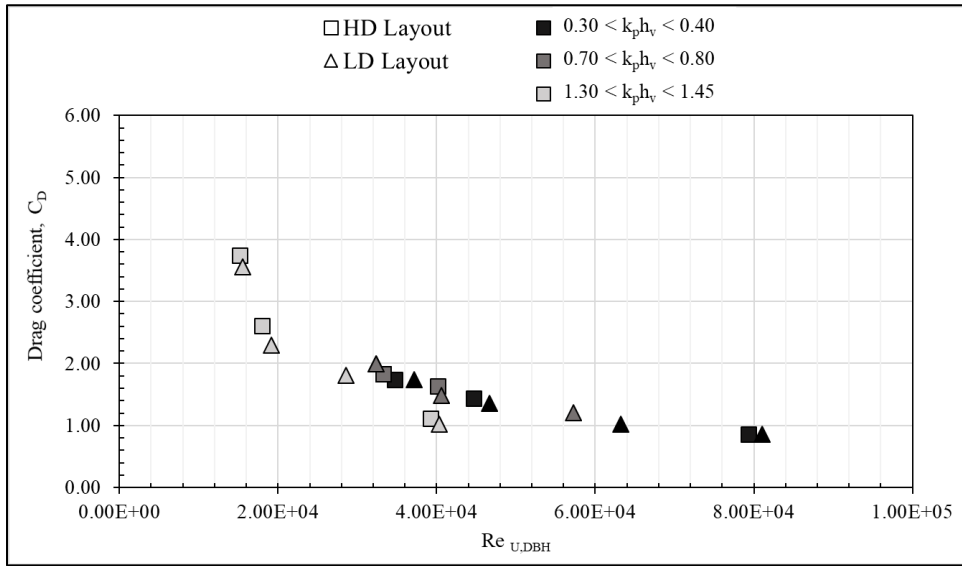


Figure 9-57 Drag coefficient, C_D versus the Reynolds number, $Re_{U,DBH}$, for the high-density (HD) (squares) and low-density (LD) (triangles) layouts designated by relative water depth, $k_p h_v$, range.

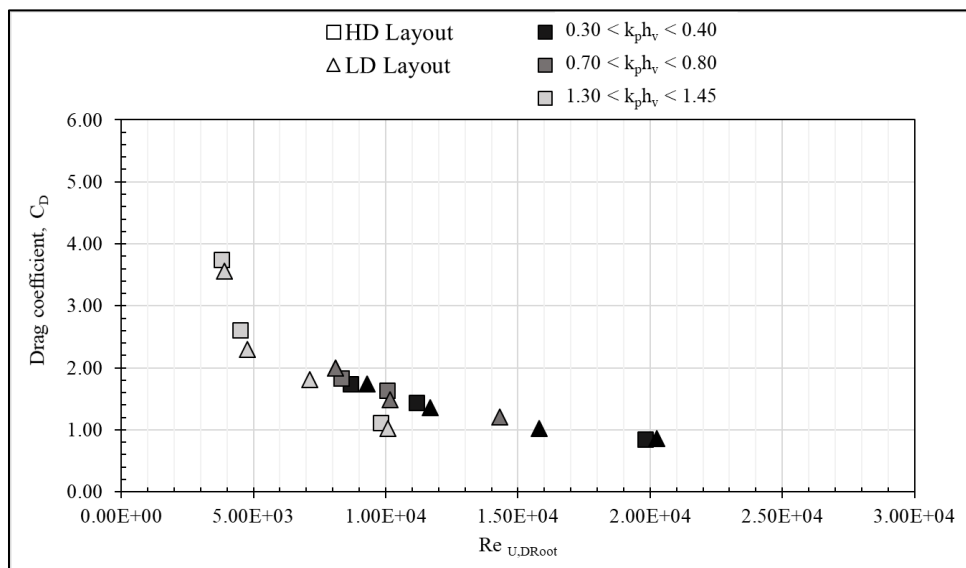


Figure 9-58 Drag coefficient, C_D , versus the Reynolds number, $Re_{U,DRoot}$, for the high-density (HD) (squares) and low-density (LD) (triangles) layouts designated by relative water depth, $k_p h_v$, range.

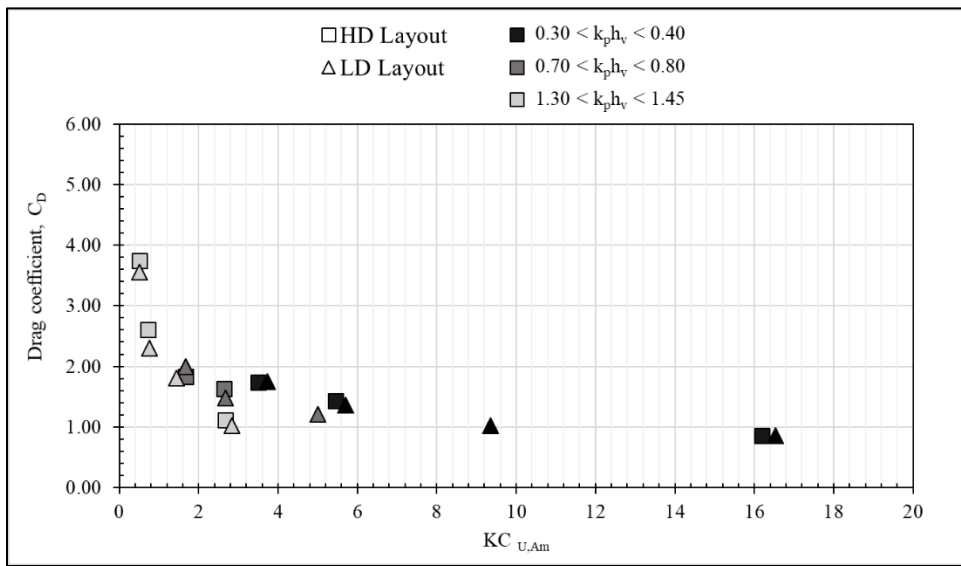


Figure 9-59 Drag coefficient, C_D , versus the Keulegan-Carpenter number, $KC_{U,Am}$, for the high-density (HD) (squares) and low-density (LD) (triangles) layouts designated by relative water depth, $k_p h_v$, range.

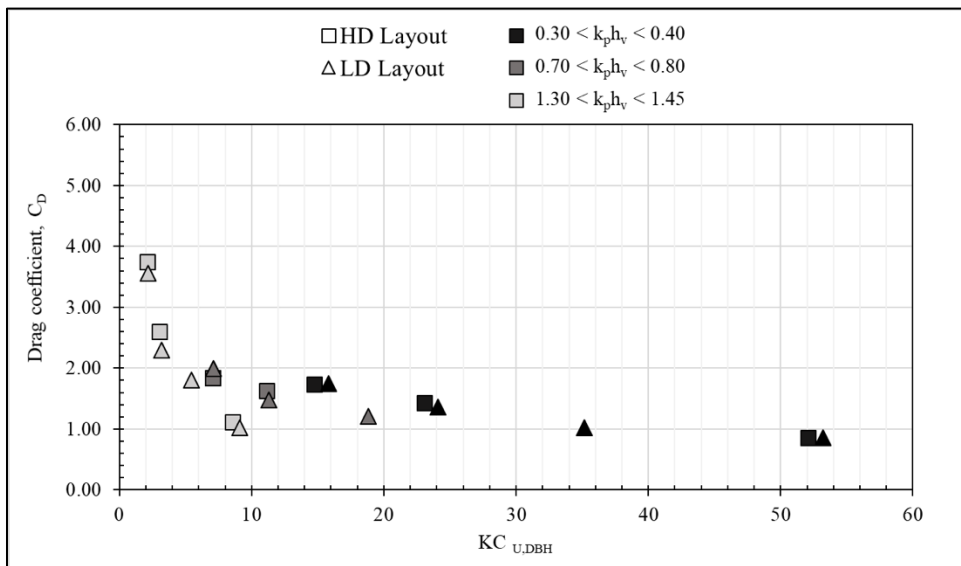


Figure 9-60 Drag coefficient, C_D , versus the Keulegan-Carpenter number, $KC_{U,DBH}$, for the high-density (HD) (squares) and low-density (LD) (triangles) layouts designated by relative water depth, $k_p h_v$, range.

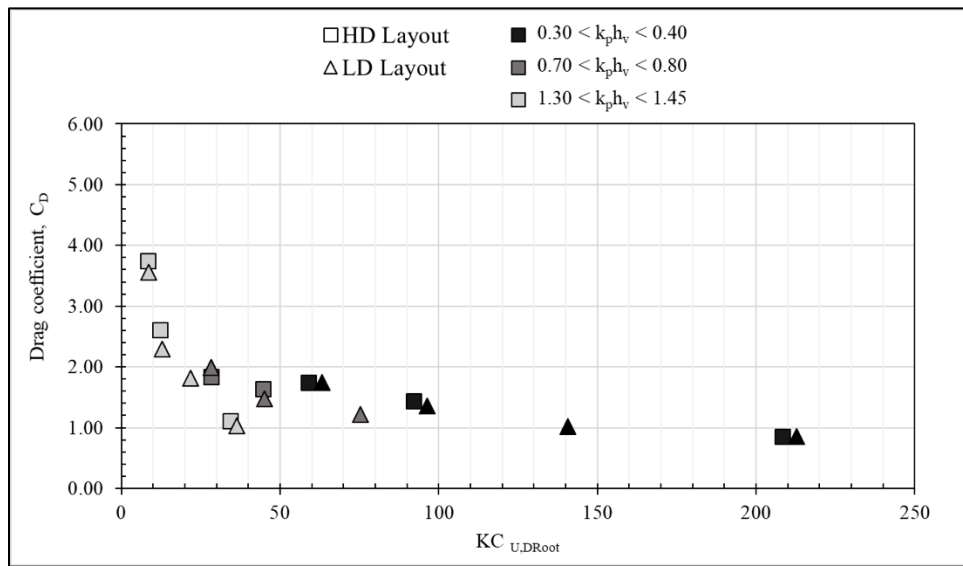


Figure 9-61 Drag coefficient, C_D , versus the Keulegan-Carpenter number, $KC_{U,DRoot}$, for the high-density (HD) (squares) and low-density (LD) (triangles) layouts designated by relative water depth, $k_p h_v$, range.

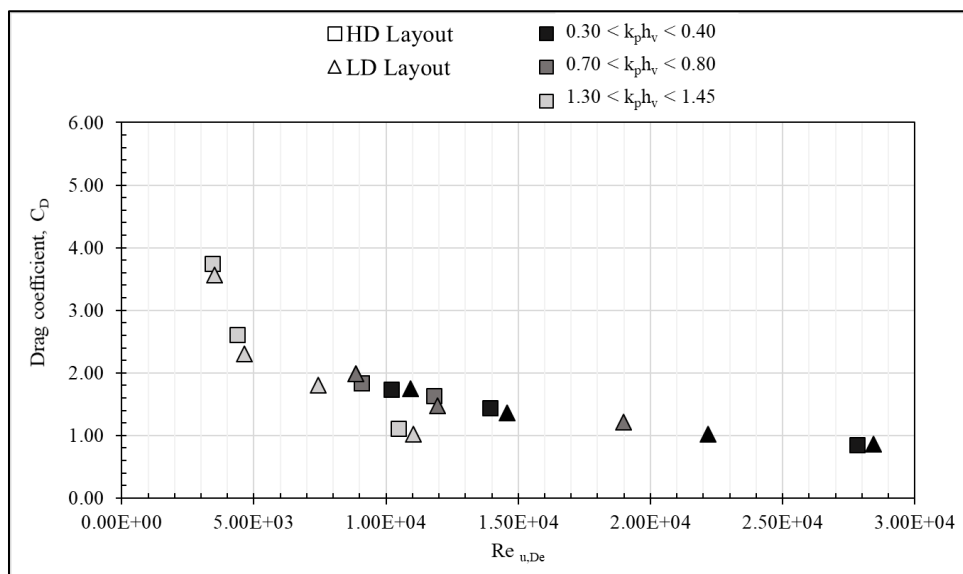


Figure 9-62 Drag coefficient, C_D , versus the Reynolds number, $Re_{u,De}$, for the high-density (HD) (squares) and low-density (LD) (triangles) layouts designated by relative water depth, $k_p h_v$, range.

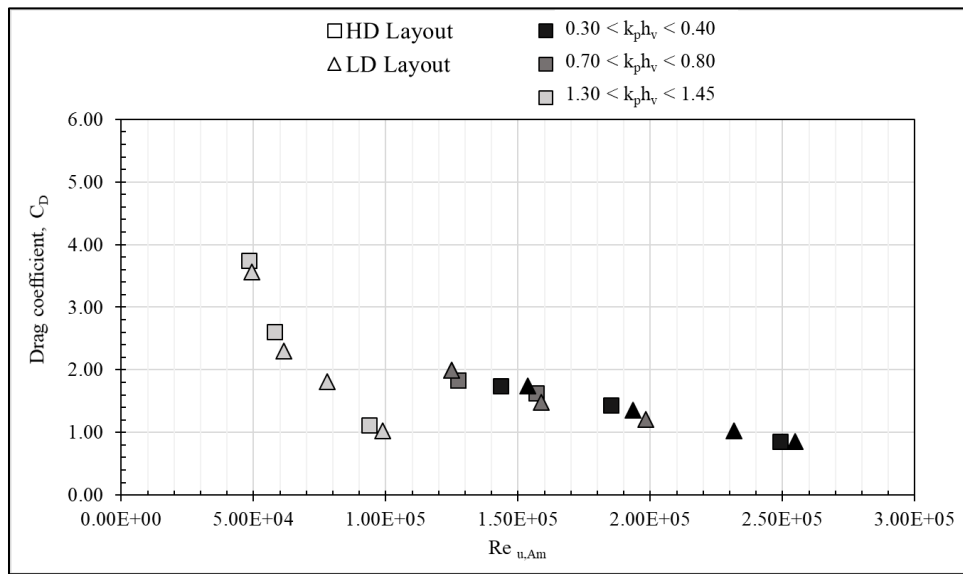


Figure 9-63 Drag coefficient, C_D , versus the Reynolds number, $Re_{u,Am}$, for the high-density (HD) (squares) and low-density (LD) (triangles) layouts designated by relative water depth, $k_p h_v$, range.

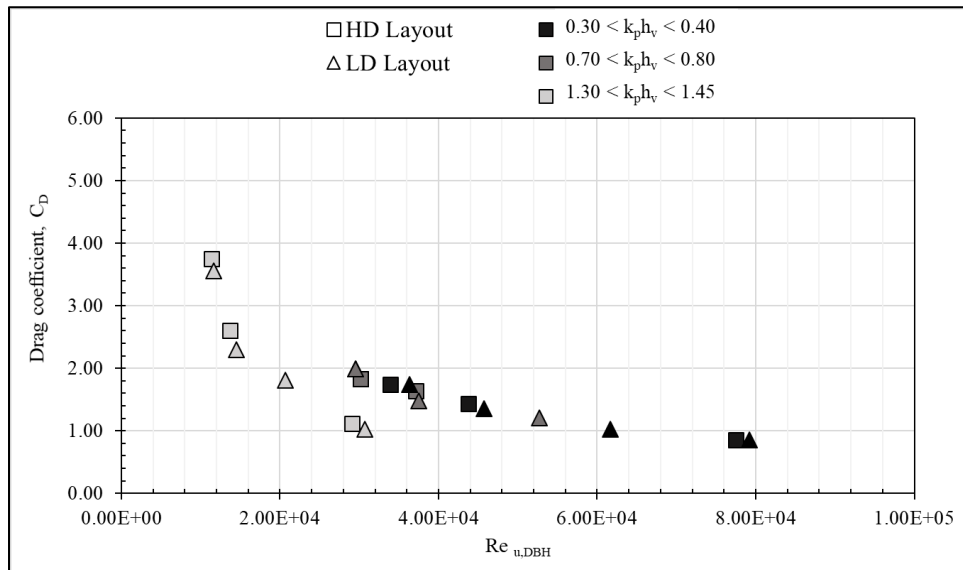


Figure 9-64 Drag coefficient, C_D , versus the Reynolds number, $Re_{u,DBH}$, for the high-density (HD) (squares) and low-density (LD) (triangles) layouts designated by relative water depth, $k_p h_v$, range.

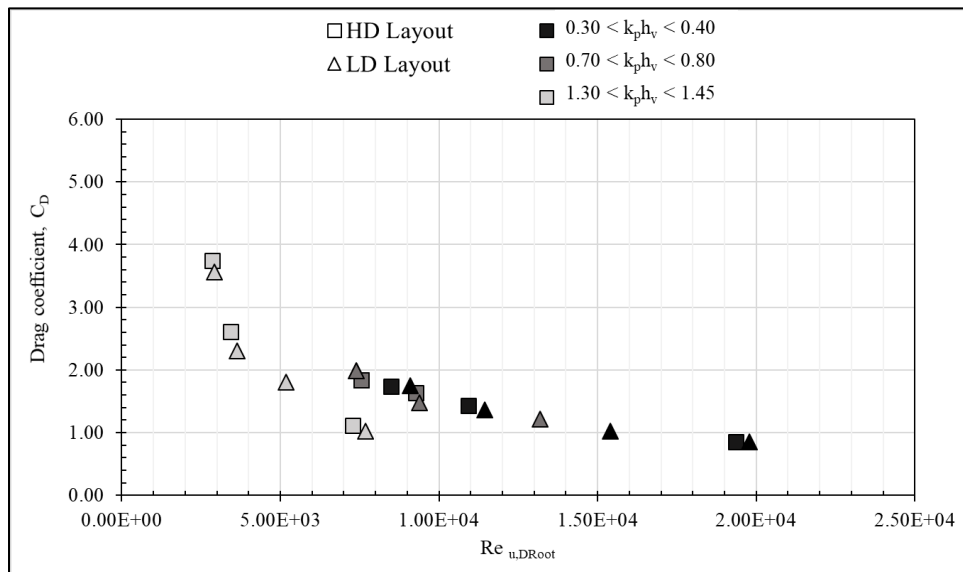


Figure 9-65 Drag coefficient, C_D , versus the Reynolds number, $Re_{u,DRoot}$, for the high-density (HD) (squares) and low-density (LD) (triangles) layouts designated by relative water depth, $k_p h_v$, range.

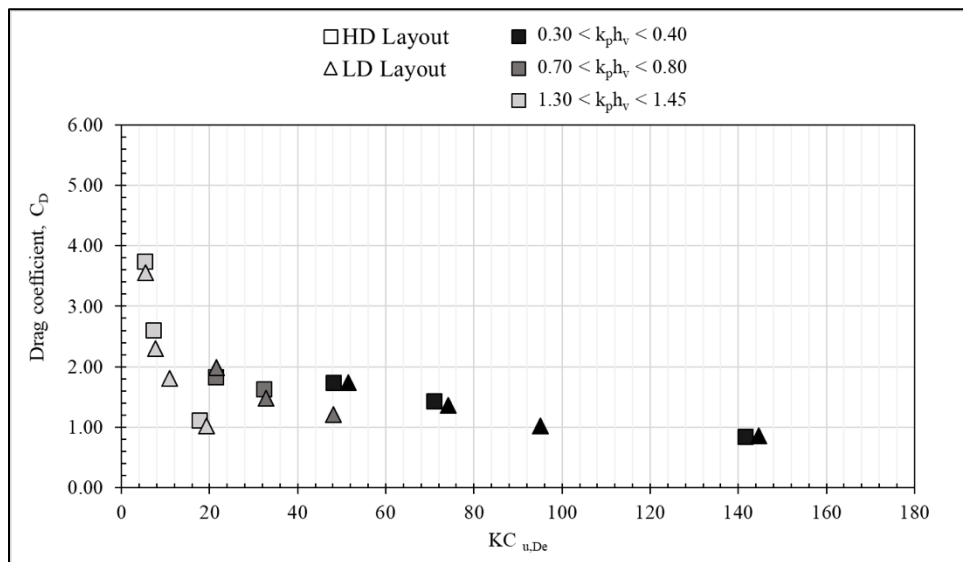


Figure 9-66 Drag coefficient, C_D , versus the Keulegan-Carpenter number, $KC_{u,De}$, for the high-density (HD) (squares) and low-density (LD) (triangles) layouts designated by relative water depth, $k_p h_v$, range.

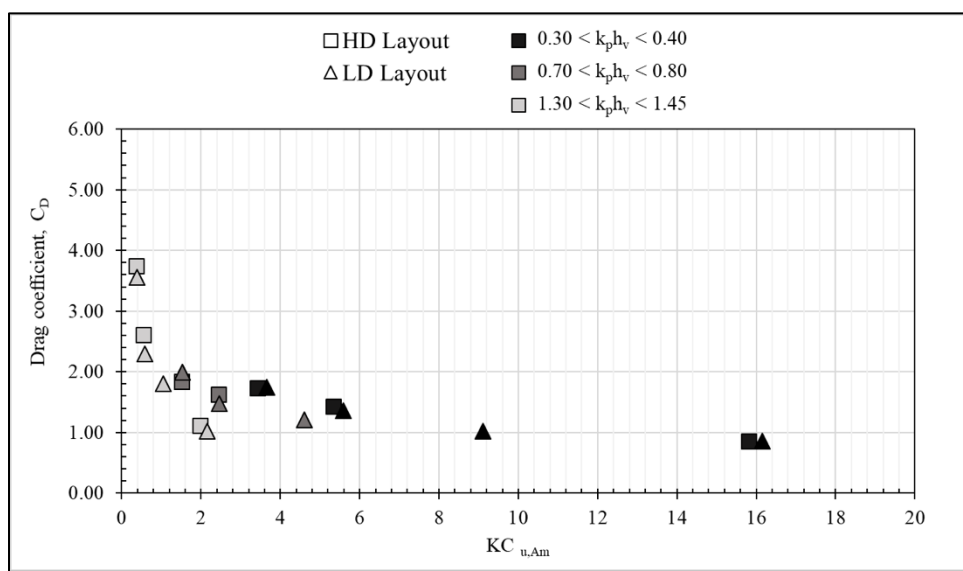


Figure 9-67 Drag coefficient, C_D , versus the Keulegan-Carpenter number, $KC_{u,Am}$, for the high-density (HD) (squares) and low-density (LD) (triangles) layouts designated by relative water depth, $k_p h_v$, range.

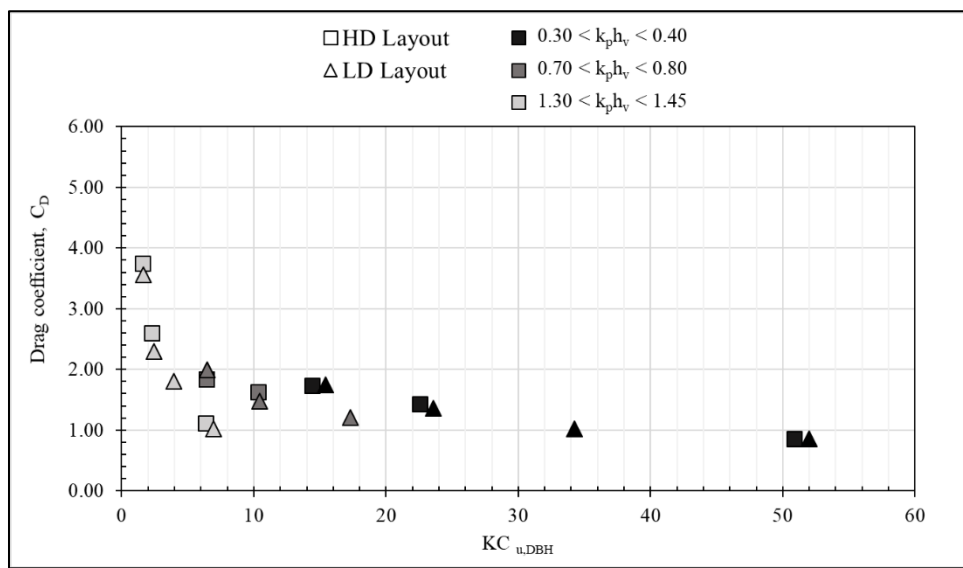


Figure 9-68 Drag coefficient, C_D , versus the Keulegan-Carpenter number, $KC_{u,DBH}$, for the high-density (HD) (squares) and low-density (LD) (triangles) layouts designated by relative water depth, $k_p h_v$, range.

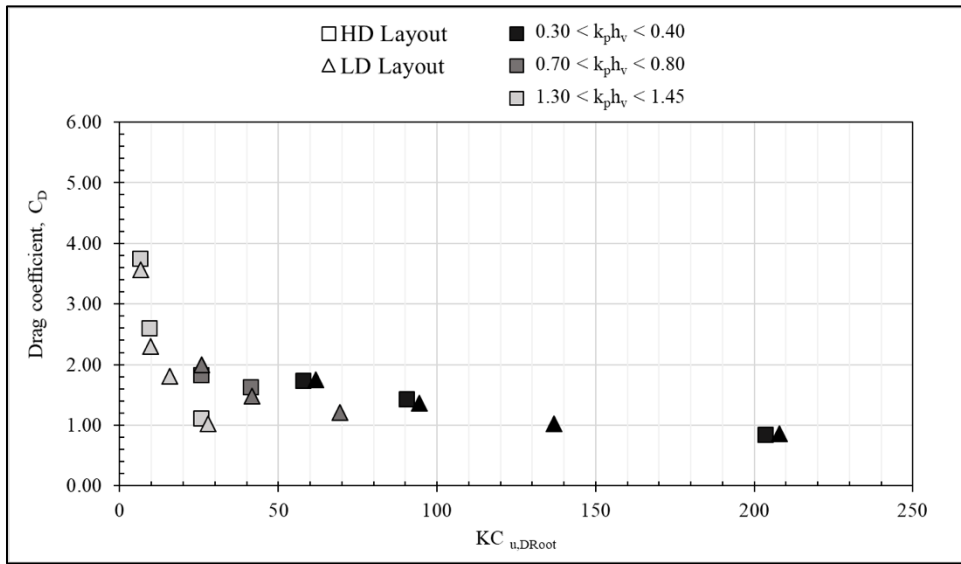


Figure 9-69 Drag coefficient, C_D , versus the Keulegan-Carpenter number, $KC_{u,DRoot}$, for the high-density (HD) (squares) and low-density (LD) (triangles) layouts designated by relative water depth, $k_p h_v$, range.

Appendix J.4 Combined Uncertainty

Modified equation from Mendez and Losada (2004), Equation (28).

$$C_D = \frac{3\sqrt{\pi}}{A_{t,m} N H_{rms,i} k} \frac{(\sinh(2kh)+2kh)\sinh(kh))}{\sinh^3(kd)+3\sinh(kd)} \tilde{\alpha} \quad (28)$$

$$A = A_{t,m} \quad (29)$$

$$B = \tilde{\alpha} \quad (30)$$

$$C = C_D \quad (31)$$

$$D = \frac{3\sqrt{\pi}}{N H_{rms,i} k} \frac{(\sinh(2kh)+2kh)\sinh(kh))}{\sinh^3(kd)+3\sinh(kd)} \quad (32)$$

$$C = \frac{D}{A} B \quad (33)$$

$$f = C \quad (34)$$

$$f = \frac{D}{A} B \quad (35)$$

$$\sigma_C = \left[\left(\left(\frac{\partial f}{\partial A} \right) \sigma_A \right)^2 + \left(\left(\frac{\partial f}{\partial B} \right) \sigma_B \right)^2 + \left(\left(\frac{\partial f}{\partial D} \right) \sigma_D \right)^2 \right]^{\frac{1}{2}} \quad (36)$$

σ_C = standard deviation of variable C

σ_A = standard deviation of variable A

σ_B = standard deviation of variable B

σ_D = standard deviation of variable D

Assumptions made:

- Variable's variations have a normal distribution
- Variable variations are independent from each other

Assuming $\left(\left(\frac{\partial f}{\partial D} \right) \sigma_D \right)^2$ is small:

$$\sigma_C = \left[\left(\left(\frac{D_B}{A^2} \right) \sigma_A \right)^2 + \left(\left(\frac{D}{A} \right) \sigma_B \right)^2 \right]^{\frac{1}{2}} \quad (37)$$

$$\sigma_C = \frac{D_B}{A} \left[\left(\frac{\sigma_A}{A} \right)^2 + \left(\frac{\sigma_B}{B} \right)^2 \right]^{\frac{1}{2}} \quad (38)$$

$$\frac{\sigma_C}{C_D} = \left[\left(\frac{\sigma_{A_{t,m}}}{A_{t,m}} \right)^2 + \left(\frac{\sigma_\alpha}{\alpha} \right)^2 \right]^{\frac{1}{2}} \quad (39)$$

$$\frac{\sigma_{C_D}}{C_D} = \left[\left(\frac{\sigma_{A_{t,m}}}{A_{t,m}} \right)^2 + \left(\frac{\sigma_\alpha}{\alpha} \right)^2 \right]^{\frac{1}{2}} \quad (40)$$

σ_{C_D} = Standard deviation of the drag coefficient, C_D (-)

C_D = Drag coefficient (-)

$\sigma_{A_{t,m}}$ = Standard deviation of the mean projected area per unit height per tree, $A_{t,m}$ (m^2/m)

$A_{t,m}$ = Mean projected area per unit height per tree (m^2/m)

σ_α = Standard deviation of the wave height decay coefficient, α (m)

α = Wave height decay coefficient (m)

Appendix J.5 Previous Studies Comparison

Table 9-22 Summary table of present and previous studies best fit equations for the drag coefficient, C_D , as a function of the Reynolds number, Re .

Study	Vegitation Type	Wave Type	Scale	Equation	R^2	Reynolds Number, Re_{DBH} Range
Present Study	Lab - Mangroves	Random	1:1	$C_D = 0.67 + \left(\frac{32800}{Re_{DBH}}\right)^{1.35}$	0.92	15207 - 81018
Proposed Equations for Maza et al. (2019)	Lab -Mangroves	Regular & Random waves	1:12	$C_D = -0.499 + \left(\frac{2195000}{Re_{DBH}}\right)^{0.085} \text{ Regular}$	0.016	8439 - 12928 (unscaled)
				$C_D = -0.144 + \left(\frac{110000}{Re_{DBH}}\right)^{0.046} \text{ Random}$	0.014	1711 - 8439 (unscaled)
Chang et al. (2019)	Lab -Mangroves	Regular	1:7	$C_D = -4.3803 + \left(\frac{9.9117 \times 10^4}{Re_{DBH}}\right)^{0.3956}$	-	263 - 1038 (unscaled)
Anderson et al. (2014)	Lab -Emergent & Near Emergent	Random	NA	$C_D = 0.76 + \left(\frac{744.2}{Re}\right)^{1.27}$	-	638 - 2345
Ozeren et al. (2014)	Lab - Emergent	Regular & Random waves	NA	$C_D = 2.1 + \left(\frac{793}{Re}\right)^{2.39} \text{ Regular}$	-	342 - 4215
				$C_D = 1.5 + \left(\frac{1230}{Re}\right)^{0.95} \text{ Random}$		233 - 1607
Hu et al. (2014)	Lab -Emergent	Regular waves + Current	NA	$C_D = 1.04 + \left(\frac{730}{Re}\right)^{1.37}$	-	300-4700

Appendix K Experimental Results, Regular waves

Appendix K.1 Wave Attenuation

For the regular wave analysis, H represents the total spectral estimate of the significant wave height, H_{m0} .

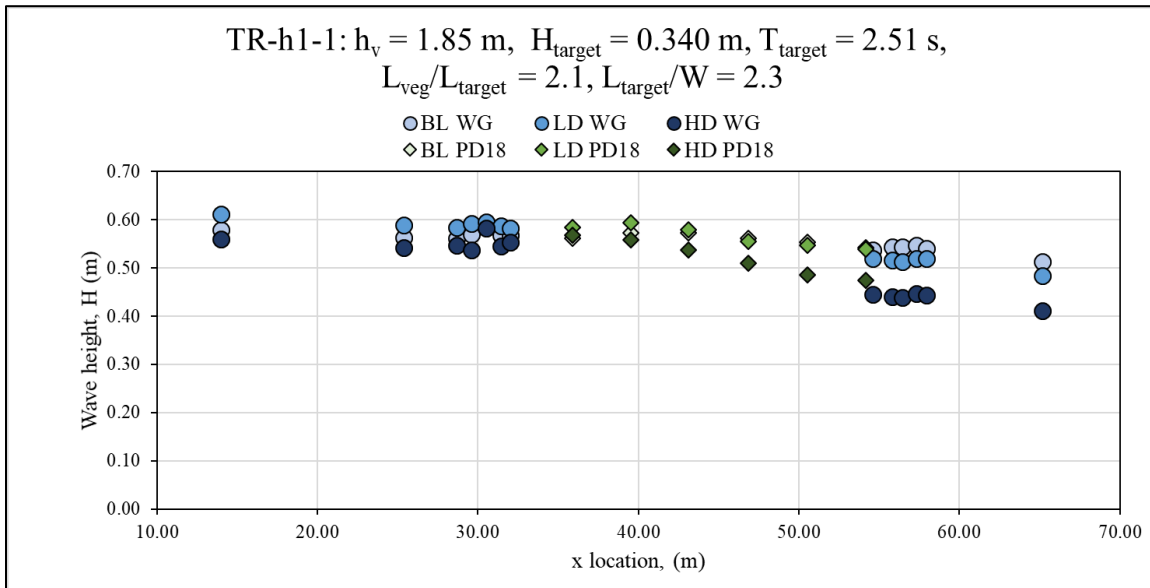


Figure 9-70 Wave height, H , with respect to x location for wave gauges (WG, circles) and pressure gauges (PD, diamonds) for the high-density (HD) (dark colors), low-density (LD) (intermediate colors), and baseline (BL) (light colors) layouts for regular wave case TR-h1-1.

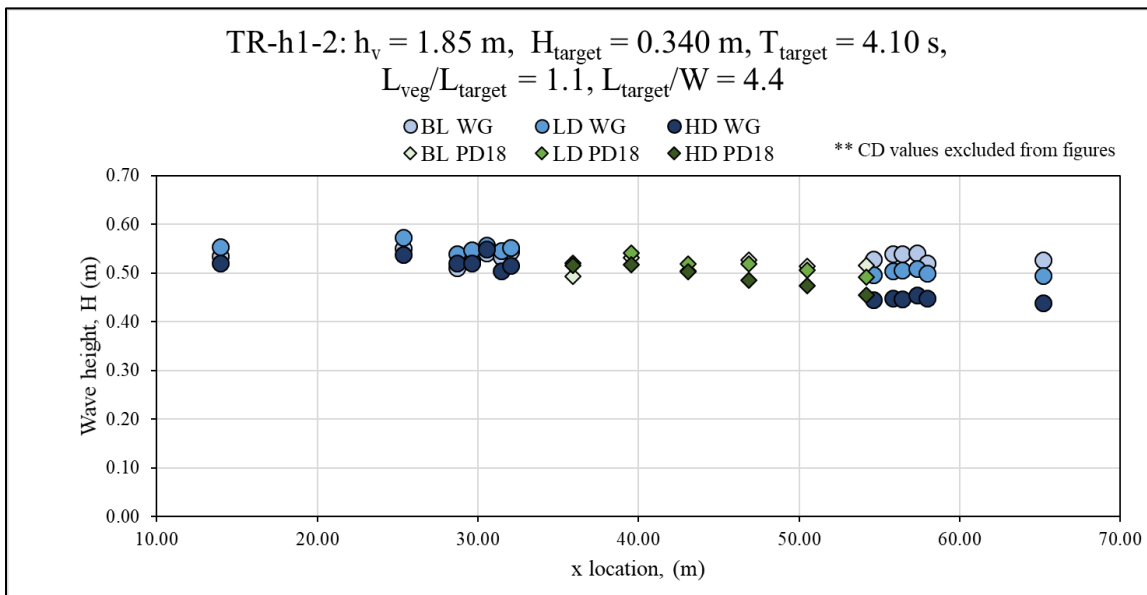


Figure 9-71 Wave height, H , with respect to x location for wave gauges (WG, circles) and pressure gauges (PD, diamonds) for the for the high-density (HD) (dark colors), low-density (LD) (intermediate colors), and baseline (BL) (light colors) layouts for regular wave case TR-h1-2.

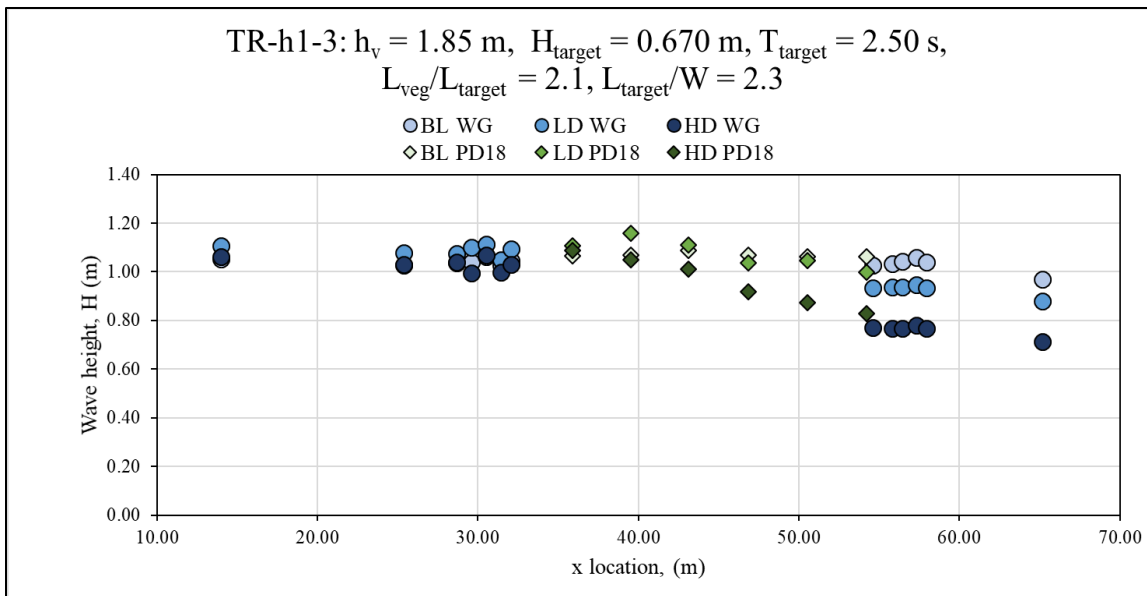


Figure 9-72 Wave height, H , with respect to x location for wave gauges (WG, circles) and pressure gauges (PD, diamonds) for the high-density (HD) (dark colors), low-density (LD) (intermediate colors), and baseline, (BL) (light colors) layouts for regular wave case TR-h1-3 .

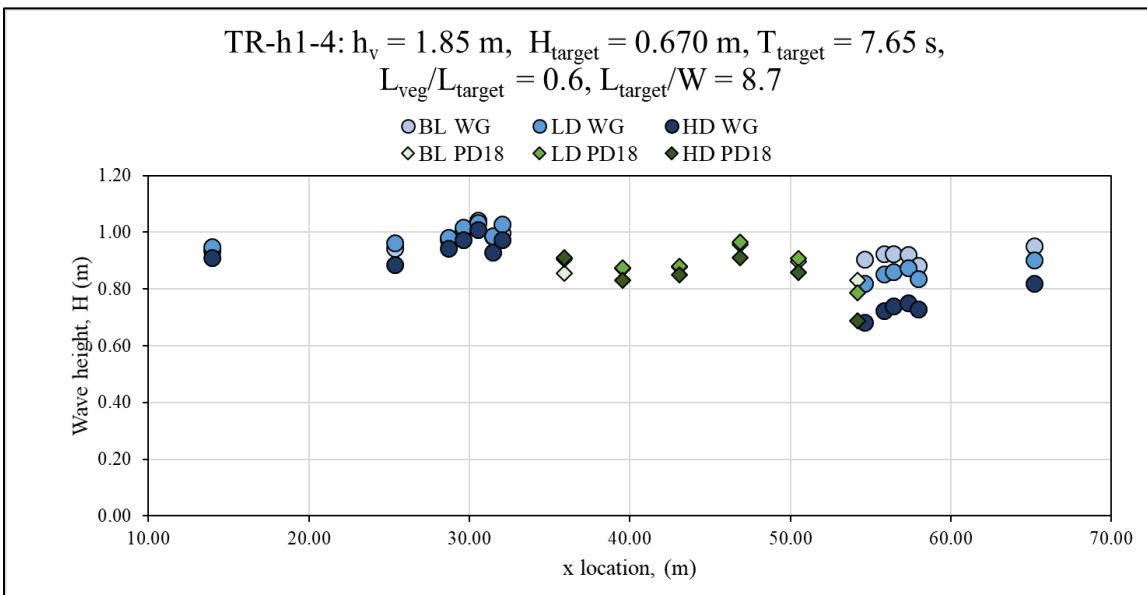


Figure 9-73 Wave height, H , with respect to x location for wave gauges (WG, circles) and pressure gauges (PD, diamonds) for the high-density (HD) (dark colors), low-density (LD) (intermediate colors), and baseline (BL) (light colors) layouts for regular wave case TR-h1-4.

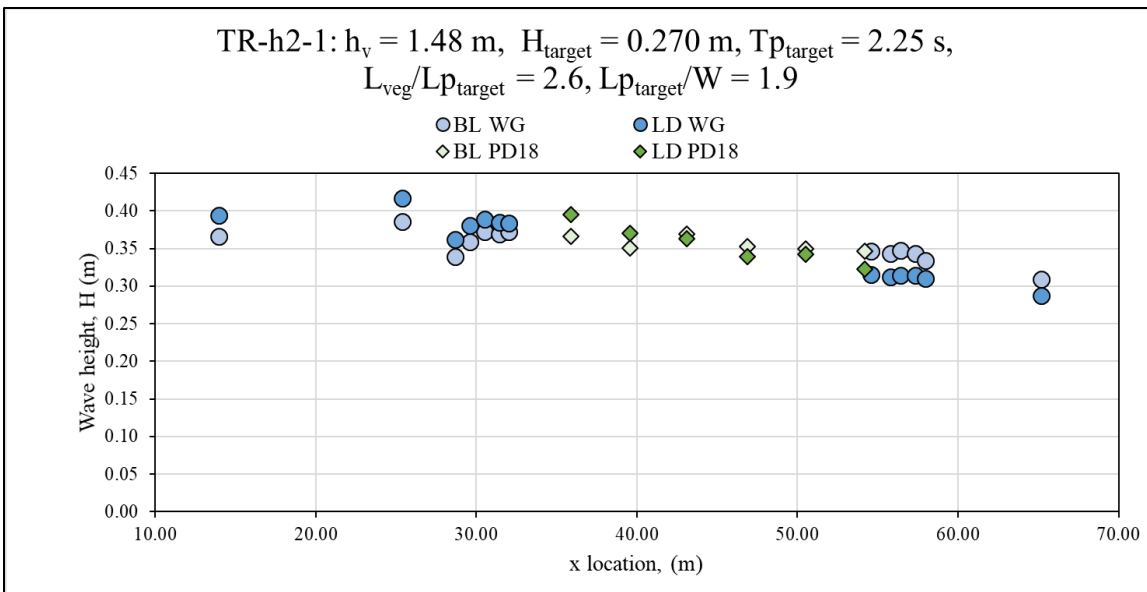


Figure 9-74 Wave height, H , with respect to x location for wave gauges (WG, circles) and pressure gauges (PD, diamonds) for the low-density (LD) (intermediate colors), and baseline (BL) (light colors) layouts for regular wave case TR-h2-1.

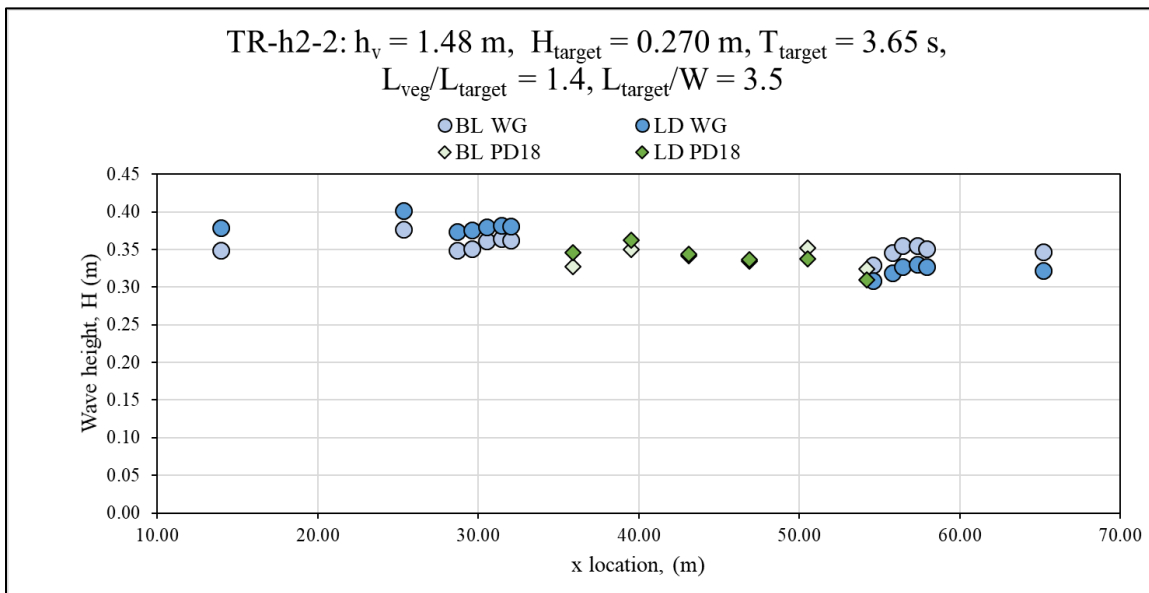


Figure 9-75 Wave height, H , with respect to x location for wave gauges (WG, circles) and pressure gauges(PD, diamonds) for the low-density (LD) (intermediate colors), and baseline (BL) (light colors) layouts for regular wave case TR-h2-2.

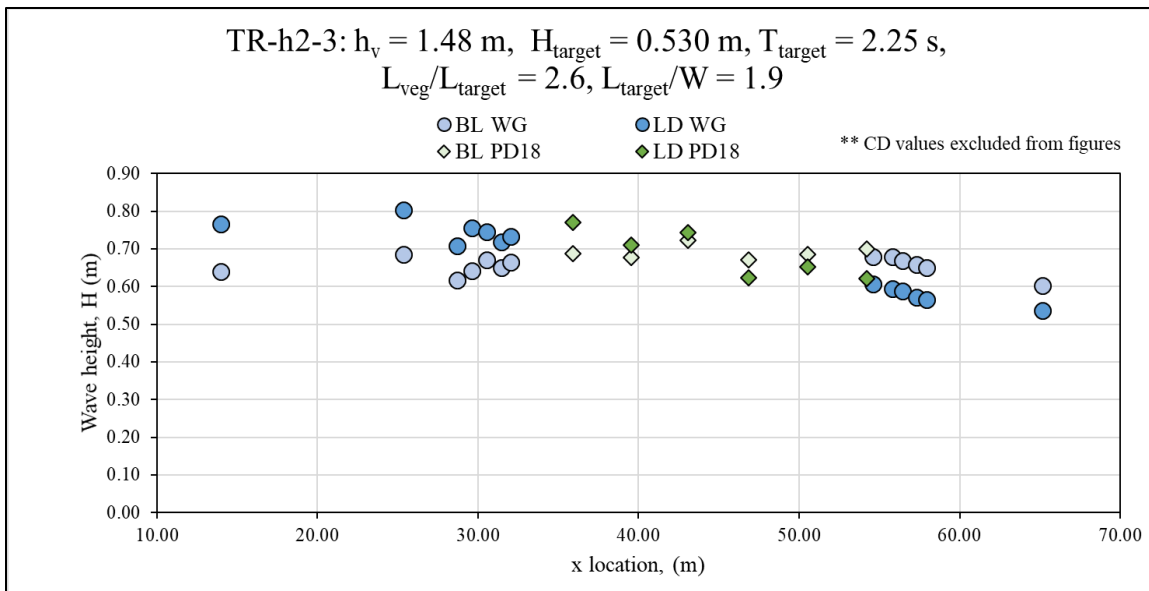


Figure 9-76 Wave height, H , with respect to x location for wave gauges (WG, circles) and pressure gauges (PD, diamonds) for the low-density (LD) (intermediate colors), and baseline (BL) (light colors) layouts for regular wave case TR-h2-3.

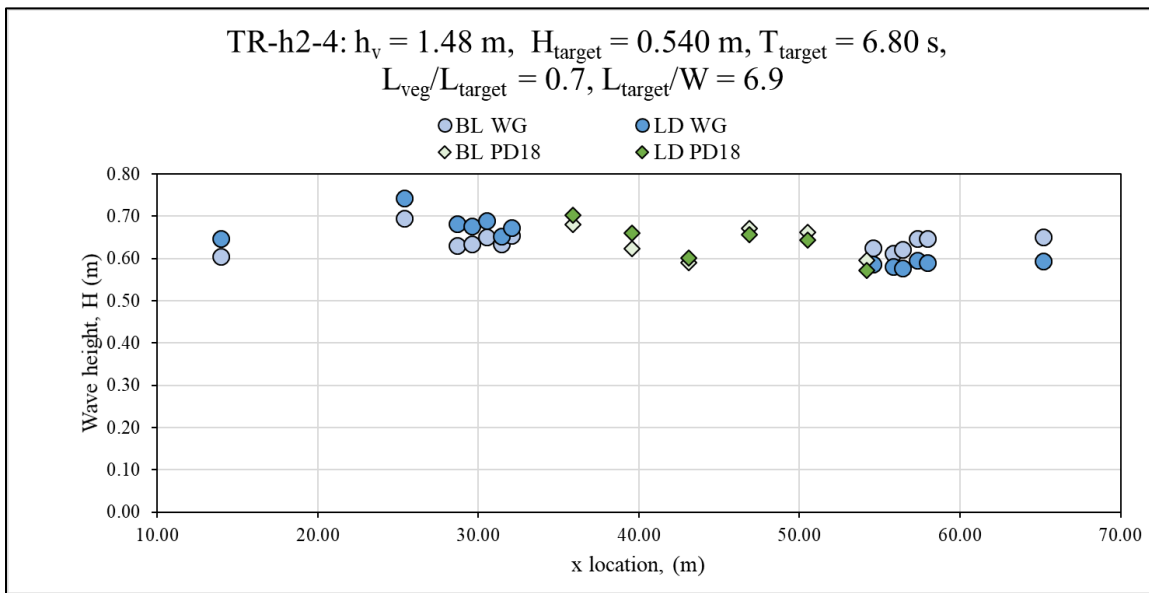


Figure 9-77 Wave height, H , with respect to x location for wave gauges (WG, circles) and pressure gauges (PD, diamonds) for the low-density (LD) (intermediate colors), and baseline (BL) (light colors) layouts for regular wave case TR-h2-4.

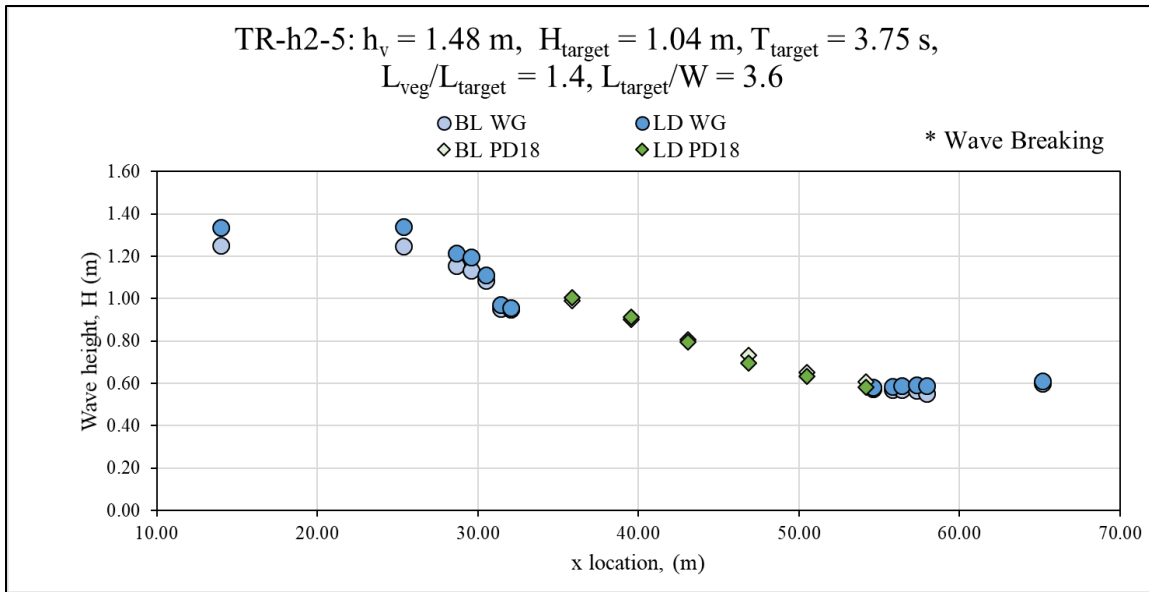


Figure 9-78 Wave height, H , with respect to x location for wave gauges (WG, circles) and pressure gauges (PD, diamonds) for the low-density (LD) (intermediate colors), and baseline (BL) (light colors) layouts for regular wave case TR-h2-5.

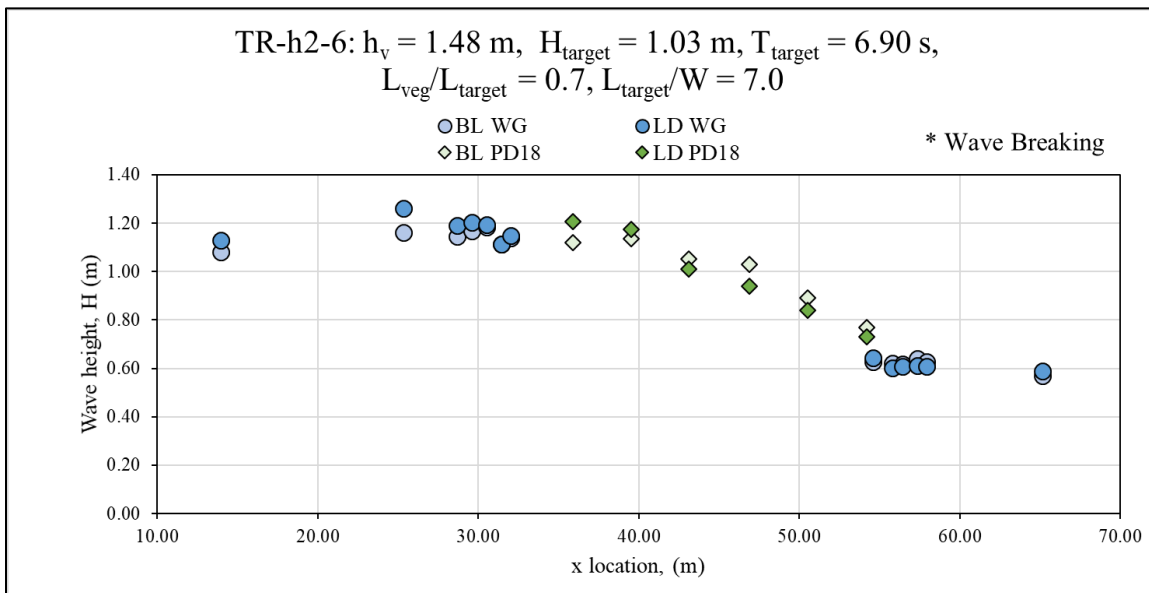


Figure 9-79 Wave height, H , with respect to x location for wave gauges (WG, circles) and pressure gauges (PD, diamonds) for the low-density (LD) (intermediate colors), and baseline (BL) (light colors) layouts for regular wave case TR-h2-6.

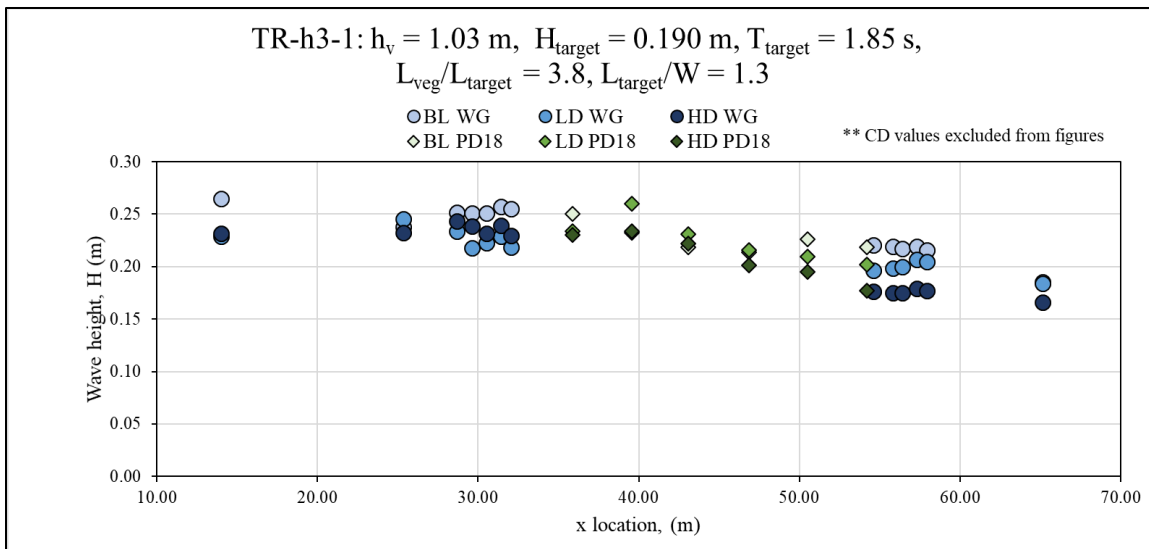


Figure 9-80 Wave height, H , with respect to x location for wave gauges (WG, circles) and pressure gauges(PD, diamonds) for the high-density (HD) (dark colors), low-density (LD) (intermediate colors), and baseline (BL) (light colors) layouts for regular wave case TR-h3-1.

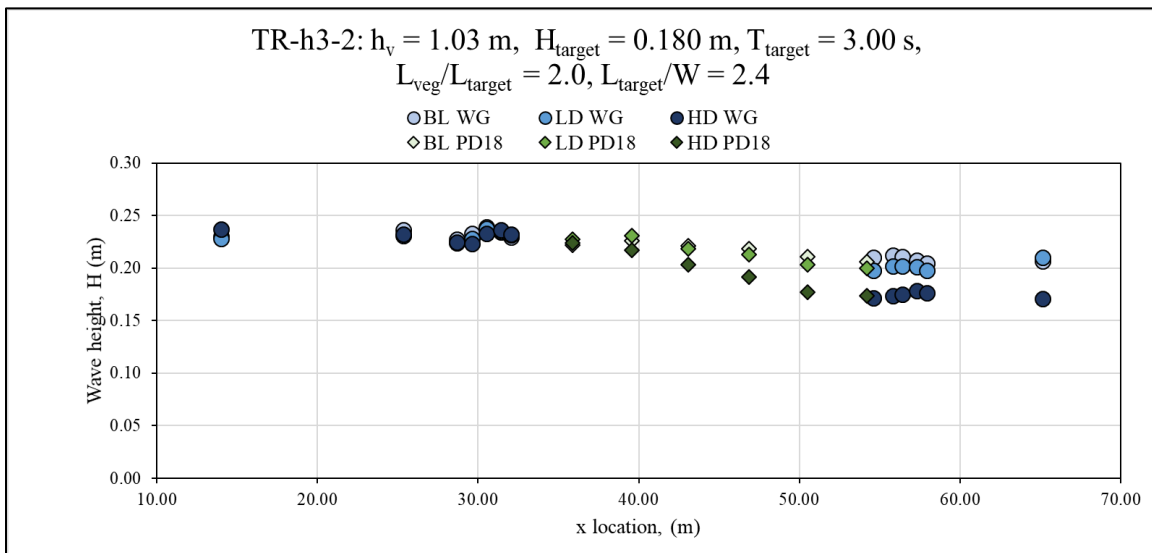


Figure 9-81 Wave height, H , with respect to x location for wave gauges (WG, circles) and pressure gauges(PD, diamonds) for the HD (dark colors), LD (intermediate colors), and BL (light colors) layouts for regular wave case TR-h3-2.

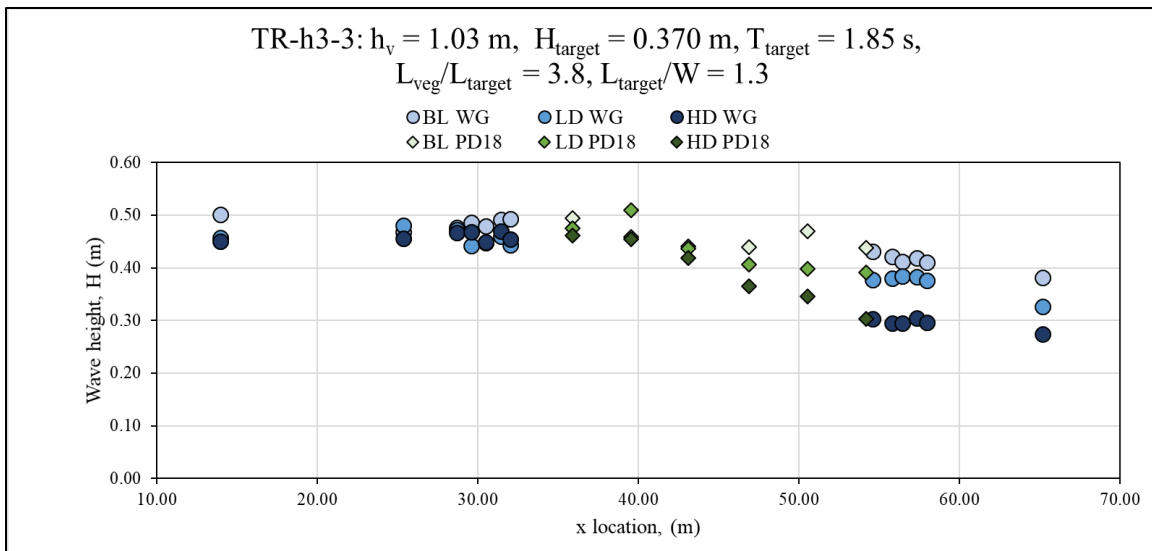


Figure 9-82 Wave height, H , with respect to x location for wave gauges (WG, circles) and pressure gauges (PD, diamonds) for the high-density (HD) (dark colors), low-density (LD) (intermediate colors), and baseline (BL) (light colors) layouts for regular wave case TR-h3-3.

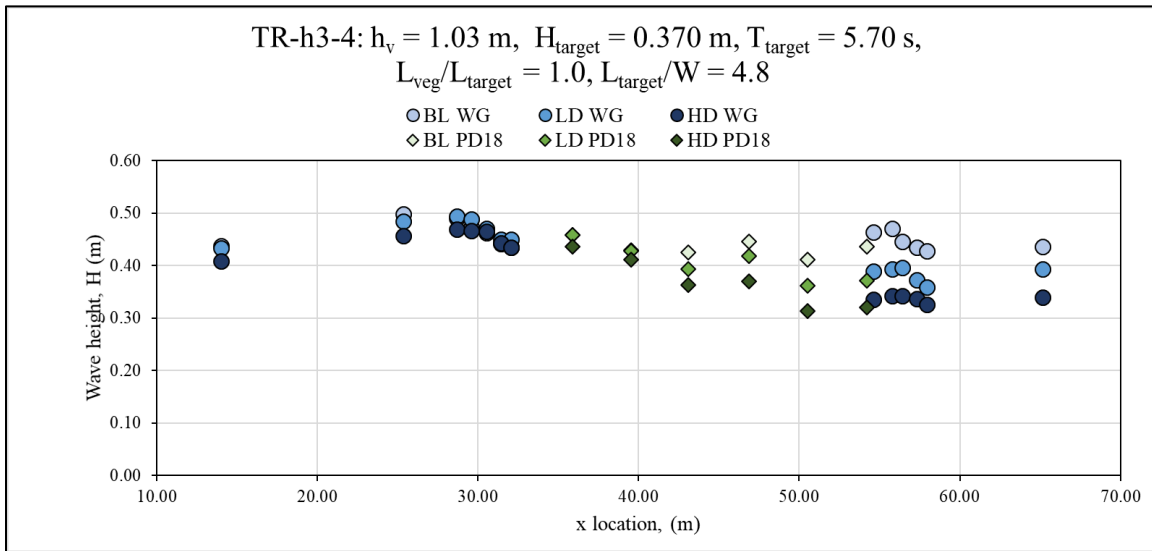


Figure 9-83 Wave height, H , with respect to x location for wave gauges (WG, circles) and pressure gauges (PD, diamonds) for the high-density (HD) (dark colors), low-density (LD) (intermediate colors), and baseline (BL) (light colors) layouts for regular wave case TR-h3-4.

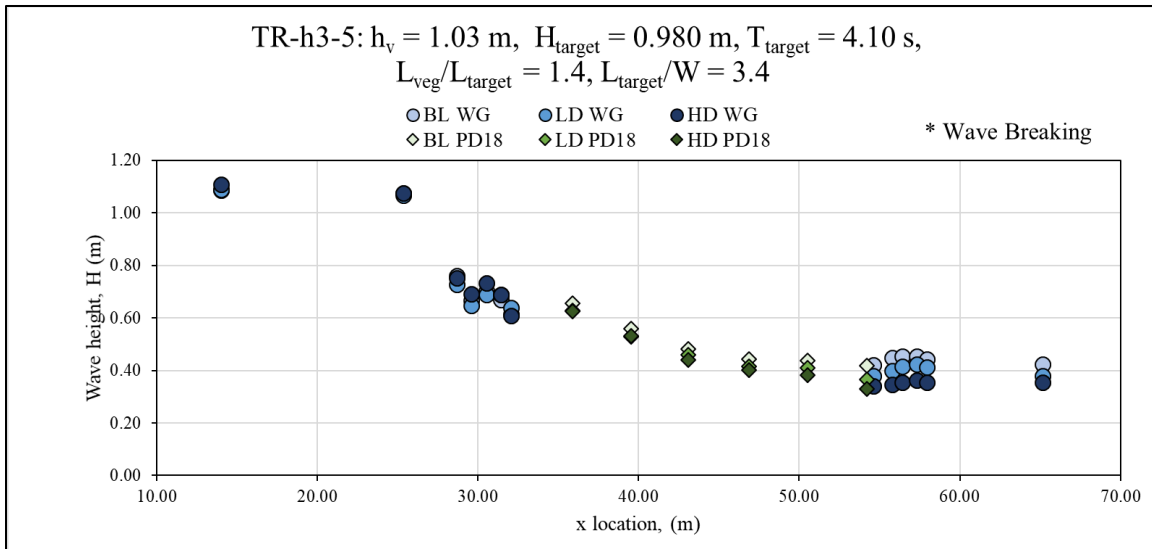


Figure 9-84 Wave height, H , with respect to x location for wave gauges (WG, circles), and pressure gauges (PD, diamonds) for the high-density (HD) (dark colors), low-density (LD) (intermediate colors), and baseline (BL) (light colors) layouts for regular wave case TR-h3-5.

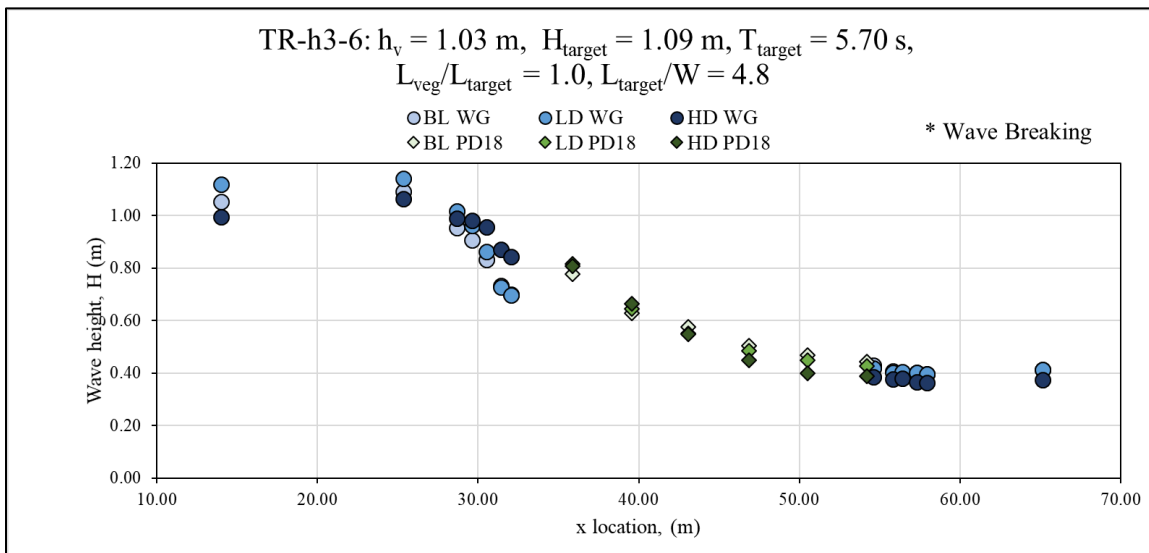


Figure 9-85 Wave height, H , with respect to x location for wave gauges (WG, circles) and pressure gauges (PD, diamonds) for the high-density (HD) (dark colors), low-density (LD) (intermediate colors), and baseline (BL) (light colors) layouts for regular wave case TR-h3-6.

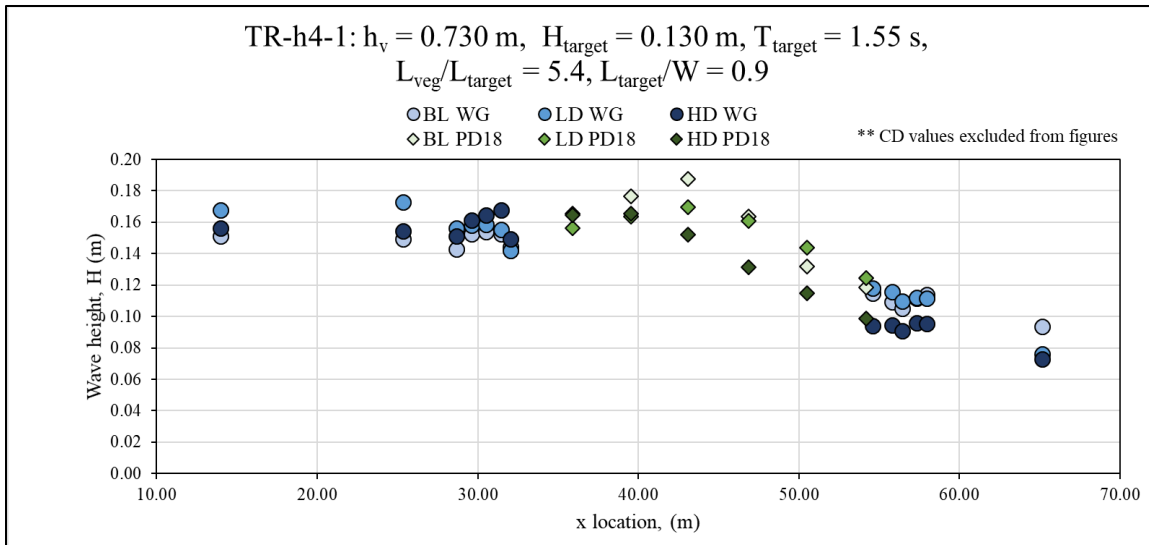


Figure 9-86 Wave height, H with respect to x location for wave gauges (WG, circles) and pressure gauges (PD, diamonds) for the high-density (HD) (dark colors), low-density (LD) (intermediate colors), and baseline (BL) (light colors) layouts for regular wave case TR-h4-1.

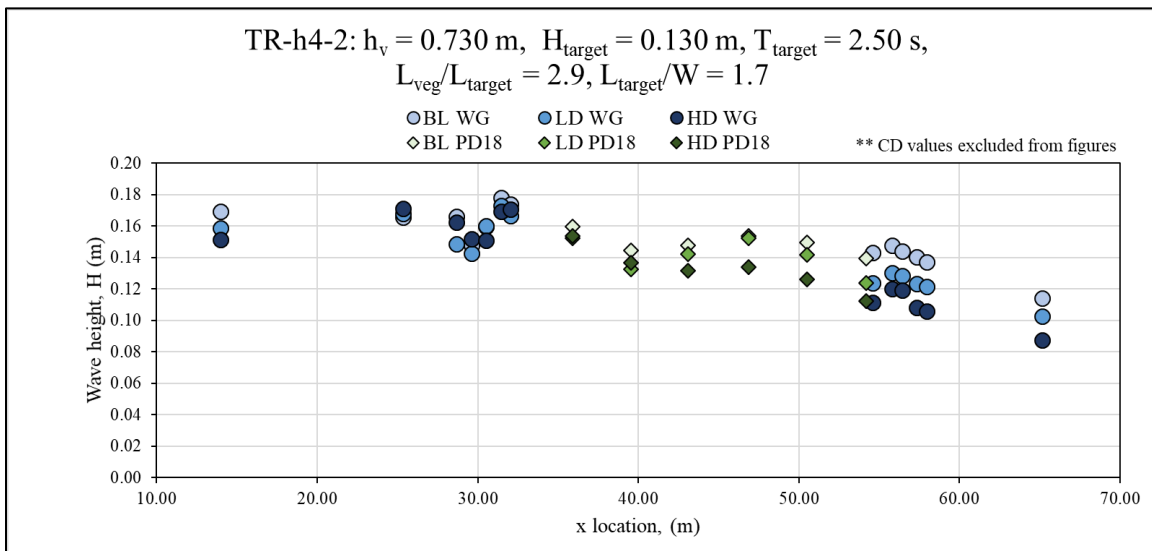


Figure 9-87 Wave height, H , with respect to x location for wave gauges (WG, circles) and pressure gauges(PD, diamonds) for the high-density (HD) (dark colors), low-density (LD) (intermediate colors), and baseline (BL) (light colors) layouts for regular wave case TR-h4-2.

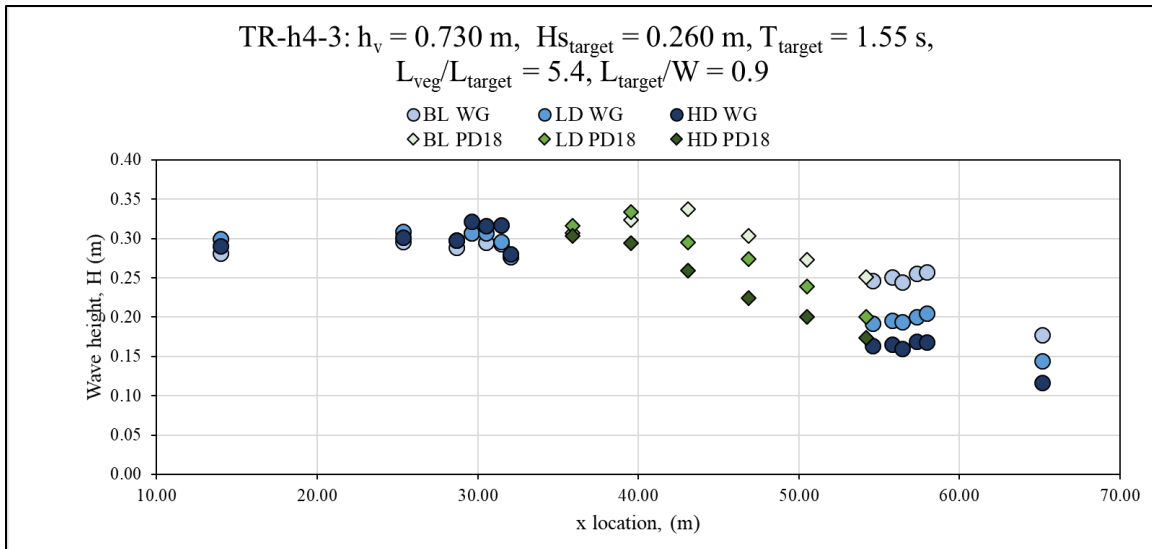


Figure 9-88 Wave height, H , with respect to x location for wave gauges (WG, circles) and pressure gauges(PD, diamonds) for the high-density (HD) (dark colors), low-density (LD) (intermediate colors), and baseline(BL) (light colors) layouts for regular wave case TR-h4-3.

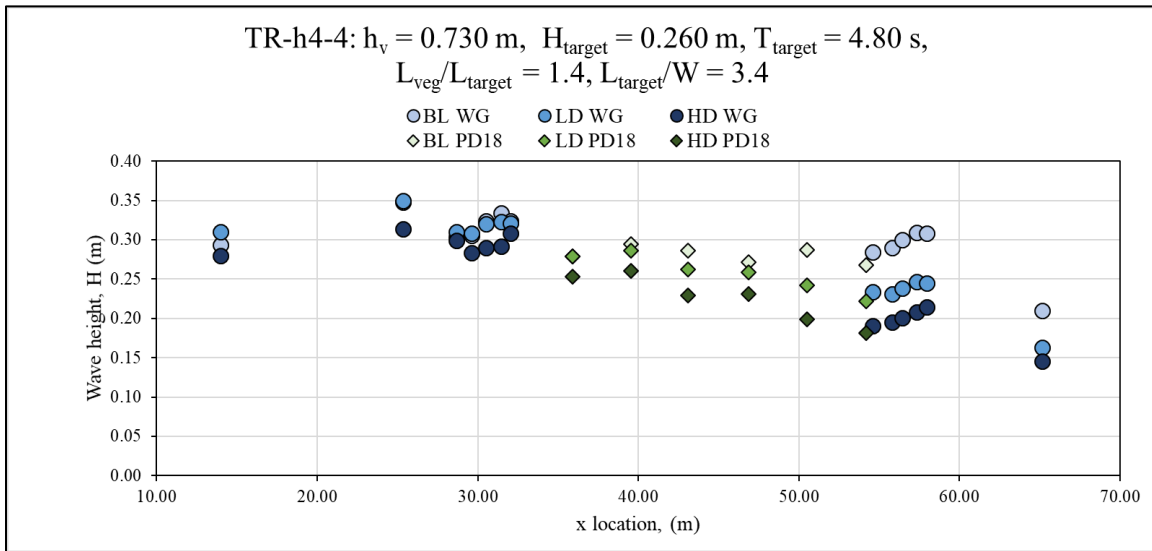


Figure 9-89 Wave height, H , with respect to x location for wave gauges (WG, circles) and pressure gauges(PD, diamonds) for the high-density (HD) (dark colors), low-density (LD) (intermediate colors), and baseline (BL) (light colors) layouts for regular wave case TR-h4-4.

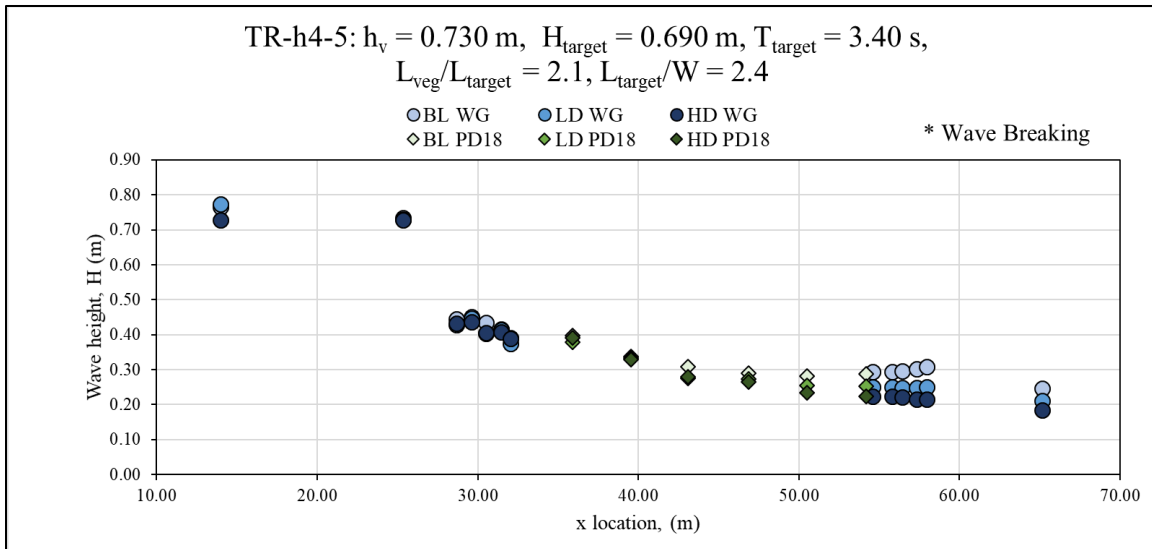


Figure 9-90 Wave height, H , with respect to x location for wave gauges (WG, circles) and pressure gauges(PD, diamonds) for the high-density (HD) (dark colors), low-density (LD) (intermediate colors), and baseline (BL) (light colors) layouts for regular wave case TR-h4-5.

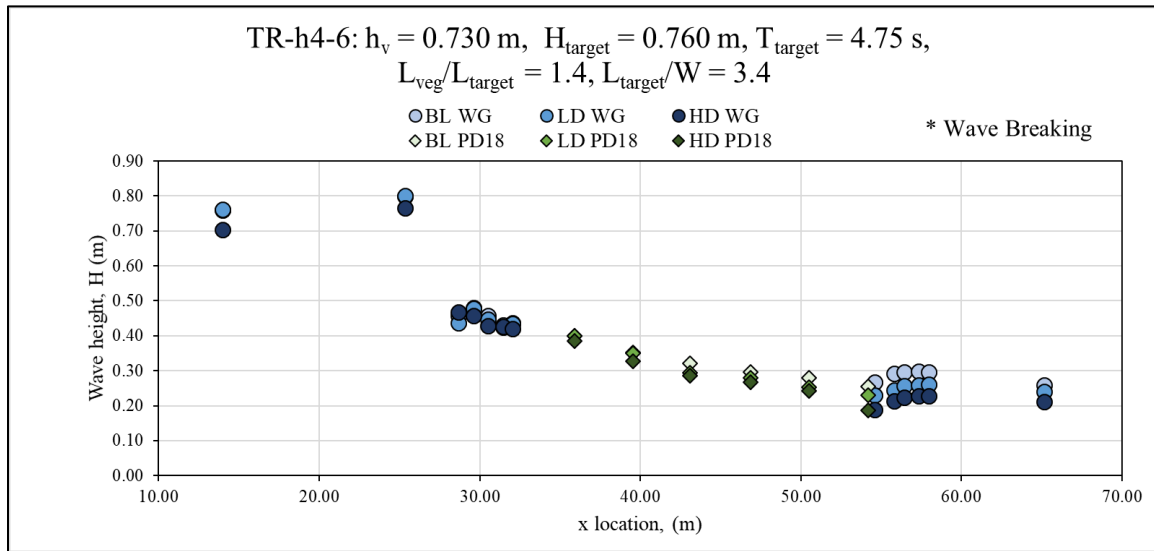


Figure 9-91 Wave height, H , with respect to x location for wave gauges (WG, circles) and pressure gauges(PD, diamonds) for the high-density (HD) (dark colors), low-density (LD) (intermediate colors), and baseline (BL) (light colors) layouts for regular wave case TR-h4-6.

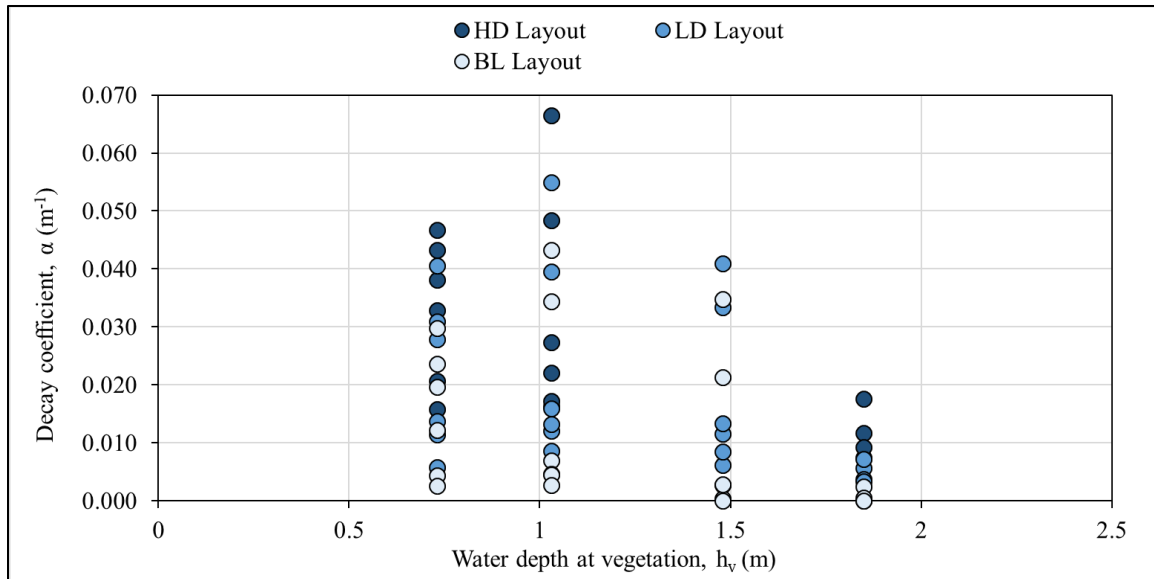


Figure 9-92 Wave height decay coefficient, α , versus the water depth at the vegetation, h_v , for the High-density (HD) (dark blue circles), low-density (LD) (intermediate blue circles), and baseline (BL) (light blue circles) layouts.

Table 9-23 Table of wave height decay coefficients, α , and $\alpha \pm \sigma$, for the regular wave cases with measured H and T values at PD18-1.

Trial	Layout	h_v	H PD18 -1	T PD18 -1	α	σ	$\alpha - \sigma$	$\alpha + \sigma$
(-)	(-)	(m)	(m)	(s)	(m^{-1})	(m)	(m^{-1})	(m^{-1})
TR-h1-1	HD	1.85	0.57	2.52	1.2E-02	1.4E-03	1.0E-02	1.3E-02
	LD	1.85	0.58	2.52	5.7E-03	1.6E-03	4.1E-03	7.3E-03
	BL	1.85	0.56	2.52	2.4E-03	1.5E-03	9.3E-04	3.9E-03
TR-h1-2**	HD	1.85	0.52	4.10	7.5E-03	1.4E-03	6.1E-03	8.9E-03
	LD	1.85	0.52	4.10	3.8E-03	2.1E-03	1.7E-03	5.9E-03
	BL	1.85	0.49	4.10	1.0E-05	2.8E-03	-2.8E-03	2.8E-03
TR-h1-3	HD	1.85	1.09	2.52	1.8E-02	2.4E-03	1.5E-02	2.0E-02
	LD	1.85	1.11	2.48	7.3E-03	3.3E-03	4.0E-03	1.1E-02
	BL	1.85	1.07	2.48	5.0E-04	8.7E-04	-3.8E-04	1.4E-03
TR-h1-4	HD	1.85	0.91	7.80	9.2E-03	9.2E-03	7.4E-05	1.8E-02
	LD	1.85	0.90	7.80	3.4E-03	6.6E-03	-3.2E-03	1.0E-02
	BL	1.85	0.86	7.80	1.7E-05	5.0E-03	-5.0E-03	5.0E-03
TR-h2-1	LD	1.48	0.40	2.24	1.2E-02	2.1E-03	9.5E-03	1.4E-02
	BL	1.48	0.37	2.24	2.7E-03	2.1E-03	5.9E-04	4.8E-03
TR-h2-2	LD	1.48	0.35	3.64	6.1E-03	3.4E-03	2.8E-03	9.5E-03
	BL	1.48	0.33	3.64	4.1E-04	3.4E-03	-3.0E-03	3.8E-03
TR-h2-3**	LD	1.48	0.77	2.24	1.3E-02	5.6E-03	7.8E-03	1.9E-02
	BL	1.48	0.69	2.24	1.1E-05	2.8E-03	-2.8E-03	2.8E-03
TR-h2-4	LD	1.48	0.70	6.83	8.5E-03	5.6E-03	2.9E-03	1.4E-02
	BL	1.48	0.68	6.83	2.9E-03	6.3E-03	-3.4E-03	9.1E-03
TR-h2-5*	LD	1.48	1.01	3.72	4.1E-02	3.3E-03	3.8E-02	4.4E-02
	BL	1.48	0.99	3.72	3.5E-02	2.2E-03	3.3E-02	3.7E-02
TR-h2-6*	LD	1.48	1.21	6.83	3.3E-02	6.7E-03	2.7E-02	4.0E-02
	BL	1.48	1.12	6.83	2.1E-02	8.3E-03	1.3E-02	3.0E-02
TR-h3-1**	HD	1.03	0.23	1.86	1.6E-02	4.5E-03	1.2E-02	2.1E-02
	LD	1.03	0.23	1.86	1.2E-02	6.7E-03	5.5E-03	1.9E-02
	BL	1.03	0.25	1.86	7.0E-03	4.5E-03	2.5E-03	1.2E-02
TR-h3-2	HD	1.03	0.22	2.98	1.7E-02	2.0E-03	1.5E-02	1.9E-02
	LD	1.03	0.23	2.98	8.7E-03	2.0E-03	6.6E-03	1.1E-02
	BL	1.03	0.22	2.98	4.7E-03	1.7E-03	3.0E-03	6.3E-03
TR-h3-3	HD	1.03	0.46	1.86	2.7E-02	6.1E-03	2.1E-02	3.3E-02
	LD	1.03	0.48	1.86	1.6E-02	6.7E-03	9.2E-03	2.3E-02
	BL	1.03	0.49	1.86	4.5E-03	4.2E-03	2.5E-04	8.7E-03
TR-h3-4	HD	1.03	0.44	5.65	2.2E-02	5.2E-03	1.7E-02	2.7E-02
	LD	1.03	0.46	5.65	1.3E-02	5.0E-03	8.3E-03	1.8E-02
	BL	1.03	0.46	5.65	2.7E-03	3.6E-03	-9.2E-04	6.2E-03
TR-h3-5*	HD	1.03	0.63	4.10	4.8E-02	5.2E-03	4.3E-02	5.4E-02
	LD	1.03	0.63	4.10	3.9E-02	5.5E-03	3.4E-02	4.5E-02
	BL	1.03	0.66	4.10	3.4E-02	7.2E-03	2.7E-02	4.2E-02
TR-h3-6*	HD	1.03	0.81	6.07	6.6E-02	6.2E-03	6.0E-02	7.3E-02
	LD	1.03	0.81	5.65	5.5E-02	7.1E-03	4.8E-02	6.2E-02
	BL	1.03	0.78	5.65	4.3E-02	5.3E-03	3.8E-02	4.9E-02
TR-h4-1**	HD	1.03	0.16	1.55	3.3E-02	1.1E-02	2.2E-02	4.4E-02
	LD	1.03	0.16	1.56	1.1E-02	9.4E-03	2.0E-03	2.1E-02
	BL	1.03	0.17	1.55	2.0E-02	1.6E-02	4.1E-03	3.5E-02
TR-h4-2**	HD	1.03	0.15	2.48	1.6E-02	4.8E-03	1.1E-02	2.1E-02
	LD	1.03	0.15	2.48	5.8E-03	7.7E-03	-1.9E-03	1.4E-02
	BL	1.03	0.16	2.48	4.3E-03	4.1E-03	2.1E-04	8.4E-03
TR-h4-3	HD	1.03	0.30	1.56	3.8E-02	8.5E-03	3.0E-02	4.7E-02
	LD	1.03	0.32	1.56	2.8E-02	1.1E-02	1.7E-02	3.9E-02
	BL	1.03	0.31	1.56	1.2E-02	8.8E-03	3.5E-03	2.1E-02
TR-h4-4	HD	1.03	0.25	4.82	2.1E-02	7.4E-03	1.3E-02	2.8E-02
	LD	1.03	0.28	4.82	1.4E-02	4.1E-03	9.7E-03	1.8E-02
	BL	1.03	0.28	4.82	2.5E-03	3.3E-03	-7.6E-04	5.8E-03
TR-h4-5*	HD	1.03	0.39	3.41	4.3E-02	5.1E-03	3.8E-02	4.8E-02
	LD	1.03	0.38	3.41	3.1E-02	7.6E-03	2.3E-02	3.9E-02
	BL	1.03	0.40	3.41	2.4E-02	7.2E-03	1.6E-02	3.1E-02
TR-h4-6*	HD	1.03	0.38	4.82	4.7E-02	8.1E-03	3.9E-02	5.5E-02
	LD	1.03	0.40	4.82	4.1E-02	3.9E-03	3.7E-02	4.4E-02
	BL	1.03	0.40	4.82	3.0E-02	1.9E-03	2.8E-02	3.2E-02

* Wave Breaking, ** C_D values excluded from figures

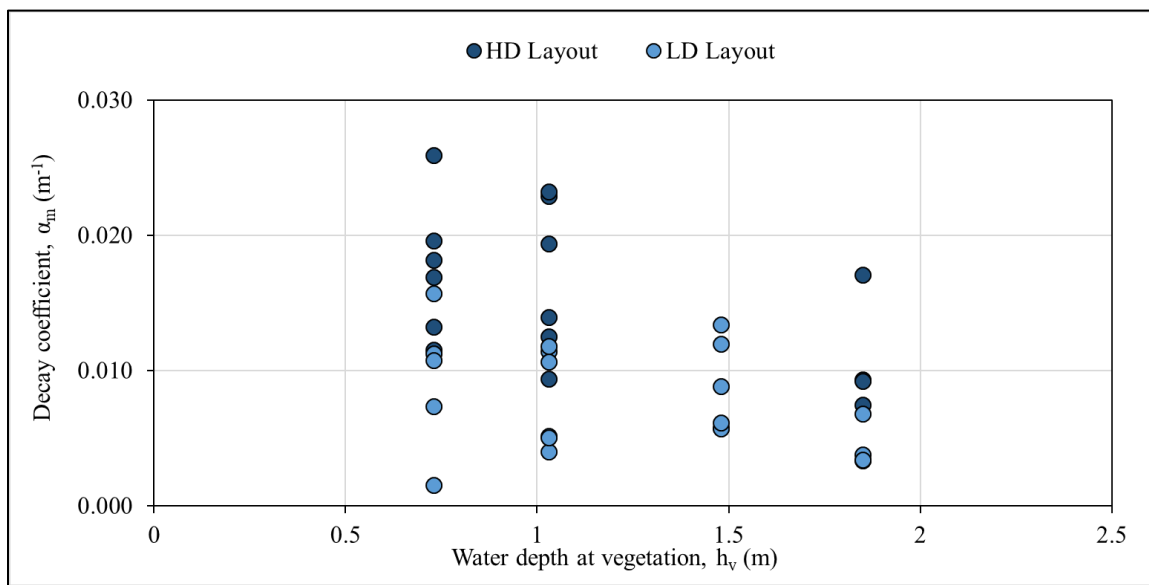


Figure 9-93 Model forest wave height decay coefficient for regular waves, α_m , versus water depth at the vegetation, h_v , for high-density (HD) (dark blue circles), low-density (LD) (intermediate blue circles), and baseline (BL) (light blue circles) layouts.

Table 9-24 Summary table of wave height decay due to model forest, α_m , and the HD/LD ratio of the α_m coefficient with measured H and T values at PD18-1 for regular wave cases.

Trial	Layout	h_v	H PD18 -1	T PD18 -1	α_m	HD/LD α_m ratio
(-)	(-)	(m)	(m)	(s)	(m ⁻¹)	(m)
TR-h1-1	HD	1.85	0.57	2.52	9.32E-03	2.8
	LD	1.85	0.58	2.52	3.32E-03	
TR-h1-2**	HD	1.85	0.52	4.10	7.44E-03	2.0
	LD	1.85	0.52	4.10	3.80E-03	
TR-h1-3	HD	1.85	1.09	2.52	1.71E-02	2.5
	LD	1.85	1.11	2.48	6.77E-03	
TR-h1-4	HD	1.85	0.91	7.80	9.22E-03	2.7
	LD	1.85	0.90	7.80	3.38E-03	
TR-h2-1	LD	1.48	0.40	2.24	8.83E-03	-
TR-h2-2	LD	1.48	0.35	3.64	5.73E-03	-
TR-h2-3**	LD	1.48	0.77	2.24	1.34E-02	-
TR-h2-4	LD	1.48	0.70	6.83	5.68E-03	-
TR-h2-5*	LD	1.48	1.01	3.72	6.13E-03	-
TR-h2-6*	LD	1.48	1.21	6.83	1.20E-02	-
TR-h3-1**	HD	1.03	0.23	1.86	9.36E-03	1.8
	LD	1.03	0.23	1.86	5.13E-03	
TR-h3-2	HD	1.03	0.22	2.98	1.25E-02	3.1
	LD	1.03	0.23	2.98	4.01E-03	
TR-h3-3	HD	1.03	0.46	1.86	2.29E-02	2.0
	LD	1.03	0.48	1.86	1.14E-02	
TR-h3-4	HD	1.03	0.44	5.65	1.94E-02	1.8
	LD	1.03	0.46	5.65	1.06E-02	
TR-h3-5*	HD	1.03	0.63	4.10	1.40E-02	2.8
	LD	1.03	0.63	4.10	5.02E-03	
TR-h3-6*	HD	1.03	0.81	6.07	2.32E-02	2.0
	LD	1.03	0.81	5.65	1.18E-02	
TR-h4-1**	HD	1.03	0.16	1.55	1.32E-02	-
	LD	1.03	0.16	1.56	-	
TR-h4-2**	HD	1.03	0.15	2.48	1.15E-02	7.6
	LD	1.03	0.15	2.48	1.51E-03	
TR-h4-3	HD	1.03	0.30	1.56	2.59E-02	1.7
	LD	1.03	0.32	1.56	1.57E-02	
TR-h4-4	HD	1.03	0.25	4.82	1.82E-02	1.6
	LD	1.03	0.28	4.82	1.12E-02	
TR-h4-5*	HD	1.03	0.39	3.41	1.96E-02	2.7
	LD	1.03	0.38	3.41	7.32E-03	
TR-h4-6*	HD	1.03	0.38	4.82	1.69E-02	1.6
	LD	1.03	0.40	4.82	1.08E-02	
Average HD/LD α_m ratio:						2.6

* Wave Breaking, **C_D values excluded from figures

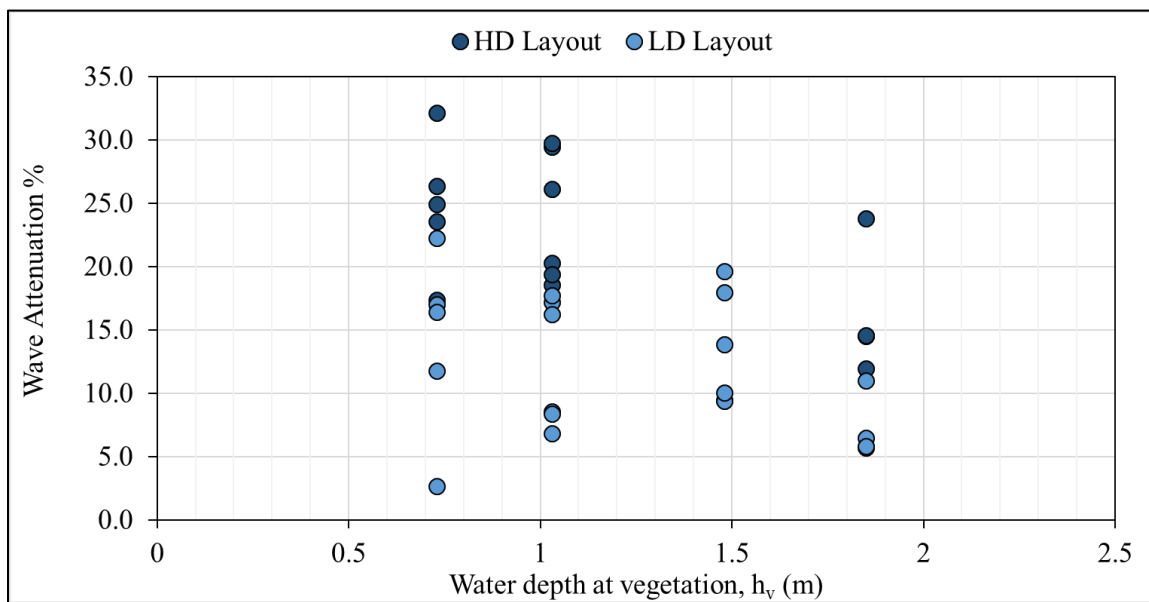


Figure 9-94 Percent of wave attenuation for the regular wave cases due to the model forest versus the water depth at the vegetation, h_v , for the high-density (HD) (dark blue circles) and low-density (LD) (intermediate blue circles) layouts.

Table 9-25 Summary table of percent of wave attenuation for the regular wave cases with measured values of H and T at PD18-1.

Trial	Layout	h_v	H PD18 - 1	T PD18 - 1	Wave Attenuation
(-)	(-)	(m)	(m)	(s)	(%)
TR-h1-1	HD	1.85	0.57	2.52	15
	LD	1.85	0.58	2.52	6
TR-h1-2**	HD	1.85	0.52	4.10	12
	LD	1.85	0.52	4.10	7
TR-h1-3	HD	1.85	1.09	2.52	24
	LD	1.85	1.11	2.48	11
TR-h1-4	HD	1.85	0.91	7.80	14
	LD	1.85	0.90	7.80	6
TR-h2-1	LD	1.48	0.40	2.24	14
TR-h2-2	LD	1.48	0.35	3.64	9
TR-h2-3**	LD	1.48	0.77	2.24	20
TR-h2-4	LD	1.48	0.70	6.83	9
TR-h2-5*	LD	1.48	1.01	3.72	10
TR-h2-6*	LD	1.48	1.21	6.83	18
TR-h3-1**	HD	1.03	0.23	1.86	15
	LD	1.03	0.23	1.86	9
TR-h3-2	HD	1.03	0.22	2.98	19
	LD	1.03	0.23	2.98	7
TR-h3-3	HD	1.03	0.46	1.86	30
	LD	1.03	0.48	1.86	17
TR-h3-4	HD	1.03	0.44	5.65	26
	LD	1.03	0.46	5.65	16
TR-h3-5*	HD	1.03	0.63	4.10	20
	LD	1.03	0.63	4.10	8
TR-h3-6*	HD	1.03	0.81	6.07	30
	LD	1.03	0.81	5.65	18
TR-h4-1**	HD	1.03	0.16	1.55	19
	LD	1.03	0.16	1.56	-
TR-h4-2**	HD	1.03	0.15	2.48	17
	LD	1.03	0.15	2.48	3
TR-h4-3	HD	1.03	0.30	1.56	32
	LD	1.03	0.32	1.56	22
TR-h4-4	HD	1.03	0.25	4.82	25
	LD	1.03	0.28	4.82	17
TR-h4-5*	HD	1.03	0.39	3.41	26
	LD	1.03	0.38	3.41	12
TR-h4-6*	HD	1.03	0.38	4.82	24
	LD	1.03	0.40	4.82	16

* Wave Breaking, **C_D values excluded from figures

Appendix K.2 Drag Coefficients

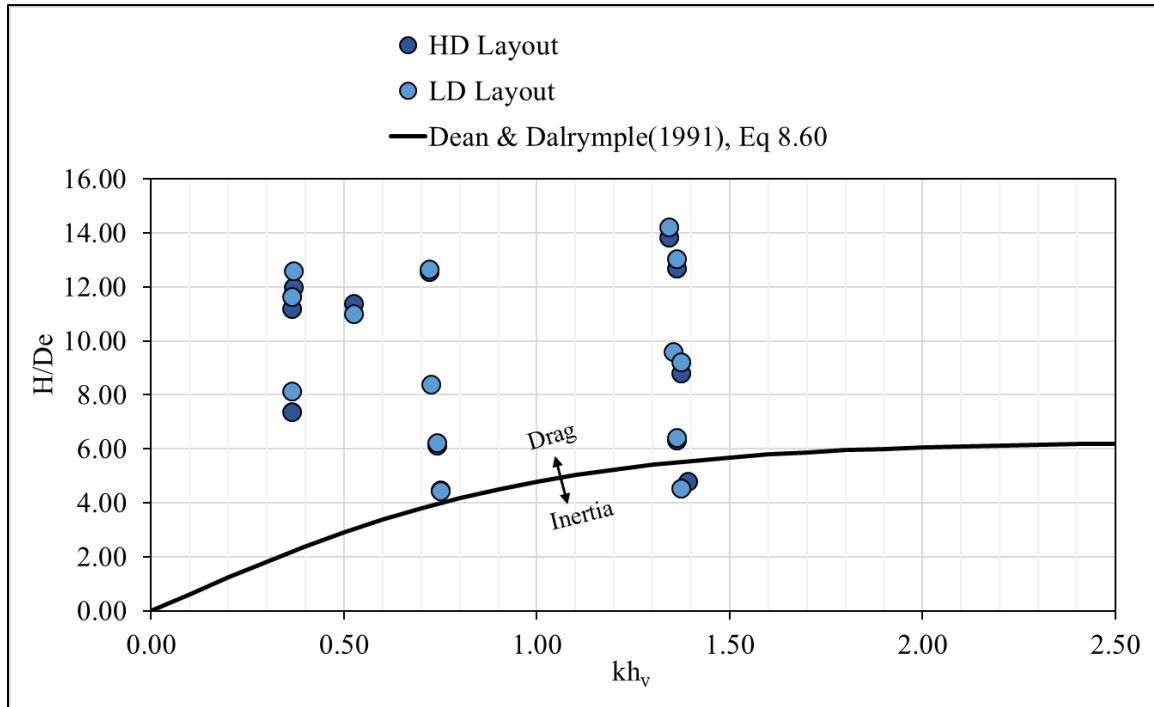


Figure 9-95 Ratio of the spectral estimation of the wave height, H , over the effective diameter, D_e , versus the relative water depth, kh_v , for the regular wave cases at the high-density (HD) (dark blue circles) and low-density (LD) (intermediate blue circles) layouts compared to Equation 8.60 from Dean and Dalrymple (1991) (solid black line).

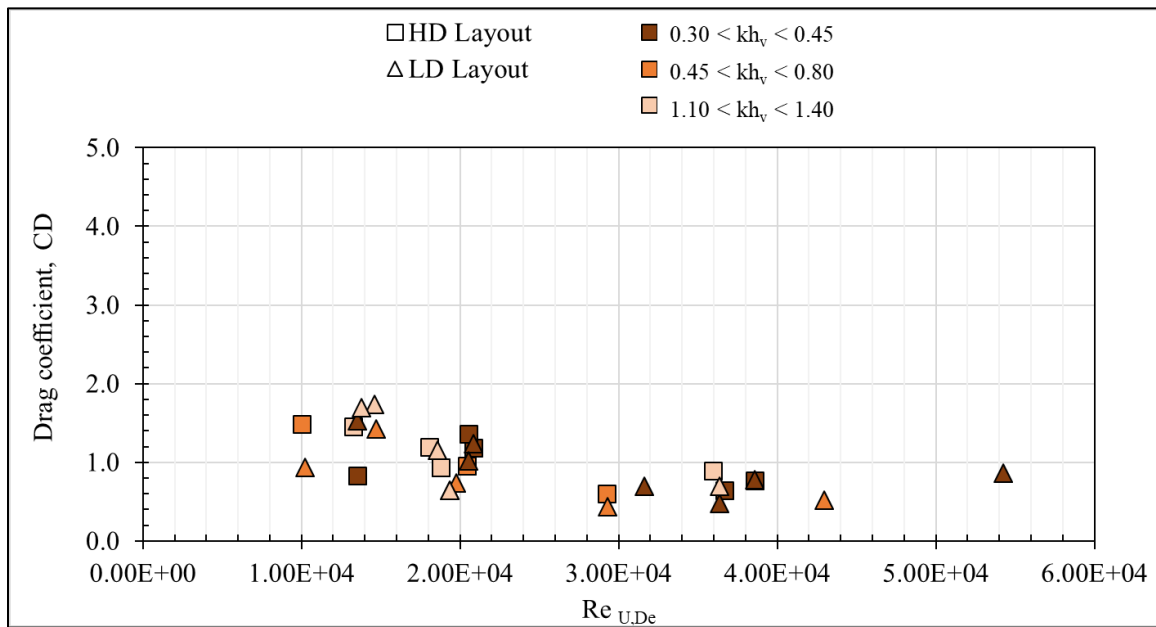


Figure 9-96 Drag coefficient, C_D , versus the Reynolds number, $Re_{U,De}$, for the regular wave cases at high-density (HD) (squares) and low-density (LD) (triangles) layouts designated by relative water depth, kh_v , range.

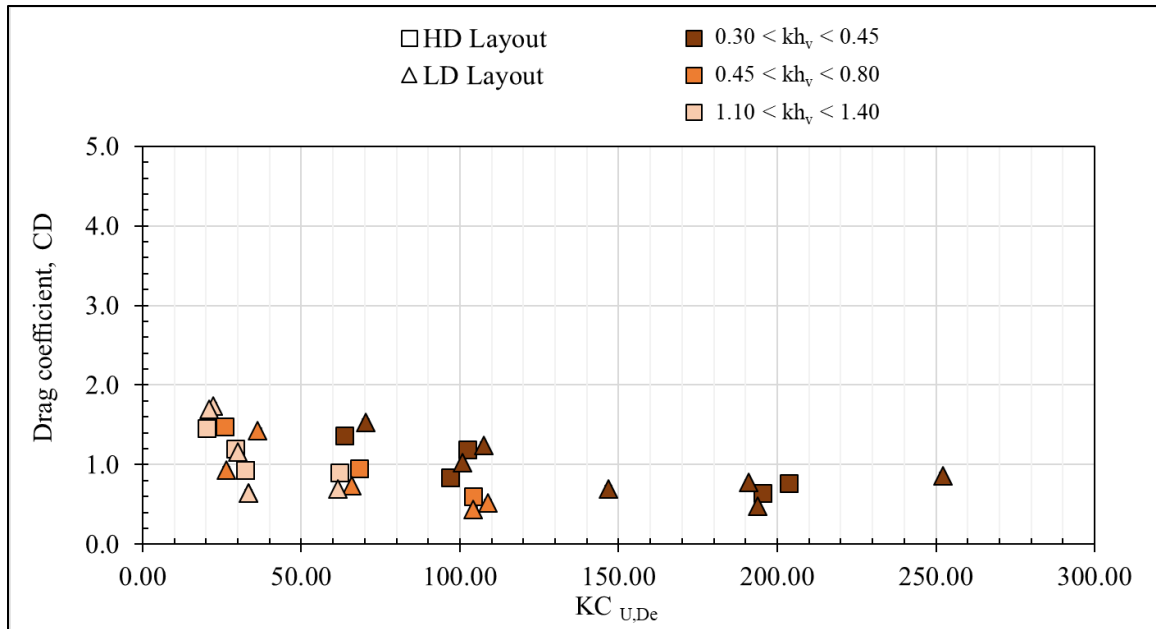


Figure 9-97 Drag coefficient, C_D , versus the Keulegan-Carpenter number, $KC_{U,De}$, for the regular wave cases at high-density (HD) (squares) and low-density (LD) (triangles) layouts designated by relative water depth, kh_v , range.

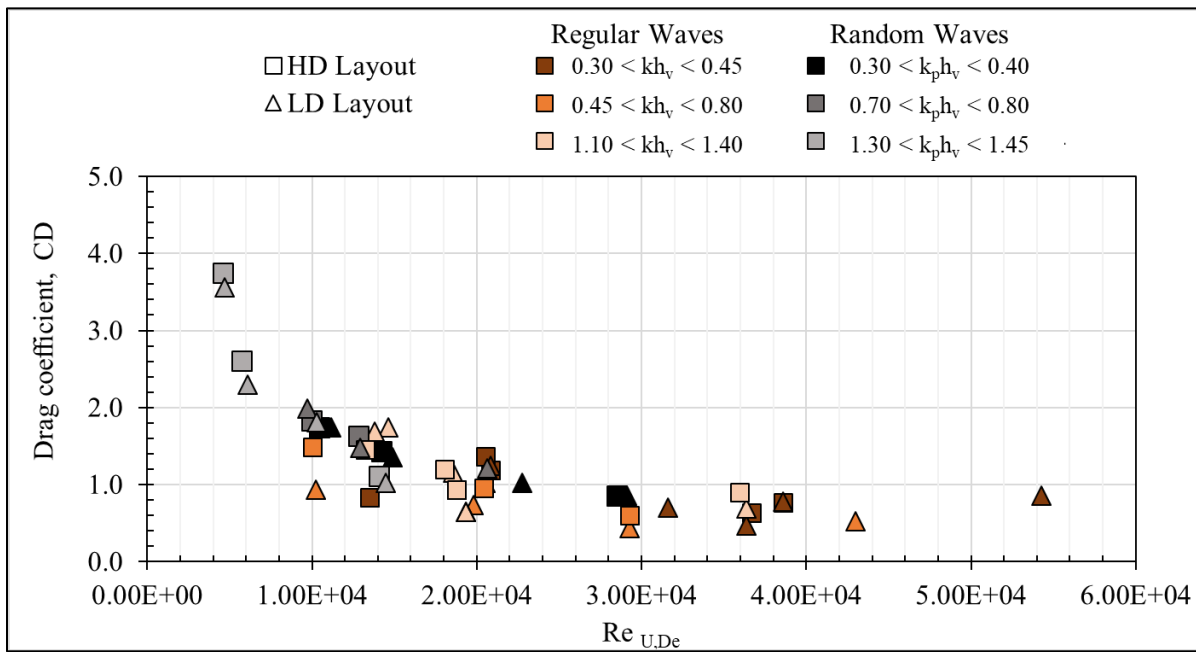


Figure 9-98 Drag coefficient, C_D , versus the Reynolds number, $Re_{U,De}$, for the regular wave cases (orange scale symbols) and random wave cases (gray scale symbols) at the high-density (HD) (squares) and low-density (LD) (triangles) layouts designated by relative water depths, kh_v , and $k_p h_v$, ranges.

Table 9-26 Summary table of regular wave cases with measured H and T values at PD18-1, kh_v, H/D_e, Predominant force based on Figure 9-95, Re_{U,De}, KC_{U,De}, and C_D values.

Trial	Layout	<i>h_v</i>	<i>H</i> PD18 -1	<i>T</i> PD18 -1	<i>kh_v</i>	<i>H_{m0}/D_e</i>	Predominant Force	<i>Re_{U,De}</i>	<i>KC_{U,De}</i>	<i>C_D</i>
(-)	(-)	(m)	(m)	(s)	(-)	(-)	(Drag/Inertia)	(-)	(-)	(-)
TR-h1-1	HD	1.85	0.57	2.52	1.34	13.84	Drag	52313	11.6	0.94
	LD	1.85	0.58	2.52	1.34	14.24	Drag	53832	12.0	0.65
TR-h1-2**	HD	1.85	0.52	4.10	0.72	12.56	Drag	54531	19.7	0.90
	LD	1.85	0.52	4.10	0.72	12.66	Drag	54975	19.9	0.91
TR-h1-3	HD	1.85	1.09	2.52	1.34	26.47	Drag	100095	22.2	0.90
	LD	1.85	1.11	2.48	1.37	26.96	Drag	101193	22.1	0.69
TR-h1-4	HD	1.85	0.91	7.80	0.36	22.21	Drag	102044	70.2	0.64
	LD	1.85	0.90	7.80	0.36	22.02	Drag	101171	69.6	0.47
TR-h2-1	LD	1.48	0.40	2.24	1.35	9.61	Drag	40606	8.0	1.74
TR-h2-2	LD	1.48	0.35	3.64	0.72	8.41	Drag	40860	13.1	1.42
TR-h2-3**	LD	1.48	0.77	2.24	1.35	18.71	Drag	79066	15.6	1.35
TR-h2-4	LD	1.48	0.70	6.83	0.37	17.08	Drag	87831	52.9	0.70
TR-h2-5*	LD	1.48	1.01	3.72	0.71	24.47	Drag	119381	39.2	0.52
TR-h2-6*	LD	1.48	1.21	6.83	0.37	29.31	Drag	150760	90.7	0.86
TR-h3-1**	HD	1.03	0.23	1.86	1.36	6.32	Drag	28262	4.6	0.98
	LD	1.03	0.23	1.86	1.36	6.42	Drag	28716	4.7	1.06
TR-h3-2	HD	1.03	0.22	2.98	0.74	6.15	Drag	31588	8.3	1.48
	LD	1.03	0.23	2.98	0.74	6.24	Drag	32082	8.4	0.93
TR-h3-3	HD	1.03	0.46	1.86	1.36	12.68	Drag	56708	9.3	1.19
	LD	1.03	0.48	1.86	1.36	13.06	Drag	58366	9.6	1.15
TR-h3-4	HD	1.03	0.44	5.65	0.37	12.00	Drag	65415	32.6	1.19
	LD	1.03	0.46	5.65	0.37	12.59	Drag	68666	34.2	1.24
TR-h3-5*	HD	1.03	0.63	4.10	0.52	17.21	Drag	91964	33.2	0.59
	LD	1.03	0.63	4.10	0.52	17.23	Drag	92066	33.2	0.43
TR-h3-6*	HD	1.03	0.81	6.07	0.34	22.17	Drag	121211	64.9	0.77
	LD	1.03	0.81	5.65	0.37	22.38	Drag	122008	60.8	0.77
TR-h4-1**	HD	1.03	0.16	1.55	1.39	4.79	Inertia	23827	3.2	1.36
	LD	1.03	0.16	1.56	1.37	4.55	Inertia	-	-	-
TR-h4-2**	HD	1.03	0.15	2.48	0.75	4.48	Drag	25739	5.6	1.40
	LD	1.03	0.15	2.48	0.75	4.44	Drag	25488	5.6	0.37
TR-h4-3	HD	1.03	0.30	1.56	1.37	8.83	Drag	44090	6.1	1.45
	LD	1.03	0.32	1.56	1.37	9.21	Drag	46012	6.3	1.69
TR-h4-4	HD	1.03	0.25	4.82	0.36	7.37	Drag	45007	19.1	1.36
	LD	1.03	0.28	4.82	0.36	8.14	Drag	49707	21.1	1.53
TR-h4-5*	HD	1.03	0.39	3.41	0.52	11.38	Drag	68010	20.5	0.95
	LD	1.03	0.38	3.41	0.52	11.02	Drag	65885	19.8	0.73
TR-h4-6*	HD	1.03	0.38	4.82	0.36	11.20	Drag	68454	29.1	0.83
	LD	1.03	0.40	4.82	0.36	11.65	Drag	71178	30.2	1.02

* Wave Breaking, **C_D values excluded from figures

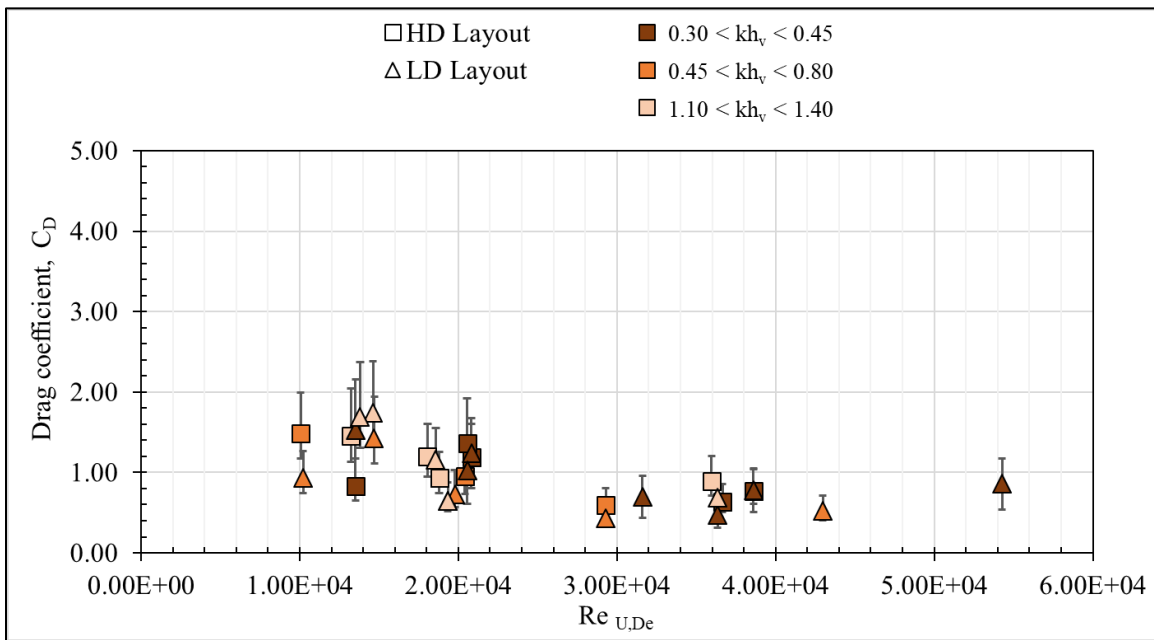


Figure 9-99 Drag coefficient, C_D , versus the Reynolds number, $Re_{U,De}$, for the regular wave cases at high-density (HD) (squares) and low-density (LD) (triangles) layouts designated by relative water depth, $k_p h_v$, range with limit bars (grey vertical bars) due to the mean projected area per unit height per tree uncertainty, $A_{t,m} \pm \sigma_{t,m}$.

Table 9-27 Summary table of regular wave cases with measured H and T values at PD18-1, kh_v, Re_{U,De}, C_D, C_D, A_{t,m} + σ_{t,m}, and C_D, A_{t,m} - σ_{t,m}, values.

Trial	Layout	h _v	H PD18 -1	T PD18 -1	kh _v	Re _{U,De}	C _D	C _D , A _m + σ _m	C _D , A _m - σ _m
(-)	(-)	(m)	(m)	(s)	(-)	(-)	(-)	(-)	(-)
TR-h1-1	HD	1.85	0.57	2.52	1.34	52313	0.94	0.74	1.26
	LD	1.85	0.58	2.52	1.34	53832	0.65	0.51	0.87
TR-h1-2**	HD	1.85	0.52	4.10	0.72	54531	0.90	0.72	1.22
	LD	1.85	0.52	4.10	0.72	54975	0.91	0.73	1.23
TR-h1-3	HD	1.85	1.09	2.52	1.34	100095	0.90	0.71	1.21
	LD	1.85	1.11	2.48	1.37	101193	0.69	0.55	0.93
TR-h1-4	HD	1.85	0.91	7.80	0.36	102044	0.64	0.51	0.86
	LD	1.85	0.90	7.80	0.36	101171	0.47	0.38	0.64
TR-h2-1	LD	1.48	0.40	2.24	1.35	40606	1.74	1.37	2.38
TR-h2-2	LD	1.48	0.35	3.64	0.72	40860	1.42	1.12	1.95
TR-h2-3**	LD	1.48	0.77	2.24	1.35	79066	1.35	1.06	1.85
TR-h2-4	LD	1.48	0.70	6.83	0.37	87831	0.70	0.55	0.96
TR-h2-5*	LD	1.48	1.01	3.72	0.71	119381	0.52	0.41	0.72
TR-h2-6*	LD	1.48	1.21	6.83	0.37	150760	0.86	0.68	1.18
TR-h3-1**	HD	1.03	0.23	1.86	1.36	28262	0.98	0.78	1.32
	LD	1.03	0.23	1.86	1.36	28716	1.06	0.84	1.43
TR-h3-2	HD	1.03	0.22	2.98	0.74	31588	1.48	1.17	2.00
	LD	1.03	0.23	2.98	0.74	32082	0.93	0.74	1.26
TR-h3-3	HD	1.03	0.46	1.86	1.36	56708	1.19	0.95	1.61
	LD	1.03	0.48	1.86	1.36	58366	1.15	0.91	1.56
TR-h3-4	HD	1.03	0.44	5.65	0.37	65415	1.19	0.94	1.60
	LD	1.03	0.46	5.65	0.37	68666	1.24	0.99	1.68
TR-h3-5*	HD	1.03	0.63	4.10	0.52	91964	0.59	0.47	0.80
	LD	1.03	0.63	4.10	0.52	92066	0.43	0.34	0.58
TR-h3-6*	HD	1.03	0.81	6.07	0.34	121211	0.77	0.61	1.04
	LD	1.03	0.81	5.65	0.37	122008	0.77	0.61	1.05
TR-h4-1**	HD	1.03	0.16	1.55	1.39	23827	1.36	1.05	1.91
	LD	1.03	0.16	1.56	1.37	-	-	-	-
TR-h4-2**	HD	1.03	0.15	2.48	0.75	25739	1.40	1.09	1.98
	LD	1.03	0.15	2.48	0.75	25488	0.37	0.29	0.52
TR-h4-3	HD	1.03	0.30	1.56	1.37	44090	1.45	1.13	2.05
	LD	1.03	0.32	1.56	1.37	46012	1.69	1.31	2.37
TR-h4-4	HD	1.03	0.25	4.82	0.36	45007	1.36	1.06	1.92
	LD	1.03	0.28	4.82	0.36	49707	1.53	1.19	2.15
TR-h4-5*	HD	1.03	0.39	3.41	0.52	68010	0.95	0.74	1.34
	LD	1.03	0.38	3.41	0.52	65885	0.73	0.57	1.03
TR-h4-6*	HD	1.03	0.38	4.82	0.36	68454	0.83	0.65	1.17
	LD	1.03	0.40	4.82	0.36	71178	1.02	0.79	1.44

* Wave Breaking, **C_D values excluded from figures

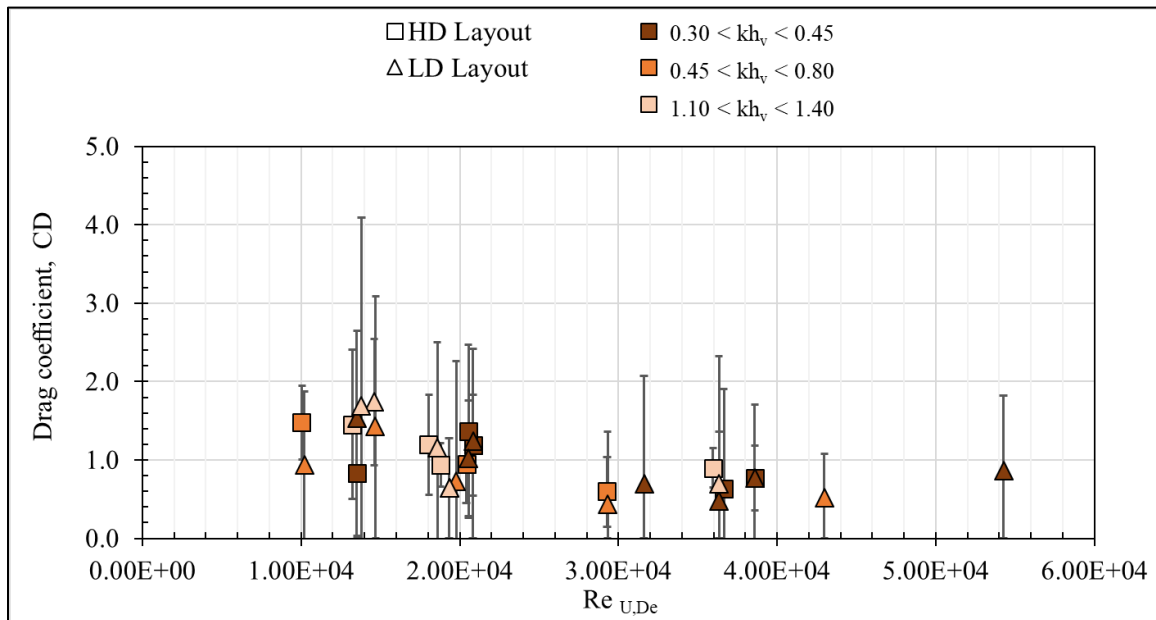


Figure 9-100 Drag coefficients, C_D , versus the Reynolds number, $Re_{U,De}$, for the regular wave cases at the high-density (HD) (squares) and low-density (LD) (triangles) layouts designated by relative water depth, kh_v , range with limit bars (grey vertical bars) due to the best fit wave height decay uncertainty, $\alpha_m \pm \sigma$.

Table 9-28 Summary table of the regular wave cases with measured H and T values at PD18-1, kh_v, Re_{U,De}, C_D, C_D, α_m + σ, and C_D, α_m - σ values.

Trial	Layout	h _v	H PD18 -1	T PD18 -1	kh _v	Re _{U,De}	α _m - σ	α _m + σ	C _D	C _D , α _m - σ	C _D , α _m + σ
(-)	(-)	(m)	(m)	(s)	(-)	(-)	(m ⁻¹)	(m ⁻¹)	(-)	(-)	(-)
TR-h1-1	HD	1.85	0.57	2.52	1.34	52313	7.94E-03	1.07E-02	0.94	0.80	1.07
	LD	1.85	0.58	2.52	1.34	53832	1.69E-03	4.94E-03	0.65	0.00	0.96
TR-h1-2**	HD	1.85	0.52	4.10	0.72	54531	6.04E-03	8.85E-03	0.90	0.73	1.07
	LD	1.85	0.52	4.10	0.72	54975	1.68E-03	5.93E-03	0.91	0.40	1.43
TR-h1-3	HD	1.85	1.09	2.52	1.34	100095	1.47E-02	1.95E-02	0.90	0.77	1.02
	LD	1.85	1.11	2.48	1.37	101193	3.52E-03	1.00E-02	0.69	0.00	1.02
TR-h1-4	HD	1.85	0.91	7.80	0.36	102044	5.67E-05	1.84E-02	0.64	0.00	1.27
	LD	1.85	0.90	7.80	0.36	101171	-3.24E-03	1.00E-02	0.47	0.00	1.40
TR-h2-1	LD	1.48	0.40	2.24	1.35	40606	4.72E-03	1.29E-02	1.74	0.93	2.55
TR-h2-2	LD	1.48	0.35	3.64	0.72	40860	-9.98E-04	1.25E-02	1.42	0.00	3.08
TR-h2-3**	LD	1.48	0.77	2.24	1.35	79066	2.23E-03	2.45E-02	1.35	0.23	2.48
TR-h2-4	LD	1.48	0.70	6.83	0.37	87831	-5.53E-03	1.69E-02	0.70	0.00	2.08
TR-h2-5*	LD	1.48	1.01	3.72	0.71	119381	-4.50E-04	1.27E-02	0.52	0.00	1.08
TR-h2-6*	LD	1.48	1.21	6.83	0.37	150760	-1.38E-03	2.53E-02	0.86	0.00	1.82
TR-h3-1**	HD	1.03	0.23	1.86	1.36	28262	4.86E-03	1.38E-02	0.98	0.51	1.45
	LD	1.03	0.23	1.86	1.36	28716	-1.52E-03	1.18E-02	1.06	0.00	2.42
TR-h3-2	HD	1.03	0.22	2.98	0.74	31588	1.05E-02	1.45E-02	1.48	1.24	1.71
	LD	1.03	0.23	2.98	0.74	32082	1.98E-03	6.04E-03	0.93	0.46	1.41
TR-h3-3	HD	1.03	0.46	1.86	1.36	56708	1.68E-02	2.90E-02	1.19	0.87	1.51
	LD	1.03	0.48	1.86	1.36	58366	4.70E-03	1.81E-02	1.15	0.47	1.83
TR-h3-4	HD	1.03	0.44	5.65	0.37	65415	1.42E-02	2.46E-02	1.19	0.87	1.51
	LD	1.03	0.46	5.65	0.37	68666	5.60E-03	1.57E-02	1.24	0.00	1.83
TR-h3-5*	HD	1.03	0.63	4.10	0.52	91964	8.75E-03	1.92E-02	0.59	0.37	0.82
	LD	1.03	0.63	4.10	0.52	92066	-4.64E-04	1.05E-02	0.43	0.00	0.89
TR-h3-6*	HD	1.03	0.81	6.07	0.34	121211	1.70E-02	2.95E-02	0.77	0.56	0.98
	LD	1.03	0.81	5.65	0.37	122008	4.71E-03	1.89E-02	0.77	0.31	1.24
TR-h4-1**	HD	1.03	0.16	1.55	1.39	23827	2.45E-03	2.39E-02	1.36	0.00	2.46
	LD	1.03	0.16	1.56	1.37	-	-1.77E-02	1.12E-03	-	-	-
TR-h4-2**	HD	1.03	0.15	2.48	0.75	25739	6.72E-03	1.63E-02	1.40	0.82	1.99
	LD	1.03	0.15	2.48	0.75	25488	-6.22E-03	9.24E-03	0.37	0.00	2.28
TR-h4-3	HD	1.03	0.30	1.56	1.37	44090	1.74E-02	3.44E-02	1.45	0.98	1.93
	LD	1.03	0.32	1.56	1.37	46012	4.50E-03	2.68E-02	1.69	0.48	2.89
TR-h4-4	HD	1.03	0.25	4.82	0.36	45007	1.08E-02	2.55E-02	1.36	0.81	1.92
	LD	1.03	0.28	4.82	0.36	49707	7.13E-03	1.54E-02	1.53	0.00	2.09
TR-h4-5*	HD	1.03	0.39	3.41	0.52	68010	1.45E-02	2.47E-02	0.95	0.70	1.20
	LD	1.03	0.38	3.41	0.52	65885	-3.31E-04	1.50E-02	0.73	-0.03	1.50
TR-h4-6*	HD	1.03	0.38	4.82	0.36	68454	8.79E-03	2.50E-02	0.83	0.43	1.24
	LD	1.03	0.40	4.82	0.36	71178	6.86E-03	1.46E-02	1.02	0.65	1.39

* Wave Breaking, **C_D values excluded from figures

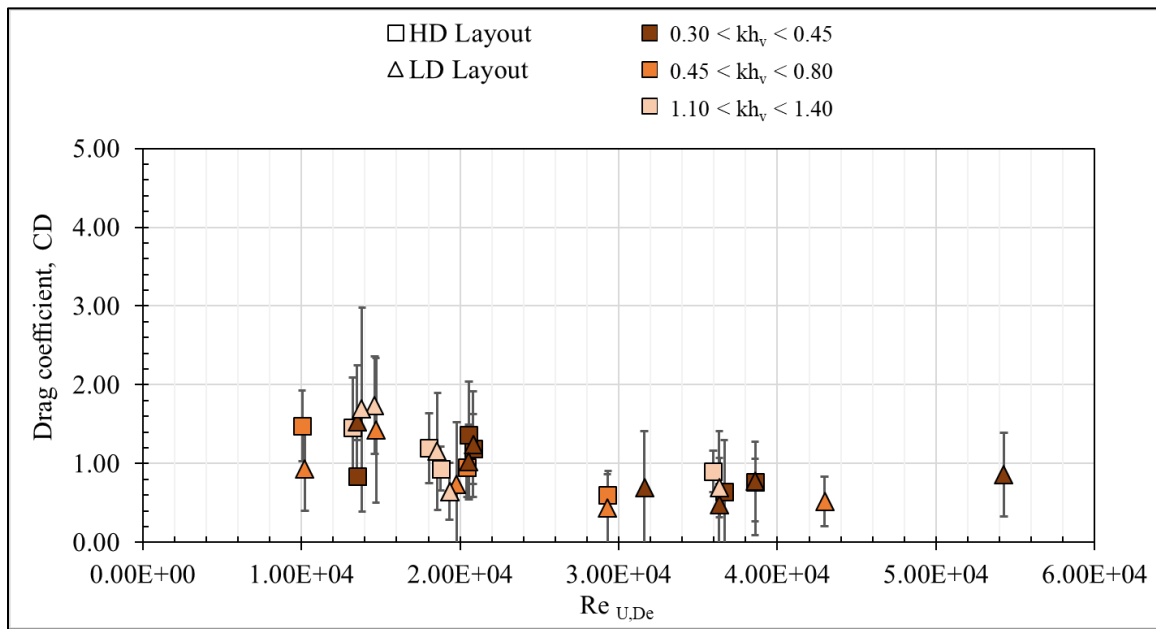


Figure 9-101 Drag coefficient, C_D , versus the Reynolds number, $Re_{U,De}$, for the regular wave cases at the high-density (HD) (squares) and low-density (LD) (triangles) layouts designated by relative water depth, kh_v , range with limit bars (grey vertical bars) from the combined uncertainty of the mean projected area per unit height per tree, $A_{t,m} \pm \sigma_{t,m}$, and the best fit wave height decay, $\alpha_m \pm \sigma$.

Table 9-29 Summary table of the regular wave cases with measured H and T values at PD18-1, kh_v, Re_{U,De}, C_D, σ_{CD}, C_D + σ_{CD}, and C_D - σ_{CD} values.

Trial	Layout	h _v	H PD18 -1	T PD18 -1	kh _v	Re _{U,De}	C _D	σ _{CD}	CD - σ _{CD}	CD + σ _{CD}
(-)	(-)	(m)	(m)	(s)	(-)	(-)	(-)	(-)	(-)	(-)
TR-h1-1	HD	1.85	0.57	2.52	1.34	52313	0.94	0.28	0.66	1.21
	LD	1.85	0.58	2.52	1.34	53832	0.65	0.36	0.29	1.01
TR-h1-2**	HD	1.85	0.52	4.10	0.72	54531	0.90	0.29	0.61	1.19
	LD	1.85	0.52	4.10	0.72	54975	0.91	0.56	0.35	1.48
TR-h1-3	HD	1.85	1.09	2.52	1.34	100095	0.90	0.26	0.63	1.16
	LD	1.85	1.11	2.48	1.37	101193	0.69	0.38	0.31	1.07
TR-h1-4	HD	1.85	0.91	7.80	0.36	102044	0.64	0.66	-0.02	1.29
	LD	1.85	0.90	7.80	0.36	101171	0.47	0.93	-0.46	1.41
TR-h2-1	LD	1.48	0.40	2.24	1.35	40606	1.74	0.62	1.12	2.36
TR-h2-2	LD	1.48	0.35	3.64	0.72	40860	1.42	0.92	0.50	2.34
TR-h2-3**	LD	1.48	0.77	2.24	1.35	79066	1.35	0.67	0.68	2.02
TR-h2-4	LD	1.48	0.70	6.83	0.37	87831	0.70	0.71	-0.02	1.41
TR-h2-5	LD	1.48	1.01	3.72	0.71	119381	0.52	0.31	0.21	0.83
TR-h2-6	LD	1.48	1.21	6.83	0.37	150760	0.86	0.53	0.33	1.39
TR-h3-1**	HD	1.03	0.23	1.86	1.36	28262	0.98	0.53	0.44	1.51
	LD	1.03	0.23	1.86	1.36	28716	1.06	1.39	-0.34	2.45
TR-h3-2	HD	1.03	0.22	2.98	0.74	31588	1.48	0.45	1.03	1.93
	LD	1.03	0.23	2.98	0.74	32082	0.93	0.53	0.40	1.46
TR-h3-3	HD	1.03	0.46	1.86	1.36	56708	1.19	0.44	0.75	1.63
	LD	1.03	0.48	1.86	1.36	58366	1.15	0.74	0.41	1.89
TR-h3-4	HD	1.03	0.44	5.65	0.37	65415	1.19	0.44	0.74	1.63
	LD	1.03	0.46	5.65	0.37	68666	1.24	0.67	0.57	1.91
TR-h3-5	HD	1.03	0.63	4.10	0.52	91964	0.59	0.27	0.32	0.86
	LD	1.03	0.63	4.10	0.52	92066	0.43	0.48	-0.05	0.91
TR-h3-6	HD	1.03	0.81	6.07	0.34	121211	0.77	0.29	0.48	1.06
	LD	1.03	0.81	5.65	0.37	122008	0.77	0.51	0.27	1.28
TR-h4-1**	HD	1.03	0.16	1.55	1.39	23827	1.36	1.17	0.18	2.53
	LD	1.03	0.16	1.56	1.37	-	-	-	-	-
TR-h4-2**	HD	1.03	0.15	2.48	0.75	25739	1.40	0.71	0.69	2.12
	LD	1.03	0.15	2.48	0.75	25488	0.37	1.91	-1.53	2.28
TR-h4-3	HD	1.03	0.30	1.56	1.37	44090	1.45	0.64	0.82	2.09
	LD	1.03	0.32	1.56	1.37	46012	1.69	1.30	0.39	2.98
TR-h4-4	HD	1.03	0.25	4.82	0.36	45007	1.36	0.68	0.68	2.04
	LD	1.03	0.28	4.82	0.36	49707	1.53	0.71	0.82	2.24
TR-h4-5	HD	1.03	0.39	3.41	0.52	68010	0.95	0.37	0.58	1.32
	LD	1.03	0.38	3.41	0.52	65885	0.73	0.79	-0.06	1.53
TR-h4-6	HD	1.03	0.38	4.82	0.36	68454	0.83	0.47	0.37	1.30
	LD	1.03	0.40	4.82	0.36	71178	1.02	0.47	0.55	1.49

* Wave Breaking, **C_D values excluded from figures

Appendix K.3 Harmonics

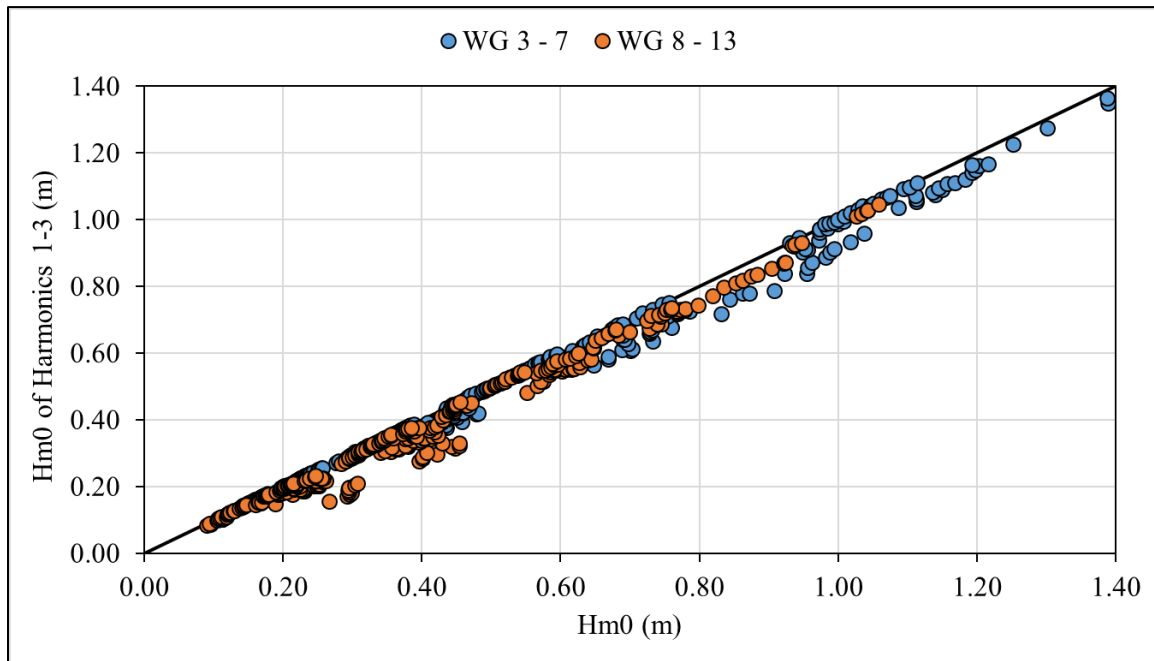


Figure 9-102 Spectral estimate of the significant wave height, H_{m0} , using harmonics 1 -3 versus the calculated spectral estimate of the significant wave height, H_{m0} , for the regular wave cases for WG 3 – 7 (blue circles) and WG 8 – 12 (orange circles). Black line represents agreement between values.

On average 98% and 93% of the total energy for the regular wave cases were contained in harmonics 1 – 3 for WG 3 – 7 and WG 8 – 12, respectively.

Table 9-30 Summary table of the average variance, var_{avg} , for harmonics 1 – 3 at WG 3 – 7 with the corresponding standard deviation of the variance, $\text{var}_{\text{avg}} \sigma$, for the baseline (BL) layout.

Trial	Layout	h_v	WG 3 - 7 var_{avg} , Harmonic 1	$\text{var}_{\text{avg}} \sigma$, Harmonic 1	WG 3 - 7 var_{avg} , Harmonic 2	$\text{var}_{\text{avg}} \sigma$, Harmonic 2	WG 3 - 7 var_{avg} , Harmonic 3	$\text{var}_{\text{avg}} \sigma$, Harmonic 3
(-)	(-)	(m)	(m ²)	(m ²)	(m ²)	(m ²)	(m ²)	(m ²)
TR-h1-1	BL	1.85	2.04E-02	6.01E-04	2.66E-04	6.50E-05	4.12E-06	2.77E-06
TR-h1-2**	BL	1.85	1.65E-02	6.44E-04	1.14E-03	1.64E-04	5.08E-05	1.18E-05
TR-h1-3	BL	1.85	6.37E-02	1.29E-03	3.75E-03	2.76E-04	3.85E-04	4.48E-05
TR-h1-4	BL	1.85	5.06E-02	2.07E-03	8.58E-03	1.08E-03	2.10E-03	4.43E-04
TR-h2-1	BL	1.48	8.15E-03	5.46E-04	7.27E-05	1.83E-05	1.52E-06	1.33E-06
TR-h2-2	BL	1.48	7.57E-03	2.65E-04	3.21E-04	4.08E-05	9.11E-06	4.29E-06
TR-h2-3**	BL	1.48	2.48E-02	1.62E-03	7.59E-04	1.41E-04	3.84E-05	1.94E-05
TR-h2-4	BL	1.48	2.09E-02	6.51E-04	3.18E-03	1.52E-04	7.39E-04	2.14E-04
TR-h2-5*	BL	1.48	4.93E-02	6.59E-03	1.19E-02	3.06E-03	2.88E-03	1.03E-03
TR-h2-6*	BL	1.48	5.16E-02	2.45E-03	1.64E-02	8.92E-04	6.54E-03	5.29E-04
TR-h3-1**	BL	1.03	3.97E-03	8.06E-05	3.23E-05	4.54E-06	6.50E-07	2.61E-07
TR-h3-2	BL	1.03	3.26E-03	1.18E-04	9.80E-05	1.54E-05	2.65E-06	1.48E-06
TR-h3-3	BL	1.03	1.42E-02	3.67E-04	5.30E-04	5.11E-05	3.31E-05	9.19E-06
TR-h3-4	BL	1.03	1.06E-02	1.45E-03	1.97E-03	2.26E-04	5.03E-04	1.34E-04
TR-h3-5*	BL	1.03	1.70E-02	2.18E-03	4.56E-03	9.22E-04	1.26E-03	4.40E-04
TR-h3-6*	BL	1.03	2.17E-02	4.41E-03	7.66E-03	2.28E-03	3.29E-03	1.25E-03
TR-h4-1**	BL	0.73	1.37E-03	8.79E-05	1.17E-05	3.24E-06	1.18E-07	8.76E-08
TR-h4-2**	BL	0.73	1.69E-03	2.35E-04	3.75E-05	2.03E-05	1.00E-06	8.20E-07
TR-h4-3	BL	0.73	4.97E-03	3.51E-04	1.23E-04	2.74E-05	5.75E-06	3.32E-06
TR-h4-4	BL	0.73	4.96E-03	2.23E-04	9.10E-04	2.40E-04	4.27E-04	1.64E-04
TR-h4-5*	BL	0.73	7.42E-03	5.16E-04	1.78E-03	5.05E-04	5.04E-04	7.01E-05
TR-h4-6*	BL	0.73	7.75E-03	8.76E-04	1.91E-03	1.53E-04	5.69E-04	1.35E-04

* Wave Breaking, **C_D values excluded from figures

Table 9-31 Summary table of the average variance, var_{avg} , for harmonics 1 – 3 at WG 8 – 12 with the corresponding standard deviation of the variance, $\text{var}_{\text{avg}} \sigma$, for baseline (BL) layout.

Trial	Layout	h_v	WG 8 - 12 var_{avg} , Harmonic 1	$\text{var}_{\text{avg}} \sigma$, Harmonic 1	WG 8 - 12 var_{avg} , Harmonic 2	$\text{var}_{\text{avg}} \sigma$, Harmonic 2	WG 8 - 12 var_{avg} , Harmonic 3	$\text{var}_{\text{avg}} \sigma$, Harmonic 3
(-)	(-)	(m)	(m^2)	(m^2)	(m^2)	(m^2)	(m^2)	(m^2)
TR-h1-1	BL	1.85	1.79E-02	3.05E-04	2.44E-04	3.48E-05	4.56E-06	2.35E-06
TR-h1-2**	BL	1.85	1.67E-02	5.43E-04	1.11E-03	1.52E-04	4.60E-05	1.70E-05
TR-h1-3	BL	1.85	6.27E-02	1.73E-03	2.97E-03	2.51E-04	2.25E-04	4.13E-05
TR-h1-4	BL	1.85	2.05E-02	3.52E-04	8.00E+01	8.00E+01	8.80E-03	4.88E-04
TR-h2-1	BL	1.48	7.02E-03	2.33E-04	5.75E-05	8.62E-06	9.94E-07	3.60E-07
TR-h2-2	BL	1.48	7.21E-03	4.35E-04	2.96E-04	1.25E-04	8.91E-06	4.72E-06
TR-h2-3**	BL	1.48	2.61E-02	1.19E-03	8.34E-04	1.56E-04	5.14E-05	2.85E-05
TR-h2-4	BL	1.48	9.70E-03	5.77E-04	9.21E-03	5.46E-04	3.74E-03	3.12E-04
TR-h2-5*	BL	1.48	1.24E-02	7.43E-04	3.19E-03	2.00E-04	4.18E-04	5.03E-05
TR-h2-6*	BL	1.48	1.11E-02	3.04E-04	7.08E-03	1.72E-04	1.65E-03	4.22E-04
TR-h3-1**	BL	1.03	2.66E-03	6.13E-05	1.88E-05	5.31E-06	2.45E-07	2.18E-07
TR-h3-2	BL	1.03	2.58E-03	7.87E-05	7.50E-05	1.25E-05	1.75E-06	4.75E-07
TR-h3-3	BL	1.03	8.88E-03	4.39E-04	2.32E-04	4.82E-05	1.21E-05	7.85E-06
TR-h3-4	BL	1.03	4.03E-03	7.04E-04	5.85E-03	3.15E-04	1.65E-03	1.62E-04
TR-h3-5*	BL	1.03	4.04E-03	3.22E-04	2.08E-03	1.25E-04	1.75E-04	2.52E-05
TR-h3-6*	BL	1.03	3.77E-03	6.86E-04	1.04E-03	1.14E-04	7.16E-04	1.64E-04
TR-h4-1**	BL	0.73	6.70E-04	4.39E-05	2.92E-06	1.28E-06	5.09E-08	2.78E-08
TR-h4-2**	BL	0.73	1.21E-03	5.34E-05	2.95E-05	1.60E-05	6.19E-07	2.43E-07
TR-h4-3	BL	0.73	3.00E-03	1.27E-04	6.64E-05	2.55E-05	3.51E-06	2.63E-06
TR-h4-4	BL	0.73	2.45E-03	5.00E-04	2.11E-03	9.21E-05	6.12E-04	8.54E-05
TR-h4-5*	BL	0.73	2.36E-03	1.89E-04	1.19E-04	2.74E-05	3.09E-05	2.39E-05
TR-h4-6*	BL	0.73	1.10E-03	1.44E-04	6.40E-04	6.75E-05	1.49E-04	1.93E-05

* Wave Breaking, ** C_D values excluded from figures

Table 9-32 Summary table of the average variance, var_{avg} , for harmonics 1 – 3 at WG 3 – 7 with the corresponding standard deviation of the variance, $\text{var}_{\text{avg}} \sigma$, and ratio of HD var_{avg} /BL var_{avg} , for the high-density (HD) layout.

Trial	Trial #	Layout	h_v	Wave Breaking	WG 3 - 7 var_{avg} , Harmonic 1	$\text{var}_{\text{avg}} \sigma$, $\frac{\text{HD var}_{\text{avg}}}{\text{BL var}_{\text{avg}}}$	WG 3 - 7 var_{avg} , Harmonic 2	$\text{var}_{\text{avg}} \sigma$, $\frac{\text{HD var}_{\text{avg}}}{\text{BL var}_{\text{avg}}}$	WG 3 - 7 var_{avg} , Harmonic 3	$\text{var}_{\text{avg}} \sigma$, $\frac{\text{HD var}_{\text{avg}}}{\text{BL var}_{\text{avg}}}$	
(-)	(-)	(-)	(m)	(-)	(m^2)	(m^2)	(-)	(m^2)	(-)	(m^2)	(-)
TR-h1-1	1	HD	1.85	-	1.89E-02	1.04E-03	0.93	2.39E-04	9.79E-05	0.90	3.38E-06
TR-h1-2**	2	HD	1.85	-	1.60E-02	8.57E-04	0.97	1.01E-03	1.75E-04	0.89	4.23E-05
TR-h1-3	3	HD	1.85	-	6.18E-02	3.29E-03	0.97	3.62E-03	4.35E-04	0.96	3.59E-04
TR-h1-4	4	HD	1.85	-	4.89E-02	2.82E-03	0.97	7.60E-03	5.06E-04	0.89	1.95E-03
TR-h3-1**	11	HD	1.03	-	3.49E-03	1.49E-04	0.88	1.91E-05	8.26E-06	0.59	6.06E-07
TR-h3-2	12	HD	1.03	-	3.22E-03	1.36E-04	0.99	8.53E-05	6.40E-06	0.87	1.71E-06
TR-h3-3	13	HD	1.03	-	1.27E-02	4.78E-04	0.89	3.81E-04	7.72E-05	0.72	2.15E-05
TR-h3-4	14	HD	1.03	-	1.11E-02	1.22E-03	1.04	1.72E-03	3.53E-04	0.87	3.53E-04
TR-h3-5*	15	HD	1.03	Y	1.90E-02	1.90E-03	1.12	5.73E-03	1.11E-03	1.26	1.82E-03
TR-h3-6*	16	HD	1.03	Y	2.80E-02	4.18E-03	1.29	1.03E-02	9.36E-04	1.34	5.75E-03
TR-h4-1**	17	HD	0.73	-	1.57E-03	1.44E-04	1.14	1.30E-05	6.82E-06	1.12	2.00E-07
TR-h4-2**	18	HD	0.73	-	1.59E-03	1.79E-04	0.94	2.86E-05	1.35E-05	0.76	1.25E-06
TR-h4-3	19	HD	0.73	-	5.67E-03	6.00E-04	1.14	1.54E-04	3.99E-05	1.25	7.49E-06
TR-h4-4	20	HD	0.73	-	3.95E-03	1.25E-04	0.80	7.63E-04	1.76E-04	0.84	2.63E-04
TR-h4-5*	21	HD	0.73	Y	7.42E-03	3.24E-04	1.00	1.78E-03	4.41E-04	1.00	4.98E-04
TR-h4-6*	22	HD	0.73	Y	7.32E-03	7.57E-04	0.94	2.02E-03	2.19E-04	1.06	4.80E-04

* Wave Breaking, ** C_D values excluded from figures

Table 9-33 Summary table of the average variance, var_{avg} , for harmonics 1 – 3 at WG 8 – 12 with the corresponding standard deviation of the variance, $\text{var}_{\text{avg}} \sigma$, and ratio of HD $\text{var}_{\text{avg}} / \text{BL} \text{var}_{\text{avg}}$, for the high-density (HD) layout.

Trial	Trial #	Layout	h_v	Wave Breaking	WG 8 - 12 var_{avg} , Harmonic 1	$\text{var}_{\text{avg}} \sigma$, Harmonic 1	$\frac{\text{HD} \text{var}_{\text{avg}}}{\text{BL} \text{var}_{\text{avg}}}$	WG 8 - 12 var_{avg} , Harmonic 2	$\text{var}_{\text{avg}} \sigma$, Harmonic 2	$\frac{\text{HD} \text{var}_{\text{avg}}}{\text{BL} \text{var}_{\text{avg}}}$	WG 8 - 12 var_{avg} , Harmonic 3	$\text{var}_{\text{avg}} \sigma$, Harmonic 3	$\frac{\text{HD} \text{var}_{\text{avg}}}{\text{BL} \text{var}_{\text{avg}}}$
(-)	(-)	(-)	(m)	(-)	(m^2)	(m^2)	(-)	(m^2)	(m^2)	(-)	(m^2)	(m^2)	(-)
TR-h1-1	1	HD	1.85	-	1.15E-02	2.13E-04	0.64	1.08E-04	2.37E-05	0.44	1.88E-06	6.38E-07	0.41
TR-h1-2**	2	HD	1.85	-	1.19E-02	1.70E-04	0.71	5.37E-04	1.36E-04	0.49	1.64E-05	7.27E-06	0.36
TR-h1-3	3	HD	1.85	-	3.19E-02	4.00E-04	0.51	1.08E-03	1.01E-04	0.36	6.18E-05	1.60E-05	0.27
TR-h1-4	4	HD	1.85	-	1.34E-02	2.15E-04	0.65	1.11E-02	1.82E-03	0.65	6.40E-03	5.73E-04	0.73
TR-h3-1**	11	HD	1.03	-	1.90E-03	2.33E-05	0.72	8.09E-06	2.14E-06	0.43	2.90E-07	5.23E-08	1.19
TR-h3-2	12	HD	1.03	-	1.83E-03	3.31E-05	0.71	3.57E-05	7.25E-06	0.48	6.28E-07	3.16E-07	0.36
TR-h3-3	13	HD	1.03	-	5.16E-03	1.56E-04	0.58	6.26E-05	6.63E-06	0.27	1.88E-06	1.38E-06	0.16
TR-h3-4	14	HD	1.03	-	3.18E-03	3.55E-04	0.79	3.05E-03	2.13E-04	0.52	6.00E-04	2.59E-05	0.36
TR-h3-5*	15	HD	1.03	Y	3.62E-03	3.85E-04	0.90	2.01E-03	3.85E-04	0.97	3.51E-04	1.08E-04	2.01
TR-h3-6*	16	HD	1.03	Y	3.39E-03	7.36E-04	0.90	1.51E-03	1.39E-04	1.45	1.57E-03	2.95E-04	2.19
TR-h4-1**	17	HD	0.73	-	4.76E-04	1.93E-05	0.71	1.56E-06	6.46E-07	0.53	2.71E-08	1.41E-08	0.53
TR-h4-2**	18	HD	0.73	-	7.67E-04	7.16E-05	0.64	1.15E-05	3.59E-06	0.39	2.35E-07	1.51E-07	0.38
TR-h4-3	19	HD	0.73	-	1.43E-03	4.68E-05	0.47	1.27E-05	5.49E-06	0.19	2.83E-07	2.99E-07	0.08
TR-h4-4	20	HD	0.73	-	1.03E-03	2.26E-04	0.42	1.17E-03	4.54E-05	0.56	2.16E-04	3.62E-05	0.35
TR-h4-5*	21	HD	0.73	Y	2.38E-03	7.60E-05	1.01	7.36E-05	7.30E-05	0.62	4.60E-06	3.60E-06	0.15
TR-h4-6*	22	HD	0.73	Y	8.97E-04	1.92E-04	0.82	1.07E-03	2.04E-04	1.68	5.49E-05	2.47E-05	0.37

* Wave Breaking, ** C_D values excluded from figures

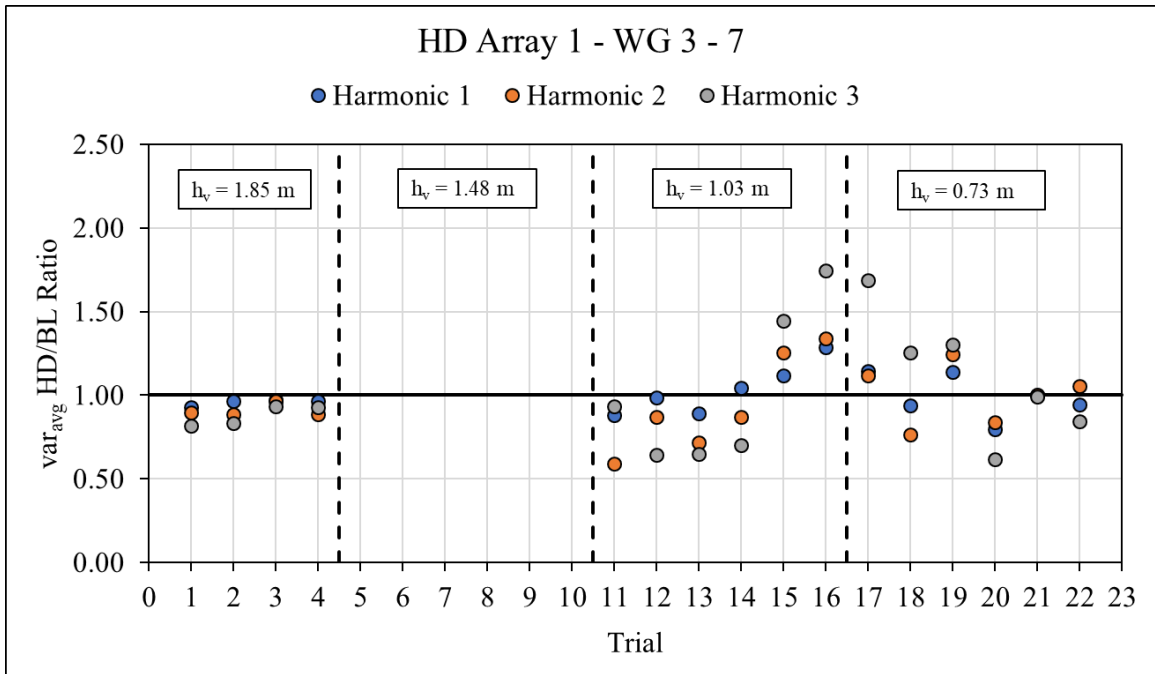


Figure 9-103 Ratio of HD/BL var_{avg} , versus Trial number for harmonic: 1 (blue circles), 2 (orange circles), and 3 (grey circles) for WG 3 – 7. Trial number found in Table 9-32.

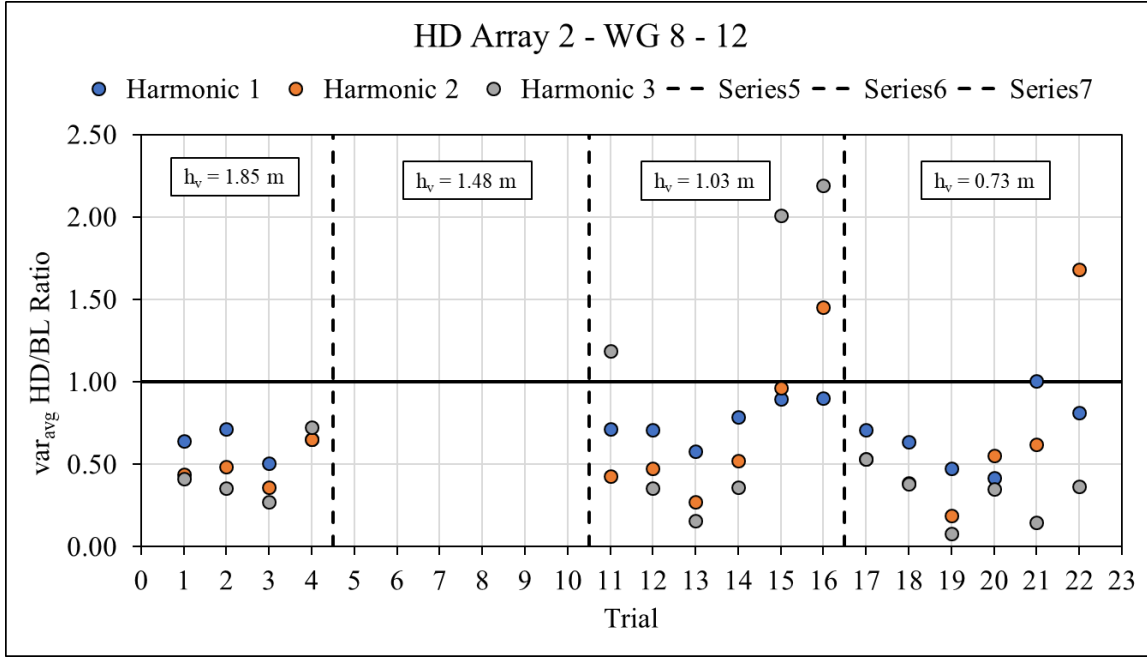


Figure 9-104 Ratio of HD/BL var_{avg}, versus Trial number for harmonic: 1 (blue circles), 2 (orange circles), and 3 (grey circles) for WG 8 – 12. Trial number found in Table 10-33.

Table 9-34 Summary table of the average variance, var_{avg}, for harmonics 1 – 3 at WG 3 – 7 with the corresponding standard deviation of variance, var_{avg} σ, and ratio of LD var_{avg}/BL var_{avg}, for the low-density (LD) layout.

Trial	Trial #	Layout	h _v	Wave Breaking	WG 3 - 7 var _{avg} , Harmonic 1		var _{avg} σ, Harmonic 1	HD var _{avg} / BL var _{avg}	WG 3 - 7 var _{avg} , Harmonic 2		var _{avg} σ, Harmonic 2	HD var _{avg} / BL var _{avg}	WG 3 - 7 var _{avg} , Harmonic 3		var _{avg} σ, Harmonic 3	HD var _{avg} / BL var _{avg}
					(-)	(-)	(m)	(-)	(m ²)	(m ²)	(-)	(m ²)	(m ²)	(-)	(m ²)	(-)
TR-h1-1	1	LD	1.85	-	2.15E-02	3.71E-04	1.05	2.92E-04	8.37E-05	1.10	5.64E-06	2.95E-06	1.37			
TR-h1-2**	2	LD	1.85	-	1.75E-02	2.75E-04	1.06	1.16E-03	1.56E-04	1.02	5.04E-05	8.39E-06	0.99			
TR-h1-3	3	LD	1.85	-	6.94E-02	2.56E-03	1.09	3.85E-03	3.79E-04	1.03	3.38E-04	4.43E-05	0.88			
TR-h1-4	4	LD	1.85	-	5.27E-02	1.95E-03	1.04	9.19E-03	9.57E-04	1.07	2.44E-03	4.57E-04	1.16			
TR-h2-1	5	LD	1.48	-	8.93E-03	4.03E-04	1.10	9.14E-05	2.12E-05	1.26	2.95E-06	1.53E-06	1.94			
TR-h2-2	6	LD	1.48	-	8.48E-03	9.79E-05	1.12	4.49E-04	4.14E-05	1.40	1.17E-05	3.33E-06	1.28			
TR-h2-3**	7	LD	1.48	-	3.21E-02	1.74E-03	1.30	1.24E-03	3.16E-04	1.63	8.27E-05	4.60E-05	2.16			
TR-h2-4	8	LD	1.48	-	2.33E-02	9.42E-04	1.11	4.06E-03	2.80E-04	1.27	1.11E-03	2.53E-04	1.51			
TR-h2-5*	9	LD	1.48	Y	5.27E-02	7.74E-03	1.07	1.32E-02	4.47E-03	1.11	3.45E-03	1.54E-03	1.20			
TR-h2-6*	10	LD	1.48	Y	5.26E-02	4.03E-03	1.02	1.93E-02	1.29E-03	1.18	7.17E-03	6.15E-04	1.10			
TR-h3-1**	11	LD	1.03	-	3.10E-03	1.71E-04	0.78	1.64E-05	4.01E-06	0.51	7.59E-07	5.87E-07	1.17			
TR-h3-2	12	LD	1.03	-	3.26E-03	1.47E-04	1.00	8.91E-05	1.93E-05	0.91	2.75E-06	1.82E-06	1.04			
TR-h3-3	13	LD	1.03	-	1.24E-02	7.09E-04	0.87	4.36E-04	6.54E-05	0.82	2.78E-05	1.40E-05	0.84			
TR-h3-4	14	LD	1.03	-	1.13E-02	1.46E-03	1.06	2.09E-03	2.46E-04	1.06	4.98E-04	1.73E-04	0.99			
TR-h3-5*	15	LD	1.03	Y	1.75E-02	1.17E-03	1.03	4.95E-03	1.12E-03	1.09	1.36E-03	5.34E-04	1.08			
TR-h3-6*	16	LD	1.03	Y	2.43E-02	6.33E-03	1.12	9.69E-03	3.28E-03	1.27	4.33E-03	1.96E-03	1.32			
TR-h4-1**	17	LD	0.73	-	1.47E-03	1.14E-04	1.07	1.31E-05	3.00E-06	1.12	8.18E-08	9.49E-08	0.69			
TR-h4-2**	18	LD	0.73	-	1.54E-03	2.45E-04	0.91	3.39E-05	2.04E-05	0.90	1.48E-06	1.85E-06	1.47			
TR-h4-3	19	LD	0.73	-	5.17E-03	3.69E-04	1.04	1.31E-04	2.20E-05	1.06	7.88E-06	3.72E-06	1.37			
TR-h4-4	20	LD	0.73	-	4.74E-03	1.60E-04	0.95	8.70E-04	2.03E-04	0.96	4.22E-04	1.48E-04	0.99			
TR-h4-5*	21	LD	0.73	Y	7.14E-03	4.28E-04	0.96	1.77E-03	5.32E-04	1.00	4.99E-04	1.04E-04	0.99			
TR-h4-6*	22	LD	0.73	Y	7.44E-03	6.78E-04	0.96	1.95E-03	1.63E-04	1.02	5.77E-04	2.34E-04	1.01			

* Wave Breaking, **C_D values excluded from figures

Table 9-35 Summary table of the average variance, var_{avg} , for harmonics 1 – 3 at WG 8 – 12 with the corresponding standard deviation of the variance, $\text{var}_{\text{avg}} \sigma$, and ratio of LD $\text{var}_{\text{avg}} / \text{BL} \text{var}_{\text{avg}}$, for the low-density (LD) layout.

Trial	Trial #	Layout	h_v	Wave Breaking	WG 8 - 12 var_{avg} , Harmonic 1	$\text{var}_{\text{avg}} \sigma$, Harmonic 1	$\frac{\text{HD} \text{var}_{\text{avg}}}{\text{BL} \text{var}_{\text{avg}}}$	WG 8 - 12 var_{avg} , Harmonic 2	$\text{var}_{\text{avg}} \sigma$, Harmonic 2	$\frac{\text{HD} \text{var}_{\text{avg}}}{\text{BL} \text{var}_{\text{avg}}}$	WG 8 - 12 var_{avg} , Harmonic 3	$\text{var}_{\text{avg}} \sigma$, Harmonic 3	$\frac{\text{HD} \text{var}_{\text{avg}}}{\text{BL} \text{var}_{\text{avg}}}$
(-)	(-)	(-)	(m)	(-)	(m^2)	(m^2)	(-)	(m^2)	(m^2)	(-)	(m^2)	(m^2)	(-)
TR-h1-1	1	LD	1.85	-	1.63E-02	1.06E-04	0.91	2.08E-04	2.97E-05	0.85	4.82E-06	2.27E-06	1.06
TR-h1-2**	2	LD	1.85	-	1.49E-02	2.95E-04	0.89	7.92E-04	1.27E-04	0.72	3.24E-05	5.15E-06	0.70
TR-h1-3	3	LD	1.85	-	5.10E-02	4.60E-04	0.81	2.37E-03	1.72E-04	0.80	2.06E-04	4.56E-05	0.92
TR-h1-4	4	LD	1.85	-	1.72E-02	3.58E-04	0.84	1.50E-02	1.50E-03	0.89	8.37E-03	6.41E-04	0.95
TR-h2-1	5	LD	1.48	-	5.80E-03	9.73E-05	0.83	4.29E-05	9.02E-06	0.75	1.43E-06	8.34E-07	1.44
TR-h2-2	6	LD	1.48	-	6.06E-03	3.17E-04	0.84	2.21E-04	7.54E-05	0.74	7.49E-06	3.87E-06	0.84
TR-h2-3**	7	LD	1.48	-	1.95E-02	1.25E-03	0.75	3.56E-04	1.66E-04	0.43	2.01E-05	1.39E-05	0.39
TR-h2-4	8	LD	1.48	-	8.41E-03	2.99E-04	0.87	7.63E-03	3.66E-04	0.83	3.49E-03	2.85E-04	0.93
TR-h2-5*	9	LD	1.48	Y	1.32E-02	3.50E-04	1.06	4.68E-03	5.59E-04	1.47	7.50E-04	3.51E-05	1.79
TR-h2-6*	10	LD	1.48	Y	1.06E-02	2.89E-04	0.95	6.55E-03	3.50E-04	0.93	2.28E-03	3.69E-04	1.38
TR-h3-1**	11	LD	1.03	-	2.46E-03	8.07E-05	0.92	1.46E-05	3.55E-06	0.77	3.83E-07	1.69E-07	1.57
TR-h3-2	12	LD	1.03	-	2.44E-03	4.69E-05	0.94	6.71E-05	1.50E-05	0.89	1.56E-06	6.75E-07	0.89
TR-h3-3	13	LD	1.03	-	8.51E-03	1.90E-04	0.96	1.74E-04	3.34E-05	0.75	5.44E-06	3.11E-06	0.45
TR-h3-4	14	LD	1.03	-	3.36E-03	4.67E-04	0.84	4.02E-03	2.32E-04	0.69	9.69E-04	7.12E-05	0.59
TR-h3-5*	15	LD	1.03	Y	4.05E-03	4.34E-04	1.00	3.15E-03	1.57E-04	1.51	9.01E-05	3.40E-05	0.52
TR-h3-6*	16	LD	1.03	Y	4.35E-03	7.29E-04	1.15	1.51E-03	8.43E-05	1.46	1.63E-03	3.20E-04	2.28
TR-h4-1**	17	LD	0.73	-	6.90E-04	4.81E-05	1.03	3.81E-06	1.37E-06	1.30	6.34E-08	5.13E-08	1.24
TR-h4-2**	18	LD	0.73	-	9.42E-04	4.82E-05	0.78	2.09E-05	8.98E-06	0.71	4.15E-07	4.28E-07	0.67
TR-h4-3	19	LD	0.73	-	1.97E-03	8.06E-05	0.66	2.72E-05	1.39E-05	0.41	1.95E-06	1.60E-06	0.55
TR-h4-4	20	LD	0.73	-	1.50E-03	2.75E-04	0.61	1.36E-03	5.67E-05	0.64	3.14E-04	9.33E-05	0.51
TR-h4-5*	21	LD	0.73	Y	2.53E-03	2.45E-05	1.07	6.67E-05	5.71E-05	0.56	3.55E-06	3.44E-06	0.11
TR-h4-6*	22	LD	0.73	Y	1.08E-03	1.57E-04	0.98	1.47E-03	2.88E-04	2.29	1.61E-04	1.32E-04	1.08

* Wave Breaking, **Cd values excluded from figures

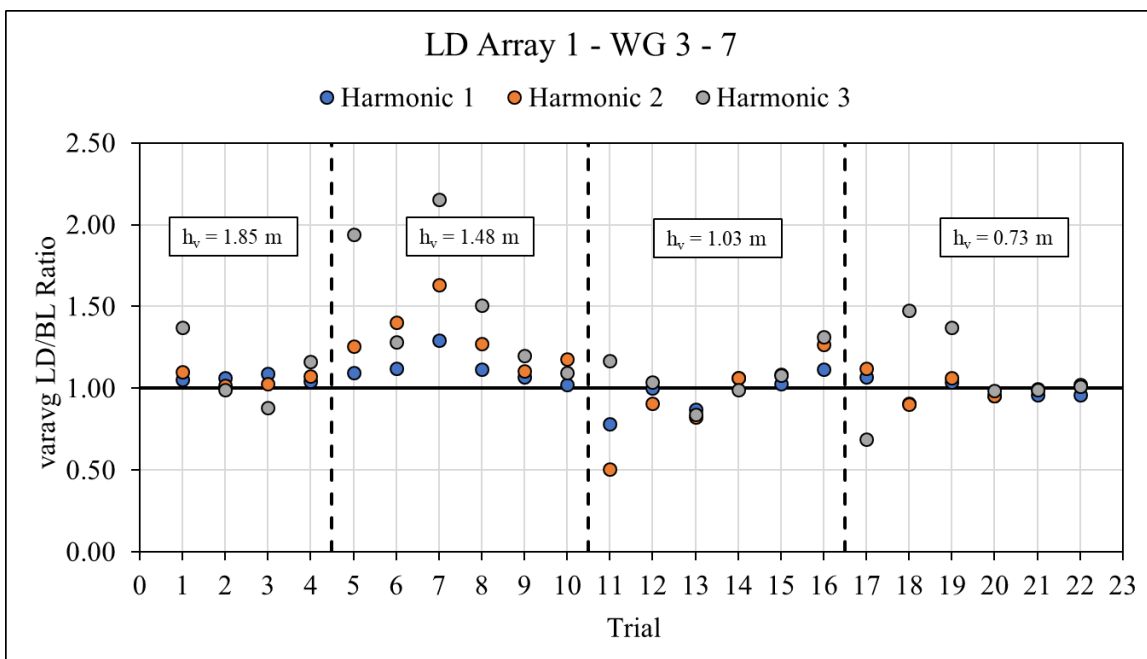


Figure 9-105 Ratio of LD/BL var_{avg} , versus Trial number for harmonic: 1 (blue circles), 2 (orange circles), and 3 (grey circles) for WG 3 – 7. Trial number found in Table 9-34.

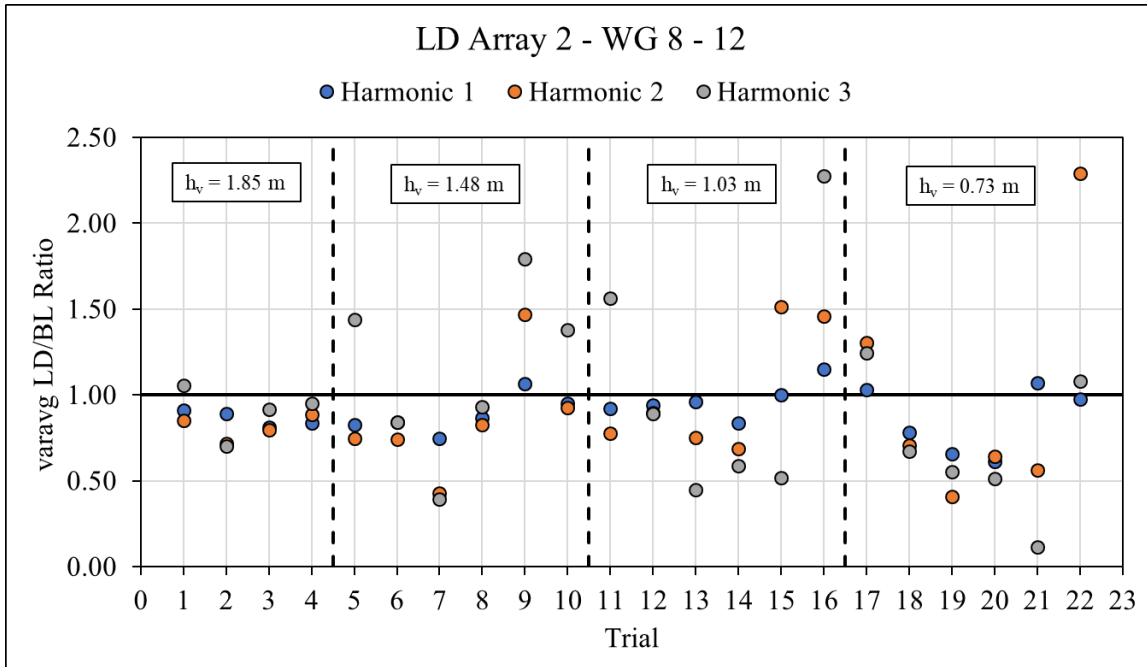


Figure 9-106 Ratio of LD/BL var_{avg} , versus Trial number for harmonic: 1 (blue circles), 2 (orange circles), and 3 (grey circles) for WG 8 – 12. Trial number found in Table 10-35.

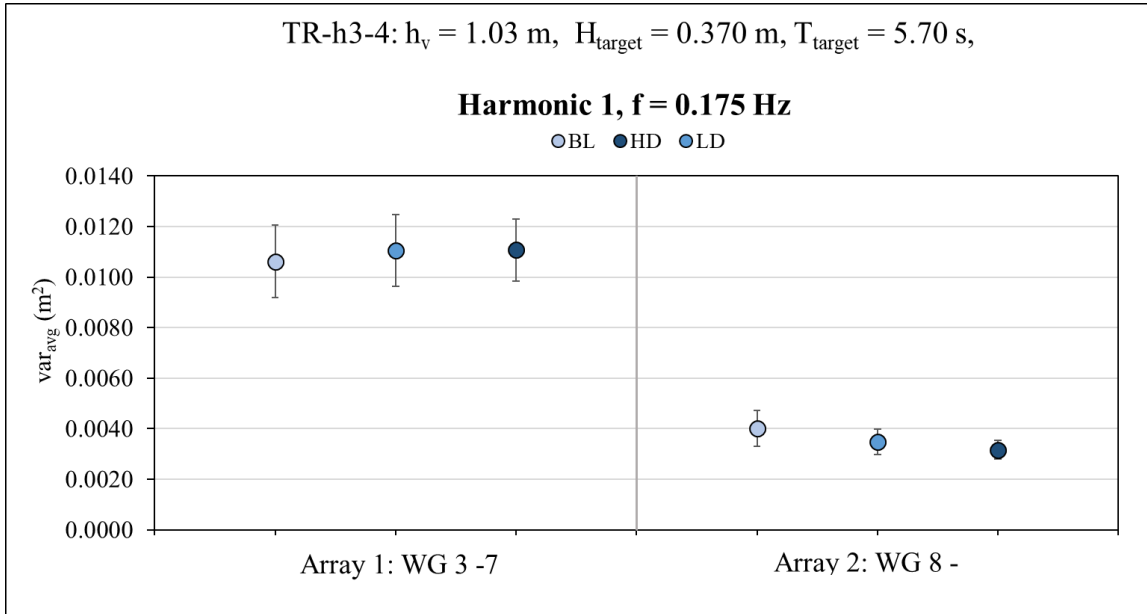


Figure 9-107 Average variance, var_{avg} , of case TR-h3-4 for harmonic 1 at the baseline (BL) (light blue circles), high-density (HD) (dark blue circles), and low-density (LD) (intermediate blue circles) layouts for WG 3-7 and WG 8 – 12 with limit bars \pm the standard deviation of the average variance, $\text{var}_{\text{avg}} \sigma$.

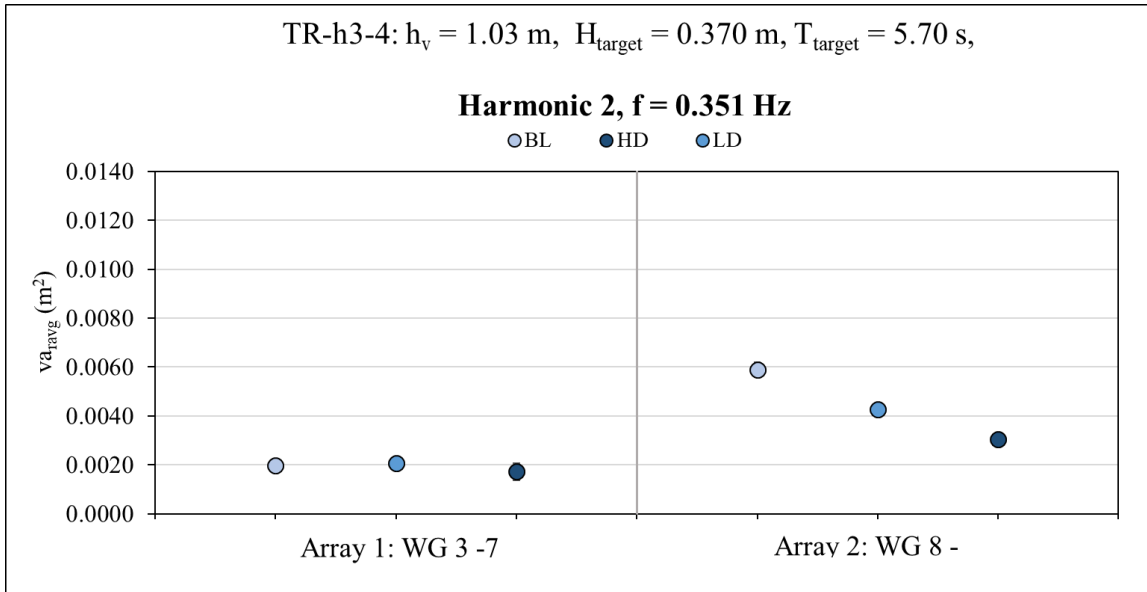


Figure 9-108 Average variance, var_{avg} , of case TR-h3-4 for harmonic 2 at the BL (light blue circles), HD (dark blue circles) and LD (intermediate blue circles) for WG 3-7 and WG 8 – 12 with limit bars \pm the standard deviation of the average variance, $\text{var}_{\text{avg}} \sigma$.

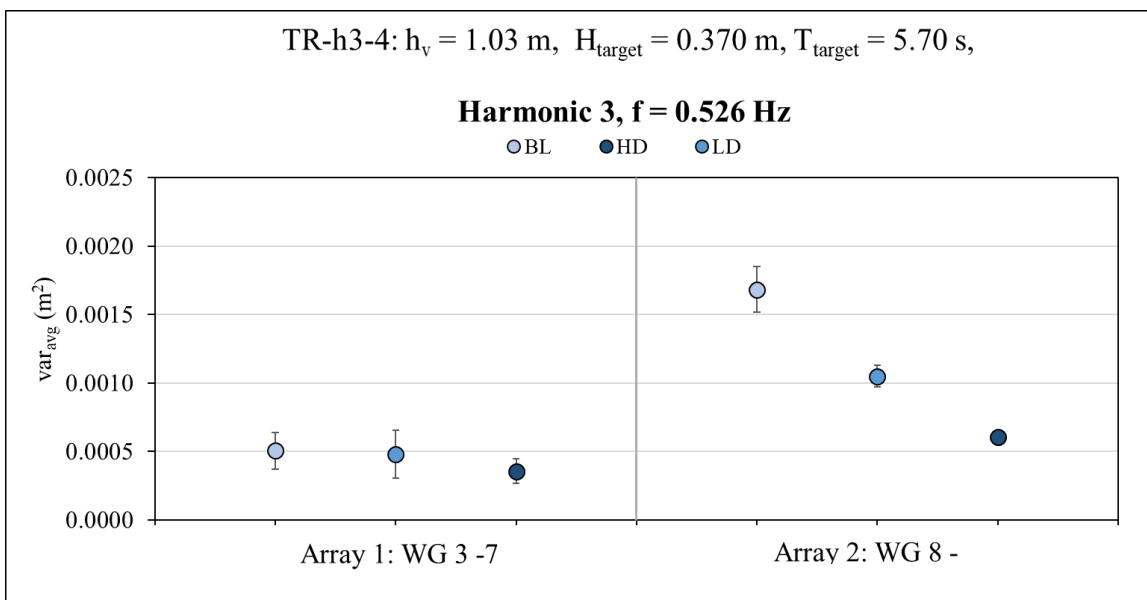


Figure 9-109 Average variance, var_{avg} , of case TR-h3-4 for harmonic 3 at the BL (light blue circles), HD (dark blue circles) and LD (intermediate blue circles) for WG 3-7 and WG 8 – 12 with limit bars \pm the standard deviation of the average variance, $\text{var}_{\text{avg}} \sigma$.

Appendix L Study Dissemination

Table 9-36 Table of presentations study's results were disseminated.

Presentation	Date	Number of attendees
ASBPA Coastal Conference. "Navigating Stormy Times"	10/13/2020	~50
NHERI DesignSafe Webinar	12/4/2020	~50
OSU Graduate Student Outreach	12/4/2020	11
Lake Worth Lagoon Initiative Habitat Working Group	05/04/2020	~50
Eastern Central Estuarine Restoration Team Steering Committee, Florida	5/25/2021	~50
Kiernan Kelty M.S. Thesis Defense	6/01/2021	44

Box links to presentation power points:

- ASBPA. "Navigating Stormy Times":
 - Box\NHERI_Mangroves\ASBPA Presentation
- NHERI DesignSafe:
 - Box\NHERI_Mangroves\12-4-2020-OSU Outreach Day
- OSU Graduate Student Outreach:
 - Box\NHERI_Mangroves\12-4-2020-OSU Outreach Day
- Lake Worth Lagoon Initiative Habitat Working Group (LWLI):
 - Box\NHERI_Mangroves\2021_05_04_LWLI_Habitat_Meeting_Dan_Tori_Kiernan
- East Central Estuarine Restoration Team Steering Committee, FL (ECERT):

- Box\NHERI_Mangroves\2020_05_25_ECERT_Meeting_Dan_Tori_Kiernan
- Kiernan Kelty M.S. Thesis Defense:
 - Box\NHERI_Mangroves\2021_06_01_Kelty MS Thesis defense\Kelty_MS_defense_PPT_final